

# RESUMMATION OF NON-GLOBAL LOGARITHMS

Inaugural dissertation  
of the Faculty of Science,  
University of Bern

presented by  
MARCEL BALSIGER  
from Belp/BE

Supervisor of the doctoral thesis:  
PROF. DR. THOMAS BECHER  
Institute for Theoretical Physics  
Albert Einstein Center for Fundamental Physics  
University of Bern

Original document saved on the web server of the University Library of Bern



This work is licensed under a  
Creative Commons Attribution-Non-Commercial-No derivative works 2.5 Switzerland  
licence. To see the licence go to <http://creativecommons.org/licenses/by-nc-nd/2.5/ch/> or write  
to Creative Commons, 171 Second Street, Suite 300, San Francisco, California 94105, USA.

## Copyright Notice

This document is licensed under the Creative Commons Attribution-Non-Commercial-No derivative works 2.5 Switzerland. <http://creativecommons.org/licenses/by-nc-nd/2.5/ch/>

**You are free:**



to copy, distribute, display, and perform the work

**Under the following conditions:**



**Attribution.** You must give the original author credit.



**Non-Commercial.** You may not use this work for commercial purposes.



**No derivative works.** You may not alter, transform, or build upon this work..

For any reuse or distribution, you must take clear to others the license terms of this work.

Any of these conditions can be waived if you get permission from the copyright holder.

Nothing in this license impairs or restricts the author's moral rights according to Swiss law.

The detailed license agreement can be found at:

<http://creativecommons.org/licenses/by-nc-nd/2.5/ch/legalcode.de>



RESUMMATION OF  
NON-GLOBAL LOGARITHMS

Inaugural dissertation  
of the Faculty of Science,  
University of Bern

presented by  
MARCEL BALSIGER  
from Belp/BE

Supervisor of the doctoral thesis:  
PROF. DR. THOMAS BECHER  
Institute for Theoretical Physics  
Albert Einstein Center for Fundamental Physics  
University of Bern

Accepted by the Faculty of Science.

Bern, 24.09.2020

The Dean

Prof. Dr. Zoltán Balogh



## ABSTRACT

---

Most of what we know about the laws of physics at the sub-nuclear length scale is derived from analyzing the outcomes of high-energy collisions of particles. Size and sophistication of such experiments have steadily increased, producing more accurate and precise measurements. To interpret these and to understand the underlying physics we need to develop and improve state-of-the-art theoretical tools to predict collider observables in a more refined way.

Such a tool is Soft-Collinear Effective Theory, which is a theoretical framework for calculations that involve particles at widely separated energy scales. In a collider experiment, such hierarchies are very common. In the analysis of detector patterns after a collision event, one observes regions where a lot of energetic particles were measured close together, and a small amount of energy that is uniformly distributed in the entire detector. This name-giving collinear and soft radiation is captured by this specific effective theory.

When calculating the cross sections of such multi-scale problems, corrections that are normally suppressed by orders of the coupling constant are multiplied by a logarithm of the ratio of the scales. In the case of the interjet energy flow, for example, we have particles of high energy  $E_{\text{in}} \sim Q$  produced at the hard interaction inside the jets and soft particles of energy  $E_{\text{out}} \sim \beta Q$  outside the jets. If these scales are far separated, the logarithms  $\ln(\beta)$  become big and can ruin the perturbative expansion in the coupling constants. One needs to resum these logarithmically enhanced terms to all orders. The so-called non-global logarithms that arise in the presence of hard phase-space cuts are especially difficult to resum. A simple exponentiation of the logarithmically enhanced terms is in this case not possible.

Starting from a factorization theorem in Soft-Collinear Effective Theory, we derive a parton shower equation for the resummation of non-global logarithms. We implement the shower in a dedicated, easy-to-use computer code `NGL_RESUM` to resum such logarithms at leading logarithmic accuracy in the large- $N_c$  limit. We use tree-level event files in the common Les Houches format as input and explicitly calculate observables such as the interjet energy flow and photon isolation cone cross sections at leading-logarithmic accuracy.

Since our parton shower is derived from first principles and based on renormalization group evolution, it is clear what ingredients we have to include to perform the resummation at subleading logarithmic accuracy. After adding the observable-dependent next-to-leading order corrections for di-jet processes, we are able to take a first step towards the higher-logarithmic resummation for the interjet energy flow and the jet mass. To reach full next-to-leading logarithmic accuracy, one would also have to include the two-loop anomalous dimension. This is indeed very challenging and has not been reached thus far.

In a final step, we extend the framework to get away from the high-energy limit and include massive quarks. At this point, `NGL_RESUM` becomes a general-purpose parton shower to resum non-global logarithms at leading logarithmic accuracy for a plethora of observables. We apply it to compute the interjet energy flow in  $t\bar{t}$ -production.



## ACKNOWLEDGEMENTS

---

First and foremost I would like to thank Thomas Becher. He represents the very best supervisor any PhD student could hope for. Even though his calendar is filled by appointments of various origins, he always sacrificed time to explain problems and discuss possible solutions with utmost passion. Always cheerful when something worked, always encouraging when something did not – he has been my major motivator throughout my time as a PhD student and without him, this undertaking would have not been possible.

Further, I would also like to thank Andrea Ferrogli, professor at New York City College of Technology, and Ding Yu Shao, former Postdoc of Thomas. I will always be grateful for the time I was able to spend in New York visiting Andrea – even though the venue was cooled down to freezing temperatures, we still managed to get quite a bit of work done. And Ding Yu was always there for me to answer questions I did not dare to ask Thomas himself, especially in the early days of my studies.

I am also very grateful to have had such nice people around me at the Institute for Theoretical Physics in general and the PhD students in particular. Special thanks go to Samuel Favrod, Greg Jackson, Laetitia Laub, Joachim Monnard and Francesco Saturnino, who always formed the core of our group and will be missed dearly. I also want to thank Dario Müller, who is currently a Postdoc at Paul Scherrer Institut, for proof-reading parts of the thesis.

My thanks also reach the non-physics circles. Throughout my time at the University of Bern, I had the privilege to serve in the Swiss Armed Forces as the executive officer of Company 3, Headquarters Battalion 25. I extend my thanks to all the officers and men of this outstanding unit, especially former and current commanding officers Cpt Leandro Röthlisberger and Cpt Alesch Wasescha. It has always been a pleasure to swap my dreary office with the command post somewhere in the field. I shall forever stay "*stouz ufs drü!*".

I would also like to extend my gratitude to some former co-students that over the years turned into friends, namely Christa Biberstein (soon-to-be Heinzmann), Samuel Heinzmann, Michael Imhof and Igor Jurosevic. Simon Althaus should also not go forgotten.

Last but not least I thank Nicole Buder, who tried to keep me sane during the last phase of the doctorate.



# CONTENTS

<b>1</b>	<b>INTRODUCTION</b>	<b>1</b>
1.1	Typical scales in particle physics . . . . .	1
1.2	Collider physics: experimental side . . . . .	2
1.2.1	Accelerator . . . . .	3
1.2.2	Detector . . . . .	4
1.2.3	Cross sections . . . . .	7
1.3	Collider physics: theoretical side . . . . .	8
1.3.1	Standard Model of particle physics . . . . .	8
1.3.2	Calculation of cross sections . . . . .	9
1.3.3	Lepton colliders . . . . .	11
1.3.4	Hadron colliders . . . . .	19
1.4	Effective theories . . . . .	23
1.5	Outline . . . . .	25
<b>2</b>	<b>SOFT-COLLINEAR EFFECTIVE THEORY</b>	<b>27</b>
2.1	Energy scales of collider processes . . . . .	27
2.2	Effective Lagrangian . . . . .	29
2.2.1	Soft and collinear terms . . . . .	30
2.2.2	Interaction terms . . . . .	31
2.2.3	Decoupling transformation . . . . .	33
2.3	Resummation by resummation group evolution . . . . .	33
2.4	Resummation of logarithms in wide-angle jet cross sections . . . . .	36
<b>3</b>	<b>NON-GLOBAL LOGARITHMS IN JET AND ISOLATION CROSS SECTIONS</b>	<b>41</b>
3.1	Introduction . . . . .	41
3.2	Factorization for jet cross sections . . . . .	42
3.3	RG evolution as a parton shower . . . . .	45
3.4	Phenomenology of non-global observables . . . . .	48
3.4.1	Qualitative discussion . . . . .	48
3.4.2	Gaps between jets . . . . .	50
3.4.3	Isolation cone cross sections and photon production . . . . .	55
3.4.4	Jet-veto cross sections . . . . .	61
3.5	Conclusion . . . . .	62
3.A	Angular integration with a collinear cutoff . . . . .	63
3.B	Details of the MC algorithm . . . . .	65
3.C	NLO expansion for isolated photon production . . . . .	69
3.D	Narrow-cone limit of photon isolation . . . . .	71
<b>4</b>	<b>NLL' RESUMMATION OF JET MASS</b>	<b>73</b>
4.1	Introduction . . . . .	73
4.2	Interjet energy flow at LL' accuracy . . . . .	76
4.3	NLL' resummation for jet mass . . . . .	83
4.4	Numerical results . . . . .	86
4.4.1	Interjet energy flow . . . . .	87
4.4.2	Jet mass . . . . .	89
4.5	Conclusion and Outlook . . . . .	92

4.A	Hard and soft functions for interjet energy flow . . . . .	94
4.A.1	Hard functions in the slicing scheme . . . . .	94
4.A.2	One-loop soft functions . . . . .	95
4.B	Monte Carlo algorithm for the interjet energy flow . . . . .	96
4.C	Hard and soft functions for the jet mass . . . . .	97
4.D	Monte Carlo algorithm for the jet mass distribution . . . . .	99
4.E	Ingredients for jet mass resummation . . . . .	100
5	RESUMMATION OF NON-GLOBAL LOGARITHMS IN CROSS SECTIONS WITH MASSIVE PARTICLES . . . . .	101
5.1	Introduction . . . . .	101
5.2	Factorization for cross sections involving massive quarks . . . . .	104
5.3	Evaluation of the massive angular phase space integrals . . . . .	110
5.3.1	Boost to the center-of-mass frame . . . . .	111
5.3.2	Evaluation of the angular integral . . . . .	112
5.3.3	Positive definiteness of $\tilde{W}_{ij}^k$ . . . . .	113
5.4	Emissions from massive partons and non-global logarithms . . . . .	114
5.5	Resummation of $t\bar{t}$ production with veto on central jets . . . . .	117
5.6	Conclusion . . . . .	121
5.A	Details of the Monte Carlo algorithm . . . . .	123
5.A.1	Interface to LHE files . . . . .	124
5.A.2	Monte Carlo implementation of $\mathcal{H}_i(t)$ . . . . .	128
5.A.3	Parton shower algorithm . . . . .	133
5.B	Fixed-order expansion of the LL result . . . . .	134
5.B.1	One-loop coefficient . . . . .	134
5.B.2	Two-loop coefficient . . . . .	135
6	CONCLUSION AND OUTLOOK . . . . .	137
	BIBLIOGRAPHY . . . . .	139



## INTRODUCTION

---

*No dream is too big. No challenge is too great. Nothing we want for our future is beyond our reach.*

— Donald Trump

I started working as a theoretical physicist in the field of elementary particles almost four years ago. Four years spent dreaming about computing observables, facing challenges both big and small, naively reaching for the stars. After all this time I find it unquestionable that we should dream big, but I also have to disappoint some readers by noting that some challenges turn out to be too great. For better or worse, nature is not as simple as one might want it to be.

This introductory chapter of my thesis should drive home this fact. It is not aimed at experts, who anyhow already know all about the challenges we are facing. Every now and then, I sprinkle in some more in-depth information for readers with a master's degree in physics under their belt, but I would also want to invite laymen along for the first part of the ride.

The aim of this introduction is to review certain aspects of collider physics. After reviewing the typical length and energy scales of particle physics, I will start with the experimental tools and describe what one is able to measure and why there are limits. I will then review our theoretical understanding and explain what experimental observables at colliders are calculable and to what precision. As one of the most successful tools to achieve improved theoretical calculations, we will then introduce effective theories.

Let me point out that none of the topics covered in this chapter are treated in a thorough way and I refer the interested reader to [1–8]. Everything in this introduction is common knowledge and I will only rarely refer to the original sources in this chapter.

Before going further, I need to add some disclaimers. I will restrain myself from even trying to write down the history of science. While a short historical treatment might provide an interesting bed-time lecture, it would certainly not do justice to any or all the giants on whose shoulders we are standing. I highly recommend [9] to readers interested in the history of physics. I will also not attempt to give an in-depth introduction to general concepts like Quantum Field Theory (QFT) or the Standard Model (SM). These topics are extensively treated in standard literature, I recommend [4, 5].

### 1.1 TYPICAL SCALES IN PARTICLE PHYSICS

Let us start our journey into the world of particle physics by looking at how small the object under consideration are. The smallest distance that can be seen with the naked human eye is about  $100\ \mu\text{m}$  or  $0.1\ \text{mm}$ , which is comparable to the thickness of paper. For everything smaller than that, we need to zoom in and enlarge the picture using some technology. A bacterium is typically about one hundred times smaller, roughly  $1\ \mu\text{m} = 10^{-6}\ \text{m}$ . This length scale can still be made visible by light microscopes. The size of a sucrose molecule is again a thousand times smaller than that, around  $1\ \text{nm} = 10^{-9}\ \text{m}$ . Objects of this length scale can be enlarged by an electron microscope. But we want to go smaller. In the next few

	Unit	SI value of unit
Energy	eV	$1.602176634 \cdot 10^{-19} \text{J}$
Mass	$\frac{\text{eV}}{c^2}$	$1.782662 \cdot 10^{-36} \text{kg}$
Momentum	$\frac{\text{eV}}{c}$	$5.344286 \cdot 10^{-28} \frac{\text{kg m}}{\text{s}}$
Temperature	$\frac{\text{eV}}{k_B}$	$1.160451812 \cdot 10^4 \text{K}$
Time	$\frac{\hbar}{\text{eV}}$	$6.582119 \cdot 10^{-16} \text{s}$
Distance	$\frac{\hbar c}{\text{eV}}$	$1.97327 \cdot 10^{-7} \text{m}$

TABLE 1.1: Measurements in units of electron volts eV and comparison to SI units. Note that in natural Planck units ( $c = \hbar = G = k_B = 1$ ) the units of measurements reduce to eV and  $\text{eV}^{-1}$ .

orders of magnitude lay the radii of atoms, until one reaches the smallest neutral atom at around  $25 \text{ pm} = 25 \cdot 10^{-12} \text{ m}$ . We are however not interested in atoms, but in the building blocks thereof. The length scale we are considering in particle physics is another thousand times smaller than the atoms themselves, around  $1 \text{ fm} = 10^{-15} \text{ m}$ . Most of what we know about the laws of physics at these tiny distances is learned from high-energy collisions of elementary particles.

As one can already guess from these small numbers, in particle physics one does not generally use SI units such as meters, kilograms and joules. Instead, it is customary to measure things in electron volts eV. It is defined as the amount of kinetic energy gained by a single electron accelerating from rest through an electric potential difference of one volt in vacuum. This unit is not exclusively used to measure energy, one can also express other measurements in terms of eV. In natural Planck units – where we set the speed of light  $c$ , the reduced Planck constant  $\hbar$ , the gravitational constant  $G$  and the Boltzmann constant  $k_B$  equal to 1 – indeed all units are going to be either eV or  $\text{eV}^{-1}$ . A list of units and conversions to SI units is given in Table 1.1.

We can see from the table that  $1 \text{ GeV} = 10^9 \text{ eV}$  corresponds to the length scale of roughly  $2 \cdot 10^{-16} \text{ m}$ . This means that while eV is the unit of choice, we usually need it at the magnitude of GeV to express something at the typical distances of particle physics. This is the reason why particle physics at colliders is also called *high-energy physics*.

## 1.2 COLLIDER PHYSICS: EXPERIMENTAL SIDE

Simply speaking<sup>1</sup>, collision experiments consist of two machines, namely the accelerator and the detector. The accelerator accelerates a number of particles (such as electrons or protons) in opposite directions (beams) by a very complicated arrangement of magnetic and electric fields, such that they can smash together head-on in the center of detectors. The beams are usually arranged in such a way that particles collide with the equal but opposite momenta. In the detector, various data such as energy and momentum of particles is collected. This data is then used to identify what exactly has happened to the particles that smashed together. While this basic experimental setup has stayed the same for roughly

<sup>1</sup> Please note that everything in this introductory chapter is extremely simplified and streamlined to make it accessible for laymen.

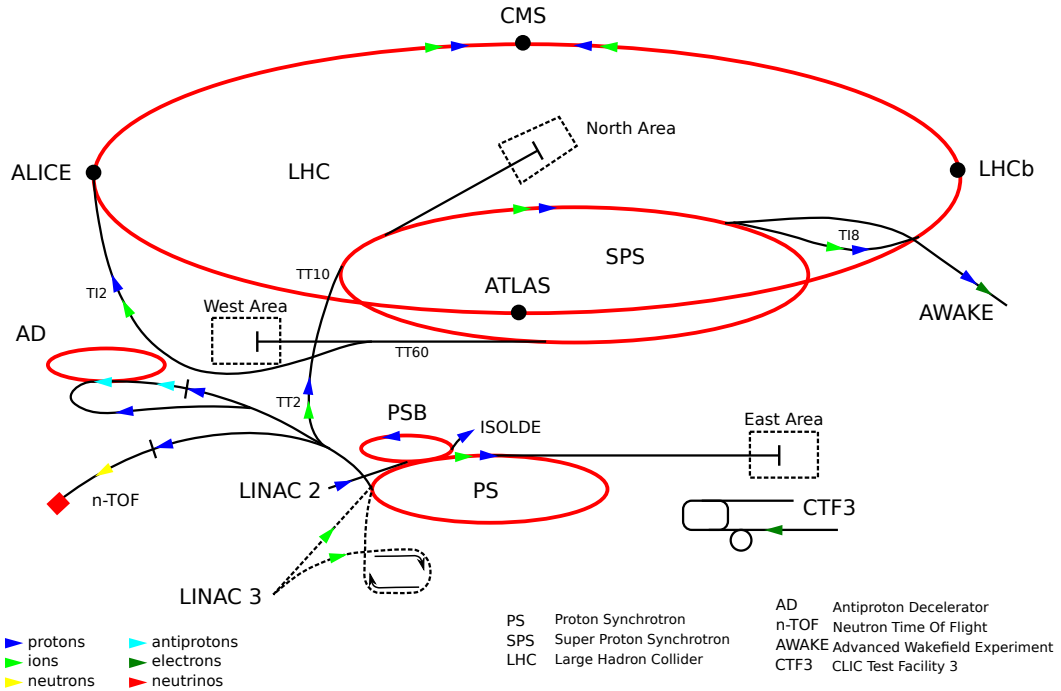


FIGURE 1.1: This schematic picture shows the accelerator complex at CERN during the second run of LHC (2015-2018). Protons that eventually collide in the LHC start in Linac 2 and get to the main ring via a succession of higher and higher energy accelerators. The four main experiments ATLAS, CMS, ALICE and LHCb are shown. The proton beams collide with a hadronic center-of-mass energy of  $\sqrt{s} = 13$  TeV. From [10].

half a century, the sophistication of the machines and accuracy of the results has improved tremendously.

### 1.2.1 Accelerator

Let us first have a look at the accelerator, specifically at the Large Hadron Collider (LHC) which produces currently the most energetic particle collisions in the world by colliding protons with protons. The LHC is located at CERN in the border region of Switzerland and France, close to Geneva. The two beams are in a pipe, up to 175 m below ground in a round tunnel with 26.7 km circumference. This makes it the largest machine in the world. A schematic view is given in Figure 1.1.

Protons that eventually collide in the detectors of LHC start their travels at Linac 2, where they get accelerated to 50 MeV ( $\sim 31.4\%$  of the speed of light) before getting injected into the Proton Synchrotron Booster. In this accelerator, the protons get accelerated to 1.4 GeV ( $\sim 91.6\%$ ) before entering the Proton Synchrotron where they reach energies of 26 GeV ( $\sim 99.94\%$ ). At this velocity, the protons enter the Super Proton Synchrotron where they get further accelerated to 450 GeV ( $\sim 99.9998\%$ ) before they are finally injected into the two directions of the main ring of the LHC. Here, the protons are accelerated to the incredible energies of 6.5 TeV ( $\sim 99.9999990\%$ , just  $\sim 3.1$  m/s slower than the speed of light!).

To get a feeling for this energy we can compare it to the kinetic energy of macroscopic objects, using the classical formula  $T = mv^2/2$  with the mass  $m$  and the velocity  $v$  of said object. Indeed, a common fly of mass  $m \approx 10$  mg would have to travel at roughly

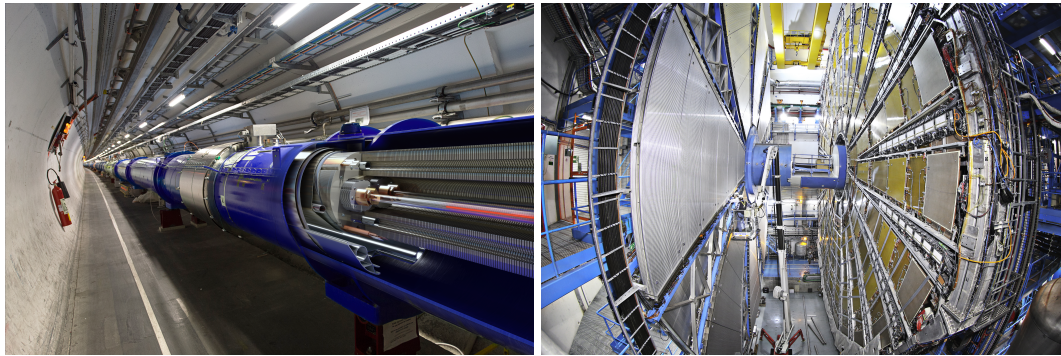


FIGURE 1.2: The left panel shows a montage of the LHC beam pipes with the two beams in the center going in opposite directions, accelerated and directed by a sophisticated arrangement of magnets. The right panel shows a small part of the ATLAS detector – it is simply impossible to obtain a picture of the entire detector. The part depicted here shows the gap between the main detector and the outer muon spectrometer disk. The diameter of the cylinder and disk is  $\sim 25$  m. The beam is fed through the pipe in the center of the picture to the interaction point. Left panel from [11], right panel from [12].

$v \approx 1.6$  km/h to reach the energy of 6.5 TeV. This is less than half the normal walking speed of humans, which does hardly sound impressive for the world's largest machine, right? Wait.

Of course the LHC does not only have one single proton flying in each of the two directions. The particles end up in 2556 bunches per direction, each bunch containing  $1.15 \cdot 10^{11}$  protons. Let us now look at two vehicles, namely a motorbike (Harley Davidson Fat Bob including rider,  $m \approx 380$  kg) and the current Swiss Army main battle tank (Panzer 87 Leopard WE,  $m \approx 56.5$  t). Let us compare the energy of the  $1.15 \cdot 10^{11}$  protons in one bunch to the kinetic energy of the motorbike. Again using the classical formula of kinetic energy, one single bunch of protons carries as much energy as a motorbike including its rider traveling at  $\sim 90$  km/h. The energy of all protons in the 2556 bunches flying in one direction is comparable to the kinetic energy of the main battle tank driving at  $\sim 375$  km/h, which corresponds roughly to the highest velocity of a Formula 1 car ever measured. Remember that the total energy of the protons in the LHC is actually equivalent to two such tanks at that speed, one going in each direction.

### 1.2.2 Detector

After this short rundown on how the protons get accelerated before the collisions happen, we will now look at the machine measuring the particles after the collision. We stay in Switzerland and discuss the largest of the four main detector experiments at the LHC, namely ATLAS (the acronym standing for *A Toroidal LHC Apparatus*).

The interaction point where the two beams collide lies in the center of the huge machine, which is shaped like a cylinder around the beam pipe. The ATLAS detector has a diameter of 25 m and a length of 46 m. The machine is built onion-like around the interaction point with layers upon layers of detectors as depicted in Figure 1.3. These layers can be separated into multiple sections serving different purposes, and we will now go over them from the center.

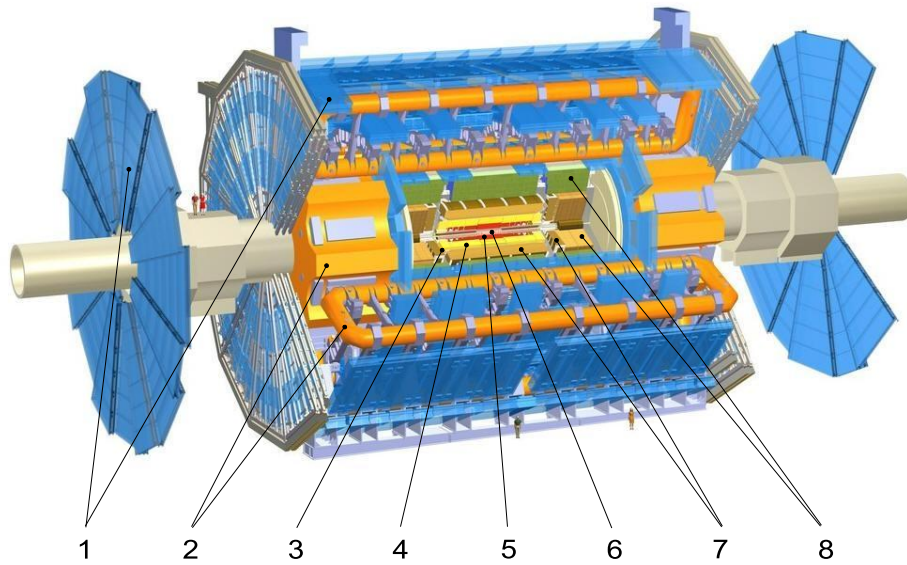


FIGURE 1.3: Schematic picture of the ATLAS detector with (1) muon spectrometers, (2) toroid magnets, (3) solenoid magnet, (4) transition radiation tracker, (5) semi-conductor tracker, (6) pixel detector, (7) liquid argon calorimeter and (8) tile calorimeter. The beams enter through the pipe from the left and right and interact at the center. From [13].

The section closest to the interaction point is fittingly called the Inner Detector. Its radius starts a few centimeters away from the interaction point and reaches about 1.2 m. It is surrounded by a solenoid magnet (number 3 in Figure 1.3) creating a magnetic field of 2 T, which causes charged particles flying away from the interaction point to curve throughout the Inner Detector due to Lorentz force. By tracking its path, one can therefore make statements about the charge and the momentum of the particle. The path gets first tracked by the pixel detector (6) whose first layers are mounted directly on the beam pipe to be as close to the interaction point as possible. The second type of detectors are the silicon semi-conductor trackers (5), another sophisticated arrangement of electronic chips to track the trajectories of the particles. Note that these two kinds of detectors are finely segmented and close enough to the interaction point that they allow the reconstruction of bottom and charm quarks that can travel a few mm before decaying, as the trajectories of the decay products are not traced back to the interaction point (we will see this in Figure 1.4). The outermost part of the Inner Detector is finally the transition radiation tracker (4), which is a straw-tube detector that provides additional information on the particle tracks as well as on the likelihood of the measured particle being an electron. It consists of gas-filled tubes that give a signal if the contained gas gets ionized.

The second section, starting outside the solenoid magnet surrounding the Inner Detector, is the Calorimeters which are about 4 m in radius. The energy of the particles (both charged and neutral) gets absorbed in these layers. There are two kinds of calorimeters to be found, namely the lead and liquid argon electromagnetic calorimeter (7) that interacts electromagnetically with the particles and the iron-scintillating hadronic calorimeter (or tile calorimeter) (8), which absorbs the energy via the strong force.

The only stable particles that travel through the Calorimeters without losing most (or all) of their energy are neutrinos and muons. Outside the Calorimeters, the section called the



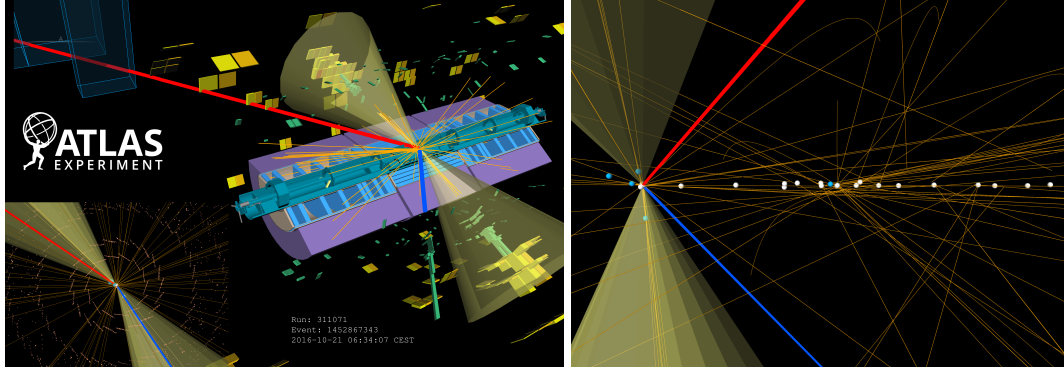


FIGURE 1.4: Event 1452867343 of Run 311071, measured on October 21, 2016, is a candidate for an event where the two colliding protons generated a  $t\bar{t}$  pair that decayed into  $b$ -tagged jets (yellow cones), one electron of transverse momentum  $p_T = 228$  GeV (blue line) and one muon of  $p_T = 154$  GeV (red line). The energies measured by the electromagnetic calorimeter are shown in green, the deposits in the hadronic calorimeter in yellow. The bottom left zoom in the left panel presents the view alongside the beam-axis, with reconstructed trajectories of the measured particles. In the right panel, we look from the side at the colliding beams. The white blobs represent primary vertices where hadrons collided, and the azure ones show vertices compatible with the decay of bottom quarks. From [14].

Muon Spectrometer (1) starts and ranges to the full extent of the detector with its diameter of roughly 25 m. As the name suggests, this section is all about the tracking of muons. It also contains the name-giving toroidal magnets (2) which generate a magnetic field of 4 T. This again curves the trajectories of the muons to allow for a second measurement of their momenta in addition to the one measured in the Inner Detector.

It is not possible to directly measure neutrinos in a collider. They are the only stable particles not detectable by the ATLAS detector, and their energy is appropriately called *missing energy*. It is literally the energy missing, when one sums over the energies of the final state particles and compares this to the energy of the colliding particles.

There is one additional major difficulty in the analysis of collider experiments that can not be stressed enough. Particle detectors are only able to detect stable particles, and they will never get a signal from short-lived or confined elementary particles. More specifically, they can only measure photons, electrons, muons and hadrons. Other particles, like the tau leptons, can not be detected because they will already have decayed into various other particles before the chance to measure them occurred. Also quarks and gluons can not be detected; due to color confinement these elementary particles can not appear isolated. They are forming hadrons, either baryons (consisting of three quarks) or mesons (consisting of one quark and one anti-quark). Let me again emphasize the fact that photons, electrons and muons are the only elementary particles measured in a direct way and that all measurements on the strong force are done by detecting composite particles.

In Figure 1.4 we can see the result of the analysis of a collision measured by ATLAS. It is a candidate for an event where the protons collided and a top quark and anti-quark (a  $t\bar{t}$  pair) was produced at the left-most white blob in the right panel. As the top quark has a very short life-time, it decayed into a bottom quark and a  $W^+$ -boson. The bottom quark survived for a little while and then decayed into various other particles (at the cyan blobs in the right panel) and the  $W^+$ -boson became a lepton and a neutrino. As the same thing

happened to the top anti-quark, two leptons (red and blue line) and two bottom-tagged jets (yellow cones) were measured.

Even though the elementary quanta of the strong force can not be measured directly, they can be reconstructed with high accuracy from the detected hadronic jets, regions where a lot of hadronic energy was measured close together. Due to momentum conservation, it is logical to assume that the summed momentum of the particles in each of the two jets is approximately equal to the momentum of the bottom quarks. The very difficult procedure of inferring the fundamental process from analyzing the positions, energies and constituents of the measured particles is called *event reconstruction*.

At least one additional complication arises, visible in Figure 1.4 as the white blobs. As we have seen, the hadrons in the beam do not come one-by-one but in bunches of many. In the case of the LHC, the hadrons collide in bunches of  $1.15 \cdot 10^{11}$  protons each. Generally, one does not expect to have only one proton-proton pair of each bunch interacting. In fact, at Run 2 of the LHC there are about 140 hadron pairs interacting in each collision of the bunches. These interactions of multiple hadrons in the same bunches is called the *pile-up*. While theoretically also occurring in lepton colliders, the probability of the leptons to interact with each other is small enough to experience almost no pile-up.

### 1.2.3 Cross sections

Let us have a look at what one can learn by such experiments as discussed above. One might be surprised that one can learn something about nature from collisions in the first place. As an everyday example, there is nothing much to be learned from smashing two billiard balls together, as the outcome is predetermined from the initial conditions, specifically by the two momenta with which they will collide. Also the more sophisticated and more closely related experiment of two motorbikes colliding head-on, both at  $\sim 90$  km/h, will hardly lead us to a better understanding of motorbikes. But at the small length scales and the high energies of the accelerated particles, quantum effects are not only relevant but dominant. Therefore, anything the detector eventually measures, is fundamentally related to probabilities. In the context of particle physics, the probability that a specific processes will happen in the collision of two particles is encoded in the quantity called the *cross section*, denoted by  $\sigma$ .

Let me first point out that the interaction happens between elementary particles. This is obvious for lepton colliders, where the beams consist of elementary particles anyway. However, this also applies on colliding hadrons. In a  $pp$  collision at ATLAS for example it is not the protons themselves that interact but their constituents (quarks and gluons).

We consider the collision of two particle beams  $A$  and  $B$  smashing together at net momentum zero. We choose the beams to be aligned with the  $z$ -axis  $p_A = (E, 0, 0, E)$  and  $p_B = (E, 0, 0, -E)$  such that a collision happens with a center-of-mass energy of  $E_{cm} = 2E$  (or Mandelstam variable  $s = (p_A + p_B)^2 = E_{cm}^2 = 4E^2$ ). Note that in hadronic beams one usually denotes the partonic center-of-mass energy – the actual energy of the interaction between the elementary particles – as  $\sqrt{\hat{s}}$  to distinguish it from the beam energy  $\sqrt{s}$ . The number of particles in one bunch of each beam is  $N_A$  and  $N_B$ . The cross section of a certain outcome is then given by

$$\sigma = \frac{(\text{Number of events with certain outcome})}{N_A N_B} \mathcal{A}, \quad (1.1)$$

where  $\mathcal{A}$  is the beams' cross-sectional area and does also contain information on resolution and blind spots of the detector.

As we have already discussed, a particle accelerator does not only accelerate one bunch of particles at a time, but collisions happen at a frequency of  $f$  times per second, such that the number of events of a certain outcome per second in a detector is given by

$$R = L \sigma = f \frac{N_A N_B}{\mathcal{A}} \sigma, \quad (1.2)$$

where  $L$  stands for the instantaneous luminosity of the accelerator.

To calculate a specific cross section, one needs to reconstruct the events and classify each of them by testing, whether it fulfills the conditions of a certain observable. This leads to the rate  $R$ , which after division by the luminosity  $L$  gives the cross section  $\sigma$  of the specific observable under consideration. This number can then be compared to theoretical predictions made for a certain center-of-mass energy corresponding to  $\sqrt{s}$ .

The observables that one can extract from experiments are manifold. Probably the most intuitive one would be the total cross section which is the probability that *anything* happens when smashing the particles together. In this case the "certain outcome" corresponds to "any outcome other than beams passing through each other". Other possible observables are for example the cross section of photon production (events that, after reconstruction, contain a photon of at least a given energy without hadronic particles close by) or the cross section to measure no hadronic jets at all in a certain region of the collider.

The level of precision at which experimentalists are able to extract the cross sections of various observables at the LHC is remarkable. Now we have to try to understand these results from the theoretical side.

### 1.3 COLLIDER PHYSICS: THEORETICAL SIDE

While it is impossible to prove a theory, one can confirm or refute it according to measurements. And even if a theory might approximate experimental results in some regime, it must not contain the whole truth (and so far, no theory does and most likely never will). Newtonian mechanics for example works very well in everyday life for slow-moving large objects that are not too massive but breaks down for small objects (where quantum effects become important), high velocities (leading to the theory of special relativity) or when masses become large (leading to the theory of general relativity). Therefore, once one has found a suitable theory to describe some experiments, one needs to further test in which regime this theory holds.

#### 1.3.1 *Standard Model of particle physics*

A tremendous success in theoretical particle physics was (and is) the development of the Standard Model of particle physics (SM). It contains three of the four fundamental forces, namely the electromagnetic, weak and strong interactions, leaving out only the gravitational force. The SM describes the known and experimentally observed elementary particles amazingly well.

The SM Lagrangian is given in Figure 1.5. In this form, it looks like a tiny back-of-the-envelope kind of formula. However, if one goes into the details and actually explains all terms, it turns out to not be that simple. I refer the interested reader to [4] and [5].

Predictions calculated using the SM are confirmed time and time again. While some light deviations provide fertile breeding ground for speculations about various expansions of the



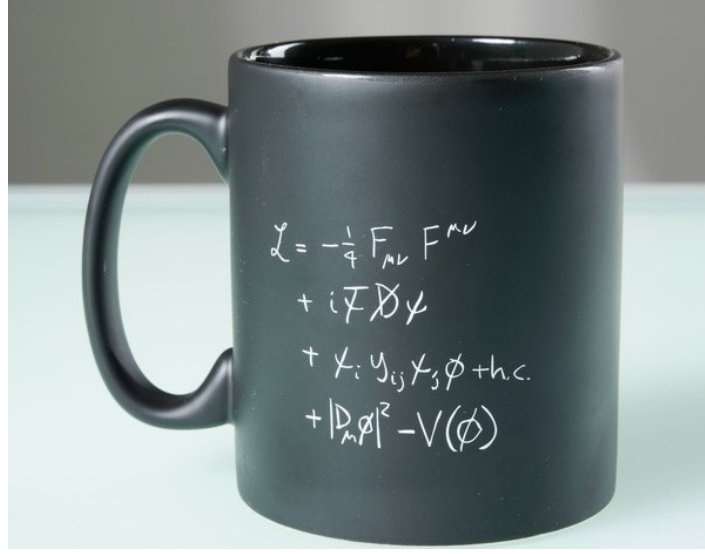


FIGURE 1.5: A famous formula, to be found on many physicists blackboards and desks: the Lagrangian of the Standard Model of particle physics. From [15].

SM, experimental measurements have so far not found any critically statistical significant deviation thereof. The SM is indeed so successful that *new physics* is the terminology used for particle physics that is not explained by it.

However triumphant the SM may be, its predictions are expected to break down at high enough energies not yet reached by any experimental setup. But even if experiments found any deviations from the SM, the theory would not be rendered invalid but merely incomplete. Indeed, the incompleteness of the SM is well known, as it does not even try to explain gravitation, dark matter or dark energy.

### 1.3.2 Calculation of cross sections

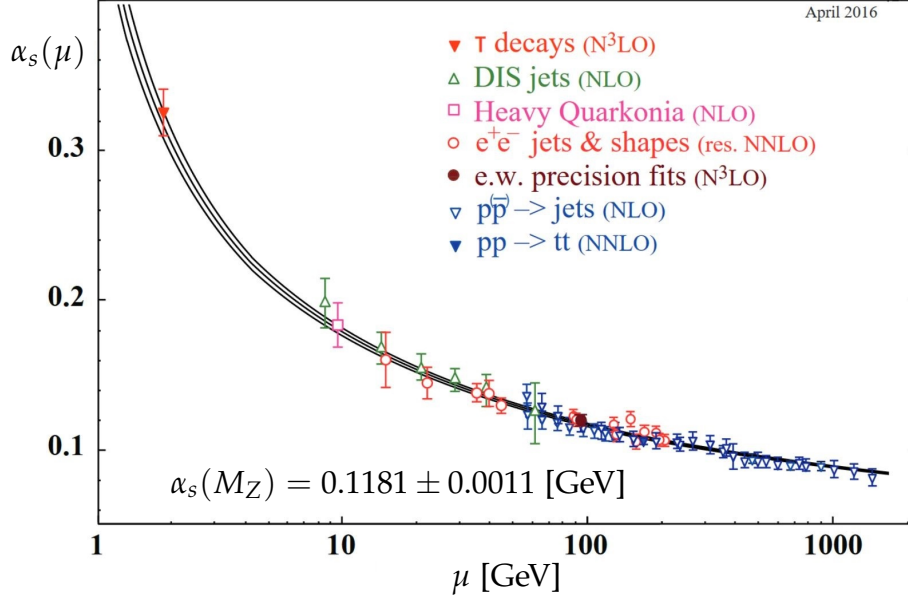
Let us look at how one derives theoretical predictions of cross sections as measured in experiments. As we have seen in Section 1.2, a collision consists of two initial particles  $A$  and  $B$  that become  $N$  final state particles. The cross section of such a  $2 \rightarrow N$  scattering is calculated by evaluating the master formula

$$\sigma_{AB \rightarrow N} = \frac{1}{2s} \int d\Phi_N |\mathcal{M}_{AB \rightarrow N}(p_A, p_B, \Phi_N)|^2, \text{ with} \quad (1.3)$$

$$\begin{aligned} d\Phi_N &= \left( \prod_{i=1}^N \frac{d^4 p_i}{(2\pi)^4} (2\pi) \delta(p_i^2 - m_i^2) \theta(p_i^0) \right) (2\pi)^4 \delta^4(p_A + p_B - \sum p_i), \\ &= \left( \prod_{i=1}^N \frac{d^3 p_i}{(2\pi)^3 2E_i} \right) (2\pi)^4 \delta^4(p_A + p_B - \sum p_i), \end{aligned} \quad (1.4)$$

where  $p_A$  and  $p_B$  denote the momenta of the colliding particles and  $p_i$  the  $N$  on-shell momenta of the final state over which we integrate. The matrix element (or scattering amplitude)  $\mathcal{M}_{AB \rightarrow N}(p_A, p_B, \Phi_N)$  contains the whole information of the exact process that happens in the scattering, everything else in (1.3) is kinematics.

As already pointed out, interactions happen between elementary particles. This means that in the case of hadron colliders the scattering takes place between constituents of the

FIGURE 1.6: Running strong coupling  $\alpha_s(\mu)$ . Adapted from [16].

hadrons. Therefore, the cross section of a scattering process with two incoming hadrons and  $N$  outgoing elementary particles  $h_1 h_2 \rightarrow N$  reads

$$\sigma_{h_1 h_2 \rightarrow N} = \frac{1}{2s} \sum_{a,b} \int_0^1 \frac{dx_a}{x_a} \frac{dx_b}{x_b} f_{a/h_1}(x_a, \mu_F) f_{b/h_2}(x_b, \mu_F) \int d\Phi_N |\mathcal{M}_{ab \rightarrow N}(\Phi_N, \mu_F, \mu_R)|^2. \quad (1.5)$$

The Parton Distribution Functions (PDFs)  $f_{p/h}(x, \mu)$  can be interpreted as probabilities to find the parton  $p$  in hadron  $h$ . Note that the PDFs depend on  $x$ , which is the fraction of light-cone momentum  $p$  has in respect to  $h$ . So the partonic center-of-mass energy, which we have already encountered in Section 1.2.3, can be given as

$$\sqrt{\hat{s}} = \sqrt{x_a x_b s}. \quad (1.6)$$

We have also two scales appearing in the hadron collider master formula (1.5), namely the factorization scale  $\mu_F$  and the renormalization scale  $\mu_R$ .

The PDFs provide the very nontrivial link between the incoming hadrons and the elementary particles that scatter. If we have two beams delivering protons  $p$  as in the LHC, one might expect to have them both having the PDFs

$$f_{u/p}^{\text{naive}}(x, \mu) = 2 \delta\left(x - \frac{1}{3}\right) \quad \text{and} \quad f_{d/p}^{\text{naive}}(x, \mu) = \delta\left(x - \frac{1}{3}\right), \quad (1.7)$$

while all other PDFs are zero. This would mean that each proton consists of two up quarks  $u$  and one down quark  $d$  and each of those elementary particles would be carrying  $x = 1/3$  of the full energy of the hadron. However, things are much more complicated in reality. First of all, already the quarks in the classical picture need to stick together somehow, therefore gluons need to be present. And we should remember that in QFT, particles get produced and annihilated all the time. In particular, it is possible to observe additional quarks not present in the naive picture of the proton. These so-called sea partons can also become the interacting partons. It is not possible to calculate the PDFs theoretically and one has to resort

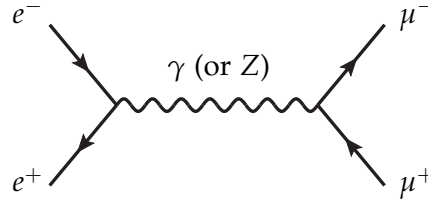


FIGURE 1.7: Leading-order (or tree-level) Feynman diagrams of muon pair production at an electron-positron collider  $e^+e^- \rightarrow \mu^+\mu^-$ .

to experimental methods to extract them. We will come back to a more thorough discussion of the PDFs in Section 1.3.4.

Let us also talk about the scales  $\mu_R$  and  $\mu_F$ . The strong coupling  $\alpha_s(\mu)$  is scale dependent, see Figure 1.6. The renormalization scale  $\mu_R$  corresponds to the scale at which the parameter  $\alpha_s(\mu)$  gets evaluated for the specific process. The factorization scale  $\mu_F$  represents the scale at which the PDFs get determined. It is customary to find a characteristic scale  $\mu$  of the considered process (either given by the mass of some intermediate particle or some function of the final-state momenta) and then use  $\mu_F = \mu_R = \mu$  as the default scales. Both the factorization scale and the renormalization scale gets then usually varied by a factor of two up and down to estimate the theoretical uncertainties.

The partonic matrix element  $\mathcal{M}_{ab \rightarrow N}(\Phi_N, \mu_F, \mu_R)$  in the hadron collider master formula (1.5) serves exactly the same purpose as in the lepton collider master formula; it contains all the information on how the partons  $a$  and  $b$  become the  $N$  particles after the scattering.

We will now dive into the calculation of cross sections at lepton colliders and discuss the production of each of the experimentally measurable particles. After the mechanisms are clear, we will revisit the hadron collider.

### 1.3.3 Lepton colliders

As we have seen in Section 1.2, detectors can measure photons, leptons (electrons and muons) and hadrons. Considering an electron-positron collider, the scattering lepton pair may annihilate into a photon or a Z-boson. This vector boson however can not be a "real" one, meaning that it can not be measured by the detector as it will have to decay (due to momentum conservation) and is therefore called *intermediate* (or messenger/virtual) particle. It can decay into a lepton or quark pair.

#### 1.3.3.1 Lepton production

Let us first focus on lepton pair production. This process at leading order is shown diagrammatically in Figure 1.7. First let me point out that the initial electron-positron pair could emit more than one particle. Each of these particles might be an intermediate or a real one. Real emissions of the kind depicted in Figure 1.9 would be called *initial state radiation* (ISR), which we will come back to later. If it were an intermediate one, it could either connect to another leptonic leg in the diagram, see Figure 1.8, or decay into other particle pairs. Also the lepton pair on the right hand side of the diagram, the one into which the intermediate particle decays, can radiate additional particles, both real and intermediate (see Figures 1.8 and 1.10). These kinds of real emissions would then be called *final state radiation* (FSR), which we will come back to later.

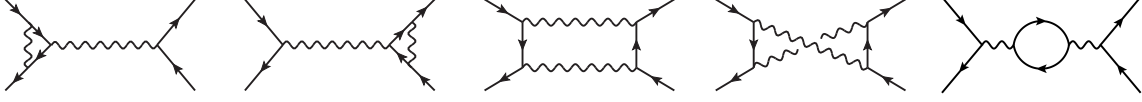


FIGURE 1.8: Feynman diagrams for the virtual corrections at next-to-leading order (one loop) to the process  $e^+e^- \rightarrow \mu^+\mu^-$ . The sum of those diagrams yields  $\sigma_{e^+e^- \rightarrow 2}^{(1)}$ .

Note that each additional node in a diagram comes with a factor of  $e$  in the matrix element. In the case of an additional intermediate particle, there are always two nodes per connecting line, forming a so-called *loop*. In the case of a real emission correction, this factor will appear twice in the cross section due to the matrix element getting squared, see (1.3). For this reason we can say that both the real and virtual corrections come with a factor of  $\alpha = e^2/4\pi$  each.

Just as we have seen for the strong coupling, the electromagnetic coupling also depends on the energy scale at which we evaluate it, but for our purposes it suffices to treat it as the fine-structure constant  $\alpha \approx 1/137$ . This means that any cross section with an additional electromagnetic radiation or a loop correction is suppressed by a factor of  $1/137$ . One speaks of the diagrams displayed in Figure 1.7 with no additional  $\alpha$ -suppressed terms as the *leading-order contribution* (LO), and the calculation of diagrams with such corrections as *higher-order contributions*. What one traditionally does in theoretical particle physics is calculate the cross sections order-by-order in  $\alpha$

$$\begin{aligned} \text{LO: } \sigma &= c^{(0)} + \mathcal{O}(\alpha), \\ \text{NLO: } \sigma &= c^{(0)} + c^{(1)}\alpha + \mathcal{O}(\alpha^2), \\ \text{N}^n\text{LO: } \sigma &= c^{(0)} + c^{(1)}\alpha + c^{(2)}\alpha^2 + \dots + c^{(n)}\alpha^n + \mathcal{O}(\alpha^{n+1}), \end{aligned} \quad (1.8)$$

where NLO stands for *next-to-leading order*, NNLO for *next-to-next-to-leading order* and so on. The coefficients  $c^{(i)}$  are independent of the coupling constant. Note that if we introduce the strong force, this expansion is not only done in  $\alpha$  but also in  $\alpha_s$ .

The full cross section is then the sum of the cross sections at each order

$$\sigma_{e^+e^- \rightarrow N} = \sigma_{e^+e^- \rightarrow 2}^{(0)} + \left[ \sigma_{e^+e^- \rightarrow 2}^{(1)} + \sigma_{e^+e^- \rightarrow 3}^{(1)} \right] + \left[ \sigma_{e^+e^- \rightarrow 2}^{(2)} + \sigma_{e^+e^- \rightarrow 3}^{(2)} + \sigma_{e^+e^- \rightarrow 4}^{(2)} \right] + \dots, \quad (1.9)$$

where the number in the upper index stands for the order of additional couplings  $\alpha$  compared to the leading-order diagrams, corresponding to the number of loops plus the number of additional real emissions. Note that while individual cross sections  $\sigma_{e^+e^- \rightarrow i}^{(j)}$  may suffer from divergences, the sum inside the brackets is always going to give a finite value. To derive the cross section at NLO, for example, we have to calculate the diagrams of Figures 1.9 and 1.10, both contributing to  $\sigma_{e^+e^- \rightarrow 3}^{(1)}$ . These diagrams are all *infrared (IR) divergent*, which means that they become singular for photons at low energy. To cancel these divergences, we need to add all the one-loop diagrams with two final state particles  $\sigma_{e^+e^- \rightarrow 2}^{(1)}$ , depicted in Figure 1.9.

Let us assume that an experiment at an electron-positron collider measured a muon pair  $\mu^+\mu^-$  (among  $N - 2$  other particles) in the final state. We want to calculate the leading-order contribution with a photon  $\gamma$  as the messenger particle. The full matrix element obtained by evaluating the Feynman diagram in Figure 1.7 reads

$$i\mathcal{M}_{e^+e^- \rightarrow \gamma \rightarrow \mu^+\mu^-} = (-ie)\bar{v}_\alpha(p_{e^+})\gamma_\alpha^\mu u_\beta(p_{e^-}) \frac{-ig_{\mu\nu}}{k^2} (-ie)\bar{u}_\delta(p_{\mu^-})\gamma_\delta^\nu v_\epsilon(p_{\mu^+}), \quad (1.10)$$

with the spinors  $u$  and  $v$  for particles and anti-particles, Dirac matrices  $\gamma$  and the momentum of the virtual photon  $k^\nu = p_{e^-}^\nu + p_{e^+}^\nu = p_{\mu^-}^\nu + p_{\mu^+}^\nu$ .

For the sake of simplicity I do not want to get too deep into the details and refer the reader to Section 13.3 of [5] for the explicit derivation. However, I want to point out that we need to average over the polarizations of the incoming particles as electron-positron colliders usually do not polarize the beams. Also, most detectors are unable to measure the spin of the registered particles. Therefore we need to sum over the spins of the final state particles. So we need to replace the squared matrix element in (1.3) by the squared matrix element summed over the spins (final states) and polarizations (initial states) divided by a factor of four (averaging polarizations). After going into the high-energy limit by setting the masses of the leptons to zero  $m_e = m_\mu = 0$ , which we are allowed to do since the kinetic energies of the particles are much higher than their masses, we have

$$|\mathcal{M}_{e^+e^- \rightarrow \gamma \rightarrow \mu^+\mu^-}|^2 \rightarrow \frac{1}{4} \sum_{\text{spins}} |\mathcal{M}_{e^+e^- \rightarrow \gamma \rightarrow \mu^+\mu^-}|^2 = \frac{2e^4}{s^2} (t^2 + u^2), \quad (1.11)$$

with Mandelstam variables

$$s = (p_{e^-} + p_{e^+})^2 = (p_{\mu^-} + p_{\mu^+})^2, \quad (1.12)$$

$$t = (p_{e^-} - p_{\mu^-})^2 = (p_{e^+} - p_{\mu^+})^2, \quad (1.13)$$

$$u = (p_{e^-} - p_{\mu^+})^2 = (p_{e^+} - p_{\mu^-})^2. \quad (1.14)$$

Energy-momentum conservation in (1.4) eliminates four of the six integrations and as we have a fixed total energy  $\sqrt{s} = E_{CM}$ , one additional degree of freedom is lost. Therefore, we can express the  $e^+e^- \rightarrow 2$  scattering in only one variable and one usually chooses this to be the scattering angle (angle  $\theta$  between the incoming electron and the outgoing muon). After the integrations, the LO cross section reads

$$\sigma_{e^+e^- \rightarrow \gamma \rightarrow \mu^+\mu^-}^{(0)} = \frac{\alpha^2}{4E_{CM}^2} \int_0^{2\pi} d\phi \int_0^\pi d\theta \sin \theta (1 + \cos^2 \theta) = \frac{4\pi\alpha^2}{3E_{CM}^2}. \quad (1.15)$$

To get the full leading-order cross section of  $\sigma_{e^+e^- \rightarrow \mu^+\mu^-}$ , one would also have to calculate the diagram with the Z-boson as the messenger particle. To streamline this introductory chapter, I will not discuss this here and refer the interested reader to Section 2.1.3. of [3].

Note that if we want to extend the calculations to include higher-order corrections, any additional order comes with a much higher complexity as one has to include many more diagrams per order. As we have seen, already the NLO corrections come with nine diagrams, each of which is much more involved to calculate than the LO one.

### 1.3.3.2 Photon production via Initial State Radiation

Now let us go back to the discussion of ISR as depicted in Figure 1.9. This is one of the leading-order possibilities to have a photon detected in a lepton collision. As we have pointed out before, such emissions come suppressed by a factor of  $\alpha \sim 1/137$ . However, such matrix elements also come with an internal electron propagator. Assuming that it is the electron that emits the photon, corresponding to the left panel of Figure 1.9, the momentum of the virtual electron may be written as  $p_{e^*} = p_{e^-} - p_\gamma$  which leads to a factor of

$$|\mathcal{M}_{e^+e^- \rightarrow \gamma \rightarrow \mu^+\mu^- \gamma}|^2 \propto \frac{1}{p_{e^*}^2 - m_e^2} = \frac{1}{(p_{e^-} - p_\gamma)^2 - m_e^2} = \frac{1}{-2p_{e^-} \cdot p_\gamma}. \quad (1.16)$$

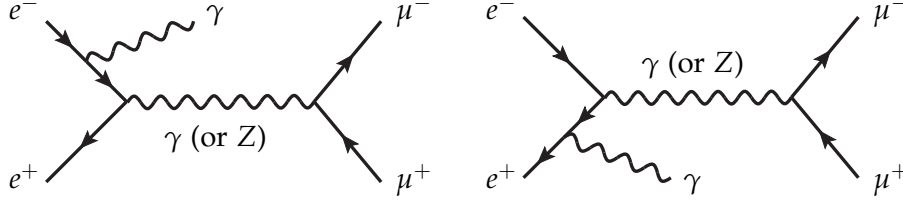


FIGURE 1.9: Feynman diagrams contributing to the process  $e^+e^- \rightarrow \mu^+\mu^-\gamma$  via initial state radiation (ISR).

This factor obviously blows up, if  $p_{e^-} \cdot p_\gamma \rightarrow 0$ . There are two possibilities how this can occur. Firstly, we can encounter a *soft singularity*, which happens if the energy of the photon becomes very small, and secondly, a *collinear singularity* may occur, meaning that the momenta of the incoming electron and the outgoing photon are roughly in the same direction. This means that especially in these two regions, where the photon is soft or emitted in a collinear fashion, the suppression by  $\alpha \sim 1/137$  becomes meaningless. Of course, this goes doubly for the photons which are soft *and* collinear at the same time. The importance of these soft and collinear regions can not be overstated. Indeed, in Chapter 2 we will build an entire effective field theory around them.

In the case of ISR and remembering the experimental setup, it may seem like the above-mentioned problems are of theoretical nature only. For a) it is not possible to detect the photons carrying a very small amount of energy in the calorimeters (as they are drowned in the noise) and b) it is not possible to have a detecting panel in the exact direction of the beam. This means that theoretical calculations of ISR in the experimentally measurable regime are automatically finite.

We can for example always apply a hard cutoff on the energy at the lower end of the phase space integral (1.4), essentially accounting for point a) above. The cost we have is a logarithm of this cutoff entering the calculation. Note that with the imposed cutoff, we evaluate the cross section of the muon pair with an additional real photon of at least the cutoff's energy. Without such a cutoff, we have an IR divergence that cancels against the virtual corrections at NLO, as already discussed above.

Point b) from above, the collinear emission pattern, must be accounted for. While we can not measure such photons, they still get produced and take away some energy from the electron. Intuitively, this problem gets solved by introducing a *splitting amplitude* that splits the incoming electron beam into an electron of energy  $x\sqrt{s}/2 = (1-z)\sqrt{s}/2$  and a photon of energy  $z\sqrt{s}/2 = (1-x)\sqrt{s}/2$ . The electron at lower energy then still annihilates with the positron to create other leptons. This branching off of a photon from the electron is very similar to the hadron PDFs we already met. After detailed analysis, one finds the differential cross section to encounter ISR from the electron to be

$$\frac{d\sigma_{e^+e^- \rightarrow \gamma \rightarrow \mu^+\mu^-\gamma}^{\text{ISR}}}{dx} = f_e(x) d\sigma_{e^+e^- \rightarrow \gamma \rightarrow \mu^+\mu^-}^{(0)}(xs), \text{ with} \quad (1.17)$$

$$f_e(x) = \frac{\alpha}{2\pi} \left[ \frac{1+x^2}{1-x} \right] \ln \frac{\mu}{m_e}. \quad (1.18)$$

Here, the function  $f_e(x)$  represents the probability to have an electron with an energy between  $\sqrt{xs}/2$  and  $\sqrt{(x+dx)s}/2$  and  $d\sigma_{e^+e^- \rightarrow \gamma \rightarrow \mu^+\mu^-}^{(0)}(xs)$  is the leading-order cross section of muon pair production with reduced Mandelstam variable  $s \rightarrow xs$ . To perform the above computation, one has to introduce a factorization scale  $\mu$ . Its interpretation will be discussed



below. The derivation of this formula may be found in Section 2.2 of [3] and in more detail in Section 17.5 of [4].

Note that (1.18) as it stands does not reflect the *full* electron probability. One also needs to include a factor proportional to  $\delta(1-x)$ , accounting for the leading-order case where no photon gets emitted.

Naturally, if we observe a PDF-like function that gives the probability to find an electron in the electron beam, there is also a probability to encounter a photon. This probability function to find a photon of energy between  $zE$  and  $(z+dz)E$  is given at leading order by

$$f_\gamma(z) = f_e(1-z). \quad (1.19)$$

As the entire discussion of the electron beam splitting into an electron and a photon also applies on the positron beam (see right panel of Figure 1.9), this leads to the observation of  $\gamma$ - $e^\pm$ -scattering and even  $\gamma$ - $\gamma$ -scattering in lepton colliders.

Probably the most interesting part of (1.18) is the logarithm of  $\mu/m_e$ . The factorization scale  $\mu$  is related to the minimal amount of transverse momentum  $p_T = \sqrt{p_x^2 + p_y^2}$  relative to the beam (z-axis) a particle must have to get measured by the detector and not to get lost in the beam. A photon which has less transverse momentum  $p_T < \mu$  is undetectable and must be treated as if it belongs to the beam itself. The logarithm comes from the integral of the photon over the unobservable phase space region  $p_T < \mu$ . It should not come as a surprise that ISR depends on the sensitivity of detectors, and indeed if one saw all radiation  $\mu = m_e$ , we would recreate the naive picture with

$$f_e^{(0)}(x) = \delta(1-x) \text{ and } f_\gamma^{(0)}(z) = 0, \quad (1.20)$$

corresponding to an electron-only beam. We see that photons of ISR that are radiated close to the beam are in fact not simply reduced by a factor of  $\alpha$  as expected, but also enhanced by a factor of  $\ln(\mu/m_e)$ . If  $\mu$  is far away from  $m_e$ , this second factor may very well be of order  $\sim 1/\alpha$  and the cross section with an emitted photon can become of the same size as the cross section without. Therefore, the expansion in terms of  $\alpha$  as shown in (1.8) breaks down and to obtain accurate predictions for lepton pair production, we need to treat the terms proportional to  $(\alpha/\pi)^m \ln^m(\mu/m_e)$  for arbitrary  $m$  as of the same order as the LO term. This leads to an expansion of this single-logarithmic observable as

$$\begin{aligned} \text{LL: } \sigma &= \sum_{m=0}^{\infty} b_{0,m} \alpha^m L^m + \mathcal{O}(\alpha^k L^{k-1}), \\ \text{NLL: } \sigma &= \sum_{m=0}^{\infty} b_{0,m} \alpha^m L^m + \sum_{m=0}^{\infty} b_{1,m} \alpha^m L^{m-1} + \mathcal{O}(\alpha^k L^{k-2}), \\ \text{N}^n\text{LL: } \sigma &= \sum_{m=0}^{\infty} b_{0,m} \alpha^m L^m + \dots + \sum_{m=0}^{\infty} b_{n,m} \alpha^m L^{m-n} + \mathcal{O}(\alpha^k L^{k-n-1}), \end{aligned} \quad (1.21)$$

where  $L$  is the large logarithm  $\ln(\mu/m_e)$  and LL stands for *leading logarithmic accuracy*. The inclusion of these infinite sums of logarithmically enhanced terms is called *resummation*.

In the case of ISR at lepton colliders this problem is solvable, as the distribution functions  $f_e$  and  $f_\gamma$  obey a system of differential equations, known as the Gribov-Lipatov equations

$$\frac{df_\gamma(x, \mu)}{d \ln \mu} = \frac{\alpha}{\pi} \int_x^1 \frac{dz}{z} \left\{ P_{e \rightarrow \gamma}(z) \left[ f_{e^-} \left( \frac{x}{z}, \mu \right) + f_{e^+} \left( \frac{x}{z}, \mu \right) \right] + P_{\gamma \rightarrow \gamma}(z) f_\gamma \left( \frac{x}{z}, \mu \right) \right\}, \quad (1.22)$$

$$\frac{df_{e^-}(x, \mu)}{d \ln \mu} = \frac{\alpha}{\pi} \int_x^1 \frac{dz}{z} \left\{ P_{e \rightarrow e}(z) f_{e^-} \left( \frac{x}{z}, \mu \right) + P_{\gamma \rightarrow e}(z) f_{\gamma} \left( \frac{x}{z}, \mu \right) \right\}, \quad (1.23)$$

$$\frac{df_{e^+}(x, \mu)}{d \ln \mu} = \frac{\alpha}{\pi} \int_x^1 \frac{dz}{z} \left\{ P_{e \rightarrow e}(z) f_{e^+} \left( \frac{x}{z}, \mu \right) + P_{\gamma \rightarrow e}(z) f_{\gamma} \left( \frac{x}{z}, \mu \right) \right\}, \quad (1.24)$$

with the splitting functions

$$P_{e \rightarrow e}(z) = \frac{1+z^2}{(1-z)_+} + \frac{3}{2} \delta(1-z), \quad P_{e \rightarrow \gamma}(z) = \frac{1+(1-z)^2}{z}, \quad (1.25)$$

$$P_{\gamma \rightarrow e}(z) = z^2 + (1-z)^2, \quad P_{\gamma \rightarrow \gamma}(z) = -\frac{2}{3} \delta(1-z). \quad (1.26)$$

The plus-distribution in  $P_{e \rightarrow e}(z)$  is defined as

$$\int_x^1 \frac{g(z)}{(1-z)_+} = \int_x^1 \frac{g(z) - g(1)}{1-z}, \quad (1.27)$$

such that  $1/(1-z)_+ = 1/(1-z)$  for  $z \neq 1$  to regulate the denominator. Using the Gribov-Lipatov equations and the starting conditions at  $\mu = m_e$  reading

$$f_{e^-}(x, \mu = m_e) = \delta(1-x) \quad \text{and} \quad f_{e^+}(x, \mu = m_e) = f_{\gamma}(x, \mu = m_e) = 0, \quad (1.28)$$

we can calculate the distribution functions. The physical meaning of the Gribov-Lipatov functions is that if we shift  $\mu \rightarrow \mu + \delta\mu$ , the previously detectable photons of  $p_T \in [\mu, \mu + \delta\mu]$  become invisible (part of the beam) and therefore included in  $f_{\gamma}$ . The electron beam at  $\mu > m_e$  consists of electrons, photons and positrons and if the energy of one of the leptonic partons becomes  $x E$ , it can emit an ISR photon of energy  $x E$  and transverse momentum  $p_T \in [\mu, \mu + \delta\mu]$ . The Gribov-Lipatov equations are constructed in such a way that both the net electron constituent and the total momentum of the physical electron are conserved

$$\int_0^1 dx (f_{e^-}(x, \mu) - f_{e^+}(x, \mu)) = 1 \quad \text{and} \quad \int_0^1 dx x (f_{e^-}(x, \mu) + f_{e^+}(x, \mu) + f_{\gamma}(x, \mu)) = 1. \quad (1.29)$$

The constituents of the positron beam are exactly the same, as are the Gribov-Lipatov equations. One simply needs to replace the electron-beam initial conditions (1.28) with its positron-beam counterpart, obtained by  $f_{e^-}(x, \mu = m_e) \leftrightarrow f_{e^+}(x, \mu = m_e)$ .

### 1.3.3.3 Photon production via Final State Radiation

Now we want to turn our attention to the other side of the diagrams and look at photons emitted from the muons via FSR. The diagrams are given in Figure 1.10. FSR can be treated analogous to ISR. However, there is one major difference, namely that photons collinear to the muons can be detected (while soft ones still go unobserved if  $E_{\gamma} < E_{\min}$ ).

If we write down the matrix element of the diagrams in Figure 1.10 and integrate over the phase space, we end up with the total cross section of photon production via muon pair production at LL

$$\sigma_{e^+e^- \rightarrow \gamma \rightarrow \mu^+ \mu^- \gamma}^{\text{FSR}} = \frac{\alpha}{\pi} \ln \frac{Q^2}{E_{\text{iso}}^2} \ln \frac{Q^2}{m_{\mu}^2} \sigma_{e^+e^- \rightarrow \gamma \rightarrow \mu^+ \mu^-}^{(0)}. \quad (1.30)$$



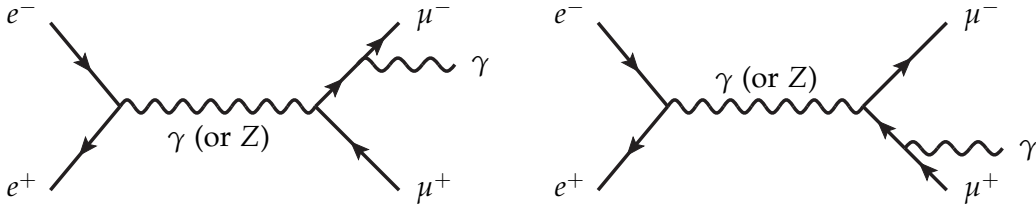


FIGURE 1.10: Feynman diagrams contributing to the process  $e^+e^- \rightarrow \mu^+\mu^-\gamma$  via final-state radiation (FSR).

Of special interest are the two logarithms appearing, where  $\ln(Q^2/E_{\text{iso}}^2)$  comes from the soft region and  $\ln(Q^2/m_\mu^2)$  from the collinear one. We emphasize that above result is only given at LL, which in this case comes enhanced by the two logarithms. The single-logarithmic and constant parts are omitted. The product of these two logarithms is known as the *Sudakov double logarithm*. Sudakov has first discovered these kind of logarithms in the calculation of the quantum electrodynamic vertex function and his findings were translated and published in [17].

#### 1.3.3.4 Hadron production

Let us now discuss, how one can calculate the hadrons eventually measured in a detector.

As we have already pointed out multiple times, the theoretical calculations of scattering processes are based on elementary particles. Quarks and gluons, in terms of which the perturbative expansion is formulated, can however not be measured by detectors, as they are not color-neutral. As we have seen in Figure 1.4, the measured jets allow for a reconstruction of the elementary particles created at the interaction point. From the theoretical side, we therefore first have to calculate the cross section of producing quarks and gluons, and then apply a mechanism that eventually turns them into hadrons. This procedure is called *hadronization*. It is non-perturbative and very complicated to study. As all existing approaches rely on phenomenological models, it is complex to quantify their accuracy.

Some observables however do not depend on the hadronization. For example, the total cross section of creating hadrons in an electron-positron collider is given by

$$\sigma_{e^+e^- \rightarrow \text{hadrons}} = \sigma_{e^+e^- \rightarrow \text{partons}} \cdot P(\text{partons} \rightarrow \text{hadrons}). \quad (1.31)$$

We can then use the probability  $P(\text{partons} \rightarrow \text{hadrons}) = 1$ , as the partons have to become hadrons somehow. Of course this is an intuitive, rather naive picture but it turns out to be correct in the high-energy limit. In Section 18.4 of [4] one may find a more rigorous approach, leading to the same result up to corrections of order  $\Lambda_{\text{QCD}}^4/Q^4$ .

This lets us start by looking at the creation of partons from an electron-positron annihilation and worry about hadronization later. At leading order, we encounter the same diagrams as we had in lepton pair production, depicted in Figure 1.7 with  $\mu^- \rightarrow q$  and  $\mu^+ \rightarrow \bar{q}$ . Also the calculation is the same, except that we have a factor of  $ieQ_q$  in the matrix element for the vertex between the quarks and messenger photon instead of  $-ie$ , where  $Q_q$  is the charge of the quark. Therefore, the LO cross section to measure any hadrons reads

$$\sigma_{e^+e^- \rightarrow \text{hadrons}} = 3 \sum_q Q_q^2 \sigma_{e^+e^- \rightarrow \mu^+\mu^-} + \mathcal{O}(\alpha^3) + \mathcal{O}(\alpha^2\alpha_s). \quad (1.32)$$

The factor of 3 comes from the three possible color charges and the sum over  $q$  goes over all quarks that *can* be created in the collider running at the respective energy. For example, no

calculation of this cross section had to include the top quark, as the production threshold of a  $t\bar{t}$  pair has not been reached so far by any lepton collider.

Measurements of the dimensionless ratio of the cross sections of the total hadronic  $e^+e^-$ -scattering divided by the one of muon pair production

$$R_{\text{had}}^\gamma = \frac{\sigma_{e^+e^- \rightarrow \gamma \rightarrow \text{hadrons}}}{\sigma_{e^+e^- \rightarrow \gamma \rightarrow \mu^+\mu^-}} \quad (1.33)$$

have confirmed that the parton model provides an accurate picture. In these measurements one can observe a step-like increase of  $R$  whenever the center-of-mass energy  $\sqrt{s}$  reaches new production thresholds. As the top pair production threshold has never been reached in an electron-positron collider, the maximal ratio was (at leading order)

$$R_{\text{had}}^\gamma = 3 \left( 3 \cdot \left( -\frac{1}{3} \right)^2 + 2 \cdot \left( \frac{2}{3} \right)^2 \right) = 3.67. \quad (1.34)$$

The messenger particle of the interaction at energies far below the  $Z$ -mass is usually a photon, but the total ratio  $R_{\text{had}}$  should also include the ratio of the diagrams involving a  $Z$ -boson as the messenger particle. For an electron-positron collider with its center-of-mass energy close to the  $Z$ -mass, the  $R$ -ratio at leading order in  $\alpha_s$  is obtained as

$$R_{\text{had}} = 20.09. \quad (1.35)$$

This observable was measured very precisely and the experimental results are only  $\sim 3.5\%$  higher, a difference that decreases further once we include loop corrections to the theoretical calculations.

Let us now come back to the procedure of hadronization which is usually modeled using Monte Carlo techniques. The two most common schemes are *string fragmentation* and *cluster fragmentation*. In both approaches there are many free parameters which need to be adjusted (tuned) to measured data.

The string fragmentation method gets its name from the idea of *color strings*. When looking at the  $q\bar{q}$  pair created at LO in a lepton collider, one can say that the two partons form a color string (as together, they need to be color-neutral). As these primary quarks are flying in opposite directions due to momentum conservation, they can not form a bound state with each other, because their invariant mass is much larger than the binding energy  $\sqrt{s} \gg \Lambda_{\text{QCD}} \sim 200 \text{ MeV}$ . This is where string fragmentation comes in – one takes this color string and breaks it in half by spontaneously creating a secondary quark and anti-quark, transforming the original color string between the primary quarks into two new color strings, each connecting a primary and a secondary quark. These color strings are fragmented again and again, until the invariant mass of the string is  $\sim 1 \text{ GeV}$ , and these strings are then forming the mesons. A similar but more involved method can be used to formulate the creation of baryons. As already pointed out, there are many free parameters such as string tension, breaking point, momentum distribution of the secondary quark pairs, and so on. This method is for example used in the parton shower code PYTHIA.

The cluster fragmentation model works similarly to splitting functions. Basically, one assumes the two quarks created at the interaction to emit gluons, and these gluons are again emitting other gluons and/or decay into a  $q\bar{q}$  pair. One then recombines the hadrons by looking at the color information of the particles that end up close to each other. This method is for example used in the parton shower code HERWIG.

We need to remember that the main part of the collision energy gets carried away by the initial  $q\bar{q}$  pair. Hadronization merely smears out these directions, creating a jet around each of them. To compare theoretical calculations to experiments, it is often good enough to treat the center of a measured jet as the direction of an elementary particle produced at the interaction point. The sum of all the measured hadronic momenta in the jet is approximately equal to the momentum of the quark which initiated the jet, as all those measured hadronic particles observed in a jet are assumed to come from the same initial elementary particle. Hadronization can be thought of as the theoretical counterpart to event reconstruction, but it works the other way around. Instead of measuring a jet and reconstructing its origin, we know the particle that became the mother of all the hadronic partons ending in the jet.

It should be obvious to the reader that in terms of photon production from ISR or FSR it does not matter whether we have a lepton pair or quark pair in the final state. However, in a quark pair we observe an additional type of FSR, namely gluons emitted from the  $q$  or  $\bar{q}$ . At  $\mathcal{O}(\alpha_s)$ , where we have a quark pair and a gluon in the final state  $\sigma_{e^+e^- \rightarrow q\bar{q}g}$ , we can measure three hadronic jets if the gluon was emitted at a large angle in respect to the quark pair.

A very important tool to calculate the transition from a parton created at the interaction point to a measured hadron are the already mentioned parton showers. They are a collection of Monte Carlo simulations which take a final state parton as calculated using perturbative theory and turn it into detectable hadrons. However, the only part reliably calculable is parton branching, which can be computed perturbatively using resummation methods. The rest is non-perturbative and therefore needs to be extracted from experimental data and comes with significant uncertainties.

#### 1.3.4 Hadron colliders

Now we want to look at a hadron collider with two proton beams such as the LHC. In general, the same procedures apply that we already discussed for the lepton collider. However, as we have already seen in the master formula for hadron colliders (1.5), hadrons consist of multiple partons which renders the calculation of cross sections much more complicated.

This brings a multitude of difficulties, one of them being that the interacting particles do not come with a fixed energy. The interaction between the partons happens at the partonic center-of-mass energy  $\sqrt{\hat{s}} = \sqrt{x_1 x_2 s}$ , where  $x_i$  is the fraction of the proton momenta carried by the parton from beam  $i \in \{1, 2\}$ . In general we have  $x_1 \neq x_2$ , which means that the center-of-mass frame of the interacting partons is not equal to the lab frame, where the hadronic center of mass lies. The two systems are in fact moving with a relative velocity of  $\beta = \frac{x_1 - x_2}{x_1 + x_2}$ . As these fractions differ for each measured event, they need to be reconstructed from the measured particles. This is only possible up to a certain degree, as most events include invisible particles such as neutrinos. These kinds of kinematic uncertainties complicate the analysis of hadron collider results.

##### 1.3.4.1 Parton Distribution Functions

To decide which partons in the hadrons are the interacting ones, we can use the PDFs  $f_{p/h}(x, \mu)$ . We already encountered those in the master formula (1.5), but postponed the proper treatment. In the meanwhile, we met the splitting functions of the lepton beams and are now perfectly well equipped to tackle the PDFs.

PDFs are partly fulfilling the same purpose as ISR in lepton colliders, as they also account for radiation too close to the beam to be detected. In addition, they also account for the probability of having additional sea partons in the hadron. The set of evolution equations to account for the parton distributions in QCD (the analogue of the Gribov-Lipatov equations) are given by the Altarelli-Parisi equations

$$\frac{df_g(x, \mu)}{d \ln \mu} = \frac{\alpha_s(\mu^2)}{\pi} \int_x^1 \frac{dz}{z} \left\{ P_{q \rightarrow g}(z) \sum_q \left[ f_q\left(\frac{x}{z}, \mu\right) + f_{\bar{q}}\left(\frac{x}{z}, \mu\right) \right] + P_{g \rightarrow g}(z) f_g\left(\frac{x}{z}, \mu\right) \right\}, \quad (1.36)$$

$$\frac{df_q(x, \mu)}{d \ln \mu} = \frac{\alpha_s(\mu^2)}{\pi} \int_x^1 \frac{dz}{z} \left\{ P_{q \rightarrow q}(z) f_q\left(\frac{x}{z}, \mu\right) + P_{g \rightarrow q}(z) f_g\left(\frac{x}{z}, \mu\right) \right\}, \quad (1.37)$$

$$\frac{df_{\bar{q}}(x, \mu)}{d \ln \mu} = \frac{\alpha_s(\mu^2)}{\pi} \int_x^1 \frac{dz}{z} \left\{ P_{q \rightarrow \bar{q}}(z) f_{\bar{q}}\left(\frac{x}{z}, \mu\right) + P_{g \rightarrow \bar{q}}(z) f_g\left(\frac{x}{z}, \mu\right) \right\}, \quad (1.38)$$

with the splitting functions

$$P_{q \rightarrow q}(z) = \frac{4}{3} \left[ \frac{1+z^2}{(1-z)_+} + \frac{3}{2} \delta(1-z) \right], \quad (1.39)$$

$$P_{q \rightarrow g}(z) = \frac{4}{3} \left[ \frac{1+(1-z)^2}{z} \right], \quad (1.40)$$

$$P_{g \rightarrow q}(z) = \frac{1}{2} [z^2 + (1-z)^2], \quad (1.41)$$

$$P_{g \rightarrow g}(z) = 6 \left[ \frac{1-z}{z} + \frac{z}{(1-z)_+} + z(1-z) + \left( \frac{11}{12} - \frac{n_f}{18} \right) \delta(1-z) \right], \quad (1.42)$$

where  $n_f$  is the number of quark flavors with  $m_q \ll \mu$ , with  $\mu$  again standing for the factorization scale. The meaning of this scale is that particles with transverse momenta  $p_T < \mu$  belong to the beams and are included in the PDFs, while particles with  $p_T > \mu$  are accounted for in the computation of the matrix elements. Of course, the physical observable is not going to depend on this scale.

While these functions are qualitatively very similar to the Gribov-Lipatov treatment of ISR photons, the main difference and complication is to find reasonable starting conditions similar to (1.28). In QED, we were able to assume that if all ISR photons were observed, we would have a clean, electron-only beam. As we have hadrons consisting of many partons, this assumption is not valid anymore and the probability to find one specific parton in the hadron is not calculable. To extract the PDFs, one therefore has to perform a fit to some experimental observables. Once this is done, we can use the PDFs to predict other observables, as they are reaction-independent and only depending on  $x$ .

To be of use when determining PDFs, observables need to check three criteria. Firstly, they need to be sensitive to as many PDFs as possible with a broad spectrum of  $x$  values (the  $\mu$ -dependence can then be computed via the Altarelli-Parisi equations). Secondly, one needs to have access on accurate calculations at the parton level, preferably to NNLO in  $\alpha_s$ . Thirdly, the contamination from new physics should be negligible and only data at energies far below the SM breaks down should be included in the fitting procedure.

As one can see in Figure 1.11 where we plot  $x \cdot f(x, \mu^2)$  for  $\mu^2 = 10 \text{ GeV}^2$  (left) and  $\mu^2 = 10^4 \text{ GeV}^2$  (right), the naive picture we painted in (1.7) of the proton consisting of two  $u$  and one  $d$  quark, each having  $x \sim 1/3$ , is somehow still visible. However, we can find many more partons in the proton than these two kinds; especially at low  $x \lesssim 0.1$ . Note that PDFs are only describing the distribution of momentum, not that of electric charge (which

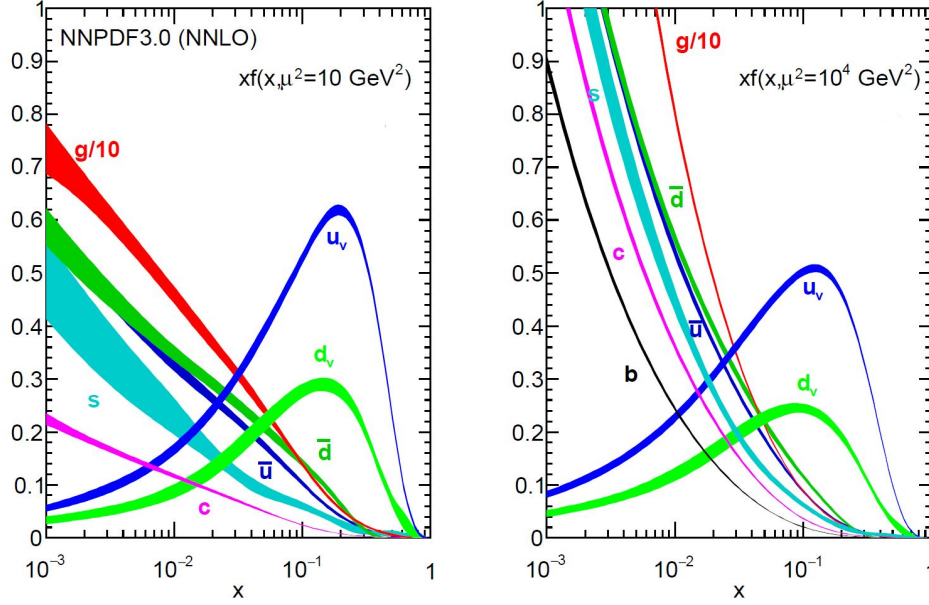


FIGURE 1.11: Proton PDFs at  $\mu^2 = 10 \text{ GeV}^2$  (left) and  $\mu^2 = 10^4 \text{ GeV}^2$  (right). On the  $x$ -axis the fraction of the hadronic energy  $x$  carried by the respective particle, on the  $y$ -axis  $x \cdot f(x, \mu^2)$ , the PDF  $f$  multiplied by  $x$  (in the case of the gluon, the PDF is divided by a factor of 10). Note that the full PDF of  $i = \{u, d\}$  is the sum of the valence quark PDFs  $f_{i_v}$  and sea quarks  $f_{i\bar{}}$ . From [16].

is carried entirely by the valence quarks  $u$  and  $d$ ). Gluons experience a similar enhancement in the soft and collinear region as the photons in ISR at lepton colliders. They are in fact highly dominating the region of very low  $x$ , as their PDFs are even reduced by a factor of 10 in the plots of Figure 1.11. One can also see the presence of sea quarks other than  $u$  and  $d$  in the protons, again of higher relevance at small  $x$ . This can be explained by their origin, which is gluon splitting. The quark PDFs are all at the same order of magnitude at small  $x$  (note that the full PDFs for the  $u$  and  $d$  quarks are the sum of the valence quark PDFs and the sea quark PDFs), while the masses of the  $b$ ,  $c$  and  $s$  reduce the respective PDFs. What should bother us at least a little bit is the size of the error bars. We can still vary the PDFs in these regions without spoiling the consistency of the data the PDFs were fitted on. This illustrates that we only achieve limited precision in our calculations, in particular for the strong force. Note that part of this uncertainty stems from experimental errors.

#### 1.3.4.2 Hard interactions, secondary interactions and underlying event

As we have seen, theoretical predictions of the outcomes of collisions between two partons are produced in an order-by-order-fashion in the electromagnetic coupling  $\alpha$  and the strong coupling  $\alpha_s$  by evaluating the master formula (1.5) for each nonzero PDF. However, this so-called hard interaction is not the only origin of measured particles, and a large amount of the physics happening at colliders can only be modeled by parton showers. In Figure 1.12 we have a look at a schematic depiction of a hadron collision as simulated by multi-purpose parton showers. We can see that much more is happening than just the hard interaction (the big red blob in the center of the picture).

The smaller red dots represent the decay of the very energetic partons created at the hard interaction. This part might still be treated in a perturbative fashion and included in the

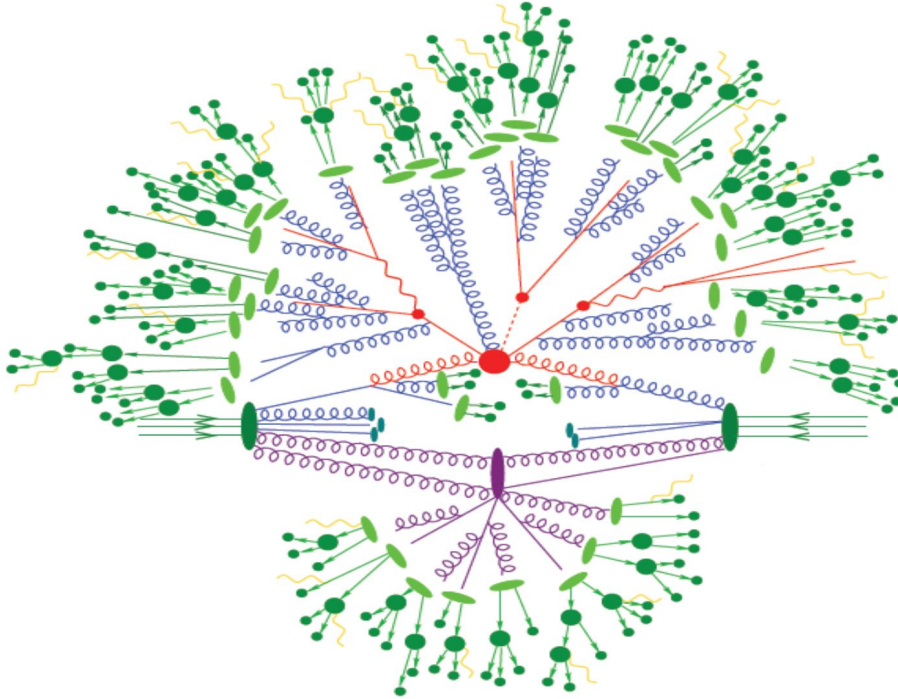


FIGURE 1.12: Schematic depiction of a hadron collision as simulated by multi-purpose parton showers. Hadrons are coming in from left and right (green ovals roughly at the center). The hard interaction happens at the red blob in the center of the picture with two gluons of the partons fusing to two quarks and a higgs. These partons radiate off some energy via FSR in the form of gluons (depicted in blue) before decaying into other particles (smaller red dots). The particles created here will loose some more energy due to FSR before eventually hadronizing into color-neutral particles that will be measured (green blobs). The two red lines on the right that are measured by the detector are leptons, the yellow wiggly lines are photons, also observed in the detector. Depicted below the blob of the hard interaction are two things, namely the ISR in blue, which also hadronizes and becomes color neutral, and in purple the underlying event. Adapted from [1].

calculation of the hard interaction in the form of an NLO matrix element. This becomes obviously much more involved with every added node.

Depicted in blue, we observe ISR and FSR which was already discussed in detail for the case of a lepton collider. Anything we discussed above also applies on hadron colliders, in particular the logarithmic enhancements. However, this kind of radiation is even more prominent at hadron colliders as the strong coupling  $\alpha_s$  is about ten times larger than the electromagnetic coupling  $\alpha$ . Also note that the emitted gluons can radiate off additional gluons, each with collinear and soft enhancements.

In the discussion of the lepton collider, we have also touched on hadronization effects. The color-neutral hadrons arising after hadronization are depicted as the green blobs in Figure 1.12. Note that the first few generations of the produced hadrons are likely too energetic and therefore unstable. They will decay further into stable hadrons, leptons (with neutrinos) and photons, which are then measured by the detector.

A feature occurring in hadron colliders which is absent in lepton colliders, is the so-called underlying event, colored purple in Figure 1.12. PDFs do not take into account the interaction of more than one parton per hadron, the left-over partons may very well



interact with each other as well. These multi-parton interactions can not be calculated in a perturbative way and need to be modeled. Luckily, even simple models seem to be sufficient and agree well with data, suggesting that the underlying event can be treated as a correction to the simple picture of the hard interaction.

When discussing the underlying event, it is also worth to point out that the initial hadrons need to recombine into a color-neutral state as well, after "loosing" a parton each to the hard interaction. This happens via ISR of the remaining partons and underlying events.

With PDFs, ISR, FSR, underlying event, hadronization and even decays of the produced hadrons, the possibilities of theoretical calculations are very limited. Except for the hard interactions, nothing can be treated perturbatively in a reliable fashion, and also the hard interaction is still suffering from uncertainties in the PDFs. ISR and FSR both feature logarithmically enhanced terms and we need to resort to resummation. The underlying event and hadronization needs to get simulated by parton showers, again coming with uncertainties that – depending on the observable – can be quite significant. One could summarize that the challenges of theoretical computations are at least as big and difficult as the ones discovered on the experimental side.

#### 1.4 EFFECTIVE THEORIES

One method to reduce the complexity of calculations in collider processes is the application of Effective Field Theories (EFTs).

The intuitive idea behind effective theories is simple. Its main statement is that one can calculate something without knowing every detail. Experts in applying effective methods are for example architects and construction workers. They are fully capable to design and construct buildings, roads and bridges without knowing anything about General Relativity or Quantum Theory, but rely mainly on Newton's laws of mechanics. In a macroscopic undertaking such as the construction of a building, the detailed short-distance interactions among elementary particles are simply irrelevant. In this context, Newton's laws are an effective theory which gives equivalent results (up to the relevant precision) to the ones obtained by the theory of General Relativity in the case of a static gravitational field and the limit of slow-moving objects (slow if compared to the speed of light). Furthermore, Newton's laws also reproduce the physics of Quantum Mechanics up to some precision.

The treatment of field theories using effective theories appears natural as well. How to implement them in a mathematically consistent way is however not always straightforward.

As an example, let us look at a relatively simple and well-known EFT, namely the multipole expansion in electrostatics. This is obviously not very closely related to collider physics, but acts as an excellent illustrative example.

The multipole expansion of the electrostatic potential reads

$$V(\vec{r}) = \frac{1}{r} \sum_{l,m} B_{l,m} \frac{1}{r^l} Y_l^m(\Omega) = \frac{1}{r} \sum_{l,m} C_{l,m} \left(\frac{a}{r}\right)^l Y_l^m(\Omega), \quad (1.43)$$

where  $Y_l^m(\Omega)$  are the standard spherical harmonics and  $B_{l,m}$  are constant coefficients that translate to  $B_{l,m} = C_{l,m} a^l$  where  $a$  is the typical spacing between charges and  $C_{l,m}$  is a dimensionless coefficient of  $\mathcal{O}(1)$ . Apart from  $a$  we have a second length scale  $r$ , the distance at which we measure the electric potential of the charges.

Far away from the charges ( $a \ll r$ ), every additional summand in the sum of (1.43) is much smaller than the one before. We can write an expansion parameter  $\delta = a/r \ll 1$ . So, at long

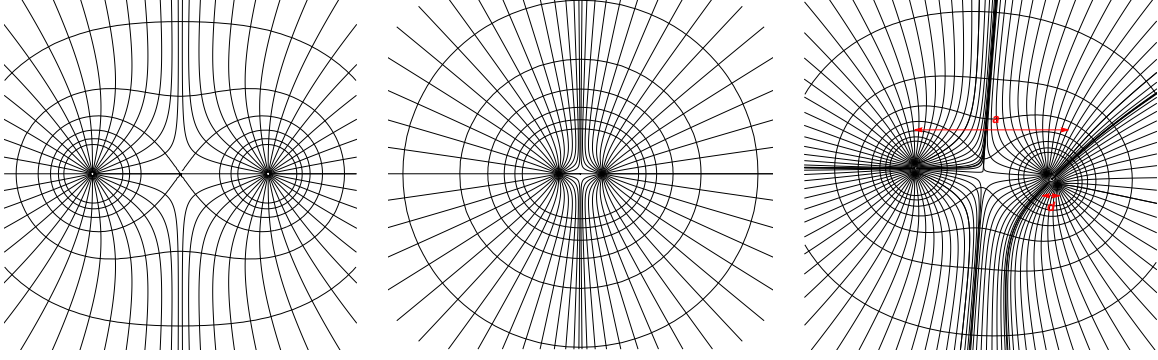


FIGURE 1.13: Electric field and equipotential lines for two point charges of the same sign from up close (left) and zoomed out (center). The panel on the right shows a charge distribution of four charges of the same sign, grouped in two batches of intrinsic scale  $d$ . As one can see, from further away one can not distinguish the two static charges from a single one. Four charges in groups of two appear at some distance like two charges, and from further away again like one single charge. From [6].

distances, the first summand provides already a good approximation (see Figure 1.13) and the second one would bring corrections of  $\mathcal{O}(\delta)$ . Experiments done at the distance  $r$  from the charge distribution can only determine the  $C_{l,m}$  up to a certain value  $l_{\max}$ , which depends on the resolution of the experiment. More accurate experiments with better resolutions would determine  $C_{l,m}$  of higher  $l$ . This truncated potential with a finite number of terms is an EFT for the full potential  $V(\vec{r})$ . The accuracy of the EFT can be systematically improved by including additional terms, each power-suppressed by  $\delta$ . The main message is that we do not need to know the exact charge distribution to have this expansion working.

If we look at the more complicated case of having the charges distributed with two intrinsic scales  $d$  and  $a \gg d$  (right panel in Figure 1.13), at a far distance  $r \gg a$  the effects appearing at distances  $a$  are dominant, and only with very precise measurement methods we can filter out anything at the scale  $d$ . If the experimental apparatus does not provide such a precise resolution, but we still need to know what happens at the short distance  $d$ , we can (at least theoretically) move the apparatus closer to the charges. At  $a \gg r \gg d$ , the effects of one batch of charges can be explored using the multipole expansion with  $\delta = d/r$ , while the effects of the other batch at far-away distance  $a \gg r$  do not matter all that much and can be treated as a constant factor.

Note that while we were using the terminology of *distance* in this example, in collider physics we are normally using *energy* as the scale-defining parameter. Everything discussed here could also be thought of in terms of the energy, as we have seen in Section 1.1. Due to their inverse relationship (see Table 1.1), the expansion in long distances corresponds to the expansion in small energies.

As already stated, this example of an EFT is not directly related to particle physics. However, there are many other examples of EFTs that treat specifically problems in particle physics but are more involved. One such example is the Fermi theory of the weak interaction, which is a low-energy EFT constructed from the SM. The expansion parameter in this theory is given by the order of the momenta  $p = |\vec{p}|$  of the particles participating in the weak decay divided by the mass of the  $W$ -boson  $m_W$ ,  $\delta = p/m_W$ , in analogy to the parameter  $a/r$  we encountered in the discussion on the multipole expansion. The expansion parameter is again very small, for example in muon decays we have  $p \approx m_\mu \approx 105 \text{ MeV}$ , compared



to  $m_W \approx 80 \text{ GeV}$ . Similar to the Fermi theory of weak interactions, one can view the SM itself as the leading terms of an EFT. This theory is called SMEFT and a considerable number of theoretical physicists are working in this field. The operators of SMEFT are the higher-dimensional operators created from SM fields, where each higher dimensional operator gets suppressed by an (unknown) *new physics scale*  $\Lambda$ , similar to the suppression by  $m_W$  in the Fermi theory. Other examples of EFTs in particle physics are the Heavy Quark Effective Theory (HQET), which describes the physics of heavy quarks at low momentum, non-relativistic QCD (NRQCD), which is similar to HQET but treats bound states, and Chiral Perturbation Theory ( $\chi$ PT), describing the interactions of pions and nucleons at low momentum transfers. These and many more examples were discussed at the Les Houches Session CVIII, and I highly recommend the lecture notes of this specific summer school [6] to the reader.

## 1.5 OUTLINE

In the next section, we will introduce an EFT which is relevant for collider physics, namely Soft-Collinear Effective Theory (SCET). To this end, we will first look at the various energy scales present in a collision to find suitable expansion parameters and write down an explicit effective Lagrangian of this theory. We will then discuss the renormalization group evolution in an example and introduce the theory behind the resummation of non-global logarithms in jet cross sections.

After this more advanced introduction to the theoretical background, the main part of this thesis consists of three articles, either published or accepted for publication in the Journal of High Energy Physics JHEP. Chapter 3 is a copy of [18]. For the calculations in this article, we wrote a dedicated computer code which resums non-global logarithms appearing in gap fractions of di-jet events and isolation cone cross sections at leading logarithmic accuracy. Because this parton shower formalism is based on first principles, the ingredients needed to achieve subleading logarithmic accuracy are clear. In Chapter 4 we provide a copy of [19]. In this work, we adapted the parton-shower code to resum non-global logarithms for the first time beyond leading order, not yet achieving full next-to-leading logarithmic accuracy but a step in between which is named  $LL'$  (for the observable of the jet mass  $NLL'$ ). Chapter 5 is finally a copy of the third article [20], which has been accepted for publication. In this article, we go beyond the high-energy limit and include massive quarks in our code to resum non-global logarithms appearing in  $t\bar{t}$ -production at  $LL$ .

In Chapter 6, we will conclude by reviewing what we have achieved and discuss what further steps can and should be taken.



## SOFT-COLLINEAR EFFECTIVE THEORY

*Eine Theorie ist desto eindrucksvoller, je grösser die Einfachheit ihrer Prämissen ist, je verschiedenartigere Dinge sie verknüpft, und je weiter ihr Anwendungsbereich ist.*

— Albert Einstein

As we have seen in Chapter 1, the challenges we face in collider physics are manifold. In the detector, we encounter energetic hadronic jets in some particular regions while measuring only soft hadronic energy in the remaining part. A useful tool to help us calculate cross sections involving particles at such widely separated energy scales is Soft-Collinear Effective Theory (SCET). This formalism is constructed specifically for processes involving energetic particles and as discussed in the last chapter, almost all knowledge we have gained in the sub-nuclear domain comes from such collisions.

## 2.1 ENERGY SCALES OF COLLIDER PROCESSES

As we have seen in Chapter 1, hadronic particles are often measured in the form of jets, which provide information about the underlying scattering of elementary particles. Other hadronic particles of small energy, for example radiated off of a high-energetic particle via FSR, may be anywhere in the detector. If we look at a simple collision with two detected jets as depicted in Figure 2.1, we encounter a clear hierarchy in energies. To quantify this hierarchy, we define the total momenta inside the jets to be  $p_j$  and  $p_{\bar{j}}$  and the momentum of soft radiation as  $p_s$ . They are hierarchically ordered as

$$Q^2 \approx (p_j + p_{\bar{j}})^2 \gg p_j^2 \sim p_{\bar{j}}^2 \gg p_s^2. \quad (2.1)$$

We observe three energy scales, namely the *hard scale*  $\sim Q^2$ , the *(anti-)collinear scale*  $\sim p_j^2 \sim p_{\bar{j}}^2$  and the *soft scale*  $\sim p_s^2$ .

When constructing SCET, the physics at the hard scale is integrated out and makes its reappearance as Wilson coefficients (coupling constants) of operators in the effective theory. These Wilson coefficients are similar in nature to the coefficients  $C_{l,m}$  in the multipole expansion of the electrostatic potential (1.43). The physics at the (anti-)collinear scale and the soft scale is obviously of special interest to collider processes as it characterizes the experimentally measured final states. The end result of a SCET analysis is often the factorization of a cross section into its respective functions

$$\sigma = H(Q^2) \cdot J(p_j^2) \otimes \bar{J}(p_{\bar{j}}^2) \otimes S(p_s^2), \quad (2.2)$$

where each function contains only the physics at the respective scale and is ignorant of the other scales. Note that the functions depend on the considered observable, just as the meaning of the symbol  $\otimes$ , which can be a product or a convolution.

To get from QCD to SCET, we need to split each quark and gluon field in QCD into modes for each scale

$$\phi = \phi_h + \phi_c + \phi_{\bar{c}} + \phi_s, \quad (2.3)$$

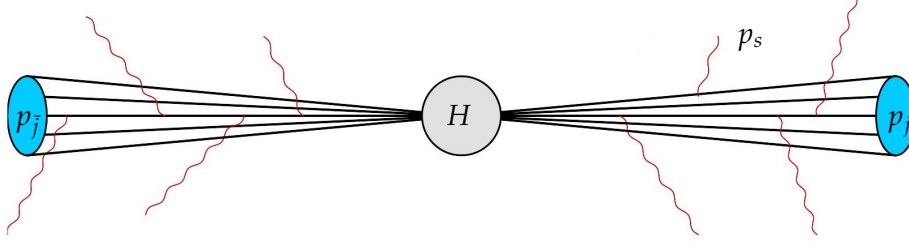


FIGURE 2.1: Schematic depiction of a di-jet process. The hard interaction  $H$  happens in the center, two elementary particles get produced that are measured as jets, with the detected momenta  $p_j$  and  $p_{\bar{j}}$ . Via FSR, some particles of small energy with momenta  $p_s$  are distributed homogeneously in the collider. Adapted from [6].

where  $\phi$  stands for a quark or a gluon field. Here,  $c$  stands for the collinear mode and is related to the jet function  $J$ . To integrate out the hard modes  $\phi_h$ , we write down the most general effective Lagrangian with the low-energy operators  $\phi_c$ ,  $\phi_{\bar{c}}$  and  $\phi_s$  and then adjust the couplings to reproduce the contribution of the hard region. This procedure is called the *matching*, as one adjusts the coupling (or the Wilson coefficients) in such a way that the full theory is reproduced. In the next section, we will derive the SCET Lagrangian of QCD in detail.

First, it is worth to explain the sudden change of notation with the  $j$  and  $\bar{j}$  getting replaced by  $c$  and  $\bar{c}$ . This comes from the fact that one introduces (light-like) reference vectors in the directions of the jets. These reference vectors correspond to the directions of the elementary particles produced at the hard interaction. The hadronic particles that get created by the decay of these particles and eventually form the jets however propagate not exactly in this direction but collinear to it.

Let us quantify this and introduce light-cone coordinates in relation to these reference vectors

$$n^\mu = p_j^\mu / p_j^0 = (1, 0, 0, 1) \quad \text{and} \quad \bar{n}^\mu = p_{\bar{j}}^\mu / p_{\bar{j}}^0 = (1, 0, 0, -1). \quad (2.4)$$

Any momentum can now be written as

$$p^\mu = (n \cdot p) \frac{\bar{n}^\mu}{2} + (\bar{n} \cdot p) \frac{n^\mu}{2} + p_\perp^\mu \equiv p_+^\mu + p_-^\mu + p_\perp^\mu, \quad (2.5)$$

and it is often very useful to give the momentum by specifying the components

$$p^\mu = (n \cdot p, \bar{n} \cdot p, p_\perp^\mu) \equiv (p_+, p_-, p_\perp^\mu). \quad (2.6)$$

Using  $n^2 = \bar{n}^2 = n \cdot p_\perp = \bar{n} \cdot p_\perp = 0$  and  $n \cdot \bar{n} = 2$ , it is easy to show that

$$p^2 = p_+ p_- + p_\perp^2, \quad \text{and} \quad p \cdot q = \frac{1}{2} (p_+ q_- + p_- q_+) + p_\perp \cdot q_\perp. \quad (2.7)$$

To discuss the (anti-)collinear and soft modes in the effective theory, let us introduce a small expansion parameter  $\lambda^2 \sim p_j^2 / Q^2 \sim p_{\bar{j}}^2 / Q^2 \ll 1$ . The momenta of the four regions in light-cone coordinates (2.6) scale as

$$\text{hard } (h) \sim (1, 1, 1)Q, \quad (2.8)$$

$$\text{collinear } (c) \sim (\lambda^2, 1, \lambda)Q, \quad (2.9)$$

$$\text{anti-collinear } (\bar{c}) \sim (1, \lambda^2, \lambda)Q, \quad (2.10)$$

$$\text{soft } (s) \sim (\lambda^2, \lambda^2, \lambda^2)Q. \quad (2.11)$$

Let me point out that the possibility of soft modes scaling as  $\sim (\lambda, \lambda, \lambda)Q$  exists for some observables and gives rise to the formalism of SCET<sub>II</sub>, where the scaling (2.11) would be named the *ultra-soft* scaling. However, we will restrict ourselves to SCET<sub>I</sub> where these modes do not occur.

If we did not know already what the scalings of our momenta were, we could have also applied the *Strategy of Regions* [21, 22]. One would start by writing down a loop integral in dimensional regularization and splitting it in several integrals by appropriately expanding the integrand region-by-region. Once the sum over the individual regions reproduces the result of the original integral and all intermediate divergences drop out, we have discovered all the regions present in our problem. This method is explained and applied on an example in Chapter 2 of [7], and I highly recommend this reference for anyone interested in the subject. As the regions are obvious in our case, we want to directly jump to the construction of the effective Lagrangian.

## 2.2 EFFECTIVE LAGRANGIAN

As we already touched on before (2.3), we start the construction of the effective Lagrangian by splitting the quark and gluon fields into fields whose momenta scale appropriately for the relevant regions

$$\psi \rightarrow \psi_c + \psi_{\bar{c}} + \psi_s \quad \text{and} \quad A^\mu \rightarrow A_c^\mu + A_{\bar{c}}^\mu + A_s^\mu. \quad (2.12)$$

To obtain tree-level SCET, one can take the QCD Lagrangian and replace the fields  $\psi$  and  $A^\mu$  by the above fields, then expand away the suppressed terms. For the sake of simplicity we want to stop discussing the anti-collinear modes from here on and stick to the collinear and soft ones. The anti-collinear parts of the Lagrangian unsurprisingly end up being analogous to the collinear ones.

To find the scalings of the terms in the Lagrangian, we need to first find the scaling of the fields. To do this, we look at their propagators, starting with the gluon propagator

$$\langle 0 | T \{ A_\mu^a(x) A_\nu^b(0) \} | 0 \rangle = \int \frac{d^4 p}{(2\pi)^4} \frac{i}{p^2 + i0} e^{-ip \cdot x} \left[ -g_{\mu\nu} + \xi \frac{p_\mu p_\nu}{p^2} \right] \delta^{ab}. \quad (2.13)$$

Note that we have to have  $x$  scaling conjugate to the momentum  $p$ , otherwise it would not be possible to get the Fourier exponent  $x \cdot p \sim \mathcal{O}(\lambda^0)$ . Let us look at the part with the gauge parameter  $\xi$  and count the dimensions in  $p$ . We have  $d^4 p p^{-2} p^{-2} p_\mu p_\nu \sim p_\mu p_\nu$ , and therefore the gluon field scales exactly like the momentum  $A_\mu \sim p_\mu$ . This gives us the soft and collinear gluon field components scaling as

$$(n \cdot A_s, \bar{n} \cdot A_s, A_{s\perp}^\mu) \sim (\lambda^2, \lambda^2, \lambda^2), \quad (2.14)$$

$$(n \cdot A_c, \bar{n} \cdot A_c, A_{c\perp}^\mu) \sim (\lambda^2, 1, \lambda). \quad (2.15)$$

So, whenever we have terms with both soft and collinear gluons, the soft ones are power suppressed except for the  $n \cdot A_s$  component.

For the quark field propagator we first look only at the soft one, reading

$$\langle 0 | T \{ \psi_s(x) \bar{\psi}_s(0) \} | 0 \rangle = \int \frac{d^4 p}{(2\pi)^4} \frac{i \not{p}}{p^2 + i0} e^{-ip \cdot x} \sim (\lambda^2)^4 \frac{\lambda^2}{(\lambda^2)^2} = \lambda^6. \quad (2.16)$$

This means that soft fermions scale as  $\psi_s(x) \sim \lambda^3$ .

The collinear fermions are more involved, because the terms of  $\not{p} = (n \cdot p) \frac{\not{n}}{2} + (\bar{n} \cdot p) \frac{\not{\bar{n}}}{2} + \not{p}_\perp$  have different scalings. This leads us to further split the collinear quark fields into

$$\psi_c = P_+ \psi_c + P_- \psi_c \equiv \xi_c + \eta_c, \quad \text{with} \quad P_+ = \frac{\not{n} \not{\bar{n}}}{4} \quad \text{and} \quad P_- = \frac{\not{\bar{n}} \not{n}}{4}, \quad (2.17)$$

with the  $P_\pm$  being projection operators  $P_\pm^2 = P_\pm$  and  $P_+ + P_- = 1$ . These two components fulfill  $\not{n} \xi_c = \not{\bar{n}} \eta_c = 0$ . The propagators of these fields read

$$\langle 0 | T \{ \xi_c(x) \bar{\xi}_c(0) \} | 0 \rangle = \int \frac{d^4 p}{(2\pi)^4} \frac{i \frac{\not{n} \not{\bar{n}}}{4} \not{p}}{p^2 + i0} e^{-ip \cdot x} = \int \frac{d^4 p}{(2\pi)^4} \frac{ip_-}{p^2 + i0} e^{-ip \cdot x} \sim (\lambda)^4 \frac{1}{\lambda^2} = \lambda^2, \quad (2.18)$$

$$\langle 0 | T \{ \eta_c(x) \bar{\eta}_c(0) \} | 0 \rangle = \dots = \int \frac{d^4 p}{(2\pi)^4} \frac{ip_+}{p^2 + i0} e^{-ip \cdot x} \sim (\lambda)^4 \frac{\lambda^2}{\lambda^2} = \lambda^4, \quad (2.19)$$

and therefore the two constituents of the collinear quark field scale as  $\xi_c(x) \sim \lambda$  and  $\eta_c(x) \sim \lambda^2$ .

To now construct the SCET-Lagrangian, we can plug the SCET-fields from (2.12) into the QCD action. At tree level, we can collect it into three summands (five, if including the anti-collinear modes), namely

$$S = S_s + S_c + S_{sc} (+S_{\bar{c}} + S_{s\bar{c}}) + \dots \quad (2.20)$$

Here,  $S_s$  contains only the terms associated to soft modes,  $S_c$  the collinear terms and  $S_{sc}$  the interactions between soft and collinear modes. Collinear and anti-collinear fields could only interact with each other via a hard momentum transfer, a discussion we will postpone for the moment.

### 2.2.1 Soft and collinear terms

We start by writing down  $S_s$ . This is a straightforward thing to do and the results read exactly as the QCD action itself

$$S_s = \int d^4 x \left( \bar{\psi}_s i \not{D}_s \psi_s - \frac{1}{4} (F_s^a)_{\mu\nu} (F_s^a)^{\mu\nu} \right), \quad (2.21)$$

where the covariant derivative and the field strength tensor are defined as

$$i \not{D}_s^\mu = i \partial^\mu + g A_s^\mu = i \partial^\mu + g (A_s^a)^\mu t^a, \quad (2.22)$$

$$ig (F_s^a)^{\mu\nu} t^a = [i \not{D}_s^\mu, i \not{D}_s^\nu] = ig \left\{ \partial^\mu (A_s^a)^\nu - \partial^\nu (A_s^a)^\mu + g f^{abc} (A_s^b)^\mu (A_s^c)^\nu \right\} t^a. \quad (2.23)$$

The reproduction of the standard QCD action in the case of soft quarks and gluons should not surprise, as the soft momenta are of equal scaling  $\lambda^2$  in each light-cone coordinate. It is also worth to point out that all terms of the action in the soft action are of  $\mathcal{O}(1)$ , as  $x^2 \sim (p_s)^{-2} \sim \lambda^{-4}$  and therefore  $d^4 x \sim \lambda^{-8}$ , canceling the scalings of the fields as given in (2.14) and (2.16).

The calculation of the purely collinear term is more intricate since it involves the splitting of the collinear quark field (2.17). It reads

$$S_c = \int d^4 x \left( (\bar{\xi}_c + \bar{\eta}_c) \left( i(n \cdot D_c) \frac{\not{n}}{2} + i(\bar{n} \cdot D_c) \frac{\not{\bar{n}}}{2} + i \not{D}_{c,\perp} \right) (\xi_c + \eta_c) - \frac{1}{4} (F_c^a)_{\mu\nu} (F_c^a)^{\mu\nu} \right), \quad (2.24)$$

which after we apply the identities  $\not{n}\xi_c = \bar{\xi}_c\not{n} = \not{n}\eta_c = \bar{\eta}_c\not{n} = \bar{\xi}_c\not{D}_{c,\perp}\xi_c = \bar{\eta}_c\not{D}_{c,\perp}\eta_c = 0$  can be reduced to

$$S_c = \int d^4x \left( \bar{\xi}_c i(n \cdot D_c) \frac{\not{n}}{2} \xi_c + \bar{\xi}_c i\not{D}_{c,\perp} \eta_c + \bar{\eta}_c i\not{D}_{c,\perp} \xi_c + \bar{\eta}_c i(\bar{n} \cdot D_c) \frac{\not{n}}{2} \eta_c - \frac{1}{4} (F_c^a)_{\mu\nu} (F_c^a)^{\mu\nu} \right). \quad (2.25)$$

The covariant derivative and the field strength tensor are defined the same way as the ones of the soft fields in (2.22) and (2.23), but with the collinear gluon fields. Note that all surviving terms are again of  $\mathcal{O}(1)$ , as we have  $x^2 \sim (p_c)^{-2} \sim \lambda^{-2}$ , and the four negative powers of  $\lambda$  from the  $d^4x$  cancel the four powers of  $\lambda$  in each of the summands, remembering that the covariant derivative scales as the collinear gluon field (2.15).

As we have both components of the collinear quark field  $\xi_c \sim \lambda$  and  $\eta_c \sim \lambda^2$  appearing and even mixing, this form is not very convenient to use. We can however perform a shift

$$\eta_c \rightarrow \eta_c - \frac{\not{n}}{2} \frac{1}{i\bar{n} \cdot D_c} i\not{D}_{c,\perp} \xi_c, \quad (2.26)$$

and get

$$S_c = \int d^4x \left( \bar{\xi}_c \frac{\not{n}}{2} \left[ i(n \cdot D_c) + i\not{D}_{c,\perp} \frac{1}{i\bar{n} \cdot D_c} i\not{D}_{c,\perp} \right] \xi_c + \bar{\eta}_c i(\bar{n} \cdot D_c) \frac{\not{n}}{2} \eta_c - \frac{1}{4} (F_c^a)_{\mu\nu} (F_c^a)^{\mu\nu} \right). \quad (2.27)$$

This eliminates the mixing, but the field  $\eta_c$  still appears. One can integrate this out, as the path integral will give a determinant  $\det \left( i(\bar{n} \cdot D_c) \frac{\not{n}}{2} \right)$ . In light-cone gauge ( $\bar{n} \cdot A_c = 0$ ) we have  $\bar{n} \cdot D_c = \bar{n} \cdot \partial = 0$  and the determinant becomes trivial. As the determinant is gauge invariant, it reduces to a trivial prefactor which drops out in the calculation of expectation values. The term of  $\eta_c$  can therefore be safely dropped from the Lagrangian.

### 2.2.2 Interaction terms

After the purely collinear and soft terms, let us now have a look at the interaction term  $S_{sc}$ . We will only treat it at leading power, the general construction is quite involved and may be found in [23].

First, we remember that the soft quark fields scale as  $\psi_s \sim \lambda^3$  while the collinear ones at leading power as  $\xi \sim \lambda$ . This power suppression leads to the absence of soft and collinear interactions of the quark fields (at leading order).

In the case of gluon fields however we do have such interactions, as we have  $n \cdot A_c \sim n \cdot A_s \sim \lambda^2$  while all other components of the soft gluon field are again power suppressed. Therefore, to introduce interactions, we can add a soft gluon field to the collinear one

$$A_c^\mu \rightarrow A_c^\mu + n \cdot A_s \frac{\bar{n}^\mu}{2}, \quad (2.28)$$

and recalculate the collinear action with this mixed field. Among the rather intuitive mixing of gluon fields, it also gives rise to the interaction

$$S_{cs} = \int d^4x \bar{\xi}_c(x) \frac{\not{n}}{2} n \cdot A_s(x) \xi_c(x). \quad (2.29)$$

The total momentum of this integral has collinear scaling such that  $x$  scales here as  $x^\mu \sim (1, \lambda^{-2}, \lambda^{-1})$ . If we expand the soft gluon field in its components

$$A_s(x_-) \approx A_s(0) + x_- \partial_+ A_s(x) + \dots, \quad (2.30)$$

$$A_s(x_+) \approx A_s(0) + x_+ \partial_- A_s(x) + \dots, \quad (2.31)$$

$$A_s(x_\perp) \approx A_s(0) + x_\perp \partial_\perp A_s(x) + \dots, \quad (2.32)$$

we see that only the correction in the first line is of  $\mathcal{O}(1)$ , as  $x_- \sim \lambda^{-2}$  and  $\partial_+ A_s(x) \sim p_{s,+} \sim \lambda^2$ . Therefore, similar to the multipole expansion of electrostatics, we can expand the soft gluon field around  $x_-$ , giving us

$$S_{cs} = \int d^4x \bar{\xi}_c(x) \frac{\not{n}}{2} n \cdot A_s(x_-) \xi_c(x). \quad (2.33)$$

We can now read off the full SCET Lagrangian from (2.21), (2.27) and (2.33) to be

$$\mathcal{L} = \bar{\psi}_s i \not{D}_s \psi_s + \bar{\xi}_c \frac{\not{n}}{2} \left[ i(n \cdot D) + i \not{D}_{c,\perp} \frac{1}{i \bar{n} \cdot D_c} i \not{D}_{c,\perp} \right] \xi_c - \frac{1}{4} (F_s^a)_{\mu\nu} (F_s^a)^{\mu\nu} - \frac{1}{4} (F_c^a)_{\mu\nu} (F_c^a)^{\mu\nu}, \quad (2.34)$$

with the covariant derivative  $D_s^\mu$  given in (2.22) and its collinear counterpart  $D_c^\mu$  which is the same as the soft one, except one replaces the soft fields by collinear ones. Also the soft field strength tensor is given above in (2.23). The interactions between soft and collinear fields happen in the newly introduced mixed covariant derivative

$$in \cdot D = in \cdot \partial + gn \cdot A_c(x) + gn \cdot A_s(x_-), \quad (2.35)$$

and the mixed field strength tensor

$$ig(F_c^a)^{\mu\nu} t^a = [iD^\mu, iD^\nu], \quad \text{with} \quad D^\mu = n \cdot D \frac{\bar{n}^\mu}{2} + \bar{n} \cdot D_c \frac{n^\mu}{2} + D_{c,\perp}^\mu. \quad (2.36)$$

Note that in addition to the terms written in (2.34), there would also be the terms of the anti-collinear modes including the mixing of anti-collinear and soft modes. They are exactly the same as the ones of the collinear fields, after exchanging  $n \leftrightarrow \bar{n}$  and  $x_- \leftrightarrow x_+$ .

It should also be pointed out that the lack of Wilson coefficients in the effective Lagrangian (2.34) is not surprising. First of all, we have the purely soft part, a copy of the QCD Lagrangian, reproducing all purely soft processes exactly. This statement is true as long as we work in dimensional regularization and do not apply a hard cutoff. Also the collinear part is equivalent to QCD, we simply integrated out the two components of  $\eta_c$  but have not done any approximations.

Matching corrections however do appear if we introduce interactions between the collinear and anti-collinear fields. Such operators would have to come with a hard momentum exchange, for example from a virtual photon decaying into a collinear quark and anti-collinear anti-quark. While operators with derivatives are usually power suppressed, the derivatives of the large light-cone component come unsuppressed in SCET. One needs to include an infinite number of such derivative operators mixing collinear and anti-collinear fields. Equivalently, one can smear out the fields, which in turn makes the theory non-local along the direction of large momentum flow. To maintain gauge invariance, one then has to introduce Wilson lines. We will not get into the details of such operators and refer the reader to Section 5.3.3 of [6].



### 2.2.3 Decoupling transformation

Let us now look at the interaction term in the SCET Lagrangian,  $\bar{\xi}_c \frac{\not{n}}{2} i(n \cdot D) \xi_c$ . By introducing the soft Wilson line

$$S_n(x) = \mathbf{P} \exp \left[ ig \int_{-\infty}^0 ds n \cdot A_s(x + sn) \right], \quad (2.37)$$

where  $\mathbf{P}$  is the path ordering of the color matrices, we can redefine the collinear fields once again

$$\xi_c(x) \rightarrow S_n(x_-) \xi_c^{(0)}(x), \quad \text{and} \quad A_c^\mu(x) \rightarrow S_n(x_-) A_c^{(0)\mu}(x) S_n^\dagger(x_-). \quad (2.38)$$

After this transformation, it is straightforward to show that

$$\begin{aligned} i(n \cdot D) \xi_c(x) &\rightarrow \left( in \cdot \partial + gn \cdot S_n(x_-) A_c^{(0)}(x) S_n^\dagger(x_-) + gn \cdot A_s(x_-) \right) S_n(x_-) \xi_c(x) \\ &= S_n(x_-) \left( in \cdot \partial + gn \cdot A_c^{(0)}(x) \right) \xi_c(x) \equiv S_n(x_-) i(n \cdot D_c^{(0)}) \xi_c(x), \end{aligned} \quad (2.39)$$

the full term in the Lagrangian now reading

$$\bar{\xi}_c \frac{\not{n}}{2} i(n \cdot D) \xi_c \rightarrow \bar{\xi}_c^{(0)} \frac{\not{n}}{2} i(n \cdot D_c^{(0)}) \xi_c^{(0)}. \quad (2.40)$$

As we can see, the soft gluon field does no longer appear in the same operator as the collinear one. This is also indicated by the superscript of the fields. Due to this absence of explicit soft fields in the interaction term, the redefinition of the fields (2.38) is called *decoupling transformation*.

A similar decoupling transformation can obviously be applied to the anti-collinear fields, leading to the rewriting of the SCET Lagrangian (including the anti-collinear part not present in (2.34)) into three disjunct terms

$$\mathcal{L}_{\text{SCET}} = \mathcal{L}_c^{(0)} + \mathcal{L}_{\bar{c}}^{(0)} + \mathcal{L}_s, \quad (2.41)$$

allowing for a separation of the states into

$$|X\rangle = |X_c\rangle \otimes |X_{\bar{c}}\rangle \otimes |X_s\rangle. \quad (2.42)$$

As all the interactions between the collinear fields and the soft fields manifest themselves in soft Wilson lines along the directions of the collinear and anti-collinear particles.

## 2.3 RESUMMATION BY RESUMMATION GROUP EVOLUTION

For completeness and before going over to the factorization of jet cross sections, let us review a specific result of Section 5.3.4 in [6] where the Sudakov form factor is considered. This is the form factor associated with a hard current that sources both a collinear and an anti-collinear fermion field which comes with a nontrivial Wilson coefficient. After decoupling transformations, the two sourced fields emit soft gluons from Wilson lines alongside their directions. A schematic picture is given in Figure 2.2.

The Sudakov form factor can be shown to factorize as

$$F(Q^2, \Lambda_j^2, \Lambda_{\bar{j}}^2) = \tilde{C}(Q^2, \mu) J(\Lambda_j^2, \mu) \bar{J}(\Lambda_{\bar{j}}^2, \mu) S(\Lambda_s^2, \mu), \quad (2.43)$$

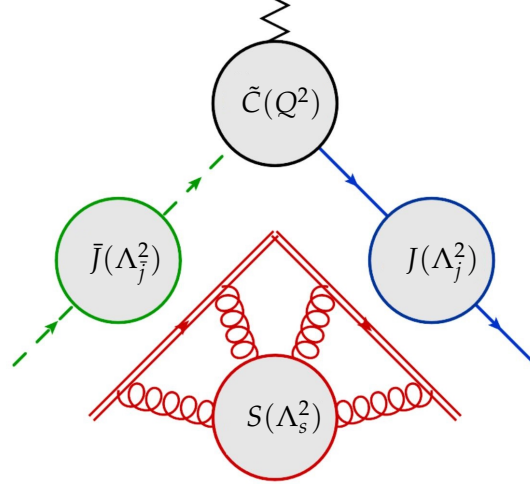


FIGURE 2.2: Schematic depiction of the Sudakov form factor, after decoupling transformations are applied. In black we see the hard part represented by the Wilson coefficient  $\tilde{C}(Q^2)$ , in green the anti-collinear quark field and in blue the collinear quark field. The red double lines represent the Wilson lines along the directions of the collinear and anti-collinear fields, sourcing the soft gluons. Adapted from [6].

where the Wilson coefficient  $\tilde{C}(Q^2, \mu)$  matches the SCET Sudakov form factor to the QCD one. It is not important to know its exact form for the discussion in this section. Note that we have the two scales  $\Lambda_j^2 \sim p_j^2$  and  $\Lambda_{\bar{j}}^2 \sim p_{\bar{j}}^2$  present in the form factor, and the scale of the soft function can be derived to be  $\Lambda_s^2 = \Lambda_j^2 \Lambda_{\bar{j}}^2 / Q^2$ .

There is another parameter appearing on the right hand side of (2.43), namely the renormalization scale  $\mu$ . It appears in the calculation of the Wilson coefficient, which a priori contains UV divergences that need to be renormalized away. After this is done, one can show that the Wilson coefficient fulfills the differential equation

$$\frac{d}{d \ln \mu} \tilde{C}(Q^2, \mu) = \left[ C_F \gamma_{\text{cusp}}(\alpha_s) \ln \frac{Q^2}{\mu^2} + \gamma_V(\alpha_s) \right] \tilde{C}(Q^2, \mu), \quad \text{with} \quad (2.44)$$

$$\gamma_{\text{cusp}}(\alpha_s) = 4 \frac{\alpha_s(\mu)}{4\pi} + \mathcal{O}(\alpha_s^2) \quad \text{and} \quad \gamma_V(\alpha_s) = -6 C_F \frac{\alpha_s(\mu)}{4\pi} + \mathcal{O}(\alpha_s^2). \quad (2.45)$$

This differential equation for the Wilson coefficient is called the *Renormalization Group (RG) equation*, and the term in the square brackets is called the *anomalous dimension*.

The above RG equation is solved by

$$\tilde{C}(Q^2, \mu) = \exp \left\{ \int_{\mu_h}^{\mu} \left[ C_F \gamma_{\text{cusp}}(\alpha_s) \ln \frac{Q^2}{\mu'^2} + \gamma_V(\alpha_s) \right] \ln \mu' \right\} \tilde{C}(Q^2, \mu_h) \equiv U(\mu_h, \mu) \tilde{C}(Q^2, \mu_h), \quad (2.46)$$

where the Wilson coefficient gets evaluated at a specific scale  $\mu_h$  and then gets evolved down to the scale  $\mu$  by the newly introduced evolution matrix  $U(\mu_h, \mu)$ . By switching the integration over the scale to the integration over the coupling coefficient  $\alpha_s$  by using

$$\frac{d\alpha_s(\mu)}{d \ln \mu} = \beta(\alpha_s(\mu)) \quad \text{and} \quad \ln \frac{\mu}{\mu_h} = \int_{\alpha_s(\mu)}^{\alpha_s(\mu_h)} \frac{d\alpha}{\beta(\alpha)}, \quad (2.47)$$

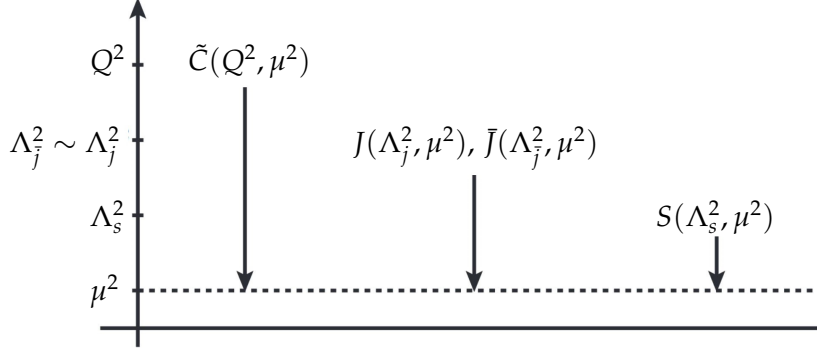


FIGURE 2.3: Schematic depiction of the resummation by RG evolution. All the factors get evaluated at their respective scales, and then run down to a common scale  $\mu$ . Adapted from [6].

the evolution factor may be written as

$$U(\mu_h, \mu) = \exp [2C_F S(\mu_h, \mu) - A_{\gamma_V}(\mu_h, \mu)] \left( \frac{Q^2}{\mu_h^2} \right)^{-C_F A_{\gamma_{\text{cusp}}}(\mu_h, \mu)}, \quad \text{with} \quad (2.48)$$

$$S(\mu_h, \mu) = - \int_{\alpha_s(\mu_h)}^{\alpha_s(\mu)} d\alpha \frac{\gamma_{\text{cusp}}(\alpha)}{\beta(\alpha)} \int_{\alpha_s(\mu_h)}^{\alpha} \frac{d\alpha'}{\beta(\alpha')}, \quad \text{and} \quad (2.49)$$

$$A_{\gamma_i}(\mu_h, \mu) = - \int_{\alpha_s(\mu_h)}^{\alpha_s(\mu)} d\alpha \frac{\gamma_i(\alpha)}{\beta(\alpha)}, \quad \text{with } i \in \{V, \text{cusp}\}. \quad (2.50)$$

As all of those quantities can be evaluated, we now have found a procedure that allows us to calculate the Wilson coefficient at a scale  $\mu_h$  and then evolve it to some arbitrary different scale  $\mu$  under the condition that  $\alpha_s(\mu)$  is reasonably small. It is of course necessary to match the Wilson coefficient to fixed-order computations evaluated at a scale  $\mu_h \sim Q$ . Note that in traditional perturbation theory, we encounter large logarithms unless  $\mu \sim Q$ . The version shown here, which traded the logarithms of the scale ratios in favor of ratios of coupling constants evaluated at the different scales, is free of large logarithms and known as *RG improved perturbation theory*. It is covered in detail in Section 1.4.3 of [6].

It is important to note that also the other functions in (2.43) fulfill their own RG equations. The ones of the collinear and the soft functions are

$$\frac{d}{d \ln \mu} J(\Lambda_j^2, \mu) = - \left[ C_F \gamma_{\text{cusp}}(\alpha_s) \ln \frac{\Lambda_j^2}{\mu^2} + \gamma_J(\alpha_s) \right] J(\Lambda_j^2, \mu), \quad (2.51)$$

$$\frac{d}{d \ln \mu} S(\Lambda_s^2, \mu) = \left[ C_F \gamma_{\text{cusp}}(\alpha_s) \ln \frac{\Lambda_s^2}{\mu^2} + \gamma_S(\alpha_s) \right] S(\Lambda_s^2, \mu), \quad (2.52)$$

and the one of the anti-collinear field is the same as the one of the collinear one (with  $\Lambda_j \rightarrow \Lambda_{\bar{j}}$  but same  $\gamma_J$ ).

As the final result of the form factor (2.43) has to be free of the renormalization scale  $\mu$ , we have

$$\begin{aligned} 0 &= \frac{d}{d \ln \mu} \left[ \tilde{C}(Q^2, \mu) J(\Lambda_j^2, \mu) \bar{J}(\Lambda_{\bar{j}}^2, \mu) S(\Lambda_s^2, \mu) \right] \\ &= C_F \gamma_{\text{cusp}} \ln \frac{Q^2}{\mu^2} + \gamma_V - C_F \gamma_{\text{cusp}} \left( \ln \frac{\Lambda_j^2}{\mu^2} + \ln \frac{\Lambda_{\bar{j}}^2}{\mu^2} \right) - 2\gamma_J + C_F \gamma_{\text{cusp}} \ln \frac{\Lambda_s^2}{\mu^2} + \gamma_S. \end{aligned} \quad (2.53)$$

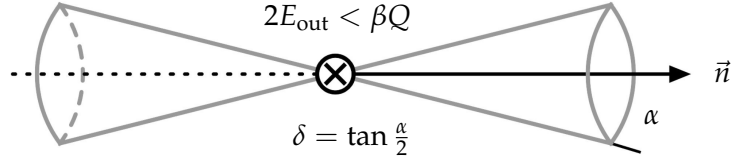


FIGURE 2.4: Di-jet production as considered in Section 2.4. The parameter  $\delta \in (0, 1)$  is related to the half-cone opening angle  $\alpha \in (0, \pi/2)$  around the jet axis  $\vec{n}$ . The parameter  $\beta \in (0, 1)$  sets the upper limit on the energy allowed outside the jet cones. From [24].

Note that it is crucial that the scale dependencies are logarithmic and come with the same coefficient  $\gamma_{\text{cusp}}$  to allow for a cancellation.

Because all functions fulfill an RG equation similar to the one we have discussed for the Wilson coefficient, we can evaluate each of them at their respective scale and then run down to a common scale  $\mu$ , where all the logarithms of  $\mu$  cancel. This is schematically pictured in Figure 2.3. The logarithms of the scales  $Q$ ,  $\Lambda_j$ ,  $\Lambda_{\bar{j}}$  and  $\Lambda_s$  are now resummed by the RG evolution.

As a last remark, the label "cusp" stems from the fact that the soft function is given by the matrix element of the two Wilson lines in two directions. They could be treated as a single Wilson line with a cusp, which is essentially what the soft gluons "see".

## 2.4 RESUMMATION OF LOGARITHMS IN WIDE-ANGLE JET CROSS SECTIONS

Let us now introduce the notation and formalism that we are going to use in the following three chapters, each of which is a copy of an article. We will look at di-jet production at an electron-positron collider, see Figure 2.4. In such processes, most of the total final state energy is shared between the particles that end up inside the two jets, while the energy homogeneously distributed outside the jets is constrained to

$$E_{\text{out}} < \frac{\beta Q}{2}. \quad (2.54)$$

We will restrain ourselves to wide-angle jets with  $\delta \sim 1$ . Note that everything in this subsection is based on the seminal paper [24], which also treats narrow-angle jets, see Figure 2.5.

The cross section of this process is a textbook example of a *non-global observable*. Such an observable is characterized by the property that radiation is only constrained in certain regions of the phase space. This definition is fulfilled in the di-jet production. We cut away part of the allowed phase space, namely by restricting the particles that are detected outside the jets to have small energies. The calculation of this non-global observable leads to *non-global logarithms*  $\ln \beta$  and  $\ln \delta$ , which can become large and one needs to resum. Because the particles of the two regions inside and outside the jets can affect each other, the resummation of these non-global logarithms becomes quite involved.

We choose light-cone coordinates  $(n \cdot p, \vec{n} \cdot p, p_{\perp})$  along the jet axis  $n^{\mu} = (1, \vec{n})$ . In these coordinates, the momenta for wide-angle jet production scale as

$$\text{hard } (h): p_h \sim (1, 1, 1)Q, \quad (2.55)$$

$$\text{soft } (s): p_s \sim (\beta, \beta, \beta)Q. \quad (2.56)$$

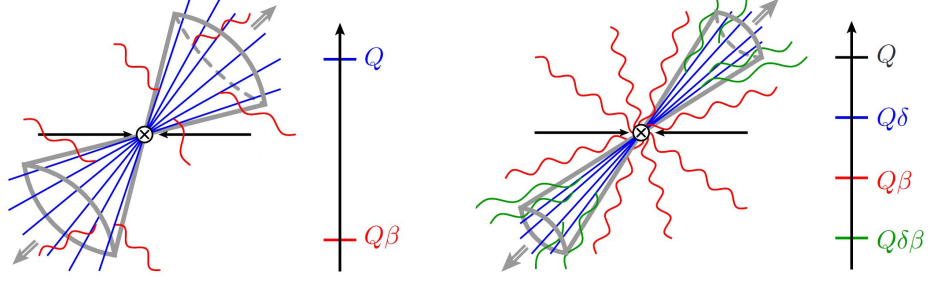


FIGURE 2.5: In the left panel, we have wide-angle jet production with the hard and soft partons in blue and red, their respective scales next to the pictorial representation. In the right panel we see the much more involved case of narrow-angle jet production, with the hard, collinear, soft and coft particles in black, blue, red and green. From [24].

The hard particles with  $p_h^2 \sim Q^2$  are forming the jets, while the soft radiation with  $p_s^2 \sim \beta^2 Q^2$  may be detected anywhere in the collider.

As a side note, if we would have jets of a narrow opening angle  $\delta \ll 1$ , we would encounter four more scales entering the game, namely

$$\text{collinear (c): } p_c \sim (\delta^2, 1, \delta)Q, \quad (2.57)$$

$$\text{anti-collinear } (\bar{c}): p_{\bar{c}} \sim (1, \delta^2, \delta)Q, \quad (2.58)$$

$$\text{coft (t): } p_t \sim (\beta\delta^2, \beta, \beta\delta)Q, \quad (2.59)$$

$$\text{anti-coft } (\bar{t}): p_{\bar{t}} \sim (\beta, \beta\delta^2, \beta\delta)Q. \quad (2.60)$$

The small-cone regions obviously reduce to the wide-cone ones if we use  $\delta \sim 1$ . The collinear particles  $p_c^2 \sim p_{\bar{c}}^2 \sim \delta^2 Q^2$  become of the same scale as the hard ones, while the coft particles  $p_t^2 \sim p_{\bar{t}}^2 \sim \beta^2 \delta^2 Q^2$  become indistinguishable from the soft ones.

Let us now return to the wide-cone jets and consider a configuration with  $m$  partons inside the two jets. We start out by mentally introducing a separate collinear field for every hard particle in the final state. Just as we have derived the Lagrangian with one collinear and one anti-collinear field in (2.34), we can write down the same SCET operators for processes with  $m$  collinear scales. This Lagrangian would then contain one copy of the ordinary QCD Lagrangian for the soft fields and  $m$  copies of the collinear part in (2.34) including the interaction term between the respective collinear fields and soft fields. Just as shown in Section 2.2.3, we can then apply a decoupling transformation in each of the  $m$  directions of the hard partons by dressing them with a Wilson line. Assuming these directions of the hard partons are given by  $n_i$  and their color representation being  $T_i$ , these Wilson lines read

$$S_i(n_i) = \mathbf{P} \exp \left( ig \int_0^\infty ds n_i \cdot A_s^a(s n_i) T_i^a \right). \quad (2.61)$$

Note that the  $S_i(n_i)$  are matrices in color space, acting on the color index of particle  $i$ , which can be either a quark or a gluon. Using these Wilson lines to redefine

$$\phi_i = S_i(n_i) \phi_i^{(0)}, \quad (2.62)$$

with  $\phi_i \in \{\xi_i, \bar{\xi}_i, A_i^\mu\}$  leaves the decoupled fields to represent the hard particles. The decoupled part of the Lagrangian takes care of the hard interaction with its matrix element  $|\mathcal{M}_m(\{p\})\rangle$  where  $\{p\}$  is the short-hand notation for the set of all hard momenta  $\{p\} =$

$\{p_1, p_2, \dots, p_m\}$ . This means that one can express a soft emission from any hard parton via the Wilson lines as an amplitude

$$\mathcal{S}_1(n_1)\mathcal{S}_2(n_2)\dots\mathcal{S}_m(n_m)\left|\mathcal{M}_m\left(\{\underline{p}\}\right)\right\rangle. \quad (2.63)$$

To calculate the amplitude for the emission of  $l$  soft partons with momenta  $k_1, k_2, \dots, k_l$ , we can compute the matrix element

$$\langle k_1, k_2, \dots, k_l | \mathcal{S}_1(n_1)\mathcal{S}_2(n_2)\dots\mathcal{S}_m(n_m) | 0 \rangle. \quad (2.64)$$

An arbitrary number of soft partons  $X_s$  therefore give rise to a contribution towards the cross section of  $m$  hard partons as

$$\begin{aligned} \mathcal{S}_m(\{\underline{n}\}, Q\beta) &= \sum_{X_s} \langle 0 | \mathcal{S}_1^\dagger(n_1)\mathcal{S}_2^\dagger(n_2)\dots\mathcal{S}_m^\dagger(n_m) | X_s \rangle \\ &\quad \times \langle X_s | \mathcal{S}_1(n_1)\mathcal{S}_2(n_2)\dots\mathcal{S}_m(n_m) | 0 \rangle \theta(Q\beta - 2E_{\text{out}}). \end{aligned} \quad (2.65)$$

The only constraint on the soft partons is that of their combined energy having an upper bound if they are outside the jets, see (2.54). This function  $\mathcal{S}_m(\{\underline{n}\}, Q\beta)$  is termed *soft function*. Of course,  $\mathcal{S}_m$  implicitly also depends on the cone angle  $\delta \sim 1$  due to its dependence on  $E_{\text{out}}$ , which is the total energy allowed *outside* the cones.

Remembering the respective master formula (1.3), the full cross section of a lepton collision having  $m$  partons inside wide-angle jets and an arbitrary number of soft gluons homogeneously distributed in the detector is given by

$$\begin{aligned} \sigma(\beta) &= \frac{1}{2Q^2} \sum_{m=2}^{\infty} \prod_{i=1}^m \int \frac{d^{d-1}p_i}{(2\pi)^{d-1}2E_i} \left\langle \mathcal{M}_m(\{\underline{p}\}) \left| \mathcal{S}_m(\{\underline{n}\}, Q\beta) \right| \mathcal{M}_m(\{\underline{p}\}) \right\rangle \\ &\quad \times (2\pi)^d \delta \left( Q - \sum_{i=1}^m E_i \right) \delta^{d-1}(\vec{p}_{\text{tot}}) \Theta_{\text{in}}(\{\underline{p}\}), \end{aligned} \quad (2.66)$$

up to power-suppressed terms of  $\mathcal{O}(\beta)$ . Note that the small soft momenta get – in proper effective-theory fashion – neglected in the  $\delta$  functions of energy-momentum conservation, the entire center-of-mass energy is used to produce the hard partons. By the  $\Theta_{\text{in}}$ -function, the hard partons are constrained to the inside of the jets.

It is our goal to provide a proper factorization between the two scales. The soft function  $\mathcal{S}_m(\{\underline{n}\}, Q\beta)$  depends on the directions of the hard partons  $\{\underline{n}\}$ , which means that we can not execute all the integrals of (2.66) before the two parts meet up. However, we can integrate over the energies of the  $m$  partons, as the soft partons have no say in which parton gets how much energy. If we extract all the possible factors from (2.66), we get the *hard function*

$$\begin{aligned} \mathcal{H}_m(\{\underline{n}\}, Q) &= \frac{1}{2Q^2} \sum_{\text{spins}} \prod_{i=1}^m \int \frac{dE_i E_i^{d-3}}{(2\pi)^{d-2}} \left| \mathcal{M}_m(\{\underline{p}\}) \right\rangle \left\langle \mathcal{M}_m(\{\underline{p}\}) \right| \\ &\quad \times (2\pi)^d \delta \left( Q - \sum_{i=1}^m E_i \right) \delta^{d-1}(\vec{p}_{\text{tot}}) \Theta_{\text{in}}(\{\underline{p}\}). \end{aligned} \quad (2.67)$$

Note that the hard functions are distributions in the solid angles of the hard partons. These distributions do in fact contain divergences, for example when two hard particles get

collinear to each other. These real-emission divergences cancel against divergences in virtual corrections to hard functions of fewer legs. It should also be stated that the hard functions depend on the cone angles via the constraint  $\Theta_{\text{in}}$  in a rather explicit fashion.

Together, the hard and soft functions allow us to write the cross section (2.66) as

$$\sigma(\beta) = \sum_{m=2}^{\infty} \langle \mathcal{H}_m(\{\underline{n}\}, Q) \otimes \mathcal{S}_m(\{\underline{n}\}, Q\beta) \rangle, \quad (2.68)$$

where the symbol  $\otimes$  takes care of the left-over integrations over the directions of the hard partons

$$\mathcal{H}_m(\{\underline{n}\}, Q) \otimes \mathcal{S}_m(\{\underline{n}\}, Q\beta) = \prod_{i=1}^m \int \frac{d\Omega(n_i)}{4\pi} \mathcal{H}_m(\{\underline{n}\}, Q) \mathcal{S}_m(\{\underline{n}\}, Q\beta), \quad (2.69)$$

and the angle brackets stand for the color trace

$$\langle A \rangle = \frac{1}{\text{tr}(\mathbf{1})} \text{tr}(A). \quad (2.70)$$

To resum the non-global logarithms of  $\ln \beta$ , one can make use of the Renormalization Group evolution of the hard function, as discussed in Section 2.3 for a simpler example. We will do this in a rather detailed fashion in Section 3.2, where we pick up the thread at the factorization theorem (2.68).





## NON-GLOBAL LOGARITHMS IN JET AND ISOLATION CROSS SECTIONS

---

*In two or three weeks we should have the article on the arXiv.*

— Ding Yu Shao, five months before the article was submitted to the arXiv

This chapter is a copy of [18], published in the Journal of High-Energy Physics (JHEP) on August 17, 2018.

### ABSTRACT

Starting from a factorization theorem in effective field theory, we derive a parton-shower equation for the resummation of non-global logarithms. We have implemented this shower and interfaced it with a tree-level event generator to obtain an automated framework to resum the leading logarithm of non-global observables in the large- $N_c$  limit. Using this setup, we compute gap fractions for dijet processes and isolation cone cross sections relevant for photon production. We compare our results with fixed-order computations and LHC measurements. We find that naive exponentiation is often not adequate, especially when the vetoed region is small, since non-global contributions are enhanced due to their dependence on the veto-region size. Since our parton shower is derived from first principles and based on renormalization-group evolution, it is clear what ingredients will have to be included to perform resummations at subleading logarithmic accuracy in the future.

### 3.1 INTRODUCTION

In the papers [24, 25] we have derived a factorization formula for exclusive jet cross sections which allows one to resum the logarithms arising in the limit where the energy  $Q_0$  outside the jets is much smaller than the energy  $Q$  inside. In these papers, we have computed different ingredients of the factorization theorem and verified that the logarithmic structure is fully reproduced at Next-to-Next-to-Leading Order (NNLO), but no resummation was performed. Also, for simplicity, we focussed on the Serman-Weinberg jet cross section, which is defined for  $e^+e^-$  colliders. In the present paper we follow up on the work [24, 25] and discuss the resummation of the leading non-global logarithms (NGLs) in detail. We show that the renormalization group (RG) equation which drives it translates into a parton-shower equation. Implementing this shower then allows us to resum a variety of non-global observables.

That the complicated pattern of logarithms for non-global observables can be obtained from an angular dipole shower was shown already in the original paper by Dasgupta and Salam who discovered them [26]. Their analysis was based on the properties of strongly-ordered QCD amplitudes. The connection to parton showers is less immediate in our treatment which is based on RG evolution in Soft-Collinear Effective Theory (SCET) [23, 27, 28] (see [7, 29] for a review). Our starting point is a factorization theorem which separates the hard radiation inside the jets (or outside the isolation cone) from the soft radiation.

The soft radiation is driven by Wilson lines along the directions of the hard partons in the process. Since there are contributions involving any number of hard partons, we end up with operators with an arbitrary number of Wilson lines and these operators mix under renormalization. The corresponding RG equation is complicated, but we will show that it takes the form of a recursive equation that can be solved using a parton-shower Monte Carlo (MC) program, which at leading-log accuracy in the large- $N_c$  limit is equivalent to the one used by Dasgupta and Salam. An advantage of our treatment is that the RG equation is not limited to leading logarithmic accuracy and we briefly discuss which ingredients and modifications will be necessary to reach higher precision. There has been a lot of recent work [30–33] on the general structure of parton showers and how to increase their accuracy. The problem at hand provides an explicit example of a shower equation derived from first principles for which it is clear what ingredients are needed to resum sub-leading logarithms.

The leading logarithms can be obtained by starting from the tree-level amplitudes and running the parton shower to generate the logarithmically enhanced terms. We have written a dedicated parton-shower code to perform the resummation and use the MADGRAPH5\_AMC@NLO framework [34] to generate the necessary tree-level amplitudes. This provides an automated framework to perform the resummation, which we use to study exclusive jet and isolation cone cross sections, both at lepton and hadron colliders. In particular, we give numerical results for dijet production with a gap between jets and compare to ATLAS measurements [35, 36] and theoretical predictions [37] based on the BMS equation [38]. We also study isolated photon production and compute the logarithms of  $\epsilon_\gamma$ , the energy fraction inside the isolation cone.

The remainder of this paper is organized as follows. In Section 3.2 we review the factorization theorem for jet cross sections with gaps or isolation cones. In Section 3.3 we will show that RG evolution of the associated Wilson coefficients is equivalent to a parton shower, and we give the necessary ingredients for LL resummation. In Section 3.4 we will apply the shower code to obtain some phenomenological predictions, namely gap fraction of dijet production and isolation cone cross section. We summarize our results and provide some further discussion in Section 3.5.

### 3.2 FACTORIZATION FOR JET CROSS SECTIONS

Consider an exclusive  $k$ -jet cross section at a lepton collider with center-of-mass energy  $Q$  in which radiation is vetoed in an angular region  $\Omega_{\text{out}}$  outside the jets. If the veto has an associated energy scale  $Q_0$ , this process fulfils a factorization formula of the form [24, 25]

$$d\sigma(Q, Q_0) = \sum_{m=k}^{\infty} \langle \mathcal{H}_m(\{\underline{n}\}, Q, \mu) \otimes \mathcal{S}_m(\{\underline{n}\}, Q_0, \mu) \rangle. \quad (3.1)$$

The factorization theorem is the leading term in an expansion of the cross section in  $\beta = Q_0/Q$ . Since the soft radiation is sensitive to the directions  $\{\underline{n}\} = \{n_1, \dots, n_m\}$  and the color charges of the hard partons, both the soft and hard functions depend on these quantities. The symbol  $\otimes$  indicates an integral over these directions and  $\langle \dots \rangle$  denotes the color trace, which is taken after combining the two functions. In (3.1) we indicate the dependence of the cross section on  $Q$  and  $Q_0$  explicitly, but it depends on the momenta of the individual jets. The cross section thus involves several individual hard energy scales, but we assume that all of them are of order  $Q$  and do not indicate them explicitly. Below,

we will compute cross sections as a function of the rapidities and the average transverse momentum of the jets.

The formula (3.1) covers a variety of situations. The most common is exclusive jet cross sections, with a veto on additional radiation outside the jets. For low values of the veto scale  $Q_0$ , the outside region is also called the “gap” between the jets. The name “gap” refers to studies of forward dijet processes without any hadrons outside the jets [39–41], which is of course problematic in a perturbative context [42]. For our work, we are interested in values of  $Q_0$  in the perturbative domain. Note that the radiation inside the gap is outside the jets; however, throughout our paper “inside” will always refer to the region of large energy. A second set of observables obeying (3.1) are isolation cone cross sections for small values of the energy inside the cone, which are relevant e.g. for photon production. In the above notation  $\Omega_{\text{out}}$  then refers to the angular region of the isolation cone and  $Q_0$  to the hadronic energy inside it.

The ingredients of the formula (3.1) develop large collinear logarithms as the jets become narrow. We have analyzed this situation in [24, 25] and have shown that the hard and soft functions factorize further in this limit. This additional factorization allows for the resummation of the associated logarithms using RG evolution. Concerning the non-global structure this is a purely technical complication, and for simplicity’s sake, we will not resum logarithms of the jet radius in the present paper. Such logarithms are of course of interest and were studied in a number of recent papers, both for exclusive and inclusive cross sections, see [43–49].

The second, more important limitation of the formula (3.1) is that it was derived for  $e^+e^-$  collisions. Naively, one would guess that one simply will need to include a convolution with parton distribution functions (PDFs) to account for incoming partons and generalize (3.1) to hadron colliders. However, the work of [50, 51] has shown that beyond the large- $N_c$  limit, the factorization properties become more complicated. The anomalous dimension which governs the hard function evolution involves Glauber (or Coulomb) phases which no longer cancel in the hadron collider case. This leads to double logarithms at higher orders which cannot be absorbed into PDFs. It will be interesting to analyze the low-energy theory in the presence of these “super-leading” logarithms. In the present work we will remain in the large- $N_c$  limit where these complications are absent.

The factorization theorem (3.1) is based on the factorization of soft radiation from a hard amplitude with  $m$  partons, which takes the form

$$S_1(n_1) S_2(n_2) \dots S_m(n_m) |\mathcal{M}_m(\{\underline{p}\})\rangle, \quad (3.2)$$

where  $S_i(n_i)$  is a Wilson line along the direction of particle  $i$  in the appropriate color representation. The soft functions are given by the matrix element squared of emissions from these Wilson lines

$$\mathcal{S}_m(\{\underline{n}\}, Q_0, \mu) = \sum_{X_s} \langle 0 | S_1^\dagger(n_1) \dots S_m^\dagger(n_m) | X_s \rangle \langle X_s | S_1(n_1) \dots S_m(n_m) | 0 \rangle \theta(Q_0 - E_{\text{out}}), \quad (3.3)$$

where the states  $X_s$  contain an arbitrary number of soft partons. The soft functions depend on the energy  $Q_0$  of the radiation and implicitly also on the shape of the region  $\Omega_{\text{out}}$  in which the energy is measured. The Wilson-line matrix elements have ultraviolet divergences which can be renormalized away and this induces a dependence on the renormalization scale  $\mu$ .

The hard functions are given by the square of the hard-scattering amplitudes, together with the phase-space constraints  $\Theta_{\text{in}}(\{\underline{p}\})$  which restrict the  $m$  hard partons to the inside of the jets,

$$\mathcal{H}_m(\{\underline{n}\}, Q, \mu) = \frac{1}{2Q^2} \sum_{\text{spins}} \prod_{i=1}^m \int \frac{dE_i E_i^{d-3}}{(2\pi)^{d-2}} |\mathcal{M}_m(\{\underline{p}\})\rangle \langle \mathcal{M}_m(\{\underline{p}\})| \\ \times (2\pi)^d \delta\left(Q - \sum_{i=1}^m E_i\right) \delta^{(d-1)}(\vec{p}_{\text{tot}}) \Theta_{\text{in}}(\{\underline{p}\}) . \quad (3.4)$$

For cone jets the phase-space constraint  $\Theta_{\text{in}}(\{\underline{p}\})$  is defined by cones around the hard partons. For recombination algorithms, on the other hand, the jet clustering constraints can be quite complicated in general and can spoil factorization. However, they simplify in our setup which considers the limit of hard partons together with (infinitely) soft radiation. This situation was considered in [52] where it was shown that for anti- $k_T$  jets, the jet boundary becomes cone-like so that the theorem (3.1) also applies to this case.

Since the cross section must be independent of the scale  $\mu$ , the scale dependence among the hard and soft functions must cancel. The one for the hard function is driven by the RG equation

$$\frac{d}{d \ln \mu} \mathcal{H}_m(\{\underline{n}\}, Q, \mu) = - \sum_{l=k}^m \mathcal{H}_l(\{\underline{n}\}, Q, \mu) \mathbf{\Gamma}_{lm}^H(\{\underline{n}\}, Q, \mu) . \quad (3.5)$$

This evolution equation is formally solved by the path ordered exponential

$$U(\{\underline{n}\}, \mu_s, \mu_h) = \mathbf{P} \exp \left[ \int_{\mu_s}^{\mu_h} \frac{d\mu}{\mu} \mathbf{\Gamma}^H(\{\underline{n}\}, \mu) \right] , \quad (3.6)$$

and the resummed cross section is then

$$d\sigma(Q, Q_0) = \sum_{l=k, m \geq l}^{\infty} \langle \mathcal{H}_l(\{\underline{n}\}, Q, \mu_h) \otimes U_{lm}(\{\underline{n}\}, \mu_s, \mu_h) \hat{\otimes} \mathcal{S}_m(\{\underline{n}\}, Q_0, \mu_s) \rangle . \quad (3.7)$$

The condition  $m \geq l$  arises because the anomalous dimension matrix is zero below the diagonal, see below. The hat in  $\hat{\otimes}$  indicates that one has to integrate over the angles of the  $(m-l)$  additional unresolved emissions. For the choice  $\mu_h \sim Q$  and  $\mu_s \sim Q_0$ , the hard and soft functions are free of large logarithms and can be expanded in the respective coupling constants  $\alpha_s(\mu_h)$  and  $\alpha_s(\mu_s)$ . At leading logarithmic accuracy, we only need these functions at leading power in  $\alpha_s$ . The soft functions then become trivial  $\mathcal{S}_m = 1$  and all higher-multiplicity hard functions are suppressed,  $\mathcal{H}_m \sim \alpha_s^{m-k} \mathcal{H}_k$ . The cross section thus simplifies to

$$d\sigma^{\text{LL}}(Q, Q_0) = \sum_{m=k}^{\infty} \langle \mathcal{H}_k(\{\underline{n}\}, Q, \mu_h) \otimes U_{km}(\{\underline{n}\}, \mu_s, \mu_h) \hat{\otimes} \mathbf{1} \rangle , \quad (3.8)$$

where the evolution factor can be evaluated with the leading-order expression for the anomalous dimension  $\mathbf{\Gamma}^H$ . We note that the Born-level cross section is given by

$$d\sigma_0(Q, Q_0) = \langle \mathcal{H}_k(\{\underline{n}\}, Q, \mu_h) \rangle . \quad (3.9)$$

This demonstrates that the starting point of the evolution is the tree-level cross section, as we have indicated earlier. The additional piece of information needed is the color structure

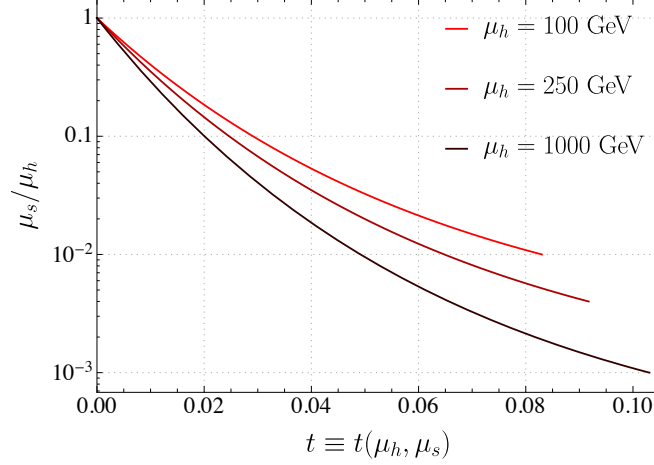


FIGURE 3.1: The relation between shower time  $t$ , hard scale  $\mu_h$  and soft scale  $\mu_s$ . We stop the lines in the plot when  $\mu_s$  reaches 1 GeV.

since the evolution changes the colors. The paper [53] has modified the MADGRAPH code in such a way that it provides the full color information. We will focus on the large- $N_c$  limit below and use the color information which MADGRAPH provides for showering its tree-level events. We will come back to this point later.

It is convenient to rewrite the exponent of the evolution matrix (3.6) at leading order in RG-improved perturbation theory in the form

$$\int_{\mu_s}^{\mu_h} \frac{d\mu}{\mu} \mathbf{\Gamma}_{nm}^H = \int_{\alpha(\mu_s)}^{\alpha(\mu_h)} \frac{d\alpha}{\beta(\alpha)} \frac{\alpha}{4\pi} \mathbf{\Gamma}_{nm}^{(1)} = \frac{1}{2\beta_0} \ln \frac{\alpha(\mu_s)}{\alpha(\mu_h)} \mathbf{\Gamma}_{nm}^{(1)}. \quad (3.10)$$

Using the one-loop anomalous-dimension matrix  $\mathbf{\Gamma}_{nm}^{(1)}$  yields leading logarithmic accuracy in the evolution. The prefactor

$$t = \frac{1}{2\beta_0} \ln \frac{\alpha(\mu_s)}{\alpha(\mu_h)} = \frac{\alpha_s}{4\pi} \ln \frac{\mu_h}{\mu_s} + \mathcal{O}(\alpha_s^2) \quad (3.11)$$

is the “evolution time”, which we will call shower time in the context of the parton shower. We start the evolution at  $t = 0$  and then evolve to larger times, which correspond to lower scales. Since we will sometimes plot quantities as a function of the shower time  $t$ , we show the relation between  $t$  and the ratio of the low scale  $\mu_s$  to the high scale  $\mu_h$  for different hard-scattering scales  $\mu_h$  in Figure 3.1. The plot makes it clear that the relevant region for perturbative calculations is  $t \lesssim 0.1$ , even after resummation.

### 3.3 RG EVOLUTION AS A PARTON SHOWER

To obtain a MC implementation of the leading-logarithmic evolution we make use of the explicit form of the one-loop anomalous dimension [24], which for  $k$ -jet production has the form

$$\mathbf{\Gamma}^{(1)} = \begin{pmatrix} \mathbf{V}_k & \mathbf{R}_k & 0 & 0 & \dots \\ 0 & \mathbf{V}_{k+1} & \mathbf{R}_{k+1} & 0 & \dots \\ 0 & 0 & \mathbf{V}_{k+2} & \mathbf{R}_{k+2} & \dots \\ 0 & 0 & 0 & \mathbf{V}_{k+3} & \dots \\ \vdots & \vdots & \vdots & \vdots & \ddots \end{pmatrix}. \quad (3.12)$$

The one-loop anomalous dimensions are given by

$$\begin{aligned}
V_m &= 2 \sum_{(ij)} (\mathbf{T}_{i,L} \cdot \mathbf{T}_{j,L} + \mathbf{T}_{i,R} \cdot \mathbf{T}_{j,R}) \int \frac{d\Omega(n_l)}{4\pi} W_{ij}^l \\
&\quad - 2i\pi \sum_{(ij)} (\mathbf{T}_{i,L} \cdot \mathbf{T}_{j,L} - \mathbf{T}_{i,R} \cdot \mathbf{T}_{j,R}) \Pi_{ij}, \\
\mathbf{R}_m &= -4 \sum_{(ij)} \mathbf{T}_{i,L} \cdot \mathbf{T}_{j,R} W_{ij}^{m+1} \Theta_{\text{in}}(n_{m+1}).
\end{aligned} \tag{3.13}$$

In [24], they were derived by considering soft limits of the amplitudes. The relevant product of soft currents leads to a dipole structure for the angular dependence given by the factor

$$W_{ij}^l = \frac{n_i \cdot n_j}{n_i \cdot n_l \, n_j \cdot n_l}. \tag{3.14}$$

Before discussing the evolution, let us explain how the anomalous dimension acts on the functions  $\mathcal{H}_m$  defined in (3.4). These functions contain both amplitudes  $|\mathcal{M}_m(\{p\})\rangle$  and their conjugate. The color matrices  $\mathbf{T}_{i,L}$  acts on the  $i$ -th parton in the amplitude while  $\mathbf{T}_{j,R}$  multiplies the conjugate, for example

$$(\mathbf{T}_{1,L} \cdot \mathbf{T}_{2,L} + \mathbf{T}_{3,R} \cdot \mathbf{T}_{4,R}) \mathcal{H}_m = \mathbf{T}_1 \cdot \mathbf{T}_2 \mathcal{H}_m + \mathcal{H}_m \mathbf{T}_3 \cdot \mathbf{T}_4. \tag{3.15}$$

and  $\mathbf{T}_{i,L} \cdot \mathbf{T}_{j,L} = \sum_a \mathbf{T}_{i,L}^a \cdot \mathbf{T}_{j,L}^a$ . This is the usual color-space notation [54, 55]. While we do not indicate this notationally, the color matrices in the real-emission operator  $\mathbf{R}_m$  are different. They take an amplitude with  $m$  partons and associated color indices and map it into an amplitude with  $m+1$  partons. Explicitly, we have

$$\mathbf{T}_{i,L} \cdot \mathbf{T}_{j,R} \mathcal{H}_m = \mathbf{T}_i^a \mathcal{H}_m \mathbf{T}_j^a. \tag{3.16}$$

and the index  $a$  is the color of the emitted gluon. Note that there is no sum over the color  $a$ . The color sum will only be taken at the end after multiplying with the soft function. We nevertheless use the scalar product notation  $\mathbf{T}_{i,L} \cdot \mathbf{T}_{j,R}$  since it allows us to suppress the color indices, which is one of the advantages of the color-space formalism. However, when applying the real emission operator  $\mathbf{R}_m$  one needs to keep in mind that one changes into new color space and that subsequent applications of color matrices can act on the new color index.

We have explicitly indicated the imaginary part of the virtual diagrams in the anomalous dimension (3.13). The corresponding Glauber phase arises from cutting the two lines between which the virtual gluon is exchanged and arises when  $i$  and  $j$  are both incoming or outgoing, and the factor  $\Pi_{ij}$  is defined to be 1 in this case and 0 otherwise. For  $e^+e^-$  collisions, this part immediately vanishes due to color conservation  $\sum_i \mathbf{T}_i = 0$  but it is present in hadronic collisions and induces the super-leading logarithms discovered in [50, 51].

Let us now discuss the solution of the RG at leading logarithmic accuracy. Using the simple structure of the anomalous dimension matrix (3.12) and changing variables from  $\mu$  to  $t$ , the RG equation (3.5) reads

$$\frac{d}{dt} \mathcal{H}_m(t) = \mathcal{H}_m(t) V_m + \mathcal{H}_{m-1}(t) \mathbf{R}_{m-1}, \tag{3.17}$$

where we have suppressed the dependence on the other variables. The solution of the homogenous part of the equation is simply an exponential and we can thus rewrite (3.17) as

$$\mathcal{H}_m(t) = \mathcal{H}_m(t_0) e^{(t-t_0)V_m} + \int_{t_0}^t dt' \mathcal{H}_{m-1}(t') \mathbf{R}_{m-1} e^{(t-t')V_m}. \tag{3.18}$$

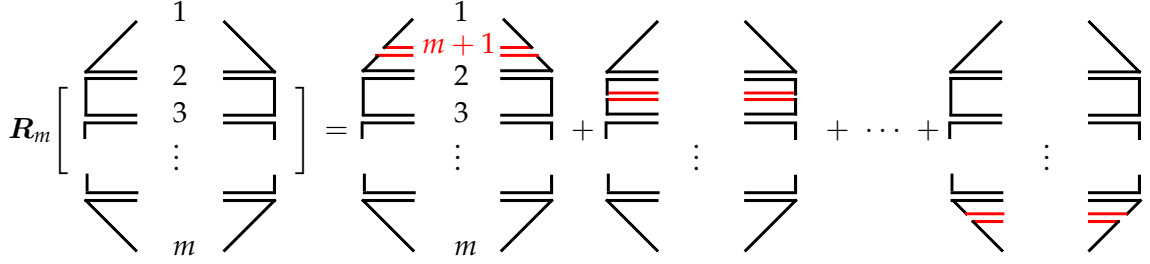


FIGURE 3.2: The action of the operator  $\mathbf{R}_m$  on an amplitude with  $m$  legs in the large- $N_c$  limit. The double and single lines represent gluons and quarks, respectively.

This is the form in which parton-shower equations are usually presented: we evolve from  $t_0$  to time  $t$  either without an emission (the first part), or by adding an additional emission to a lower-leg amplitude. In this context  $e^{(t-t')V_m}$  is usually called the Sudakov factor, but since our problem is single logarithmic, this nomenclature does not quite fit. To map to expression (3.8), we note that

$$\mathcal{H}_m(t) \equiv \mathcal{H}_k(\{\underline{n}\}, Q, \mu_h) U_{km}(\{\underline{n}\}, \mu_s, \mu_h), \quad (3.19)$$

and that the initial condition is  $\mathcal{H}_m(0) = 0$  for all  $m > k$ . To solve the equation for a process with  $k$  jets, one starts with  $m = k$  and then uses (3.18) iteratively to generate all higher functions

$$\begin{aligned} \mathcal{H}_k(t) &= \mathcal{H}_k(0) e^{tV_k}, \\ \mathcal{H}_{k+1}(t) &= \int_0^t dt' \mathcal{H}_k(t') \mathbf{R}_k e^{(t-t')V_{k+1}}, \\ \mathcal{H}_{k+2}(t) &= \int_0^t dt' \mathcal{H}_{k+1}(t') \mathbf{R}_{k+1} e^{(t-t')V_{k+2}}, \\ \mathcal{H}_{k+3}(t) &= \dots \end{aligned} \quad (3.20)$$

To get the resummed result, one evolves to the appropriate value of  $t$ , which is set by the scales  $\mu_h$  and  $\mu_s$  in (3.11). The leading-logarithmic cross section is obtained from the sum

$$\begin{aligned} d\sigma_{\text{LL}}(Q, Q_0) &= \sum_{m=k}^{\infty} \langle \mathcal{H}_m(t) \hat{\otimes} \mathbf{1} \rangle \\ &= \langle \mathcal{H}_k(t) + \int \frac{d\Omega_1}{4\pi} \mathcal{H}_{k+1}(t) + \int \frac{d\Omega_1}{4\pi} \int \frac{d\Omega_2}{4\pi} \mathcal{H}_{k+2}(t) + \dots \rangle, \end{aligned} \quad (3.21)$$

where we have explicitly written out the angular integrations over the additional emissions generated by the shower.

To perform the integrations over the intermediate times and the angles of the emissions, one has to resort to MC methods. Implementing the above equations is difficult because the hard functions and anomalous dimension are matrices in the color space of the involved partons and the dimension of this space rapidly grows for higher particle multiplicities. For this reason a full implementation of color into a parton shower has so far not been achieved, but there are methods to systematically expand around the large- $N_c$  limit [56–58]. Here, we will work in the strict large- $N_c$  limit and use the trace basis for the color structure, so that emissions only arise between neighbouring legs

$$\mathbf{T}_i \cdot \mathbf{T}_j \rightarrow -\frac{N_c}{2} \delta_{i,j\pm 1} \mathbf{1}, \quad (3.22)$$



and each loop or real emission simply leads to an additional factor of  $N_c$ . We have discussed this point in detail in [24] and reproduce an illustration from this paper in Figure 3.2 which shows how the real-emission operator  $\mathbf{R}_m$  acts on an amplitude with  $m$  legs. The amplitude at large  $N_c$  can be viewed as a set of color dipoles and the real emission operator adds a new leg, splitting an existing dipole into two new ones. Similarly, the virtual correction operator (3.13) reduces to a sum of integrals for each dipole involving neighbouring legs

$$\mathbf{V}_m = -4N_c \mathbf{1} \sum_i \int \frac{d\Omega(n_l)}{4\pi} W_{i,i+1}^l \quad (3.23)$$

in the large- $N_c$  limit. The treatment of color is of course completely standard and exactly what is implemented in all existing parton-shower programs. In our practical implementation, we work with Les Houches Event Files (LHEF) [59] obtained by computing the tree-level amplitudes with MADGRAPH5\_AMC@NLO. The event files provide the directions of the hard partons in  $\mathcal{H}_k(t)$  as well as their color connections. We can thus read out all the necessary information to start the shower and to generate  $\mathcal{H}_m(t)$  for  $m > k$ .

Individually both  $\mathbf{R}_m$  and  $\mathbf{V}_m$  suffer from collinear divergences. These cancel in physical observables, but need to be regularized in our shower since we want to exponentiate the virtual corrections, see (3.18). A simple way to achieve this is to regularize the dipole as

$$W_{ij}^l \rightarrow W_{ij}^l \theta(n_l \cdot n_i - \lambda^2) \theta(n_l \cdot n_j - \lambda^2) \quad (3.24)$$

in both  $\mathbf{R}_m$  and  $\mathbf{V}_m$ . The virtual integral (3.23) with this regulator is analyzed in detail in Appendix 3.A. To efficiently generate the real emissions, it is advantageous to use the rapidity  $\hat{y}$  and the azimuthal angle  $\hat{\phi}$  in the center-of-mass frame of the dipole as integration variables, the details can again be found in the Appendix 3.A. Another way of regularizing the integrals is to impose a cut on the rapidity  $\hat{y}$ , as was done by [26]. In Appendix 3.B, we give a detailed description of the MC algorithm and compare the different cutoffs.

### 3.4 PHENOMENOLOGY OF NON-GLOBAL OBSERVABLES

In this section we use our simulation code for phenomenological studies and analyze the numerical impact of the resummation for gaps between jets and isolation cone cross sections for photon production. We will also explain why NGLs for jet-veto cross sections are negligible for the cut parameters used at the LHC.

#### 3.4.1 Qualitative discussion

Before we perform detailed studies, it is useful to start with a qualitative discussion of the size and form of the leading NGLs. For concreteness, let us consider a dijet cross section in  $e^+e^-$  with a gap of size  $\Delta y$  between the jets, in which radiation above an energy  $Q_0$  is vetoed. This interjet energy flow is the poster child of a non-global observable and was studied for example in [24, 60, 61].

If the soft radiation would arise entirely from the two Wilson lines associated with the original partons, the leading logarithms would exponentiate as

$$\frac{\sigma_{\text{GL}}^{\text{LL}}}{\sigma_0} = \exp(-8 C_F t \Delta y), \quad (3.25)$$



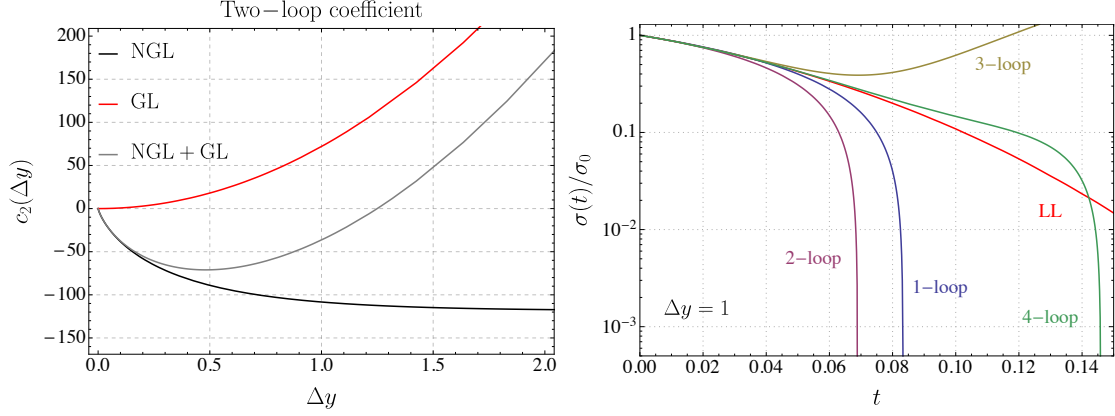


FIGURE 3.3: Left: Two-loop global and non-global coefficients as a function of the gap size  $\Delta y$ . Right: Comparison of the LL resummation and fixed-order results up to four loops, for  $\Delta y = 1$ .

where the variable  $t = \frac{\alpha_s}{4\pi} \ln \frac{Q}{Q_0}$  up to running coupling effects, see (3.11). For dijet production, these logarithms arise from  $\mathcal{S}_2$  and are called *global* to distinguish them from the complicated pattern from the operators with more Wilson lines. One observes that for these global contributions, each large logarithm is multiplied by the size of the gap  $\Delta y$ , which is of course expected since one has to recover the inclusive cross section as the gap size becomes zero. In the opposite limit, the prefactor  $\Delta y \rightarrow \infty$  corresponds to the collinear logarithm which multiplies the soft logarithm present in  $t$ . The quantity shown in (3.25), the ratio of the cross section with a rapidity gap to the inclusive cross section, is called the gap fraction and corresponds to the fraction of events with radiation in the gap below the veto-scale  $Q_0$ .

The leading NGLs to the same observable arise at two-loops and are given by [24, 61]

$$\frac{\sigma_{\text{NGL}}^{\text{LL}}}{\sigma_0} = 4 C_F C_A \left[ -\frac{2\pi^2}{3} + 4 \text{Li}_2 \left( e^{-2\Delta y} \right) \right] t^2. \quad (3.26)$$

This contribution arises from a hard gluon emission inside one of the jets, which in turn emits a soft gluon into the gap between the jets. It is encoded in the term  $\mathcal{H}_3 \otimes \mathcal{S}_3$  in the factorization formula (3.1).

In Figure 3.3, we numerically compare the two-loop global and non-global coefficients as a function of the gap size  $\Delta y$ , working in the large- $N_c$  limit. When the veto area is small, the gap fraction is dominated by the non-global part, but with increasing veto area the global logarithms become more and more important. Since the two contributions have opposite sign, cancellations between global and non-global contributions can occur at intermediate values of the gap size. To understand this behavior better, it is instructive to expand (3.26) in the small  $\Delta y$  region

$$\frac{\sigma_{\text{NGL}}^{\text{LL}}}{\sigma_0} = 4 C_F C_A \left[ 8 \Delta y (\ln(2\Delta y) - 1) - 4 \Delta y^2 + \dots \right] t^2. \quad (3.27)$$

The expansion (3.27) shows that the two-loop non-global logarithmic term is only suppressed by a single power of  $\Delta y$ , while the global piece involves two powers. The reason for this scaling is that in the non-global piece only one gluon is in the gap of size  $\Delta y$ , while in the global piece both gluons are. One further observes that in the large- $N_c$  limit the  $\Delta y^2$  part of the non-global piece precisely cancels the global piece. Phenomenologically, the limit of a

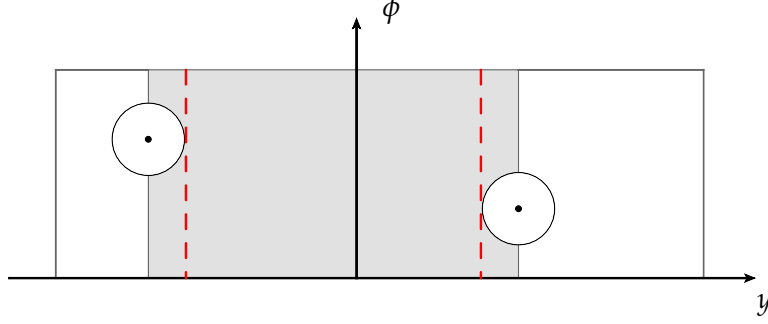


FIGURE 3.4: Definition of the gap region for a dijet system in the rapidity and azimuthal plane, as used by ATLAS [35]. If a jet with transverse momentum larger than  $Q_0$  is radiated into the gray region, the event is vetoed. The two dashed red lines indicate the boundary of the approximated veto region used in [37].

small gap is for example relevant for isolation cone cross sections, where the veto typically is only applied in a small angular region. Below, we will see an explicit example where the higher-order global and non-global effects cancel for a photon isolation cross section.

Interestingly, the leading term in (3.27) involves a logarithm of  $\Delta y$ . This contribution corresponds to a collinear enhancement which arises when both the gluon in the gap and the one outside are close to the boundary. These types of collinear logarithms were studied in the recent paper [62] which presented a version of the BMS equation which allows for their all-order resummation. It would be interesting to analyze this in our effective field theory framework. The corresponding effective theory would involve boundary modes to describe the emissions near the gap boundary. The problem is however challenging because the gap fraction is suppressed by a power of  $\Delta y$  in the limit  $\Delta y \rightarrow 0$ .

### 3.4.2 Gaps between jets

We now perform the resummation for the gap fraction at the LHC, as measured by the ATLAS experiment [35, 36]. The gap fraction is defined as the fraction of dijet events that do not have an additional jet with transverse momentum greater than a given veto scale  $Q_0$  in the rapidity interval bounded by the dijet system, and we will study it as a function of  $\bar{p}_T$ , the average transverse momentum of the two leading jets. More explicitly, the gap fraction is defined as the ratio of the cross sections with and without veto,

$$R(\bar{p}_T, Q_0) = \frac{\sigma_{2\text{-jet}}(\bar{p}_T, Q_0)}{\sigma_{2\text{-jet}}(\bar{p}_T, Q_0 = \bar{p}_T)}. \quad (3.28)$$

Since  $\bar{p}_T$  is computed using the two leading jets, the transverse momentum of the jet inside the gap is by definition smaller than  $\bar{p}_T$  so that the denominator in the formula is simply the inclusive two jet cross section. Below, we will compute  $R(\bar{p}_T, Q_0)$  for different gap sizes defined by the rapidity difference  $\Delta y$  between the two leading jets. The precise geometry of the gap is shown in Figure 3.4. The jets are reconstructed with the anti- $k_T$  jet algorithm with  $R = 0.6$  and are required to have rapidity  $|y| < 4.4$ .

The ATLAS paper [35] observed that MC predictions are not always consistent with ATLAS data. For example the NLO predictions matched to PYTHIA [63] and HERWIG [64] using POWHEG [65] are lower than the experimental data, especially in the region of large  $\bar{p}_T$  and rapidity difference  $\Delta y$  between the jets. Specifically, for  $210 \text{ GeV} < \bar{p}_T < 240 \text{ GeV}$  and  $4 < \Delta y < 5$ , POWHEG+HERWIG underestimates the data by about 40%, and POWHEG+PYTHIA by about 20%.

For small values of  $Q_0$ , the gap fraction  $R(\bar{p}_T, Q_0)$  involves large logarithms of the form  $\alpha_s^n \ln^m \bar{p}_T / Q_0$ . It is interesting to perform systematic soft gluon resummations to try to understand the difference between theoretical prediction and experimental data. The resummation of the leading logarithms has been studied in the papers [37, 66, 67]. In [66, 67] the authors resummed all global logarithms with full colour information and the non-global effects were included by reweighting with a  $K$  factor. The most detailed theoretical study so far was [37], which resummed all large logarithms at LL in the large- $N_c$  limit by solving the BMS equation and also compared directly to the experimental measurement. One limitation of this work is that the veto region was approximated by a rectangle in the rapidity and azimuthal angle plane, see Figure 3.4. This made it possible to obtain all NGLs by boosting the same solution of the BMS equation. In our computation we will take into account the exact veto region used by ATLAS. Rather than relying on the BMS equation, we will use our parton shower to resum the large logarithms.

Formula (3.1) was derived for leptonic collisions. The factorization formula for dijet production at hadron colliders also includes PDFs  $f_a(x, \mu)$  and has the form

$$\begin{aligned} \frac{d\sigma(Q_0)}{d\Delta y d\bar{p}_T} &= \sum_{a,b=q,\bar{q},g} \int dx_1 dx_2 f_a(x_1, \mu) f_b(x_2, \mu) \\ &\times \sum_{m=2}^{\infty} \langle \mathcal{H}_m^{ab}(\{\underline{n}\}, \hat{s}, \bar{p}_T, \mu) \otimes \mathcal{W}_m(\{\underline{n}\}, \bar{p}_T, Q_0, \mu) \rangle, \end{aligned} \quad (3.29)$$

where  $\hat{s} = x_1 x_2 s$  is the partonic center-of-mass energy. The functions  $\mathcal{W}_m(\{\underline{n}\}, \bar{p}_T, Q_0, \mu)$  consist of a matrix element of the Wilson lines in the operator  $\mathcal{S}_{m+2}$  for the incoming and outgoing partons, together with collinear fields of the two incoming ones. The functions  $\mathcal{W}_m$  contain rapidity logarithms due to Glauber gluon exchanges, which induce a dependence on the large scale  $\bar{p}_T$ . This dependence has to be present in order to cancel the scale dependence of the super-leading logarithms mentioned in Section 3.3. These double logarithms of  $\mu / \bar{p}_T$  arise from evolving the hard function and have a scale dependence which cannot cancel against the single-logarithmic scale dependence of the purely soft matrix element and the PDFs. We will discuss the factorization for hadron-collider observables in detail in a forthcoming paper. For the moment, we will concentrate on the leading logarithms in the large- $N_c$  limit, where these complications are absent and the resummed cross section takes the simple form

$$\frac{d\sigma(Q_0)}{d\Delta y d\bar{p}_T} = \sum_{a,b=q,\bar{q},g} \int dx_1 dx_2 f_a(x_1, \mu_f) f_b(x_2, \mu_f) H_2^{ab}(\hat{s}, \Delta y, \bar{p}_T, \mu_h) \langle U_{2m}(\mu_s, \mu_h) \hat{\otimes} 1 \rangle. \quad (3.30)$$

The hard function  $H_2^{ab}$  accounts for the process with two partons in the final state, and all kinematics and color information is encoded in the hard events generated by MADGRAPH. The tree-level generator computes the exact color dependence of the amplitudes, but to interface with a parton shower such as PYTHIA, it randomly assigns a possible large- $N_c$  dipole color structure to each tree-level event. We use this color information to start our shower, which then computes the evolution from 2 partons in the final state to  $m$  partons, as encoded in the matrix elements  $U_{2m}$  defined in (3.6). Since we use full tree-level amplitudes, our hard function also contains terms of subleading color. The paper [53] has modified MADGRAPH in such a way that the full color information is written into the event file. Using this, one could perform a computation in the strict large- $N_c$  limit.

We choose  $\mu_f = \mu_h = \bar{p}_T$  as the central values for the factorization and hard scales, and set the soft scale to be  $\mu_s = Q_0$ . A lower value of  $\mu_f$  would enhance the gap fraction and

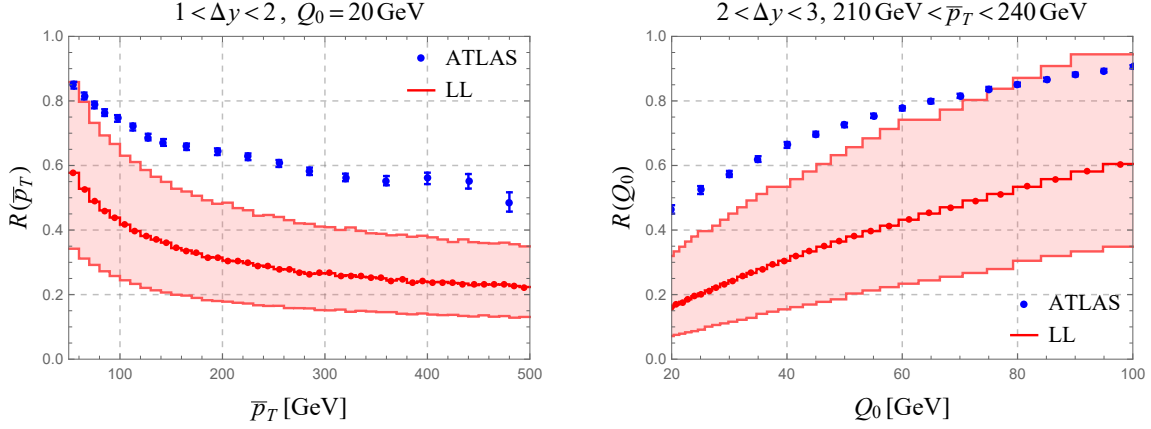


FIGURE 3.5: The gap fraction as a function of the jet transverse momentum  $\bar{p}_T$  (left plot) and the gap energy  $Q_0$  (right plot). The red line shows the LL result for the gap fraction; the error band is obtained from scale variation. The ATLAS data is plotted in blue.

bring our results closer to the ATLAS measurements. However, the high value is appropriate since the hard anomalous dimension has two parts, a soft contribution related to non-global logarithms and a collinear part inducing the usual Altarelli-Parisi evolution. In our shower, we only evolve with the soft part of the anomalous dimension and to avoid the necessity for additional collinear evolution we have to evaluate the PDFs at the high scale.

In our calculations we use NNPDF23LO [68] PDF sets with  $\alpha_s(m_Z) = 0.130$  and use one-loop running for  $\alpha_s$ . In Figure 3.5 we show the resummed gap fraction in comparison with the ATLAS measurements [35]. In the left plot, we keep  $Q_0 = 20$  GeV fixed and vary the transverse momentum  $\bar{p}_T$  of the jets, while the right plot shows the gap fraction as a function of  $Q_0$  for  $210 \text{ GeV} < \bar{p}_T < 240 \text{ GeV}$ . ATLAS has performed measurements for different rapidity separations between the jets. We want to avoid collinear enhancements and focus on fairly central jets, since we do not resum collinear logarithms for the time being. Specifically, we use  $1 < \Delta y < 2$  in the left plot and  $2 < \Delta y < 3$  in the right one. To estimate the uncertainty of our predictions we vary the scales  $\mu_h$  and  $\mu_s$  by a factor of two around their default values  $\mu_h = \bar{p}_T$  and  $\mu_s = Q_0$ . The  $\mu_s$  variation is larger, except at low  $\bar{p}_T$ . In the plots we show the envelope of the two variations. We observe that the results are marginally compatible with the experimental measurements within the fairly large uncertainty bands, but it is clear that the theoretical description at LL accuracy is fairly poor. This should be contrasted to the  $\mathcal{O}(\alpha_s)$  fixed-order result shown in orange and the result obtained with PYTHIA [69] (solid green line) shown in Figure 3.6. We will call the  $\mathcal{O}(\alpha_s)$  prediction leading order (LO), even though strictly speaking the leading-order gap fraction is  $R(\bar{p}_T, Q_0) = 1$ . Neither the fixed-order result nor PYTHIA describe the ATLAS perfectly, but both yield a better description than the LL result. (In their paper ATLAS uses POWHEG matched PYTHIA, which agrees with the data well for this rapidity range, but starts deviating at higher rapidities.)

Before speculating about the source of the poor agreement of the LL result with the measurement, it is interesting to compare to [37], which also computed the gap fraction at LL accuracy and compared to the ATLAS data. Superficially, the results presented in this paper show better agreement with data. The reason is two-fold. First of all, the authors not only show the data of the measurement where the gap is defined by the two most energetic jets, but also the experimental results for the case where the gap and  $\bar{p}_T$  is defined by the

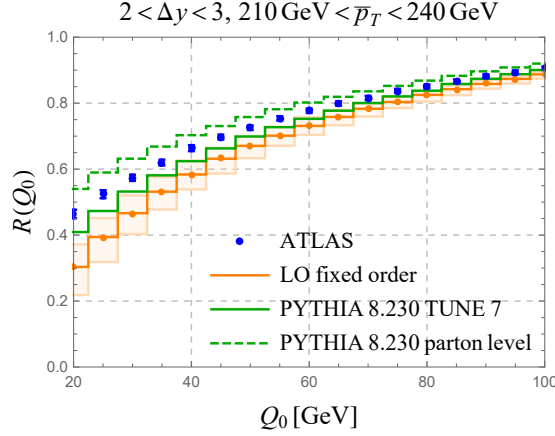


FIGURE 3.6: The gap fraction for different gap energies  $Q_0$  as measured by ATLAS (blue) compared to the fixed-order result at LO (orange) and PYTHIA results (solid green: with hadronization using Tune 7, dashed green: partonic result without hadronization and underlying event).

two most forward and most backward jets. This second criterion leads to lower gap fractions, which agree better with the LL resummed result, but – as the authors of [37] readily admit – is not really appropriate to be compared against the theoretical predictions. Choosing the two most forward and backward jets to define the gap implies a veto on further radiation in the forward and backward direction, which is not imposed in the theoretical computation. Using the highest- $p_T$  jets to define the dijet system, also their gap fractions are below the measurements. They are somewhat higher than our results because [37] approximates the gap by a rectangular region in the rapidity and azimuthal angle, see Figure 3.4, so their veto region is smaller than the experimental gap by about one unit of rapidity (the jet radius is  $R = 0.6$ ), which increases their gap fraction and brings it closer to data. Adopting their definition of the gap region, we find that our results are consistent with their findings; the remaining small numerical differences can be attributed to the fact that they work in the strict large- $N_c$  limit, while we include the full result for the tree-level amplitudes.

Of course, our computation in the large- $N_c$ , leading-logarithmic approximation is rather crude. There are several sources of corrections which could push the results closer to the experimental results. They are (a) higher-logarithmic terms, such as the constant pieces of the one-loop hard and soft functions, (b) power corrections suppressed by  $Q_0/\bar{p}_T$ , (c) terms of subleading color, or (d) hadronisation and underlying event corrections. Let us rule out the last possibility first. In the experimental measurement, the gap energy  $Q_0$  is not defined as the total energy or transverse momentum inside the jet, but as the transverse momentum of the leading jet inside the gap. This definition was chosen to reduce sensitivity to hadronisation and underlying event. Indeed, running PYTHIA at the partonic level (dashed green line in Figure 3.6) yields quite similar results to the full simulation (solid green line). We also doubt that subleading-color pieces can explain the difference. Theoretically, the finite- $N_c$  corrections are especially interesting in our case, because at subleading color one encounters double-logarithmic effects, while the problem is only single logarithmic in the large- $N_c$  limit. However, since the double logarithmic effects only arise at  $\alpha_s^4$ , we do not expect them to be very large. The numerical impact of the super-leading logarithms was estimated to be small in [70], but one should resum them in order to properly assess their importance.

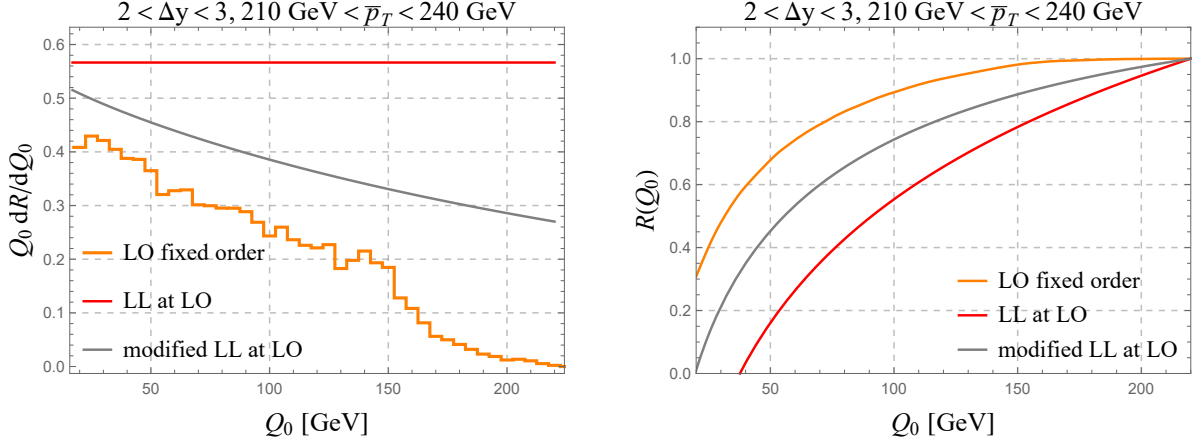


FIGURE 3.7: One emission at LL accuracy, compared to the full LO result. The modified LL shown as a gray line is obtained by implementing momentum conservation for the soft emission.

This leaves (a) and (b) as explanations. The scale hierarchy in our computation is not very large  $Q_0/\bar{p}_T \gtrsim 1/10$ , nevertheless, we expect the power corrections (b) to be moderate. To test their size, we compare in Figure 3.7 the fixed order result at  $\mathcal{O}(\alpha_s)$  to the expansion of the LL result to the same accuracy. We compute the LO fixed order result using the relation

$$R(\bar{p}_T, Q_0) = 1 - \frac{1}{\sigma_{2\text{-jet}}^{\text{LO}}(\bar{p}_T)} \int_{Q_0}^{\bar{p}_T} dQ'_0 \frac{d\sigma_{3\text{-jet}}^{\text{LO}}(\bar{p}_T, Q'_0)}{dQ'_0}. \quad (3.31)$$

At LO, the integrand in (3.31) is obtained by computing the tree-level three-jet cross section in which the third jet is inside the gap and has transverse momentum  $Q_0$ . To see the power corrections, it is interesting to take the logarithmic derivative of the gap fraction  $R(\bar{p}_T, Q_0)$  with respect to  $Q_0$ . This removes any constant so that we directly see the difference of the leading-power log term to the full result. As it should be, the full LO result (orange line) approaches the LL coefficient (red line) for small  $Q_0$ . At the same time the plot shows that the LL derivative is completely off at large  $Q_0$ , where the derivative of the full LO tends to zero. The fact that  $R$  becomes constant at large  $Q_0$  implies that power corrections must cancel against the leading-power terms in this region. More generally, the unitarity condition  $R(\bar{p}_T, Q_0 = \bar{p}_T) = 1$  links power corrections (b) and higher-logarithmic terms (a).

One type of power suppressed terms arises from expanding away the soft momenta in the momentum-conservation  $\delta$ -functions. In our factorization theorem, the momenta in the hard functions at the high scale are conserved, but the soft momenta are neglected. Neglecting the soft momentum  $k_s$  enhances the three-jet rate in (3.31) because the jets can then be produced at the low partonic center-of-mass energy  $\hat{s} = (p_{J_1} + p_{J_1})^2$  instead of the correct value  $\hat{s} = (p_{J_1} + p_{J_1} + k_s)^2$  at which the PDFs are smaller due to the suppression of larger momentum fractions. To gauge the size of this effect, we have used our MC code to compute  $dR/dQ_0$  for the first emission with the full  $\hat{s}$ . Since we know the  $k_T = Q_0$  of the emission as well as the direction, we can reconstruct the vector  $k$  and the associated  $\hat{s}$ . In practice, we first boost to the partonic center-of-mass frame, correct  $\hat{s}$  and then boost back. Doing so, we obtain the gray line in Figure 3.7. The modification due to momentum conservation accounts for about half of the difference between LL and the full LO. A similar study was performed in [67] who found that they could reproduce the full LO result with good accuracy with a suitable modification of the parton luminosity. However,



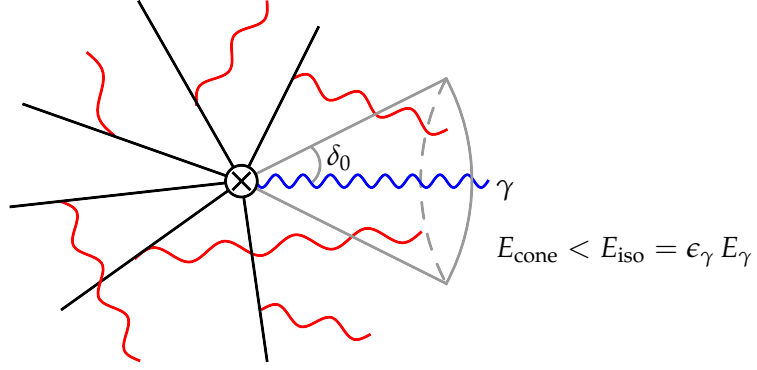


FIGURE 3.8: Pictorial representation of the factorization for isolated photon production. The black lines represent hard partons, while the wavy red lines indicate soft radiation. The energy inside the isolation cone of half-angle  $\delta_0$  is restricted to be smaller than  $\epsilon_\gamma E_\gamma$ .

their modification involved parameters which were chosen by hand. Parton showers such as PYTHIA implement momentum conservation, so that these types of kinematic power corrections are accounted for and their effect was also studied in the recent paper [71]. It is significant, but by itself not large enough to account for the difference we observe. It would be quite interesting to see whether one can modify our shower in such a way that momentum conservation is fulfilled without modifying the leading power terms but we will not pursue this issue further for the moment.

What can and certainly should be done is to extend the resummation to subleading logarithmic accuracy. This will add the virtual corrections to  $\mathcal{H}_2^{ab}$  and the function  $\mathcal{H}_3^{ab}$  at the high scale, together with the  $\mathcal{O}(\alpha_s)$  corrections for all the soft functions at the low scale. It will also require the two-loop anomalous dimension in the evolution to lower scales. Computing these corrections and implementing them into a MC is of course a major undertaking. To get a feeling for their size, one can first evaluate the NLL result at  $\mathcal{O}(\alpha_s)$ . One reason that the higher-log terms are significant is that we have not resummed collinear logarithms for the moment, but with  $\Delta y = 3$ , these are already of the same order of magnitude as the soft logarithms. Using the results [24, 25] this can be done and we plan to implement also the collinear resummation in the future. A related issue is that large rapidity differences lead to forward-scattering kinematics at hadron colliders, which induces its own logarithmic enhancements. A method to resum these terms was put forward in [72] and implemented in the HEJ code. Recently, the HEJ results were merged with PYTHIA [73]. This combines both types of resummations and improves the description of the ATLAS data, but to improve our understanding of gap observables, it will be important to perform measurements for kinematical situations in which only a single source of large logarithms is present so that one can separately study the different effects.

### 3.4.3 Isolation cone cross sections and photon production

A second important class of non-global observables are cross sections with isolation cones inside which only soft hadronic radiation is allowed. The most important example is photon production, where an isolation cone is needed to separate the direct production of a photon in the underlying hard collision from the photons which arise in hadron decays such as  $\pi^0 \rightarrow \gamma\gamma$ . Imposing that  $E_{\text{iso}}$ , the hadronic energy inside the cone with half-opening angle



$\delta_0$ , is much smaller than the photon energy  $E_\gamma$  suppresses energetic photons originating from decays of boosted hadrons. Similar cuts are also used to isolate leptons, for example in SUSY searches. Imposing the isolation requirement induces logarithms  $\alpha_s^n \ln^n \epsilon_\gamma$ , with  $\epsilon_\gamma = E_{\text{iso}}/E_\gamma$ , into the perturbative computation and in the following we want to study their resummation.

Already at the parton level, there are two mechanisms to produce a photon. In addition to the direct emission, one can produce an energetic quark which then fragments into a photon accompanied by a collinear quark. This second mechanism involves the fragmentation function, a non-perturbative object which needs to be extracted from data. In general, the two partonic contributions are not individually well-defined. At NLO, the direct production suffers from a divergence when the quark becomes collinear to the photon and this divergence is absorbed into the fragmentation function. The isolation cone suppresses fragmentation since it limits the amount of radiation which accompanies the photon. Indeed, Frixione has shown that one can modify the isolation criterion to eliminate fragmentation altogether [74]. For any angle  $\delta < \delta_0$ , where  $\delta_0$  is the isolation cone angle, he imposes that the energy inside the cone of half-opening angle  $\delta$  is smaller than

$$E_{\text{iso}}(\delta) = \epsilon_\gamma E_\gamma \left( \frac{1 - \cos \delta}{1 - \cos \delta_0} \right)^n, \quad (3.32)$$

with  $n > 0$ . Together with radiation collinear to the photon, this smooth-cone isolation eliminates the fragmentation contribution, which is centered at  $\delta = 0$ . This simplifies the theoretical computations and is appealing because it eliminates the poorly known fragmentation function. Up to now, all NNLO computations of photon production [75–77] rely on the Frixione cone for isolation, while the result with a fixed cone is only known at NLO in the form of the JETPHOX code [78]. Due to the granularity of the calorimeter, a smooth criterion such as (3.32) cannot be directly implemented in experiments which therefore use fixed-cone isolation. To compare with experimental data, the NNLO results tune the parameters  $\epsilon_\gamma$  and  $n$  such that the NLO predictions using (3.32) are numerically similar to fixed-cone computations including fragmentation. Below, we will derive such a parameter relation based on the analysis of soft radiation.

The logarithms we want to study become large in the limit  $\epsilon_\gamma \rightarrow 0$ . In this limit the radiation inside the cone becomes very soft. It is well known that the emission of soft quarks is power suppressed and for this reason, fragmentation is a power suppressed effect for  $\epsilon_\gamma \rightarrow 0$  which we do not need to consider. (The same holds true for threshold resummation studied in [79] and implemented into the numerical code PETER [80].) As we discussed above, in the hadron collider case there are some interesting open issues and we therefore first derive a factorization theorem for  $e^+e^-$ . The kinematics is shown in Figure 3.8. One has hard partons outside the cone with energies of the order of the photon energy  $E_\gamma$  and soft radiation inside the cone. This is precisely the situation captured by (3.1), except that the soft region is now defined by the photon instead of the hard jets. Specializing the general formula to the photon case, we have

$$\frac{d\sigma(\epsilon_\gamma, \delta_0)}{dx_\gamma} = \sum_{m=2}^{\infty} \langle \mathcal{H}_{\gamma+m}(\{\underline{n}\}, E_\gamma, Q, \delta_0) \otimes \mathcal{S}_m(\{\underline{n}\}, \epsilon_\gamma E_\gamma, \delta_0) \rangle, \quad (3.33)$$

where the photon energy is parameterized as  $E_\gamma = x_\gamma Q/2$ . The hard functions  $\mathcal{H}_{\gamma+m}$  are the squared amplitudes for the photon and  $m$ -parton process and are defined as in (3.4). In addition to the integrals over the energies of the  $m$  partons at fixed directions

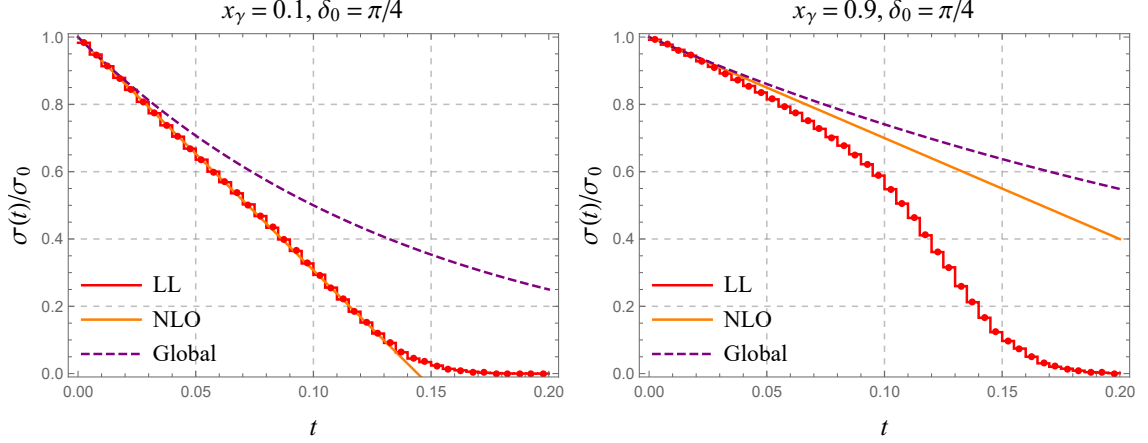


FIGURE 3.9: Effect of the isolation cut in  $e^+e^- \rightarrow \gamma + X$ . The plot shows a comparison of the resummed result (red line) with the one-loop contribution (orange line) and the global logarithms (dashed purple line).

$\{\underline{n}\} = \{n_1, \dots, n_m\}$  outside the isolation cone, they include an integral over the photon phase space together with its constraints (the energy  $E_\gamma$  in the example (3.33)). The soft functions are given by the Wilson line matrix element (3.3) with the energy constraint applied to radiation inside the photon cone.

We will use the automated framework of the previous chapter to resum the large logarithms in the isolation cone cross section, but it is interesting to first analyze the NLO cross section analytically. The NLO correction to the soft function  $\mathcal{S}_2$  with two Wilson lines in  $d = 4 - 2\epsilon$  dimensions is given by the integral

$$\mathcal{S}_2(\{n_1, n_2\}, \epsilon_\gamma, E_\gamma, \delta, \epsilon) = 1 - \mathbf{T}_1 \cdot \mathbf{T}_2 g_s^2 \tilde{\mu}^{2\epsilon} \int \frac{d^{d-1}k}{(2\pi)^{d-1}2\omega} \frac{2 n_1 \cdot n_2}{n_1 \cdot k n_2 \cdot k} \theta(E_{\text{iso}} - \omega), \quad (3.34)$$

where  $\omega = |\vec{k}|$  is the gluon energy. Note that the soft gluon can also be outside the isolation cone, but this part of the integration is scaleless and vanishes. Exactly the same integral is relevant for  $\mathcal{S}_m$ , which involves a sum over all pairs of hard partons. In Appendix 3.C, the full computation of  $\mathcal{S}_2$  is performed analytically. To avoid technicalities and get a qualitative understanding, we will now perform an approximate computation. Since all hard partons are outside while the soft gluon is inside the cone, the dipole factor is not singular. If the cone is narrow and the hard partons are not too close to the cone, we can approximate the gluon direction with the photon direction so that

$$\frac{n_1 \cdot n_2}{n_1 \cdot k n_2 \cdot k} \approx \frac{1}{\omega^2} \frac{n_1 \cdot n_2}{n_1 \cdot n_\gamma n_2 \cdot n_\gamma} = \frac{1}{\omega^2} W_{12}^\gamma. \quad (3.35)$$

The one-loop correction to the soft function then simplifies to

$$\mathcal{S}_2 \approx 1 + C_F \frac{2g_s^2}{(2\pi)^{d-2}} W_{12}^\gamma \int_0^\infty \frac{d\omega}{\omega} \left( \frac{\tilde{\mu}}{\omega} \right)^{2\epsilon} \int_{\text{cone}} \frac{d\Omega}{4\pi} \theta(E_{\text{iso}} - \omega). \quad (3.36)$$

For a fixed cone-energy  $E_{\text{iso}}$ , the energy integration produces a divergence with an associated logarithm, which gets multiplied by the angular area of the cone, in line with the discussion in Section 3.4.1. The situation is interesting for isolation cones because the logarithms are typically large (experiments often restrict the isolation energy to a few GeVs), while the area

tends to be small. If we substitute  $E_{\text{iso}} \rightarrow E_{\text{iso}}(\delta)$  from (3.32) into (3.36), we can compute the soft function for the smooth-cone. In the approximation (3.35), we find that the smooth-cone result is obtained from the fixed cone one-loop result using the substitution

$$\ln \frac{\epsilon_\gamma E_\gamma}{\mu} \longrightarrow \ln \frac{\epsilon_\gamma e^{-n} E_\gamma}{\mu}. \quad (3.37)$$

In other words, the smooth-cone isolation is more restrictive than fixed-cone isolation by a factor  $e^n$ . A computation such as [77] which uses smooth-cone isolation with  $\epsilon_\gamma = 0.1$  and  $n = 2$ , therefore has the same size logarithms as a fixed-cone computation with  $\epsilon_\gamma = 0.01$ . For photon energies of a few hundred GeVs, this indeed matches up with the fixed-cone isolation criterion

$$E_T^{\text{iso}} = 4.8 \text{ GeV} + 0.0042 E_\gamma^T \quad (3.38)$$

used in the ATLAS analysis [81]. ATLAS uses a cone of  $R = 0.4$  in the rapidity and azimuthal-angle plane. A particle is considered to be inside the cone (and therefore belongs to the “out”-region), if  $\Delta y^2 + \Delta\phi^2 < R^2$ , where  $\Delta y$  is the rapidity difference and  $\Delta\phi$  the difference of the azimuthal angle between the particle and the photon.

As we discussed in Section 3.4.1 above, the two-loop non-global and global logarithms can cancel each other out and for photon isolation results displayed in Figure 3.9, this effect is quite pronounced. In this plot we consider  $e^+e^- \rightarrow \gamma + X$  with an isolation cone with half-angle  $\delta_0 = \pi/4$  and compare the resummed result with the one-loop logarithm and with the global contribution, which is given by the exponential of the one-loop logarithm. We observe that higher-order effects are quite small down to relatively low isolation energies which correspond to larger values of  $t$  in the figure. Resumming the global logarithms leads to a much larger effect, which cancels after accounting also for the non-global contribution. By now there are many papers in the SCET literature which resum observables up to non-global contributions. This example demonstrates that such estimates of higher-order terms are not always reliable. In the present example this incomplete resummation leads to worse predictions than no resummation at all.

Finally, let us analyze photon isolation in hadronic collisions. Of course, in this case the same caveats apply that we discussed for gaps between jets: a full factorization analysis for hadronic collisions is not yet available. We will therefore again work in the large- $N_c$  limit and resum the leading logarithms captured by evolving the hard function from the scale  $\mu_h \approx E_T^\gamma$  down to the soft scale  $\mu_s \approx E_T^{\text{iso}}$ . We need to evaluate the PDFs at the hard scale  $\mu_f = \mu_h$ , as explained in the gaps-between-jets case.

The small angular size  $R$  of the veto region suppresses higher-order corrections and the overall effect of the isolation cone is therefore moderate. At the same time, the typical scale ratios  $\epsilon_\gamma$  that arise in experimental measurements can be quite large. We have discussed in Section 3.4.1 that the global logarithms scale as  $\alpha_s^n R^{2n} \ln^n(\epsilon_\gamma)$ , while the non-global ones scale as  $\alpha_s^n R^2 \ln^{n-1}(R) \ln^n(\epsilon_\gamma)$ , since they involve only a single gluon in the veto region. For small  $R$ , the non-global logarithms completely dominate the cross section. In order to verify this, we extract large logarithms up to two-loop from our parton-shower code. Explicitly, as is shown in [24], the first two coefficients in the expansion

$$\sigma(t)/\sigma_0 = 1 + \mathcal{S}^{(1)}t + \mathcal{S}^{(2)}t^2 + \dots \quad (3.39)$$

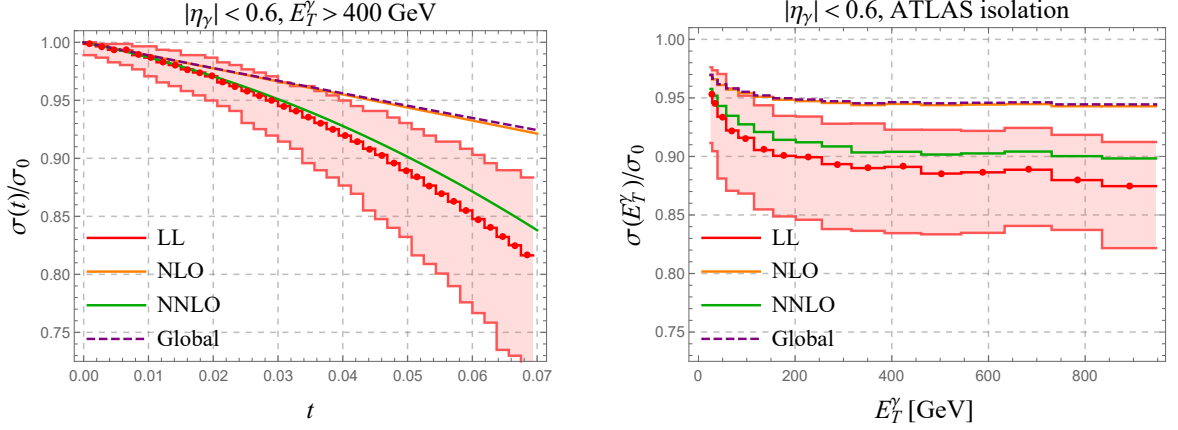


FIGURE 3.10: Ratio of the  $pp \rightarrow \gamma + X$  cross section with isolation to the inclusive one. Left: Ratio as a function of  $t$  (or equivalently  $\epsilon_\gamma$ ) for  $E_T^\gamma > 400 \text{ GeV}$ . Right: Ratio for the ATLAS isolation criterion (3.38) as a function of  $E_T^\gamma$ . In both plots we show the resummed result as well as its NLO and NNLO expansions obtained using the approximation (3.35). The red uncertainty bands are obtained by scale variations, see text.

in the shower time (3.11) take the form

$$\begin{aligned} \mathcal{S}^{(1)} &= -4N_c \int_{\Omega} \mathbf{3}_{\text{out}} W_{12}^3, \\ \mathcal{S}^{(2)} &= \frac{(4N_c)^2}{2!} \int_{\Omega} \left[ -\mathbf{3}_{\text{in}} \mathbf{4}_{\text{out}} \left( P_{12}^{34} - W_{12}^3 W_{12}^4 \right) + \mathbf{3}_{\text{out}} \mathbf{4}_{\text{out}} W_{12}^3 W_{12}^4 \right], \end{aligned} \quad (3.40)$$

where the subscript “in” and “out” refer to the radiation inside the jets (outside the isolation cone) and outside jets (inside the isolation cone), respectively. The coefficient of the one loop shower time  $\mathcal{S}^{(1)}$  can be calculated using our MC simulation to generate a single emission along  $n_3$  inside the cone (the “out”-region). To calculate the non-global part of the two-loop coefficient we approximate  $n_4$  with the direction of the photon as we did in (3.35), and end up with

$$\mathcal{S}_{\text{NG}}^{(2)} \approx -\frac{(4N_c)^2}{2!} \Omega_{\text{cone}} \int_{\Omega} \mathbf{3}_{\text{in}} W_{12}^3 (W_{13}^\gamma + W_{23}^\gamma - W_{12}^\gamma). \quad (3.41)$$

We then again use our MC simulation to generate vectors  $n_3$  outside the cone (in the “in”-region). Due to exponentiation, the global part of  $\mathcal{S}^{(2)}$  is one-half of the one loop correction squared. Our results are shown in the left plot in Figure 3.10, where we give evolution effects as a function of shower time as defined in (3.11). The red line shows the LL resummed result, and the orange and green lines are one-loop- and two-loop-LL contributions, respectively. The dashed purple line corresponds to the naive exponentiation of one-loop results. To obtain the red error band, one first calculates  $\tilde{\mu} = \mu_s(t)$  by inverting (3.11). Varying this scale by a factor of two, one then obtains two values  $t_{\text{low}} = t(2\tilde{\mu})$  and  $t_{\text{high}} = t(\frac{1}{2}\tilde{\mu})$ . The cross sections  $\sigma(t_{\text{high}})$  and  $\sigma(t_{\text{low}})$  are then used to define the uncertainty band. Clearly, there is a large difference between the one- and two-loop results, which is due to the  $\ln R$  dependence of the NGLs which dominate the cross section. On the other hand, the difference between NNLO and the resummation is moderate. In the right plot, we show resummation effects as function of photon transverse energy  $E_T$  for the ATLAS [81] isolation criterion (3.38). In this case, the red band is obtained by varying the soft scale by a factor two around the default

value  $\mu_s = E_T^{\text{iso}}$ . Overall, resummation changes the NLO result for the isolation effects by about a factor of two. On the other hand, since higher-order corrections beyond two loops are moderate, we don't anticipate large corrections to the NNLO computation in [77].

Until now we were focussing on logarithms of  $\epsilon_\gamma$  arising in the limit of small isolation energy, while keeping the cone radius  $R$  fixed. It is also interesting to keep  $\epsilon_\gamma$  fixed and consider the limit of small  $R$ . That both limits are problematic for fixed-order computations was stressed already in [78] and the small  $R$  case has been studied in detail in [82], after it was realized that for narrow cones the NLO cross section with isolation [78] becomes larger than the inclusive one [83], which is of course unphysical. In [82], the leading  $\ln R$  terms were resummed using collinear factorization. It was found that the higher-order effects are moderate for  $R \gtrsim 0.5$ , but quickly become large for smaller cone radii. The paper [78] found that  $\ln \epsilon_\gamma$  terms were moderate, but warned that the NLO computation could underestimate the overall effect. Our results in Figure 3.10 show that the nonglobal NNLO terms are as large as the NLO corrections, confirming this suspicion.

Phenomenologically, the double limit  $\epsilon_\gamma \rightarrow 0$  and  $R \rightarrow 0$  is perhaps most relevant. We will now consider this situation, in which both types of logarithms are present. The relevant factorization analysis is quite similar to the one for the narrow-cone Stermann-Weinberg cross section [24, 25]. In the following we will state and discuss the result; we refer the reader to [24, 25] for more details regarding its derivation. Explicitly, for small  $R \sim \delta_0$  the factorization formula (3.33) turns into

$$\frac{d\sigma(\epsilon_\gamma, \delta_0)}{dE_\gamma} = \frac{d\sigma_{\gamma+X}^{\text{incl}}}{dE_\gamma} + \sum_{i=q,\bar{q},g} \int dz \frac{d\sigma_{i+X}}{dE_i} \sum_{l=1}^{\infty} \langle \mathcal{J}_{i \rightarrow \gamma+l}(\{\underline{n}\}, \delta_0 E_\gamma, z) \otimes \mathcal{U}_l(\{\underline{n}\}, \epsilon_\gamma \delta_0 E_\gamma) \rangle. \quad (3.42)$$

In this formula, the first term on the right-hand side is the direct photon production cross section without photon isolation and without fragmentation. This term is obtained when considering soft radiation at parametrically large angles  $\delta \gg \delta_0$  for which one can ignore the narrow cone. Doing so renders the soft functions trivial and one can integrate over the directions of the hard partons, which yields the cross section  $\sigma_{\gamma+X}$ . The (perturbative) fragmentation contribution is part of the second term which describes the inclusive production of a parton  $i$  along the photon direction, which then fragments into a photon plus soft hadronic radiation along the direction of the small isolation cone and energetic radiation immediately outside the cone. More precisely, the term  $\sigma_{i+X}$  in the second line denotes the inclusive cross section for producing a parton  $i$  with energy  $E_i$  and momentum  $p_i$  along the direction  $n^\mu = n_\gamma^\mu$  of the photon, and the jet functions

$$\begin{aligned} \frac{\not{n}}{2} \mathcal{J}_{i \rightarrow \gamma+l}(\{\underline{n}\}, \delta_0 E_\gamma, z) &= \sum_{\text{spins}} \prod_{j=1}^l \int \frac{dE_j E_j^{d-3}}{(2\pi)^{d-2}} |\mathcal{M}_l(p_i; \{p_\gamma, \underline{p}\}) \langle \mathcal{M}_l(p_i; \{p_\gamma, \underline{p}\}) | \\ &\times 2(2\pi)^{d-1} \delta(2(1-z)E_i - \bar{n} \cdot p_{X_c}) \delta^{(d-2)}(p_{X_c}^\perp) \Theta_{\text{cone}}^n(\{\underline{p}\}) \rangle. \end{aligned} \quad (3.43)$$

describe the fragmentation of this parton into a photon with energy  $E_\gamma = zE_i$  and  $l$  additional energetic partons outside the cone, as enforced by the theta function  $\Theta_{\text{cone}}^n$  in their definition. The function  $\mathcal{U}_l$  describes soft radiation collinear to the isolation cone and consists of  $l$  Wilson lines along the energetic partons plus one additional Wilson line along the light-cone direction  $\bar{n}^\mu$  conjugate to the one of the photon direction. More details on this collinear and soft (or “coft”) mode can be found in [24, 25]. Its most important property is that the typical

invariant mass of this type of radiation has the low value  $\Lambda_{\text{coft}} = \delta_0 \epsilon_\gamma E_\gamma$ , precisely because it is both soft and collinear. In appendix 3.D, we will evaluate the narrow-cone isolation cross section at leading order and verify that the QCD result maps onto the factorization theorem (3.42).

We note that the two terms in (3.42) are not separately finite: the partonic cross sections and jet functions must be viewed as Wilson coefficients of the effective theory, which must be renormalized. To perform the resummation of the large logarithms, one has to solve the associated RG-evolution equations and first evolve from the hard scale  $\mu_h \sim E_\gamma$  down to the jet scale  $\mu_j \sim \delta_0 E_\gamma$  and finally to the coft scale  $\mu \sim \delta_0 \epsilon_\gamma E_\gamma$ . As we discussed above, the quantity  $\sum_l \langle \mathcal{J}_{i \rightarrow \gamma+l} \otimes \mathcal{U}_l \rangle$  describes the fragmentation of the parton  $i$  into a photon plus soft and collinear radiation. It has exactly the same scale dependence as the standard photon fragmentation function, see [84, 85]. The first step of RG evolution, which generates the logarithms of  $R$  through the ratio  $\mu_j/\mu_h$ , is thus governed by the standard RG evolution of the fragmentation function. Logarithms of  $\epsilon_\gamma$  are only generated in the second step, via the evolution from  $\mu_j \sim \delta_0 E_\gamma$  down to  $\mu \sim \delta_0 \epsilon_\gamma E_\gamma$ . We postpone a study of the numerical size of the  $\ln R$  terms to future work.

#### 3.4.4 Jet-veto cross sections

Rejecting events with hard jets can be important to make precise measurements at hadron colliders. An example is the process  $p p \rightarrow W^+ W^-$  at the LHC, where the veto is used to reduce the background from top-quark pair production with subsequent  $t \rightarrow b l \nu$  decay. The cut used by ATLAS rejects events with jets of  $p_T^J > p_T^{\text{veto}} = 25$  GeV for  $|\eta^J| < 4.5$  [86], while CMS imposes  $p_T^{\text{veto}} = 30$  GeV for  $|\eta^J| < 5$  [87]. The jet-veto cut introduces logarithms  $\ln(p_T^{\text{veto}}/m_H)$ , which can spoil the convergence of perturbative calculations. Much work has been carried out to resum these large logarithms [88–92]. The resummation at NNLL+NLO accuracy has been automated for the production of an arbitrary final state with massive colorless particles within the MADGRAPH5\_AMC@NLO framework [93].

The jet-veto cross section is a non-global observable, since the cross section becomes fully inclusive in the large rapidity region near the beams, because the veto can only be imposed where detectors are present. Of course, this problem affects all hadron collider observables and in particular also hadronic event shapes. The NGLs in the jet-veto cross section have never been resummed, but [88] has analyzed the rapidity cut dependence in fixed order and by using parton showers, and concluded that it was small. The paper [94] pointed out that the non-global effects are power suppressed for the kinematic cuts used at the LHC. In order to explain this power suppression effects, let us first define two expansion parameters

$$\beta = p_T^{\text{veto}}/Q, \quad \delta = e^{-\eta_c}, \quad (3.44)$$

where  $\eta_c$  is the rapidity cut, and  $Q$  represents the hard scale for this process. E.g. for  $W^+ W^-$  production it is the invariant mass of the electroweak final state  $Q = M_{W^+ W^-}$ .

For jet-vetoed cross section at the LHC, the hierarchy between the two parameters is  $\beta \sim 0.1 \gg \delta \sim 0.01$ . Analyzing which momentum regions are relevant, one finds that collinear modes contributing to jet-veto resummation have light-cone components  $(n \cdot p_c, \bar{n} \cdot p_c, p^\perp)$  scaling as  $Q(\beta^2, 1, \beta)$ , where  $n^\mu$  and  $\bar{n}^\mu$  are light-cone vectors along the beams. The typical rapidity of these particles is much smaller than the cut  $\eta_c \sim 5$  used at the LHC. Contributions sensitive to the rapidity cut  $\eta_{\text{cut}}$  are therefore power suppressed by  $\delta/\beta$ .



This parametric suppression is consistent with the small size of the fixed-order corrections computed in [88].

One can also consider the opposite hierarchy  $\beta \ll \delta \ll 1$ , as analyzed in [94]. At LHC energies, the low  $p_T^{\text{veto}}$  scale related with  $\beta$  would be non-perturbative in this situation, so it is currently only of theoretical interest. To capture the physics in the low-energy region one needs modes with the same scaling behavior as the soft mode introduced in [25]. The paper [94] analyzed the factorization for rapidity-dependent jet-veto cross sections but their analysis was restricted to global logarithms. We recently developed the necessary framework to deal with soft-recoil sensitive non-global observables in [95] and it would be interesting to derive the full formula in our framework.

### 3.5 CONCLUSION

In this paper, we have used RG methods in effective field theory to obtain a parton shower for the resummation of large logarithms in non-global observables. Our result provides an explicit example of a parton-shower equation derived from first principles which can be systematically improved. At LL level in the large- $N_c$  limit, our shower is equivalent to the Dasgupta-Salam dipole shower. We have implemented it and have interfaced it with `MADGRAPH5_AMC@NLO` to obtain a flexible framework to perform resummations. The tree-level generator is used to produce a LHE file containing the kinematic configuration and color structure of the hard partons. This information is then passed to the shower to perform the RG evolution to lower scales.

With this method we have investigated gap fractions in dijet production and isolation cone cross sections. We find that non-global contributions are especially important when the veto region is small, because the higher-order global contributions are suppressed by higher powers of the size of the veto region, while this suppression is absent for the non-global terms. We observe that the LL predictions suffer from large uncertainties, and it will be important to extend the resummation to higher accuracy in the future. In addition, there are also several other issues, which can and should be studied already at the leading logarithmic level, such as the role of momentum conservation to reduce power corrections and the resummation of collinear logarithms. For exclusive jet cross sections, we have shown in earlier work how the collinear logarithms arising for small jet radius can be resummed, and in the present work we have extended the relevant factorization to small isolation cones. As in the case of small-radius jets, we find that momentum modes are relevant, which are both soft and collinear to the cone.

To resum next-to-leading logarithms, one needs higher-order corrections to the anomalous dimension matrix and the matching coefficients. Specifically, one will need to include i.) the one-loop soft functions  $\mathcal{S}_m$  for any  $m$ , ii.) the one-loop correction to the Born-level hard function  $\mathcal{H}_k$  and the tree-level result for  $\mathcal{H}_{k+1}$ , the hard function with one additional emission. In addition, one also needs iii.) the two-loop anomalous dimension. In earlier papers, we have computed i.) and ii.) for specific processes and iii.) should have a close relation to the result of Caron-Huot in the density matrix formalism [96]. While our RG framework makes it clear which ingredients are necessary to improve the logarithmic accuracy, it will likely be nontrivial to implement these into a MC framework similar to the one we employed at LL. Nevertheless, it is important to pursue this line of research, not only to reduce the uncertainties in the observables studied here, but also because it can provide a first example of a parton shower with higher logarithmic accuracy.



Our shower code is currently restricted to the large- $N_c$  limit, but it would be interesting to go beyond this approximation, especially for hadron-collider processes, where contributions from Glauber phases arise at finite  $N_c$ . Without accounting for these in the low-energy theory, the factorization theorem would not be RG invariant because the double-logarithmic evolution of the hard functions, which produces the “super-leading” logarithms, could not be matched by the evolution of the operators in the low-energy theory. A detailed discussion of these effects will be given in a forthcoming paper.

#### ACKNOWLEDGMENTS

The research of T.B. is supported by the Swiss National Science Foundation (SNF) under grant CRSII2\_160814. The authors would like to thank Jeppe Andersen, Helen Brooks, Keith Hamilton, Johannes Michel, Pier Francesco Monni, Matthias Neubert, Simon Plätzer, Emanuele Re and Gavin Salam for useful discussions and the Munich Institute for Astro- and Particle Physics (MIAPP) of the DFG cluster of excellence "Origin and Structure of the Universe" for hospitality and support.

#### 3.A ANGULAR INTEGRATION WITH A COLLINEAR CUTOFF

With a collinear cutoff  $\lambda$  the angular integration in the anomalous dimensions  $V_m$  and  $R_m$  in (3.13) takes form

$$I(\lambda, n_i, n_j) = \int \frac{d\Omega(n_l)}{4\pi} \frac{n_i \cdot n_j}{n_i \cdot n_l n_l \cdot n_j} \theta(n_l \cdot n_i - \lambda^2) \theta(n_l \cdot n_j - \lambda^2). \quad (3.45)$$

The cutoff amounts to putting small cones around the emitting partons to avoid the collinear singularity. In the lab frame any vector  $n_l$  can be parametrised as

$$n_l = (1, \text{sech } y_l \sin \phi_l, \text{sech } y_l \cos \phi_l, \tanh y_l). \quad (3.46)$$

In order to compute (3.45), we transform the integration into the Center-Of-Mass (COM) frame of  $n_i$  and  $n_j$ , where it takes the form

$$I(\lambda, M) = \int_{-\infty}^{\infty} d\hat{y}_l \int_0^{2\pi} \frac{d\hat{\phi}_l}{2\pi} \theta \left[ \frac{M^2(1 - \tanh \hat{y}_l)}{4(1 - \beta \cos \hat{\phi}_l \text{sech } \hat{y}_l)} - \lambda^2 \right] \theta \left[ \frac{M^2(1 + \tanh \hat{y}_l)}{4(1 - \beta \cos \hat{\phi}_l \text{sech } \hat{y}_l)} - \lambda^2 \right]. \quad (3.47)$$

Here  $M^2 = 2 n_i \cdot n_j$  is the invariant mass of the  $n_i$  and  $n_j$  dipole, and  $\beta = \sqrt{1 - M^2/4}$ . The new integration variables  $\hat{y}_l$  and  $\hat{\phi}_l$  are the rapidity and azimuthal angle of the emission in the COM frame. The components  $n_l^\mu = (1, n_x, n_y, n_z)$  in the lab frame can be expressed in terms of  $\hat{y}_l$  and  $\hat{\phi}_l$  as

$$n_x = \frac{E_l}{M} \left[ \left( 1 - \frac{\cos \hat{\phi}_l \text{sech } \hat{y}_l}{\beta} \right) (\text{sech } y_i \sin \phi_i + \text{sech } y_j \sin \phi_j) + \tanh \hat{y}_l (\text{sech } y_i \sin \phi_i - \text{sech } y_j \sin \phi_j) + \frac{\text{sech } \hat{y}_l \sin \hat{\phi}_l}{\beta} (\cos \phi_i \text{sech } y_i \tanh y_j - \cos \phi_j \text{sech } y_j \tanh y_i) \right],$$

$$\begin{aligned}
n_y &= n_x (\sin \phi_{i,j} \rightarrow \cos \phi_{i,j}, \cos \phi_{i,j} \rightarrow -\sin \phi_{i,j}), \\
n_z &= \frac{E_l}{M} \left[ \left( 1 - \frac{\cos \hat{\phi}_l \operatorname{sech} \hat{y}_l}{\beta} \right) (\tanh y_i + \tanh y_j) + \tanh \hat{y}_l (\tanh y_i - \tanh y_j) \right. \\
&\quad \left. + \frac{1}{\beta} \operatorname{sech} y_i \operatorname{sech} y_j \operatorname{sech} \hat{y}_l \sin(\phi_i - \phi_j) \sin \hat{\phi}_l \right].
\end{aligned} \tag{3.48}$$

with  $M/E_l = 2 - 2\beta \cos \hat{\phi}_l \operatorname{sech} \hat{y}_l$ . The result for the components will be useful for the phase-space generation for the real emissions. To obtain the virtual corrections, we now evaluate (3.47). As long as the two cones around  $n_i$  and  $n_j$  do not touch each other, i.e. for  $M^2 > 8\lambda^2 - 4\lambda^4$ , the integration constraints implemented by the  $\theta$ -function in (3.47) reduce to

$$I_1(\lambda, M) = \int_0^{2\pi} \frac{d\hat{\phi}_l}{2\pi} \int_{-y_{\max}(\hat{\phi}_l)}^{y_{\max}(\hat{\phi}_l)} d\hat{y}_l, \tag{3.49}$$

with

$$y_{\max}(\hat{\phi}_l) = \ln \left( \beta \cos \hat{\phi}_l + \sqrt{\alpha + \beta^2 \cos^2(\hat{\phi}_l)} \right), \tag{3.50}$$

where  $\alpha = (M^2 - 2\lambda^2)/(2\lambda^2)$ . Performing these integrations, one obtains the analytical result

$$I_1(\lambda, M) = \ln \left( \frac{M^2}{2\lambda^2} - 1 \right). \tag{3.51}$$

In the region  $2\lambda^2 < M^2 < 8\lambda^2 - 4\lambda^4$  the integration boundary can be simplified to

$$I_2(\lambda, M) = \int_0^\delta \frac{d\hat{\phi}_l}{\pi} \int_{-y_{\max}(\hat{\phi}_l)}^{y_{\max}(\hat{\phi}_l)} d\hat{y}_l, \tag{3.52}$$

with  $\cos \delta = (1 - \alpha)/(2\beta)$ . Because the two cones overlap, the azimuthal angle integration is now restricted. After performing integration by parts,  $I_2$  can be reduced to a one-dimensional elliptic integral

$$I_2(\lambda, M) = \frac{2\beta}{\pi} \int_0^\delta d\hat{\phi}_l \frac{\hat{\phi}_l \sin \hat{\phi}_l}{\sqrt{\alpha + \beta^2 \cos^2 \hat{\phi}_l}}. \tag{3.53}$$

Since we do not have an analytical result, we use numerical interpolation for  $I_2(\lambda, M)$  in our parton-shower code.

The form of the collinear cutoff is of course not unique. A simpler form of the virtual integral is obtained by imposing the cutoff in the COM frame by putting a cut on  $\hat{y}$ . The angular integration then reads

$$\tilde{I}(\lambda, M) = \int_0^{2\pi} \frac{d\hat{\phi}_l}{2\pi} \int_{-\tilde{y}_{\max}}^{\tilde{y}_{\max}} d\hat{y}_l, \tag{3.54}$$

with  $\tilde{y}_{\max} = y_{\max}(0) = \ln(\beta + \sqrt{\alpha + \beta^2})$ , so that  $\tilde{I}(\lambda, M) = 2\tilde{y}_{\max}$ . This regularization scheme was used by Dasgupta and Salam [26]. We will compare MC results based on the two cutoff schemes (3.45) and (3.54) in Appendix 3.B.

## 3.B DETAILS OF THE MC ALGORITHM

In this appendix we will describe the MC algorithm in detail, working with the interjet energy flow in  $e^+e^-$  for concreteness. For this observable, the lowest multiplicity hard function has two energetic partons along back-to-back directions  $n_1$  and  $n_2$ . We can thus set  $k = 2$  in the equations in Section 3.3. For more complicated observables, such as hadron collider dijet events, we start with  $k > 2$  partons, whose directions are read from an event file produced by the MADGRAPH tree-level generator. The tree-level generator also assigns large- $N_c$  dipole color structure to each event, which we use as the starting point of our shower.

We will first spell out the algorithm and then show how it arises from the iterative solution of the RG-evolution equation of the hard functions in (3.20). The basic ingredient of the MC algorithm is a list of events. Each event  $E$  occurs at a time  $t$ , has a weight  $w$  and contains a list of  $m$  vectors  $\{n_1, n_{i_1}, \dots, n_{i_{m-2}}, n_2\}$ . This list defines the color dipoles of the events, which are given by neighbouring pairs of vectors so that the associated virtual correction is

$$V_E = V_{1i_1} + V_{i_1i_2} + \dots + V_{i_{m-2}2}, \quad (3.55)$$

with

$$V_{ij} = \int \frac{d\Omega(n_l)}{4\pi} R_{ij}^l. \quad (3.56)$$

The integrand is the real-emission matrix element

$$R_{ij}^l = 4 N_c W_{ij}^l \theta(n_l \cdot n_i - \lambda^2) \theta(n_l \cdot n_j - \lambda^2). \quad (3.57)$$

The angular integration in the presence of a collinear cutoff  $\lambda$  was discussed in detail in Appendix 3.A. Note that the quantity  $V_{ij}$  defined here is positive, while  $V_m$  in (3.23) is negative.

The MC algorithm described in the following produces a histogram of  $V_{12} \sigma_{\text{veto}}(\Omega_0, t) / \sigma_0$ . To get the gap fraction that one has to divide the result by  $V_{12}$ , the virtual correction associated with the original dipole. The algorithm involves the following steps:

1. Start at shower time  $t = 0$  from an initial event with vectors  $\{n_1, n_2\}$  and weight  $w = 1$ .
2. Generate a random time step  $\Delta t$  according to the probability distribution  $\mathcal{P}_E(t) = V_E \exp(-V_E \Delta t)$ , and insert the event weight  $w$  into the histogram at time  $t + \Delta t$ .
3. Choose a dipole associated with a pair of neighbouring vectors  $n_i$  and  $n_j$  in  $E$  with probability  $V_{ij} / V_E$ . Generate a new random vector  $n_k$  and multiply the weight by the factor  $R_{ij}^k / V_{ij}$ , expressed in the random variables chosen to generate the direction of the new vector  $n_k$ , see (3.58) below.
4. If  $n_k$  is inside the veto region, go to Step 1 and start a new event, otherwise add this new vector into  $E' = \{n_1, \dots, n_i, n_k, n_j, \dots, n_2\}$ , multiply the weight by a factor  $V_E / V_{E'}$  and return to Step (2).

To keep the weights  $w$  close to one, one works in the COM variables  $\hat{y}_k$  and  $\hat{\phi}_k$  introduced in Appendix 3.A to generate the direction of the new parton. In the dipole COM frame the integrand becomes trivial in these variables, see (3.49). However, with a lab-frame cut,

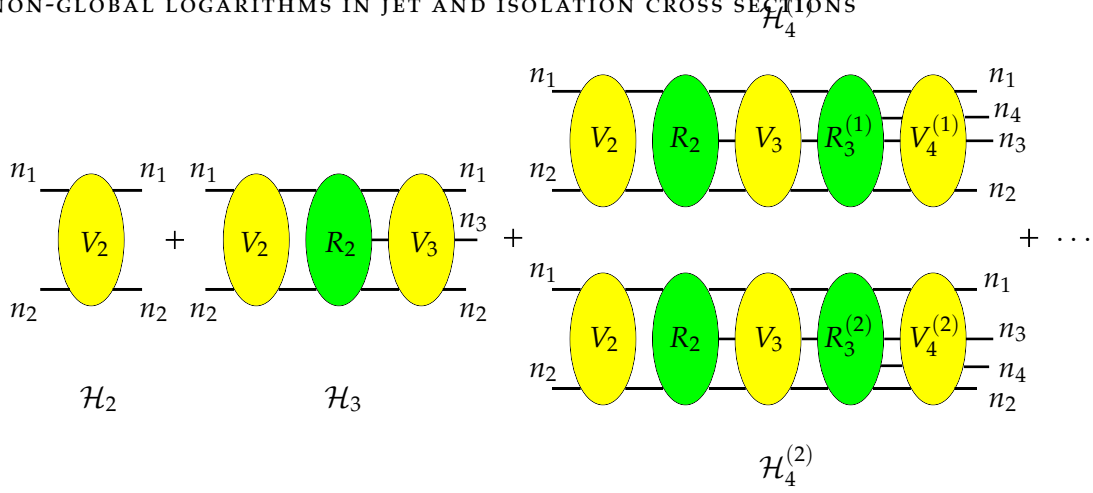


FIGURE 3.11: Diagrammatic representation of the lowest hard functions contributing to (3.59).

the integration boundary  $y_{\max}(\hat{\phi}_k)$  in the rapidity integration depends on  $\hat{\phi}_k$ . Mapping the boundary to a square introduces a weight factor

$$w = \frac{2y_{\max}(\hat{\phi}_k) \phi_{\max}}{V_{ij}/(4N_c)}. \quad (3.58)$$

If one follows Dasgupta and Salam [26] and introduces the collinear cutoff in the COM frame, the integration region is rectangular and  $w = 1$ . A second advantage of this cutoff is that the weight factor in Step 4 is always smaller than one,  $V_E/V_{E'} < 1$ . One can thus implement this factor by throwing away the event in Step 4 with probability  $V_E/V_{E'}$ . Once this is done, one has unweighted events. In contrast, with a lab-cone cutoff a small fraction of events has  $V_E/V_{E'} > 1$ .

To derive the above MC algorithm, we rewrite RG evolution solution (3.20) in a form which makes the four steps of the algorithm manifest. According to (3.21), after evolving the hard functions to the soft scale  $Q_0$ , the veto cross section takes the form

$$\hat{\sigma}_{\text{veto}}(\Omega_0, t) = \frac{V_{12}}{\sigma_0} \sigma_{\text{veto}}(\Omega_0, t) = \hat{\mathcal{H}}_2(t) + \int \frac{d\Omega_3}{4\pi} \hat{\mathcal{H}}_3(t, n_3) + \int \frac{d\Omega_3}{4\pi} \frac{d\Omega_4}{4\pi} \hat{\mathcal{H}}_4(t, n_3, n_4) + \dots, \quad (3.59)$$

where the hat indicates the factor  $V_{12}/\sigma_0$  by which we have multiplied the cross section and the hard functions  $\mathcal{H}_m$  in order to work with the same normalization as the MC simulation. In Figure 3.11 we show their diagrammatic representations. The first term  $\hat{\mathcal{H}}_2$  represents no emission down to the veto scale  $Q_0$ , corresponding to shower-time evolution from 0 to  $t$ . This purely virtual contribution takes the form

$$\hat{\mathcal{H}}_2(t) = \mathcal{P}_2(t) = V_{12} e^{-t V_{12}}. \quad (3.60)$$

As shown in Figure 3.11, the second term  $\hat{\mathcal{H}}_3$  corresponds to a situation, where no emission occurs until the shower evolves to  $t'$ , at which time a new parton is emitted along the direction  $n_3$ , after which the system evolves without further emissions to  $t$ . This yields the expression

$$\hat{\mathcal{H}}_3(t) = \int_0^t dt' \hat{\mathcal{H}}_2(t') R_{12}^3 e^{-(t-t')V_3}, \quad (3.61)$$

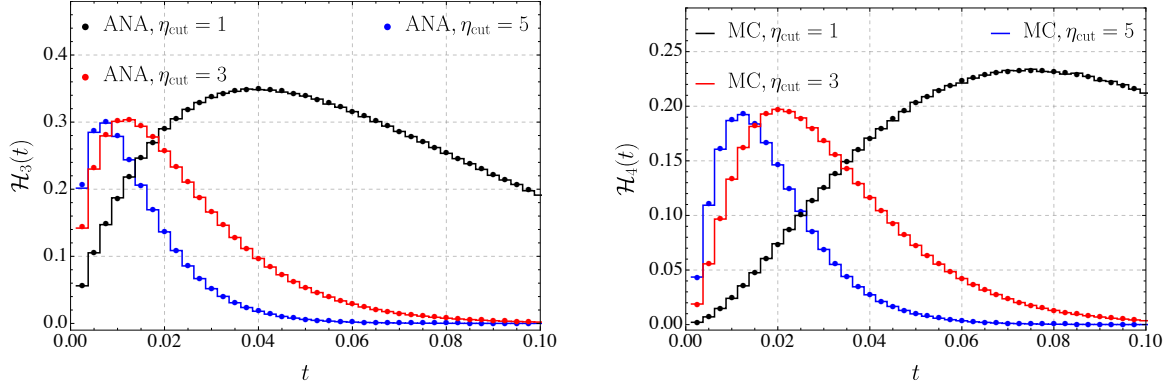


FIGURE 3.12: Numerical comparison between MC simulations and analytical calculations. The histograms represent MC simulations with different collinear cutoffs  $\eta_{\text{cut}} = 1$  (black), 3 (red) and 5 (blue). The dots are from numerically integrating their analytical expressions.

where the new virtual part is  $V_3 = V_{13} + V_{32}$ . We now rewrite (3.61) in terms of factors which can be viewed as probabilities

$$\hat{\mathcal{H}}_3(t) = \int_0^t dt' \mathcal{P}_2(\Delta t) \frac{R_{12}^3}{V_2} \frac{V_2}{V_3} \mathcal{P}_3(\Delta t'), \quad (3.62)$$

with  $\Delta t = t'$  and  $\Delta t' = t - t'$ . To get an emission probability, we normalized the angular integral to  $V_2$ . Introducing the probability  $\mathcal{P}_3$  for the second time step, we are then left with a factor  $\frac{V_2}{V_3}$  which arises as a weight in Step 4 of the algorithm.

Starting from  $\hat{\mathcal{H}}_4$ , each hard function is a sum of several terms, which correspond to the different dipoles which can emit. Specifically, for  $\hat{\mathcal{H}}_4$  we have

$$\hat{\mathcal{H}}_4(t) = \hat{\mathcal{H}}_4^{(1)}(t) + \hat{\mathcal{H}}_4^{(2)}(t), \quad (3.63)$$

where  $\hat{\mathcal{H}}_4^{(1)}$  corresponds to inserting a new parton into the dipole formed by  $n_1$  and  $n_3$  and has the form

$$\hat{\mathcal{H}}_4^{(1)}(t) = R_{13}^4 \int_0^t dt'' \hat{\mathcal{H}}_3(t'') e^{-(t-t'')V_4^{(1)}}, \quad (3.64)$$

with  $V_4^{(1)} = V_{14} + V_{43} + V_{32}$ . The second term  $\hat{\mathcal{H}}_4^{(2)}$  arises from inserting a new parton between  $n_3$  and  $n_2$ . We rewrite (3.63) in the same form as (3.62) and get

$$\hat{\mathcal{H}}_4(t) = \int_0^t dt'' \hat{\mathcal{H}}_3(t'') \left[ \frac{R_{13}^4}{V_{13}} \frac{V_{13}}{V_3} \frac{V_3}{V_4^{(1)}} \mathcal{P}_4^{(1)}(\Delta t'') + \frac{R_{32}^4}{V_{32}} \frac{V_{32}}{V_3} \frac{V_3}{V_4^{(2)}} \mathcal{P}_4^{(2)}(\Delta t'') \right], \quad (3.65)$$

where  $\Delta t'' = t - t''$ . Compared to (3.62) we encounter additional factors  $V_{13}/V_3$  and  $V_{32}/V_3$ , which represent the probability of choosing one of the two dipoles. These factors are implemented in Step (3) of the MC algorithm. No additional complications arise at higher multiplicities.

In order to check our MC simulation step by step, we can calculate  $\mathcal{H}_m$  directly from its definition, and then compare with simulation results. We show the results for  $\mathcal{H}_3$  and  $\mathcal{H}_4$  in Figure 3.12. The histograms represent the simulation results while the dots are calculated

directly. For simplicity we set the veto region to zero which means that we do not veto any radiation. We write the collinear cutoff in the form  $\lambda^2 = 1 - \tanh \eta_{\text{cut}}$  and choose different values of  $\eta_{\text{cut}}$ . We observe excellent agreement between the numerical integration and the simulation results. As a second consistency check we have verified the unitarity of the shower, i.e. we ran the full shower with the veto region to zero and checked  $\sigma_{\text{veto}}(t) = \sigma_0$  within the numerical accuracy.

We will also compare our simulation algorithm to the one used by Dasgupta and Salam [26]. As mentioned in Appendix 3.A, they impose the collinear cutoff in the COM rather than the lab frame. Furthermore, instead of computing the cross section directly, they formulate a shower for the derivative  $d\sigma_{\text{veto}}/dt$ . This form can be derived from the differential form (3.17) of the RG equation. Specifically, we have

$$\begin{aligned}
-\frac{1}{\sigma_0} \frac{d}{dt} \sigma_{\text{veto}} = & \int_{\Omega} \mathbf{3}_{\text{out}} \left[ V_2 e^{-tV_2} \right] \frac{R_{12}^3}{V_2} \\
& + \int_{\Omega} \mathbf{4}_{\text{out}} \mathbf{3}_{\text{in}} \int_0^t dt' \left[ V_2 e^{-t'V_2} \right] \frac{R_{12}^3}{V_2} \left[ V_3 e^{-(t-t')V_3} \right] \frac{R_{132}^4}{V_3} \\
& + \int_{\Omega} \mathbf{5}_{\text{out}} \mathbf{4}_{\text{in}} \mathbf{3}_{\text{in}} \int_0^t dt' \int_0^{t'} dt'' \left[ V_2 e^{-t''V_2} \right] \frac{R_{12}^3}{V_2} \left[ V_3 e^{-(t'-t'')V_3} \right] \frac{R_{13}^4}{V_{13}} \\
& \times \left\{ \frac{V_{13}}{V_3} \left[ V_4^{(1)} e^{-(t-t')V_4^{(1)}} \right] \frac{R_{1432}^5}{V_4^{(1)}} + \frac{V_{32}}{V_3} \left[ V_4^{(2)} e^{-(t-t')V_4^{(2)}} \right] \frac{R_{1342}^5}{V_4^{(2)}} \right\} \\
& + \dots,
\end{aligned} \tag{3.66}$$

with  $\int_{\Omega} l_{\text{out}} = \int \frac{d\Omega(n_l)}{4\pi} \Theta_{\text{out}}(n_l)$  and the abbreviation  $R_{1i_1i_2\dots i_m2}^l = R_{1i_1}^l + R_{i_1i_2}^l + \dots + R_{i_m2}^l$ . Equation (3.66) immediately translates into a shower algorithm. One starts with the original dipole at  $t = 0$  as before. Then, for any event  $E$  one generates a time-step according to  $\mathcal{P}_E$ , selects a dipole of the event with probability  $\frac{V_{ij}}{V_E}$ , and inserts a new vector into the dipole, splitting it into two. This is repeated until the new vector lies outside the jets (inside the veto region) at which point the shower is terminated and the value of  $t$  is inserted into the histogram. This is the shower used in [26].

A numerical comparison of the different shower formulations and cutoff schemes is shown in Figure 3.13. Scheme  $S(t)$  represents the algorithm we explain at the beginning of this appendix, and  $S'(t)$  is the dipole shower of [26] corresponding to the MC simulation of (3.66). For each algorithm, we show the two different ways to regularize the collinear divergence discussed in Appendix 3.A. The curves labelled LAB apply the cutoff (3.45) in the lab frame, the ones labelled COM impose a rapidity cut in the center-of-mass frame of the emitting dipole. The two COM curves are nearly indistinguishable, while the curves in LAB cutoff scheme display small deviations beyond  $t \gtrsim 0.1$ . Comparing the different MC runs, we observe significant noise using the LAB cutoff at larger  $t$ . While the individual weights are close to one, larger-time entries involve many steps and we end up with some events with large weight which make the simulations noisy; conversely there are also many events with low weight which makes them inefficient. While any of the algorithms work well in the phenomenologically relevant region  $t < 0.1$ , the COM scheme is clearly performing better at large  $t$  and the algorithm simulating  $S'(t)$  is especially well suited to get results at large  $t$ . A disadvantage of the  $S'(t)$  scheme is that one needs to run it without any cutoff on  $t$  in order to be able to reconstruct the function from the derivative. In contrast, one can restrict  $t$  to the phenomenologically relevant region determined by the minimum value of  $Q_0$  when directly generating the cross section. Also, when working with the cross section

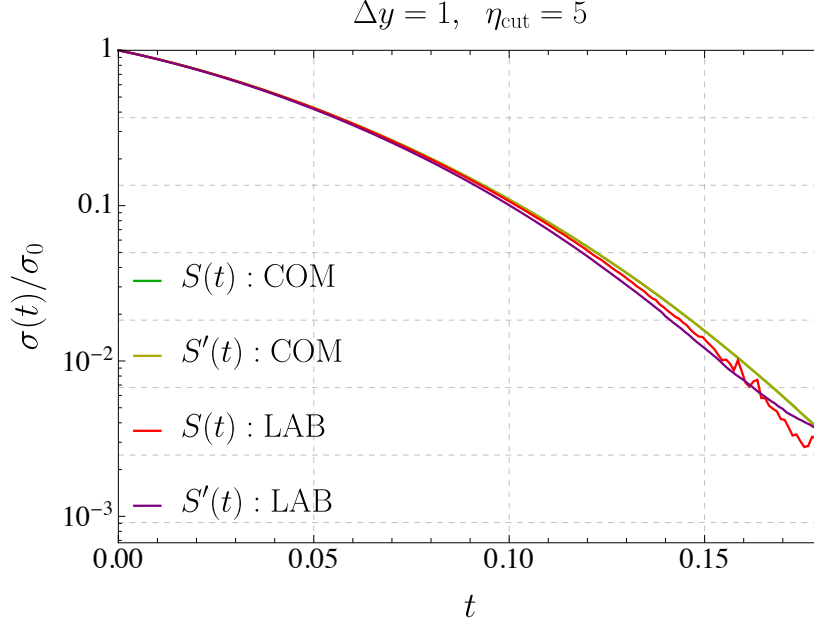


FIGURE 3.13: Numerical comparison between different simulation algorithms and collinear regularization methods (lab-cone versus center-of-mass cone). The curves labelled  $S(t)$  are obtained from simulating the cross section, the ones labelled  $S'(t)$  are obtained after simulating the derivative and integrating. The two COM curves are completely overlapping.

instead of the derivative, one can use the algorithm as an exclusive event generator and only impose the veto constraints at the end, after event generation.

### 3.C NLO EXPANSION FOR ISOLATED PHOTON PRODUCTION

In this appendix we give analytical expressions for the lowest-order hard function and the NLO soft logarithm for isolated photon production at  $e^+e^-$  colliders.

If we expand to NLO, the factorization formula (3.33) truncates at  $m = 3$  since the hard functions scale as  $\mathcal{H}_{\gamma+n} \sim \alpha_s^{n-2}$ . Expanding the ingredients in  $\alpha_s$  and using that the lowest-order soft functions are trivial  $\mathcal{S}_m = 1 + \mathcal{O}(\alpha_s)$ , the cross section reads

$$\frac{d\sigma}{dx_\gamma} = \langle \mathcal{H}_{\gamma+2}^{(0)} \otimes \mathbf{1} \rangle + \frac{\alpha_s}{4\pi} \left[ \langle \mathcal{H}_{\gamma+2}^{(0)} \otimes \mathcal{S}_2^{(1)} \rangle + \langle \mathcal{H}_{\gamma+2}^{(1)} \otimes \mathbf{1} \rangle + \langle \mathcal{H}_{\gamma+3}^{(1)} \otimes \mathbf{1} \rangle \right], \quad (3.67)$$

where the superscripts of  $\mathcal{H}_{\gamma+m}^{(n)}$  and  $\mathcal{S}_m^{(n)}$  indicate the order in  $\alpha_s$ .

The hard function  $\mathcal{H}_{\gamma+2}^{(0)}$  describes the final state with one quark, one antiquark (with momenta  $p_1$  and  $p_2$ ) and one isolated photon (with momentum  $p_\gamma$ ) in the final state. Using momentum conservation and introducing the variable  $y_1 = (p_1 + p_\gamma)^2 / (x_\gamma Q^2)$ , we can write the LO hard function as

$$\mathcal{H}_{\gamma+2}^{(0)}(y_1, Q, x_\gamma, \delta_0, \epsilon) = \sigma_0 \frac{\alpha Q_q^2}{2\pi} \frac{e^{\gamma_E \epsilon}}{\Gamma(1-\epsilon)} \left( \frac{\mu}{Q} \right)^{2\epsilon} \bar{x}_\gamma^{-\epsilon} x_\gamma^{-1-2\epsilon} \times (y_1 \bar{y}_1)^{-1-\epsilon} [2\bar{x}_\gamma + x_\gamma^2 (y_1^2 + \bar{y}_1^2 - \epsilon)], \quad (3.68)$$

with  $\bar{x}_\gamma = 1 - x_\gamma$ ,  $\bar{y}_1 = 1 - y_1$ ,  $Q_q$  is the charge of the quark flavour emitting the photon and  $\sigma_0$  the associated Born cross section. Here we eliminated the bare fine-structure constant



using  $\alpha^0 = \tilde{\mu}^{2\epsilon} \alpha = [e^{\gamma_E} \mu^2 / (4\pi)]^\epsilon \alpha$ . The Born cross section for the decay  $\gamma^* \rightarrow q\bar{q}$  is given by

$$\sigma_0 = N_c \alpha Q_q^2 Q \frac{e^{\gamma_E \epsilon} \Gamma(2 - \epsilon)}{\Gamma(2 - 2\epsilon)} \left( \frac{\mu}{Q} \right)^{2\epsilon}. \quad (3.69)$$

The dependence on  $y_1$  is the leftover angular integration after taking momentum conservation into account and enters the convolution with the soft function. The angular constraint, which enforces that the hard partons are outside the isolation cone, translates to an integration boundary in terms of  $y_c = \frac{(1 - \cos \delta_0)(1 - x_\gamma)}{2 - (1 - \cos \delta_0)x_\gamma}$  as follows:

$$\begin{aligned} \mathcal{H}_{\gamma+2}^{(0)}(\{n_1, n_2\}, Q, E_\gamma, \delta_0) \otimes \mathcal{S}_2(\{n_1, n_2\}, \epsilon_\gamma E_\gamma, \delta_0) \\ = \int_{y_c}^{1-y_c} dy_1 \mathcal{H}_{\gamma+2}^{(0)}(y_1, Q, x_\gamma, \delta_0) \mathcal{S}_2(y_1, x_\gamma, \epsilon_\gamma, \delta_0). \end{aligned} \quad (3.70)$$

As the soft function is trivial at LO (first term on the right hand side of (3.67)), we can immediately perform the integration over  $y_1$ , take the trace in color space and obtain the differential LO cross section as

$$\begin{aligned} \frac{d\sigma^{(0)}}{dx_\gamma} &= \int_{y_c}^{1-y_c} dy_1 \langle \mathcal{H}_{\gamma+2}^{(0)} \rangle \\ &= \sigma_0 \frac{\alpha Q_q^2}{\pi} \left[ \frac{2 - 2x_\gamma + x_\gamma^2}{x_\gamma} \ln \left( \frac{1 - y_c}{y_c} \right) - (1 - 2y_c) x_\gamma \right], \end{aligned} \quad (3.71)$$

in agreement with the result in [97].

The second term  $\langle \mathcal{H}_{\gamma+2}^{(0)} \otimes \mathcal{S}_2^{(1)} \rangle$  in (3.67) can be obtained by evaluating the soft function  $\mathcal{S}_2^{(1)}$  for one soft gluon inside the cone radiated off one of the Wilson lines along  $\{n_1, n_2\}$ , whose direction is parameterized by the variable  $y_1$ . The soft function reads

$$\mathcal{S}_2^{(1)} = -8 C_F \frac{1}{\epsilon} \left( \frac{\mu}{\epsilon_\gamma E_\gamma} \right)^{2\epsilon} I(\epsilon) \mathbf{1}, \quad (3.72)$$

with the angular integral

$$I(\epsilon) = \int \frac{d\Omega_k}{4\pi} \frac{n_i \cdot n_j}{n_i \cdot n_k n_k \cdot n_j} \theta(1 - \cos \delta_0 - n_k \cdot n_\gamma). \quad (3.73)$$

To extract the divergent part of the soft function, it is sufficient to evaluate the angular integral for  $d = 4$ , where it can be rewritten in the form

$$I(0) = \int_{x_{\min}}^{x_{\max}} dx \left[ 1 + \frac{2}{\pi} \arcsin \left( \frac{(1 - 2y_1) \sinh x - \xi \cosh x}{2\sqrt{y_1 y_1 (1 - \xi^2)}} \right) \right], \quad (3.74)$$

after boosting to the center-of-mass frame of the emitting dipole. We have introduced the abbreviation

$$\xi = \frac{(2 - x_\gamma) \cos \delta_0 + x_\gamma}{2 - (1 - \cos \delta_0)x_\gamma}, \quad (3.75)$$

and the integration boundaries which restrict the gluon to the inside of the isolation cone have the form

$$x_{\min} = \frac{1}{2} \ln \left[ \frac{1 + (1 - 2y_1)\xi - 2\sqrt{y_1 y_1 (1 - \xi^2)}}{1 - (1 - 2y_1)\xi + 2\sqrt{y_1 y_1 (1 - \xi^2)}} \right], \quad (3.76)$$

$$x_{\max} = \frac{1}{2} \ln \left[ \frac{1 + (1 - 2y_1)\xi + 2\sqrt{y_1 y_1 (1 - \xi^2)}}{1 - (1 - 2y_1)\xi - 2\sqrt{y_1 y_1 (1 - \xi^2)}} \right]. \quad (3.77)$$

The one-loop corrections of  $\mathcal{H}_{\gamma+2}^{(1)}$  and  $\mathcal{H}_{\gamma+3}^{(1)}$  could be extracted in numerical form using the results of [97]. However, we are only interested in the logarithmic piece, so that the divergent part of the combination is sufficient. Since the cross section is finite, the divergence must be equal and opposite to the one in  $\langle \mathcal{H}_{\gamma+2}^{(0)} \otimes \mathcal{S}_2^{(1)} \rangle$ . Explicitly, we must find that it takes the form

$$\langle \mathcal{H}_{\gamma+2}^{(1)} \otimes \mathbf{1} \rangle + \langle \mathcal{H}_{\gamma+3}^{(1)} \otimes \mathbf{1} \rangle = 8 C_F \frac{1}{\epsilon} \left( \frac{\mu}{E_\gamma} \right)^{2\epsilon} \int_{y_c}^{1-y_c} dy_1 \langle \mathcal{H}_{\gamma+2}^{(0)} \rangle I(0). \quad (3.78)$$

Adding the one-loop ingredients, we then obtain the NLO logarithmic terms as

$$\frac{d\sigma^{(1)}}{dx_\gamma} = 16 C_F \ln(\epsilon_\gamma) \int_{y_c}^{1-y_c} dy_1 \langle \mathcal{H}_{\gamma+2}^{(0)} \rangle I(0). \quad (3.79)$$

### 3.D NARROW-CONE LIMIT OF PHOTON ISOLATION

To verify the factorization theorem for narrow isolation cones (3.42), we apply the method of regions to the integral which arises in the computation of the differential cross section at leading order (3.71). To apply the method, we write (3.71) in the form

$$\frac{d\sigma^{(0)}}{dx_\gamma} = \sigma_0 \frac{\alpha Q_q^2}{2\pi} \frac{e^{\gamma_E \epsilon}}{\Gamma(1-\epsilon)} \left( \frac{\mu}{Q} \right)^{2\epsilon} \bar{x}_\gamma^{-\epsilon} x_\gamma^{-1-2\epsilon} \mathcal{I} \quad (3.80)$$

with the dimensionally regularized angular integral

$$\mathcal{I} = \int dy_1 (y_1 \bar{y}_1)^{-1-\epsilon} [2 \bar{x}_\gamma + x_\gamma^2 (y_1^2 + \bar{y}_1^2 - \epsilon)] \theta(1 - y_c - y_1) \theta(y_1 - y_c). \quad (3.81)$$

For a narrow cone we have  $y_c \approx \delta_0^2 \bar{x}_\gamma / 4 \ll 1$ . The expansion of the integral  $\mathcal{I}$  gets contributions from three regions of the integration variable  $y_1$ : the hard region  $h$ , where  $y_1$  is large  $y_c \ll y_1 \approx 1$ ; the region  $c$ , where the photon is emitted collinear to the quark ( $y_c \approx y_1 \ll 1$ ); and finally the region  $\bar{c}$ , where the photon is emitted collinear to the antiquark ( $y_c \approx \bar{y}_1 = 1 - y_1 \ll 1$ ). By expanding the integrand in each region to leading power and evaluating the resulting integrals, we get

$$\mathcal{I}_h = \int_0^1 dy_1 (y_1 \bar{y}_1)^{-1-\epsilon} [2 \bar{x}_\gamma + x_\gamma^2 (y_1^2 + \bar{y}_1^2 - \epsilon)] = -\frac{2(2 \bar{x}_\gamma + x_\gamma^2)}{\epsilon} + \mathcal{O}(\epsilon) \quad (3.82)$$

for the hard region, and for the collinear regions we have

$$\mathcal{I}_c = \mathcal{I}_{\bar{c}} = \int_{y_c}^\infty dy_1 y_1^{-1-\epsilon} [2 \bar{x}_\gamma + x_\gamma^2 (1 - \epsilon)] = \frac{y_c^{-\epsilon}}{\epsilon} [2 \bar{x}_\gamma + x_\gamma^2 (1 - \epsilon)], \quad (3.83)$$

because  $\mathcal{I}$  is symmetric under  $y_1 \leftrightarrow \bar{y}_1$ . Adding up the different contributions, we obtain

$$\begin{aligned} \frac{d\sigma^{(0)}}{dx_\gamma} &= \sigma_0 \frac{e^{\gamma_E \epsilon}}{\Gamma(1-\epsilon)} \frac{\alpha Q_q^2}{2\pi} \left( \frac{\mu}{Q} \right)^{2\epsilon} \bar{x}_\gamma^{-\epsilon} x_\gamma^{-1-2\epsilon} (\mathcal{I}_h + \mathcal{I}_c + \mathcal{I}_{\bar{c}}) \\ &= \sigma_0 \frac{\alpha Q_q^2}{\pi} \left\{ P_{\gamma \leftarrow q}(x_\gamma) \left[ -\frac{1}{\epsilon} + \ln(\bar{x}_\gamma x_\gamma^2) - \ln \frac{\mu^2}{Q^2} \right] + \right. \\ &\quad \left. P_{\gamma \leftarrow \bar{q}}(x_\gamma) \left[ +\frac{1}{\epsilon} - \ln(\bar{x}_\gamma x_\gamma^2) + \ln \frac{\mu^2}{y_c Q^2} \right] - x_\gamma \right\} + \mathcal{O}(\epsilon), \end{aligned} \quad (3.84)$$

where we show the hard and the collinear contributions separately in the second and third line. The divergences of the individual terms in (3.84) are proportional to the splitting function

$$P_{\gamma \leftarrow q}(z) = \frac{1 + (1 - z)^2}{z}, \quad (3.85)$$

confirming our earlier statement that the two parts renormalize in the same way as the fragmentation function. Adding up the two pieces one ends up with the final result

$$\frac{d\sigma^{(0)}}{dx_\gamma} = \sigma_0 \frac{\alpha Q_q^2}{\pi} \left[ P_{\gamma \leftarrow q}(x_\gamma) \ln \left( \frac{1}{y_c} \right) - x_\gamma \right]. \quad (3.86)$$

This agrees with the expansion of the full result (3.71) to leading power in  $y_c$ , verifying our region expansion.

The contributions of the different momentum regions to (3.84) are in one-to-one correspondence to terms in the factorization theorem, which at leading order reduces to

$$\frac{d\sigma^{(0)}}{dx_\gamma} = \frac{d\sigma_{\gamma+q+\bar{q}}^{\text{incl.}}}{dx_\gamma} + 2\sigma_0 \langle \mathcal{J}_{q \rightarrow \gamma+q}(\{\underline{n}\}, \delta_0 E_\gamma, x_\gamma) \otimes \mathbf{1} \rangle, \quad (3.87)$$

where the factor of two in front of the second term accounts for the identical contribution from the anti-quark. The hard region is the first term in (3.87) and corresponds the cross section without isolation on the photon. The collinear region in the second line of (3.84) corresponds to the second term in (3.87) which describes the production of a  $q\bar{q}$  pair, followed by fragmentation of the quark. We thus confirm the factorization theorem (3.42) at LO.

*Und zwar isch s wichtig, dass du folgendes o weisch;  
 S gnüegt nid, dass Du ds Brot eifach underleisch em Fleisch;  
 S'bruucht eis Brot undefür, versteisch;  
 Und eis wo d obe drüber leisch;  
 Nume wenn d so drahäre geisch;  
 Berchunnsch es Sändwitsch - eis mit Fleisch.*

— Mani Matter

This chapter is a copy of [19], published in the Journal of High-Energy Physics (JHEP) on April 2, 2019.

#### ABSTRACT

Starting from a factorization theorem in effective field theory, we present resummed results for two non-global observables: the invariant-mass distribution of jets and the energy distribution outside jets. Our results include the full next-to-leading-order corrections to the hard, jet and soft functions and are implemented in a parton-shower framework which generates the renormalization-group running in the effective theory. The inclusion of these matching corrections leads to an improved description of the data and reduced theoretical uncertainties. They will have to be combined with two-loop running in the future, but our results are an important first step towards the higher-logarithmic resummation of non-global observables.

#### 4.1 INTRODUCTION

Up to now, higher-logarithmic resummations of collider observables have only been performed for the narrow class of *global* observables which constrain radiation uniformly over the entire phase space. This category includes very inclusive observables such as selected event shapes, but it excludes all observables with hard phase-space cuts or a fixed number of jets. In recent years, a lot of progress was made in the theoretical analysis of non-global observables [18, 24, 25, 58, 62, 95, 96, 98–106]. This includes work on the structure of higher logarithms as well as studies of leading logarithms beyond the large- $N_c$  limit.

In this paper we start the computation of higher-logarithmic terms for non-global observables by analyzing two simple observables, the jet mass and the interjet energy flow, and presenting resummed predictions which include the full one-loop corrections to the relevant hard scattering processes, as well as the associated jet and soft functions. In the effective-theory framework we use for resummation [24, 25], these correspond to matching corrections and they will need to be supplemented by corrections to the renormalization-group (RG) running in the future to arrive at a complete higher-logarithmic treatment of the non-global part.

Our main goal in the present work is to develop the Monte Carlo methods to include these corrections as a step towards full higher-logarithmic resummation, but it is also interesting to

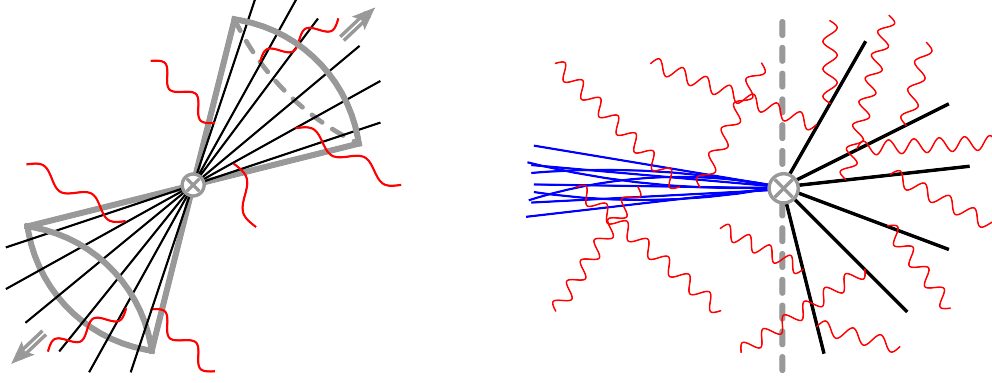


FIGURE 4.1: Pictorial representations of factorization formulas for interjet energy flow (left) and jet mass (right), see (4.1) and (4.4). The black lines represent hard radiation with typical scale  $Q$  which is constrained to be inside the cones, and the red lines depict soft radiation with a low energy scale  $Q_0$  which is allowed to populate the full phase space. In the right figure, the blue lines in the left hemisphere represent collinear radiation which is described by the inclusive jet function in (4.4).

study their numerical size, since they have never been computed for non-global observables and often dominate numerically in the global case. It is customary to add a prime to the logarithmic accuracy to indicate the presence of higher-order matching corrections. In this notation our next-to-leading-logarithmic results for the jet mass have NLL' accuracy.

In Refs. [24, 104] we have derived a factorization formula for interjet energy flow and light-jet mass. The key element is the presence of multi-Wilson-line operators which generate the intricate pattern of Non-Global Logarithms (NGLs). Explicitly, the result for interjet energy flow at a lepton collider has the form

$$\sigma(Q, Q_0) = \sum_{m=2}^{\infty} \langle \mathcal{H}_m(\{\underline{n}\}, Q, \mu) \otimes \mathcal{S}_m(\{\underline{n}\}, Q_0, \mu) \rangle, \quad (4.1)$$

where  $Q$  is the center-of-mass energy, and  $Q_0 = \beta Q$  is the energy scale above which we veto energy in the gap outside the jet cones. For simplicity, we choose the jet axis along the thrust axis. The above factorization formula neglects power corrections from  $\mathcal{O}(\beta)$  terms. The hard functions  $\mathcal{H}_m$  describe hard radiation inside the jet cone, and their characteristic scale is  $Q$  since radiation inside the cones is unrestricted. The index  $m$  represents the number of hard partons inside the jet, which propagate along the directions  $\{\underline{n}\} = \{n_1, n_2, \dots, n_m\}$ . Each of these sources soft radiation, which we describe by a Wilson line along the direction of the hard parton. The matrix elements of these Wilson lines define the soft functions  $\mathcal{S}_m(\{\underline{n}\}, Q_0, \mu)$ . To obtain the cross section, one integrates over the directions  $\{\underline{n}\}$ , which is indicated by the symbol  $\otimes$ . The hard and soft functions are matrices in the color space of the  $m$  partons and one takes the color trace  $\langle \dots \rangle$  after multiplying them. The operator definition for these functions and further explanations can be found in [24].

The second observable we consider is the jet mass distribution at a lepton collider. To define the jet mass, we use the thrust axis to split every event into two hemispheres. One can then (randomly) select one of the two jets and compute its invariant mass  $M$ , which is usually discussed in terms of the dimensionless variable  $\rho = M^2/Q^2$ . Alternatively, one computes the mass in both hemispheres and chooses the heavier mass  $\rho_h$  or lighter one

$\rho_\ell$ . Obviously, there is a relation among these observables: the jet mass distribution is simply the average of heavy-jet mass and light-jet mass one

$$\frac{d\sigma}{d\rho} = \frac{1}{2} \left( \frac{d\sigma}{d\rho_\ell} + \frac{d\sigma}{d\rho_h} \right). \quad (4.2)$$

We will call the hemisphere we select to measure the mass the *left* one, which means that the radiation in the *right* hemisphere is unconstrained.<sup>1</sup> We introduce a light-like reference four-vector  $n^\mu = (1, 0, 0, 1)$  pointing to the right along the thrust axis and an opposite vector  $\bar{n}^\mu = (1, 0, 0, -1)$  pointing to the left. The hard partons in the right hemisphere then generate the complicated pattern of soft radiation and associated NGLs. The main difference to formula (4.1) is that one also needs the standard inclusive jet functions to describe collinear radiation in the left hemisphere. Resummation effects in the jet mass distribution have been discussed in Refs. [107–111], however only in [107] the leading NGLs were resummed. Our work is based on the factorization theorem for jet mass derived in [104]. The invariant mass of the left jet is obtained from the momentum  $p_{\bar{c}}$  of the energetic particles collinear to  $\bar{n}$  and the soft partons in the left hemisphere,

$$\rho Q^2 = M^2 = (p_{\bar{c}} + p_s)^2 = p_{\bar{c}}^2 + Q \bar{n} \cdot p_s + \mathcal{O}(p_s^2). \quad (4.3)$$

In the factorization theorem, the sum results in a convolution of the soft and jet functions. To avoid this, one can work in Laplace space, where the factorization formula has the product form

$$\tilde{\sigma}(\tau) = \sum_{i=q,\bar{q},g} \tilde{j}_i(\tau Q, \mu) \sum_{m=1}^{\infty} \langle \mathcal{H}_m^i(\{\underline{n}\}, Q, \mu) \otimes \tilde{\mathcal{S}}_m(\{\underline{n}\}, \tau, \mu) \rangle, \quad (4.4)$$

where  $\tau$  is the Laplace conjugate variable of  $\rho$ , and  $\tilde{j}_i$  is the inclusive jet function [112, 113], which by now is known to three loops [114, 115]. In (4.4) the index  $m$  indicates the number of partons in the inclusive (right) hemisphere, so that  $m = 1$  at leading order (LO).

As long as we consider large jet cone sizes of  $\mathcal{O}(1)$ , the leading-logarithms (LLs) in interjet energy flow at a lepton collider are of the form  $\alpha_s^n \ln^n \beta$ . The interjet energy flow is a single logarithmic observable, because collinear logarithms cancel inside the large cone region and only soft logarithms remain. These logarithms arise from the multi-Wilson-line operators  $\mathcal{S}_m$  in (4.1) and one needs to use parton shower methods to resum the enhanced logarithms already at the LL level. In [18] we have written a dedicated parton-shower code to perform the resummation for such observables and have interfaced it with the MADGRAPH5\_AMC@NLO event generator [34]. This provides an automated framework to perform the LL resummation for single-logarithmic observables. However, collider observables are typically double logarithmic. The leading logarithms in the jet mass distribution, for example, are  $\alpha_s^n \ln^{2n} \rho$ . Even for non-global observables, these double logarithmic terms have a simple structure, and they can be factored out and treated separately. In the parton shower framework, we therefore subtract these “global” contributions and exponentiate them manually, as Dasgupta and Salam did in their original paper on NGLs [26]. Given their different nature, it is interesting to analyze both the interjet energy flow and the jet mass as examples and we will present LL’ and NLL’ improved results for single logarithmic and double logarithmic observables, separately. A second motivation to also analyze the jet mass, is that there are LEP measurements to which we can compare to, in contrast to the interjet energy flow. Unfortunately, the typical jet mass at LEP jet is quite low  $M \lesssim 10 \text{ GeV}$ , which

<sup>1</sup> In our previous paper, we called  $\rho$  the left-jet mass and denoted it by  $\rho_L$  [104].

translates to a scale of the soft radiation of  $Q_0 \sim M^2/Q \lesssim 1 \text{ GeV}$  so that non-perturbative effects are very important in the peak region of the distribution.

Our paper is organized as follows. In the next section, we will discuss LL' resummation for interjet energy flow and show how one implements the one-loop corrections to the hard and soft functions. We then move to the jet mass distribution in Section 4.3, focussing on the differences to the single-logarithmic case. We will in particular show how to subtract global logarithms in the parton shower and in the soft function. After presenting numerical results in Section 4.4 and comparing to LEP data and PYTHIA results, we conclude in Section 4.5.

#### 4.2 INTERJET ENERGY FLOW AT LL' ACCURACY

The perturbative expansion of the interjet energy flow in (4.1) suffers from large logarithms of the ratio of the hard scale  $Q$  and the soft scale  $Q_0$ . To resum these, one solves the RG equation of the hard function and evolves it from its characteristic scale  $\mu_h \sim Q$  down to a soft scale  $\mu_s \sim Q_0$ . This yields the RG-improved expression [24]

$$\sigma(Q, Q_0) = \sum_{l=2}^{\infty} \langle \mathcal{H}_l(\{\underline{n}'\}, Q, \mu_h) \otimes \sum_{m \geq l}^{\infty} \mathcal{U}_{lm}(\{\underline{n}\}, \mu_s, \mu_h) \hat{\otimes} \mathcal{S}_m(\{\underline{n}\}, Q_0, \mu_s) \rangle, \quad (4.5)$$

where the evolution factor is defined as a path-ordered exponential of the anomalous dimension

$$\mathcal{U}(\{\underline{n}\}, \mu_s, \mu_h) = \mathbf{P} \exp \left[ \int_{\mu_s}^{\mu_h} \frac{d\mu}{\mu} \mathbf{\Gamma}^H(\{\underline{n}\}, \mu) \right]. \quad (4.6)$$

The RG-evolution generates additional partons and maps the  $l$ -parton configuration along the directions  $\{\underline{n}'\} = \{n_1, \dots, n_l\}$  into an  $m$ -parton final state along the directions  $\{\underline{n}\} = \{n_1, \dots, n_l, n_{l+1}, \dots, n_m\}$ . The symbol  $\hat{\otimes}$  in (4.5) indicates the integral over the directions of the additional  $m - l$  partons generated in the evolution.

At the leading logarithmic level, we only need the one-loop anomalous dimension and can rewrite the exponent as

$$\int_{\mu_s}^{\mu_h} \frac{d\mu}{\mu} \mathbf{\Gamma}^H = \int_{\alpha_s(\mu_s)}^{\alpha_s(\mu_h)} \frac{d\alpha}{\beta(\alpha)} \frac{\alpha}{4\pi} \mathbf{\Gamma}^{(1)} = \frac{1}{2\beta_0} \ln \frac{\alpha_s(\mu_s)}{\alpha_s(\mu_h)} \mathbf{\Gamma}^{(1)} \equiv t \mathbf{\Gamma}^{(1)}. \quad (4.7)$$

In the last step, we have introduced the evolution time  $t \equiv t(\mu_h, \mu_s)$ . For a given  $\mu_h$ , there is a one-to-one correspondence of the evolution time to the low scale  $\mu_s$ . Obviously, for  $\mu_h = \mu_s$ , we have  $t = 0$ . During the evolution,  $t$  grows and goes to infinity as  $\mu_s$  hits the Landau pole. For  $\mu_h = M_Z$  and two-loop running with a Landau pole at  $\Lambda = 0.230 \text{ GeV}$ , the choice  $\mu_s = 1 \text{ GeV}$  corresponds to  $t = 0.08$ . A plot connecting  $t$  and  $\mu_s$  for different values of  $\mu_h$  can be found in Figure 1 of our previous paper [18].

In [18] we implemented the RG evolution factor  $\mathcal{U}(\{\underline{n}\}, \mu_s, \mu_h)$  in the large- $N_c$  limit using the parton shower method proposed by Dasgupta and Salam in [26]. We don't want to repeat the entire discussion here, but we give the algorithm in Appendix 4.B, since we need to extend it to compute the soft functions, as discussed below. Let us also list the one-loop



anomalous dimension, since its form will be relevant in the discussion of the jet mass below. It is given by [24]

$$\Gamma^{(1)} = \begin{pmatrix} \mathbf{V}_2 & \mathbf{R}_2 & 0 & 0 & \dots \\ 0 & \mathbf{V}_3 & \mathbf{R}_3 & 0 & \dots \\ 0 & 0 & \mathbf{V}_4 & \mathbf{R}_4 & \dots \\ 0 & 0 & 0 & \mathbf{V}_5 & \dots \\ \vdots & \vdots & \vdots & \vdots & \ddots \end{pmatrix}. \quad (4.8)$$

The entries  $\mathbf{R}_m$  and  $\mathbf{V}_m$  are angular functions associated with the emission of a real or virtual soft gluon and take the form

$$\begin{aligned} \mathbf{V}_m &= 2 \sum_{(ij)} (\mathbf{T}_{i,L} \cdot \mathbf{T}_{j,L} + \mathbf{T}_{i,R} \cdot \mathbf{T}_{j,R}) \int \frac{d\Omega(n_k)}{4\pi} W_{ij}^k, \\ \mathbf{R}_m &= -4 \sum_{(ij)} \mathbf{T}_{i,L} \cdot \mathbf{T}_{j,R} W_{ij}^{m+1} \Theta_{\text{in}}(n_{m+1}), \end{aligned} \quad (4.9)$$

where the color matrices  $\mathbf{T}_{i,L}$  act on the hard function from the left, i.e. on the amplitude, while  $\mathbf{T}_{i,R}$  acts on the conjugate amplitude. The sum runs over all unequal pairs  $(ij)$  of the  $m$  hard partons. The anomalous dimension involves the dipole radiator

$$W_{ij}^k = \frac{n_i \cdot n_j}{(n_i \cdot n_k)(n_j \cdot n_k)}, \quad (4.10)$$

which is given by the product of the associated eikonal factors. In the virtual corrections, one integrates over the direction  $n_k$  of the emission. We note that individually  $\mathbf{R}_m$  and  $\mathbf{V}_m$  suffer from collinear divergences, which cancel in the cross section. In the Monte Carlo implementation, one works with a collinear cutoff to regularize the divergences.

As long as we choose the  $\mu_h$  and  $\mu_s$  properly, the hard and soft functions will be free of large logarithms and the large logarithmic terms are resummed in the evolution factor. Because they are free of large logarithms, the higher-multiplicity hard functions are suppressed by  $\alpha_s$  as  $\mathcal{H}_l \sim \alpha_s^{l-2} \mathcal{H}_2$ . At LL level, we thus only need to include the hard function  $\mathcal{H}_2$  and the soft function is given as the unit matrix in the color space  $\mathcal{S}_m \sim 1$ . At LL accuracy, the RG-improved result (4.5) simplifies to

$$\sigma^{\text{LL}}(Q, Q_0) = \sum_{m=2}^{\infty} \langle \mathcal{H}_2(\{n_1, n_2\}, Q, \mu_h) \otimes U_{2m}(\{\underline{n}\}, \mu_s, \mu_h) \hat{\otimes} \mathbf{1} \rangle. \quad (4.11)$$

To extend these results to NLL, one needs two ingredients: the one-loop matching corrections and the corrections to the RG running due to the two-loop anomalous dimensions. The present paper focuses on the first set of corrections, i.e. LL' accuracy. Specifically, we need one-loop corrections to  $\mathcal{H}_2$ , the tree-level result for  $\mathcal{H}_3$  and the one-loop soft functions  $\mathcal{S}_m$ . We write their perturbative expansions in the form

$$\begin{aligned} \mathcal{H}_2 &= \sigma_0 \left( \mathcal{H}_2^{(0)} + \frac{\alpha_s}{4\pi} \mathcal{H}_2^{(1)} + \dots \right), & \mathcal{H}_3 &= \sigma_0 \left( \frac{\alpha_s}{4\pi} \mathcal{H}_3^{(1)} + \dots \right), \\ \mathcal{S}_m &= 1 + \frac{\alpha_s}{4\pi} \mathcal{S}_m^{(1)} + \dots \end{aligned} \quad (4.12)$$

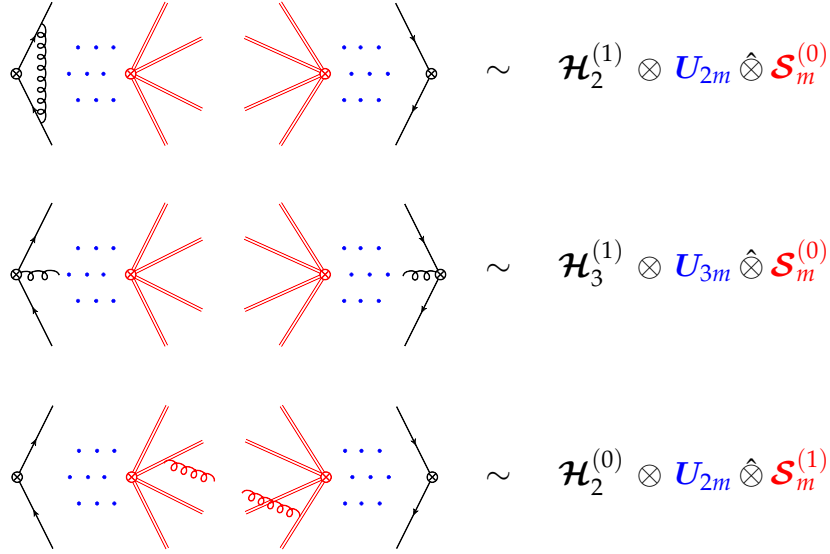


FIGURE 4.2: Pictorial representations of the different ingredients for LL' resummation of the interjet energy flow. The diagrams on the three lines correspond to the one-loop corrections from  $\mathcal{H}_2^{(1)}$ ,  $\mathcal{H}_3^{(1)}$  and  $\mathcal{S}_m^{(1)}$ , respectively. The virtual corrections to  $\mathcal{S}_m$  are scaleless and vanish.

In this notation, the full LL' resummed cross section takes the form

$$\begin{aligned}
\frac{\sigma^{\text{LL}'}(Q, Q_0)}{\sigma_0} &= \sum_{m=2}^{\infty} \langle \mathcal{H}_2^{(0)}(\{n_1, n_2\}, Q, \mu_h) \otimes U_{2m}(\{\underline{n}\}, \mu_s, \mu_h) \hat{\otimes} \mathbf{1} \rangle \\
&+ \frac{\alpha_s(\mu_h)}{4\pi} \sum_{m=2}^{\infty} \langle \mathcal{H}_2^{(1)}(\{n_1, n_2\}, Q, \mu_h) \otimes U_{2m}(\{\underline{n}\}, \mu_s, \mu_h) \hat{\otimes} \mathbf{1} \rangle \\
&+ \frac{\alpha_s(\mu_h)}{4\pi} \sum_{m=3}^{\infty} \langle \mathcal{H}_3^{(1)}(\{n_1, n_2, n_3\}, Q, \mu_h) \otimes U_{3m}(\{\underline{n}\}, \mu_s, \mu_h) \hat{\otimes} \mathbf{1} \rangle \\
&+ \frac{\alpha_s(\mu_s)}{4\pi} \sum_{m=2}^{\infty} \langle \mathcal{H}_2^{(0)}(\{n_1, n_2\}, Q, \mu_h) \otimes U_{2m}(\{\underline{n}\}, \mu_s, \mu_h) \hat{\otimes} \mathcal{S}_m^{(1)}(\{\underline{n}\}, Q_0, \mu_s) \rangle.
\end{aligned} \tag{4.13}$$

We used here that the leading-order soft function  $\mathcal{S}_m^{(0)}$  is the unit matrix  $\mathbf{1}$  in color space. The first line contains the LL result (4.11), and the remaining three lines show the different NLO corrections, which are depicted in Figure 4.2.

The hard functions  $\mathcal{H}_m$  include the momentum conservation and phase-space constraints on the hard partons. For two partons, these constraints render the integrals over the parton directions trivial. The momentum and jet direction constraints impose that the vectors  $n_1$  and  $n_2$  must point along the thrust axis and in opposite directions so that

$$\langle \mathcal{H}_2(\{n_1, n_2\}, Q, \mu) \otimes \mathcal{S}_2(\{n_1, n_2\}, Q_0, \mu) \rangle = \sigma_0 H_2(Q^2, \mu) \langle \mathcal{S}_2(\{\bar{n}, n\}, Q_0, \mu) \rangle, \tag{4.14}$$

where we have used that also the color structure is trivial for two hard partons. The function  $H_2(Q^2, \mu)$  is the standard dijet hard function

$$H_2(Q^2, \mu) = 1 + \frac{\alpha_s}{4\pi} C_F \left[ -8 \ln^2 \frac{\mu}{Q} - 12 \ln \frac{\mu}{Q} - 16 + \frac{7}{3} \pi^2 \right], \tag{4.15}$$

which arises also for global observables such as the event shape thrust. In the large- $N_c$  limit, we should replace  $C_F \rightarrow N_c/2$ .

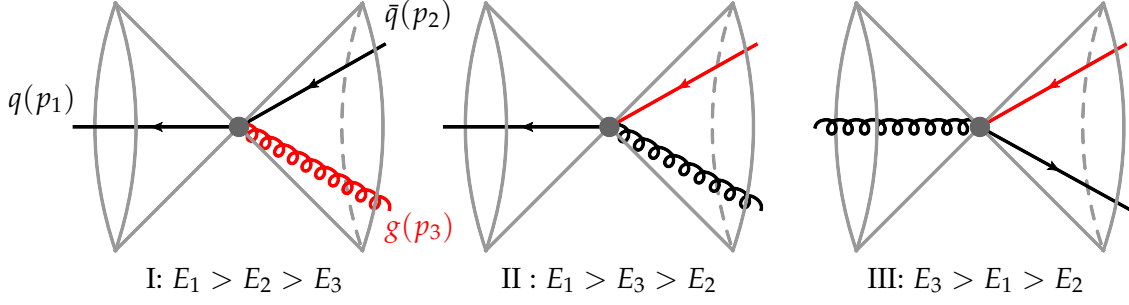


FIGURE 4.3: Kinematical configurations in the three different regions with different energy ordering. Particles with the smallest energy are drawn in red.

In [24] we have derived an expression for the hard function  $\mathcal{H}_3^{(1)}$ , which corresponds to the QCD process  $\gamma^* \rightarrow q(p_1)\bar{q}(p_2)g(p_3)$ . By definition  $\mathcal{H}_3^{(1)}$  only depends on angular information of the three partons, since their energies have already been integrated over. For convenience we split the phase space integration into different regions according to the direction of the thrust axis, which for three-parton final states points in the opposite direction of the most energetic parton. Due to momentum conservation, the three partons must be in a plane. Using invariance of the cross section under rotation around the thrust axis, in Region I only the angles  $\theta_2$  and  $\theta_3$ , between the partons and the thrust axis, are not fixed.

For convenience we parameterize these angles in terms of two variables  $u$  and  $v$  each going from 0 to 1 and defined as

$$\hat{\theta}_2 \equiv \tan \frac{\theta_2}{2} = uv, \quad \hat{\theta}_3 \equiv \tan \frac{\theta_3}{2} = v, \quad (4.16)$$

where the variable  $v$  is directly related to the larger angle  $\theta_3$ , while  $u$  characterises the relative size of the angles. Please note that the variables  $u$  and  $v$  differ from the quantities of the same name used in [24], where we defined the variables such that  $v = 1$  corresponded to the angle of the jet cone, rather than a  $90^\circ$  angle as in (4.16). Because the same hard function  $\mathcal{H}_3^{(1)}$  also arises for the jet mass studied below, we prefer to not incorporate the specific phase-space constraint into its parameterization.

The bare hard function  $\mathcal{H}_3^{(1)}$  in terms of the angles  $\hat{\theta}_2$  and  $\hat{\theta}_3$  was given in (4.4) of [104]. The corresponding representation includes a  $\theta$ -function constraint imposed to prevent the thrust axis from flipping. For simplicity, we choose the jet opening half-angle  $\alpha \leq \frac{\pi}{3}$  so that the axis constraint is automatically fulfilled. The hard function suffers from divergences when  $u$  and  $v$  go to zero. In dimensional regularization after performing  $\overline{\text{MS}}$  subtraction, the contribution of Region I to the renormalized hard function  $\mathcal{H}_3^{(1)}$  is given by

$$\begin{aligned} \mathcal{H}_{3,\text{I}}^{(1)}(u, v, Q, \mu) = C_F \Bigg\{ & \left[ 4 \ln^2 \frac{\mu}{Q} - \frac{\pi^2}{6} \right] \delta(u) \delta(v) - 8 \ln \frac{\mu}{Q} \delta(u) \left( \frac{1}{v} \right)_+ \\ & + 8 \delta(u) \left( \frac{\ln v}{v} \right)_+ + \left[ - \ln \frac{\mu}{Q} F(u, 0) + \frac{2u^2}{(1+u)^3} - F(u, 0) \ln(1+u) \right] \delta(v) \left( \frac{1}{u} \right)_+ \\ & + F(u, 0) \delta(v) \left( \frac{\ln u}{u} \right)_+ + F(u, v) \left( \frac{1}{u} \right)_+ \left( \frac{1}{v} \right)_+ \Bigg\} \Theta_{\text{in}}(v). \end{aligned} \quad (4.17)$$

The function  $\Theta_{\text{in}}(v)$  ensures that all hard emissions are inside the jet. For the interjet energy flow it is given by  $\Theta_{\text{in}}(v) = \theta(\delta - v)$ , with  $\delta = \tan \frac{\alpha}{2}$ , where  $\alpha$  is the jet opening half-angle. In the large- $N_c$  limit, the color structure of the hard functions becomes trivial and we use non-bold symbols such as  $\mathcal{H}_{3,\text{I}}^{(1)}$  to indicate the scalar quantities which are relevant in this limit. The expression for the auxiliary function  $F(u, v)$  is given by

$$F(u, v) = \frac{4 \left[ u \left[ -2 (u^2 + u + 1) v^2 + u (2u(u+1) + 1) v^4 + u + 2 \right] + 2 \right]}{(u+1)^3}. \quad (4.18)$$

Similarly, in Region II we have

$$\begin{aligned} \mathcal{H}_{3,\text{II}}^{(1)}(u, v, Q, \mu) = C_F \left\{ \left[ -\ln \frac{\mu}{Q} G(u, 0) + \frac{2}{(1+u)^3} + G(u, 0) \ln \left( \frac{u}{1+u} \right) \right] \delta(v) \right. \\ \left. + G(u, v) \left( \frac{1}{v} \right) \right\} \Theta_{\text{in}}(v), \end{aligned} \quad (4.19)$$

with the parametrization  $\hat{\theta}_3 = uv$  and  $\hat{\theta}_2 = v$ . The function  $G(u, v)$  is defined as

$$G(u, v) = \frac{4 \left[ u \left[ -2 (u^2 + u + 1) v^2 + u(u(u+2) + 2)v^4 + 2(u+1) \right] + 1 \right]}{(u+1)^3}. \quad (4.20)$$

Region III describes the situation, where the gluon is the most energetic particle and we parameterize  $\hat{\theta}_1 = uv$ ,  $\hat{\theta}_2 = v$ . The hard function reads

$$\mathcal{H}_{3,\text{III}}^{(1)}(u, v, Q, \mu) = C_F H(u, v) \Theta_{\text{in}}(v), \quad (4.21)$$

with

$$H(u, v) = \frac{4v (u^4 v^4 + u^2 v^4 + 4u^2 v^2 + u^2 + 1)}{(u+1)^2 (1 - uv^2)}. \quad (4.22)$$

Next, we will discuss how to implement the above expressions into the parton shower code. We first rewrite the angular integral in the  $\mathcal{H}_3^{(1)}$  contribution as

$$\langle \mathcal{H}_3^{(1)}(\{\underline{n}\}, Q, \mu_h) \otimes \hat{\mathcal{S}}_3(\{\underline{n}\}, \mu_h) \rangle = \int_0^1 du \int_0^1 dv \langle \mathcal{H}_3^{(1)}(u, v, Q, \mu_h) \hat{\mathcal{S}}_3(u, v, \mu_h) \rangle, \quad (4.23)$$

where we have defined  $\hat{\mathcal{S}}_3(u, v, \mu_h) = \sum_{m=3}^{\infty} \mathbf{U}_{3m}(\{\underline{n}\}, \mu_s, \mu_h) \hat{\otimes} \mathbf{1}$ , which is the LL RG evolution or parton shower soft function. To implement this formula into a Monte Carlo framework, we will randomly generate  $u$  and  $v$  and then run the shower  $\hat{\mathcal{S}}_3(u, v, \mu_h)$  for the given configuration. There is, however, one complication, namely that the hard function is a distribution and can therefore not be integrated point by point. One way to solve this problem is to evaluate  $\hat{\mathcal{S}}_3(u, v, \mu_h)$  on a grid, interpolate and then perform the integrations over  $u$  and  $v$ . This works well because  $\hat{\mathcal{S}}_3(u, v, \mu_h)$  is a smooth function of the angles as can be seen from Figure 4.4. Note in particular that the limit  $v \rightarrow 0$ , in which both angles go to zero and the two Wilson lines become collinear, is completely smooth. In this limit the quark and gluon Wilson lines combine and produce the same radiation as a single quark Wilson line, encoded in the function  $\hat{\mathcal{S}}_2$ . The relation

$$\hat{\mathcal{S}}_3(u, v=0, \mu_h) = \hat{\mathcal{S}}_2(\mu_h) \quad (4.24)$$

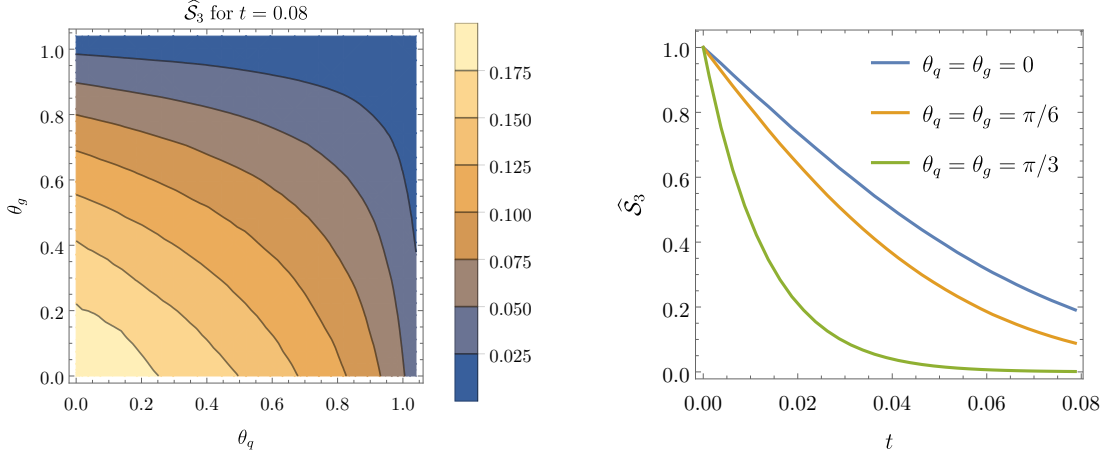


FIGURE 4.4: Left: Angular dependence of  $\hat{\mathcal{S}}_3$  for fixed evolution time  $t = 0.08$ . Note that the angles  $\theta_q$  and  $\theta_g$  of the hard partons to the jet axis must be smaller than the cone angle  $\alpha = \pi/3 \approx 1.04$ . Right: Dependence on the evolution time  $t$  at fixed angles.

will lead to important simplifications below. In the right plot, we show the evolution time dependence of the soft function  $\hat{\mathcal{S}}_3$  for fixed angles. One observes that the function falls off much faster when the hard partons approach the jet cone. In this configuration, more soft radiation exits the cone, explaining this suppression.

Interpolating the soft function  $\hat{\mathcal{S}}_3$  gives accurate results, but is not efficient since the function depends on the phase-space constraints and thus needs to be recomputed when one changes the cone angle. It is much more natural to compute the convolution (4.23) directly in the Monte Carlo code. The simplest way to implement the plus distributions in the hard function into the Monte Carlo is to use a slicing method. To explain it in a simple setting, let us for the moment only consider the  $v$  dependence and forget about the variable  $u$ . Then the convolution (4.23) takes the form

$$\mathcal{H}_3^{(1)} \otimes \hat{\mathcal{S}}_3 = \int_0^1 dv \left[ A \delta(v) + B(v) + \sum_{i=0}^1 C_i(v) \left( \frac{\ln^i v}{v} \right)_+ \right] \hat{\mathcal{S}}_3(v), \quad (4.25)$$

where  $B(v)$  represents a regular function. Thanks to relation (4.24) the  $A$  term can be combined with the LL parton shower result involving  $\hat{\mathcal{S}}_2$  and the contribution from  $B(v)$  can be computed by randomly generating  $v$ -values and running the shower for each chosen configuration. The slicing method introduces a lower cutoff  $v_0$  into the plus distribution integrals  $C_i(v)$  to ensure that  $v$  can not go to zero. With the cutoff in place, we can integrate the subtraction term, e.g.

$$\int_0^1 \frac{dv}{v} [\hat{\mathcal{S}}_3(v) - \hat{\mathcal{S}}_2] = \int_{v_0}^1 \frac{dv}{v} \hat{\mathcal{S}}_3(v) + \ln v_0 \hat{\mathcal{S}}_2 + \mathcal{O}(v_0), \quad (4.26)$$

where one can use the same Monte Carlo method as for the  $B(v)$  terms to simulate the first term with the collinear cutoff  $v_0$ , and then adds back the second term which is given by the LL parton shower result, multiplied by a logarithm of the cutoff parameter. The  $v_0$  dependence will cancel out between the two terms up to power corrections. The power corrections in the artificial parameter  $v_0$  can be neglected as long as one chooses it small enough. The slicing method involves large cancellations between the two terms on the

right-hand side of (4.26), so for numerical stability reasons one should not choose  $v_0$  too small. These two opposing requirements make slicing methods delicate, but we compared to the result using the interpolated soft function  $\widehat{\mathcal{S}}_3$  and found good consistence. The cutoff independence is demonstrated in Figure 4.12 in Appendix 4.A.

Up to now we have disregarded the  $u$  dependence, but the Monte Carlo implementation of the full equations (4.17), (4.19) and (4.21) involves nothing beyond the above discussion, except that we have to consider both integrations. As (4.24) shows, the soft function becomes trivial for  $v \rightarrow 0$  and we can combine all  $\delta(v)$  dependent terms with the parton shower for  $\widehat{\mathcal{S}}_2$ . We thus only need to apply the slicing method to the  $\delta(u) \left( \ln^i v/v \right)_+$  and  $(1/u)_+ (1/v)_+$  terms. The corresponding cutoff dependent compensation terms are collected in Appendix 4.A.

The final ingredient we need to implement is the one-loop soft function, which is defined as a sum over all dipoles

$$\begin{aligned} \frac{\alpha_s}{4\pi} \mathcal{S}_m^{(1)}(\{\underline{n}\}, Q_0, \epsilon) = \\ - g_s^2 \tilde{\mu}^{2\epsilon} \sum_{(ij)} \mathbf{T}_{i,L} \cdot \mathbf{T}_{j,R} \int \frac{d^d k}{(2\pi)^{d-1}} \delta(k^2) \theta(k^0) \frac{n_i \cdot n_j}{n_i \cdot k n_j \cdot k} \Theta_{\text{out}}(n_k) \theta(Q_0 - E_k), \end{aligned} \quad (4.27)$$

where the sum runs over all unordered pairs  $(ij)$ . In the large- $N_c$  limit only neighbouring legs give a contribution

$$\mathbf{T}_{i,L} \cdot \mathbf{T}_{j,R} \rightarrow -\frac{N_c}{2} \delta_{i,j\pm 1}. \quad (4.28)$$

We evaluate the one-loop soft function numerically within our Monte Carlo code. It is well suited for this task since it generates emissions between neighbouring dipoles in an efficient way, by randomly choosing the rapidity  $\hat{y}$  and azimuthal angle  $\hat{\phi}$  of the emission in the COM (center-of-mass) frame of the emitting dipole  $(n_i, n_j)$ . Here and in the following, we will use hats to indicate kinematic quantities in the COM frame. Our hard function shower keeps emitting additional hard partons until one of them enters the veto region at which point it terminates. In our implementation, we use this last parton in the veto region to obtain the NLO correction to the soft function. At NLO, the renormalized soft function can be expressed as

$$\mathcal{S}_m^{(1)}(\{\underline{n}\}, Q_0, \mu) = \frac{N_c}{2} \sum_{i,j=1}^m \delta_{i,j\pm 1} \int d\hat{y} \int_0^{2\pi} \frac{d\hat{\phi}}{2\pi} \left[ -4 \ln \frac{\mu}{Q_0} + 4 \ln \frac{2 |\sin \hat{\phi}|}{f_{ij}(\hat{\phi}, \hat{y})} \right] \Theta_{\text{out}}^{\text{lab}}(\hat{y}, \hat{\phi}), \quad (4.29)$$

with  $\Theta_{\text{out}}^{\text{lab}}(\hat{y}, \hat{\phi})$  constraining soft radiation to be outside of the jet cone in the lab frame. In the Monte Carlo implementation, the factor in square brackets is a weight factor for the corresponding emission. The auxiliary function  $f_{ij}(\hat{\phi}, \hat{y})$  connects the transverse momentum  $\hat{k}_T$  in the COM frame to the energy  $Q_0$  in the lab frame,  $\hat{k}_T f_{ij}(\hat{\phi}, \hat{y}) \leq Q_0$ , and is given by  $f_{ij}(\hat{\phi}, \hat{y}) = \frac{2}{M} (-\beta \cos \hat{\phi} + \cosh \hat{y})$ , where  $M^2 = 2 n_i \cdot n_j$  is the invariant “mass” of the dipole pair, and  $\beta = \sqrt{1 - M^2/4}$ . The logarithm of  $|\sin \hat{\phi}|$  arises from expanding the azimuthal angular integration in  $\epsilon$ , which is related to the space-time dimension through  $d = 4 - 2\epsilon$ . A detailed derivation of expression (4.29) can be found in Appendix 4.A.

While our slicing implementation of the hard function is simple but specific to the dijet processes and certainly not optimal, the above procedure to obtain the NLO soft function

is simple, efficient and general. Compared to the LL parton shower code, including the one-loop soft function correction (4.29) yields

$$\sum_{m=2}^{\infty} \langle \mathcal{H}_m(t) \hat{\otimes} \mathcal{S}_m^{(1)} \rangle = \langle \mathcal{H}_2(t) \mathcal{S}_2^{(1)} + \int \frac{d\Omega_1}{4\pi} \mathcal{H}_3(t) \mathcal{S}_3^{(1)} + \int \frac{d\Omega_1}{4\pi} \int \frac{d\Omega_2}{4\pi} \mathcal{H}_4(t) \mathcal{S}_4^{(1)} + \dots \rangle, \quad (4.30)$$

where one evolves the hard function from hard scale to soft scale and multiplies it with the soft function  $\mathcal{S}_m^{(1)}$  of the corresponding multiplicity. When running our Monte Carlo code we fill three histograms, one for the LL shower, one for the logarithmic part of (4.29) and one for the non-logarithmic part. Further details of the Monte Carlo algorithm, including the implementation of the one-loop soft function are given in Appendix 4.B.

The computer time needed to run the shower including the one-loop corrections depends on the maximum evolution time needed in the computation. For the interjet energy flow, we run the shower until  $t = 0.08$ , corresponding to  $\mu_s \approx 1$  GeV. For a collinear cutoff at  $\eta_{\text{cut}} = 4$  ( $\eta_{\text{cut}} = 5$ ) in the parton shower we then end up with about 15 (30) hard partons per event on average. To resolve the peak region of the jet mass, discussed in the next section, we have to run to extremely low scales  $\mu_s = 0.275$  GeV, corresponding to  $t = 0.3$ , near the Landau pole at  $\Lambda = 0.230$  GeV. At this scale, hundreds of partons are generated in each event and we need a few days of computer time on a cluster to obtain our numerical results, which will be presented in Section 4.4 below.

### 4.3 NLL' RESUMMATION FOR JET MASS

Our second task is to perform the resummation for the jet mass distribution at electron-positron colliders. In contrast to the interjet energy flow, this observable suffers from soft-collinear double logarithms. These then constitute the LL results, while the non-global structure only arises at NLL. The resummation of jet mass including the leading non-global logarithms has been discussed in [26, 66, 104, 107]. At NLL level, the non-global logarithms yield a simple overall factor which multiplies the cross section. Beyond NLL this simple factorization does not hold anymore, and one needs to include the corrections piece by piece.<sup>2</sup> The basic structure of the corrections is of course the same as for the interjet energy flow, see (4.13) and Figure 4.2, and we therefore mainly focus on the differences to this case. In addition to the double logarithms, the most important new element is that the factorization arises in Laplace space. We use the same notation as [104], where we presented NLL resummation results. For NLL' accuracy we need to keep one-loop matching corrections in the factorization formula (4.4) and the theorem then reads

$$\begin{aligned} \tilde{\sigma}(\tau, \mu_h) = & \sum_{i=q,\bar{q}} \sum_{m=1}^{\infty} \tilde{j}_i(\tau Q, \mu_h) \langle \mathcal{H}_1^i(\{\underline{n}\}, Q, \mu_h) \otimes U_{1m}(\{\underline{n}\}, \mu_s, \mu_h) \hat{\otimes} \tilde{\mathcal{S}}_m(\{\underline{n}\}, \tau, \mu_s) \rangle \\ & + \sum_{i=q,\bar{q},g} \sum_{m=2}^{\infty} \tilde{j}_i(\tau Q, \mu_h) \langle \mathcal{H}_2^i(\{\underline{n}\}, Q, \mu_h) \otimes U_{2m}(\{\underline{n}\}, \mu_s, \mu_h) \hat{\otimes} \mathbf{1} \rangle. \end{aligned} \quad (4.31)$$

In the first line we must include one-loop corrections for the quark jet function  $\tilde{j}_q$ , the hard function  $\mathcal{H}_1$  and soft functions  $\tilde{\mathcal{S}}_m$ . We do not include the  $\mathcal{O}(\alpha_s^2)$  cross terms so that the

<sup>2</sup> The recent paper [116] on the jet shape includes one-loop corrections only for the global part, which corresponds to  $m = 1$  in (4.4), and does therefore not reach full NLL' accuracy. Including the non-global structure would result in a factorization formula similar to (4.18) in [18].



first line turns into a sum of terms with the individual corrections. The hard function  $\mathcal{H}_2^i$  in the second line includes two hard partons in the right jet. Since it involves a power of  $\alpha_s$  due to the hard emission, the remaining ingredients are only needed at LO. The second line also includes a gluon-jet contribution, for the case where the  $q\bar{q}$  pair is in the right hemisphere. The one-loop hard functions are the same as for interjet energy flow, up to the different phase-space constraints. They are given in Appendix 4.C.

In Laplace space, RG-evolution is multiplicative and we can factor out and exponentiate the double logarithms. Removing the double logarithmic part is important since our shower evolution, which also takes place in Laplace space, is purely soft. The subtraction of collinear contributions will also be needed for our numerical computation of the one-loop soft function. Using standard techniques introduced in [117], we can perform the inversion to momentum space analytically at the end and write a momentum space result directly in terms of Laplace-space ingredients.

The anomalous dimension  $\Gamma^H$  in (4.8) which drives the resummation of the logarithms in interjet energy flow (4.1) can be viewed in two ways: As the hard anomalous dimension, used to evolve the hard functions to the soft scale, or as the soft anomalous dimension which evolves the soft functions to a higher scale. RG invariance of the cross section implies that the two evolutions must agree. The situation is more interesting for the light-jet mass (4.4) which involves three ingredients. In this case RG invariance translates into the statement

$$\Gamma_{lm}^{H_i}(\{\underline{n}\}, Q, \mu) = \Gamma_{lm}^{S_i}(\{\underline{n}\}, \tau, \mu) + \Gamma^{J_i}(\tau Q, \mu) \delta_{lm}, \quad (4.32)$$

where

$$\Gamma^{J_i}(\tau Q, \mu) = -2C_i \gamma_{\text{cusp}} \ln\left(\frac{\tau Q}{\mu^2}\right) + 2\gamma^{J_i}. \quad (4.33)$$

The Casimir  $C_i$  for the quark-jet channel is  $C_q = C_F$ , while the gluon configuration has  $C_g = C_A$ . In our paper [104], we have analyzed the one-loop soft anomalous dimension and found that it has the form

$$\Gamma_{lm}^{S_i}(\{\underline{n}\}, \tau, \mu) = 2C_i \gamma_{\text{cusp}} \ln\left(\frac{\tau}{\mu}\right) \delta_{lm} + \hat{\Gamma}_{lm}(\{\underline{n}\}), \quad (4.34)$$

where  $\hat{\Gamma}_{lm}$  is a regular non-logarithmic anomalous dimension, which takes the same form as (4.8), except for a subtraction to remove the collinear singularities, which give rise to the cusp piece in (4.34). The subtraction is achieved by replacing the diagonal elements in (4.8) by  $V_m \rightarrow \bar{V}_m = V_m - V_0$ , with

$$V_0 = V_0 \mathbf{1} = -4C_i \mathbf{1} \int \frac{d\Omega(n_k)}{4\pi} \frac{\bar{n} \cdot n}{\bar{n} \cdot n_k n_k \cdot n} \Theta_L(n_k), \quad (4.35)$$

where  $\Theta_L(n_k)$  ensures that the emission is in the left hemisphere with the light jet. The trivial color structure arises from color conservation

$$\sum_{i=1}^m T_0 \cdot T_i = -T_0 \cdot T_0 = -C_i \mathbf{1}. \quad (4.36)$$

Note that  $V_0$  is equal to the one-loop result (real plus virtual) for the case where there is only one hard parton on the right, which then, by momentum conservation, flies along  $n$ . The subtraction therefore removes the “global” one-loop part of the soft anomalous dimension. After this, the Monte Carlo result no longer involves collinear singularities. As before we

regularize the collinear singularities in the individual entries of  $\hat{\mathbf{F}}$  using a cutoff. The parton shower algorithm of Dasgupta and Salam [26] instead uses a veto algorithm to remove global logarithmic terms. Our subtraction of the global piece has the advantage that our Monte Carlo weights are always positive. Let us also note that the role of the subtraction is to separate out the collinear singularities, so that the same subtraction can be used for any process with the same double logarithmic structure, i.e. also in cases with more complicated geometry, where we cannot analytically compute the one-loop function.

To make use of the separation of the anomalous dimension into two pieces, we now factor the soft function as

$$\tilde{\mathcal{S}}_m^i(\{\underline{n}\}, \tau, \mu_s) = \tilde{S}_G^i(\tau, \mu_s) \hat{\mathcal{S}}_m^i(\{\underline{n}\}, \tau, \mu_s), \quad (4.37)$$

with

$$\tilde{S}_G^q \left( L_s = \ln \frac{\tau}{\mu_s}, \mu_s \right) = 1 + \frac{\alpha_s}{4\pi} C_F \left( -4L_s^2 - \frac{\pi^2}{2} \right) + \mathcal{O}(\alpha_s^2). \quad (4.38)$$

The splitting of the soft function into single and double logarithmic pieces is of course not unique. We have chosen the double-logarithmic “global” part  $\tilde{S}_G^i$  such that it includes the full one-loop result, so that the “non-global” remainder function  $\hat{\mathcal{S}}_m^i$  starts at two loops for  $m = 1$  partons in the right hemisphere. For the gluon case, we only need the tree-level result  $\tilde{S}_G^g = 1$  since the hard function for this channel is suppressed by  $\alpha_s$ .

The global piece fulfills a standard RG-evolution equation driven by the cusp piece of (4.34) which can be immediately solved in Laplace space. Using the technique introduced in [117], the associated momentum-space solution takes the form

$$S_G^i(\omega, \mu) = \exp[2C_i S(\mu_s, \mu)] \tilde{S}_G^i(\partial_{\eta_s}, \mu_s) \frac{e^{-\gamma_E \eta_s}}{\Gamma(\eta_s)} \frac{1}{\omega} \left( \frac{\omega}{\mu_s} \right)^{\eta_s}, \quad (4.39)$$

with  $\eta_s = 2C_i A_{\gamma_{\text{cusp}}}(\mu_s, \mu)$ , where the logarithm  $L_s$  has been replaced by a derivative operator with respect to  $\eta_s$ .

With the global function at hand, the Monte Carlo simulation only needs to provide the remainder  $\hat{\mathcal{S}}_m^i$ . Its single logarithmic RG-evolution is obtained by the subtracted parton shower described above and the one-loop correction for an  $m$ -parton configuration is given by

$$\hat{\mathcal{S}}_m^{i(1)}(\{\underline{n}\}, \tau, \mu_s) = \tilde{\mathcal{S}}_m^{i(1)}(\{\underline{n}\}, \tau, \mu_s) - \tilde{S}_G^{i(1)}(\tau, \mu_s), \quad (4.40)$$

which, by construction, is free from collinear logarithms. We compute this difference in the large- $N_c$  limit by running the shower until it produces a parton in the left hemisphere, which is the veto region for the present case. The outside parton is the soft emission and we then compute the relevant one-loop weight factor precisely as in (4.29). The form of the Laplace space soft function can be found in the appendix in (4.66). When the emission arises from the first dipole, which involves the left parton along  $n_0 = \bar{n}$ , we subtract the global part. For the quark-jet channel the subtraction is given by

$$\tilde{S}_G^{q(1)}(\tau, \mu) = \frac{N_c}{2} \int d\hat{y} \frac{d\hat{\phi}}{2\pi} \left[ -4 \ln \frac{\mu}{\tau} + 4 \ln \frac{2|\sin \hat{\phi}|}{g_{0j}(\hat{\phi}, \hat{y})} \right] \Theta_L(\hat{y}, \hat{\phi}) X(\hat{y}, \hat{\phi}), \quad (4.41)$$

with a re-weighting factor

$$X(\hat{y}, \hat{\phi}) = e^{2\hat{y}} / (e^{2\hat{y}} + \beta^2 - 2e^{\hat{y}} \beta \cos \hat{\phi}). \quad (4.42)$$

The factor  $X$  is simply the ratio of the radiator (4.10) associated with the original  $(\bar{n}, n)$  dipole and the one of the dipole  $(\bar{n}, n_j)$  which emits the gluon and defines the frame in which  $\hat{y}$  and  $\hat{\phi}$  are generated. The subtraction removes the collinear divergence in the  $(\bar{n}, n_j)$  dipole and yields  $\hat{S}_m^q$ . The function  $g_{ij}$  in (4.41) relates the momentum component  $\bar{n} \cdot k$  in the lab frame to the transverse momentum  $\hat{k}_T$  in the COM frame of the dipole  $(n_i, n_j)$ , analogously to the function  $f_{ij}$  in (4.29). Its explicit form is given in the appendix in (4.67).

The final ingredients in (4.31) are the one-loop jet functions, which are well known. In Laplace space, the one-loop jet function is given by

$$\tilde{j}_i \left( L_j = \ln \frac{Q\tau}{\mu^2}, \mu \right) = 1 + \frac{\alpha_s}{4\pi} \left( C_i \gamma_0^{\text{cusp}} \frac{L_j^2}{2} + \gamma_0^{J_i} L_j + c_1^{J_i} \right), \quad (4.43)$$

which translates to the momentum-space result [117]

$$J_i(p^2, \mu) = \exp \left[ -4C_i S(\mu_j, \mu) + 2A_{\gamma_{J_i}}(\mu_j, \mu) \right] \tilde{j}_i(\partial_{\eta_j}, \mu_j) \frac{e^{-\gamma_E \eta_j}}{\Gamma(\eta_j)} \frac{1}{p^2} \left( \frac{p^2}{\mu_j^2} \right)^{\eta_j}, \quad (4.44)$$

with  $\eta_j = 2C_i A_{\gamma_{\text{cusp}}}(\mu_j, \mu)$ . The relevant expressions for the ingredients are listed in Appendix 4.E. Combining the global soft function with the jet function, we obtain

$$\begin{aligned} \Sigma_i(\rho) &= Q^2 \int_0^\rho d\rho' \int_0^{Q\rho'} d\omega J_i(Q^2\rho' - Q\omega, \mu_h) S_G^i(\omega, \mu_h) \\ &= \exp \left[ 2C_i S(\mu_s, \mu_h) - 4C_i S(\mu_j, \mu_h) + 2A_{\gamma_{J_i}}(\mu_j, \mu_h) \right] \tilde{j}_i(\partial_{\eta_j}, \mu_j) \tilde{S}_G^i(\partial_{\eta_s}, \mu_s) \\ &\quad \times \frac{e^{-\gamma_E \eta}}{\Gamma(\eta + 1)} \left( \frac{Q^2 \rho}{\mu_j^2} \right)^\eta \left( \frac{Q\mu_s}{\mu_j^2} \right)^{-\eta_s}, \end{aligned} \quad (4.45)$$

where we define  $\eta = \eta_j + \eta_s$ . The full result is obtained after combining this with the subtracted shower evolution, the hard functions and the one-loop soft correction (4.40). To implement this expression in practice, we run the shower, tabulate the results for the individual contributions to (4.31) and then replace the global function  $\tilde{S}_G^i(\omega, \mu_h)$  in (4.45) by the full result which includes the hard functions, evolution and one-loop corrections.

Up to NNLL, the integrated heavy-jet mass distribution is obtained as

$$\frac{1}{\sigma_0} \int_0^{\rho_h} d\bar{\rho}_h \frac{d\sigma}{d\bar{\rho}_h} = H_2(Q^2, \mu_h) [\Sigma_q(\rho_h)]^2. \quad (4.46)$$

Using this result and relation (4.2) one obtains the light-jet mass.

#### 4.4 NUMERICAL RESULTS

In this section we will present numerical results, first for the interjet energy flow, then for the jet mass. For our plots, we work with  $Q = M_Z$  and  $\alpha_s(M_Z) = 0.1181$ , and use two-loop  $\alpha_s(\mu)$  running with  $n_f = 5$  quark flavors. To our knowledge, no measurements are available for the interjet energy flow, but we will compare our results for the jet mass to LEP measurements by ALEPH [118].

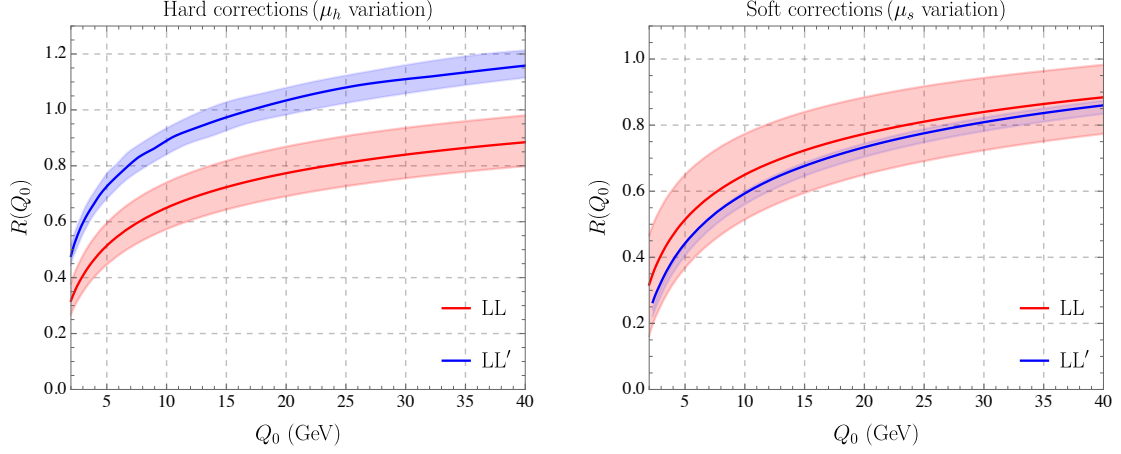


FIGURE 4.5: Left panel: Hard function corrections, with bands arising from hard scale variation. Right panel: Soft function corrections, with bands from soft scale variation.

#### 4.4.1 Interjet energy flow

For our numerical discussion we choose jet cone size parameter as  $\alpha = \pi/3$ . This is equivalent to  $\delta = \tan \frac{\alpha}{2} = 1/\sqrt{3}$ , or rapidity gap size  $\Delta y = -\ln \delta^2 \approx 1.1$ . We want to avoid small cone angles, or equivalently large rapidity gaps, in order not to have to deal with large collinear logarithms. In our plots we show the gap fraction

$$R(Q_0) = \frac{1}{\sigma_{\text{tot}}} \sigma(Q, Q_0) \equiv \int_0^{Q_0} dE_s \frac{1}{\sigma_{\text{tot}}} \frac{d\sigma}{dE_s}, \quad (4.47)$$

which is the fraction of events in which the soft radiation outside the jets has an energy  $E_s$  below the cutoff  $Q_0$ . By definition, the amount of energy in the gap must be below  $Q/2$ , otherwise the thrust axis, which defines our jet axis, would flip. The fixed order result is therefore  $R(Q_0 = Q/2) = 1$  at any order in perturbation theory. The  $\mathcal{O}(\alpha_s^0)$  result with just two back-to-back partons is of course  $R(Q_0) = 1$ , a nontrivial  $Q_0$  dependence only arises at  $\mathcal{O}(\alpha_s)$  when the third parton is inside the gap. We will refer to the  $\mathcal{O}(\alpha_s)$  result as LO.

As a first step, let us check the size of the individual corrections and investigate whether the scale dependence is reduced after including them. In Figure 4.5 we show the hard and soft corrections separately and then plot the scale bands from varying the associated scales by a factor two around their default values  $\mu_h = Q$  and  $\mu_s = Q_0$ . Compared to the LL scale bands shown in red, the scale dependence is reduced in both cases after including the corrections. We observe that the hard corrections are quite significant and positive, while the soft corrections are moderate and negative. The hard corrections have two sources, virtual corrections to  $\mathcal{H}_2$  and real emission contributions encoded in  $\mathcal{H}_3$ . The first of these is just a constant factor multiplying the LL result, while the second one comes together with the higher soft function  $\mathcal{S}_3$ . Both corrections are positive. At high values of  $Q_0$  the three parton contribution from  $\mathcal{H}_3$  is about twice as large as the one from the one-loop correction to  $\mathcal{H}_2$  and it becomes more dominant at smaller values.

It is clear that the large hard function corrections at  $Q_0 \lesssim Q/2$  must be compensated by terms which are power suppressed in  $Q_0/Q$  and are not captured by the resummation based on the factorization formula (4.1), which arises in the limit  $Q_0 \rightarrow 0$ . One can obtain these power suppressed terms by matching to the fixed-order result. More precisely, one adds to the resummed result the fixed-order prediction minus its expansion around  $Q_0$ . The

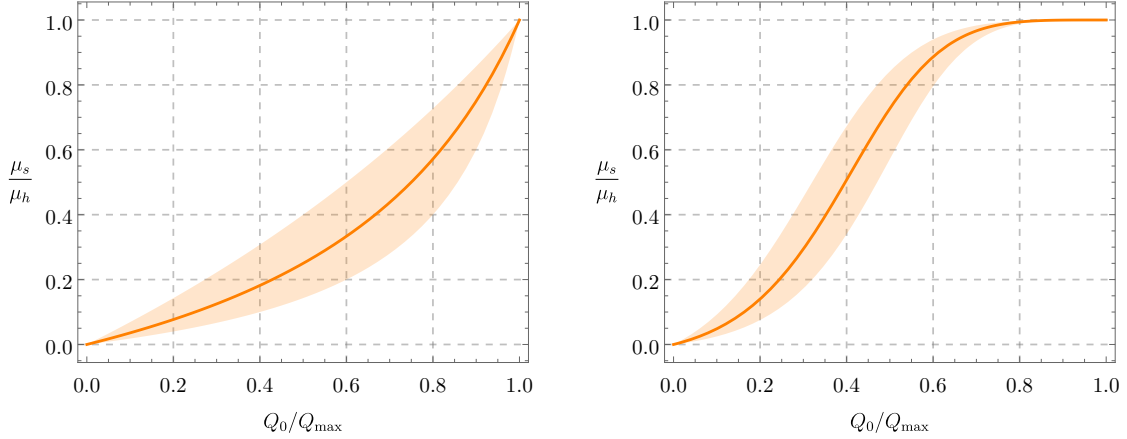


FIGURE 4.6: The profile function (4.49) for  $n = 1$  (left plot) and  $n = 4$  (right plot). We will use the  $n = 4$  function as our default choice.

subtraction removes the terms which are already included in the resummation. These power suppressed matching terms can be obtained as

$$\Delta R(Q_0) = \int_0^{Q_0} dE_s \frac{1}{\sigma_{\text{tot}}} \left( \frac{d\sigma}{dE_s} - \frac{d\sigma}{dE_s} \Big|_{E_s \rightarrow 0} \right). \quad (4.48)$$

To evaluate this integral, one computes the cross section to find a parton inside the gap and subtracts from it its soft limit. The subtraction eliminates the virtual contributions and leads to a finite integral, which one can evaluate numerically. However, even after the matching to the fixed order result, the resummed result does not yet tend to  $R(Q_0) = 1$  for  $Q_0 \rightarrow Q/2$  because we resum logarithms of  $\mu_s/\mu_h \rightarrow 1/2$  for  $\mu_s \approx Q_0$  and  $\mu_h = Q$ . To switch off the resummation, one can choose the soft scale in such a way that it approaches the hard scale  $\mu_h$  as  $Q_0 \rightarrow Q_{\text{max}} = Q/2$ . This can be achieved, for example with a *profile function* [119] of the form

$$\mu_s(Q_0) = \frac{x_s Q_0}{1 + \frac{x_s Q_0}{\mu_h} + \sum_{i=1}^n c_i \left( \frac{Q_0}{Q_{\text{max}}} \right)^i}, \quad (4.49)$$

where  $x_s = 1$  corresponds to the default choice and the scale bands can be obtained by varying the parameter  $x_s$  by a factor two. For low values of  $Q_0$ , this reduces to the standard choice  $\mu_s(Q_0) = Q_0 x_s$ . The power suppressed term in the denominator are chosen to switch off the resummation at the endpoint  $Q_0 = Q_{\text{max}}$ , similarly to what is usually achieved through a modification of the logarithms in traditional resummation. The simplest choice for (4.49) is  $n = 1$  and  $c_1 = -1$ , but we observe that the approach to fixed order is relatively slow. To make it faster, we choose  $n = 4$  and impose that the first three derivatives at the end-point vanish, explicitly  $c_1 = -4, c_2 = 6, c_3 = -4, c_4 = 1$ . We plot the two different profile functions in Figure 4.6 and will use  $n = 4$  as the default in our numerical implementation. The choice of the profile function affects the resummation of power-suppressed contributions. If the shape is important, one should of course compute, or even resum, the power corrections to resolve the difference. The first step would be to include the matching up to NNLO, which would in principle be possible since the fixed-order results are available [120–122]. In practice it would require some effort since we would need to compute the fixed-order expansion of our results (including the shower).

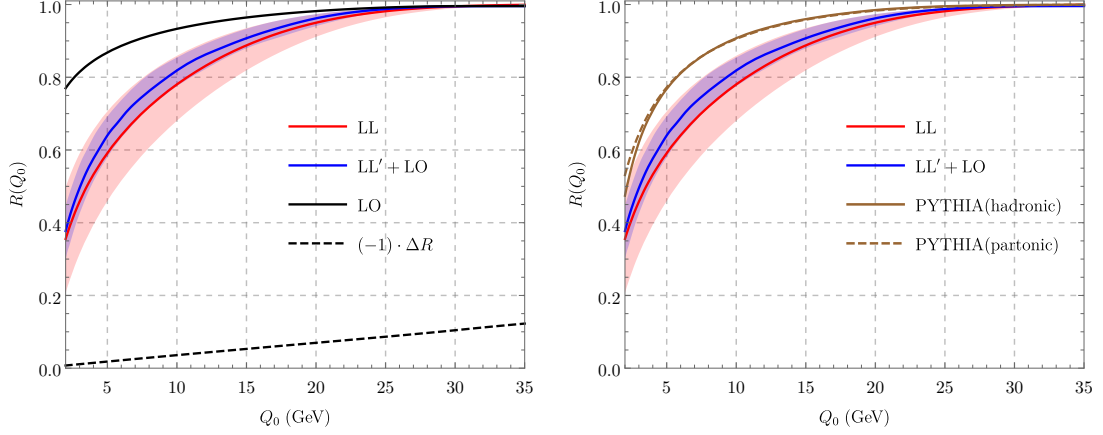


FIGURE 4.7: Comparison of our results for the interjet energy flow to fixed order (left plot) and to PYTHIA (right plot).

In Figure 4.7, we show an improved numerical result which includes the matching correction  $\Delta R(Q_0)$ , shown as a black dotted line, and uses the scale choice (4.49) to switch off the resummation at the end-point. The matching correction is negative and compensates the large hard corrections near the end-point. The LL' corrections lead to a larger gap fraction  $R(Q_0)$ . As mentioned earlier, there is unfortunately no experimental data to which we can compare our results, but we compare to PYTHIA [123]. While the two results are similar at very low  $Q_0$ , PYTHIA is higher at intermediate values. We remind the reader, that the intermediate values heavily depend on the profile function used to switch off the resummation.

#### 4.4.2 Jet mass

Let us now turn to the jet mass  $\rho$ . For interjet energy flow, we considered the integrated cross section, i.e. all events with energy in the gap below the veto, while we will look at the differential spectrum in the present case, since this is what was measured by the LEP experiments. We will however compute the spectrum by taking the derivative of the integrated cross section, which has the advantage that the spectrum is correctly normalized if the resummed prediction for the integrated cross section matches the fixed-order result at large  $\rho$ .

As a first step, we again separately plot the different ingredients and their scale dependence in Figure 4.8. In the first three plots we compare NLL to NLL' with corrections from the jet, hard and soft functions. The red bands are the NLL result with scale variation, where we vary either the jet, hard or soft scale by a factor of two around the default values  $\mu_h \sim Q$ ,  $\mu_j \sim \sqrt{\rho} Q$  and  $\mu_s \sim \rho Q$ . The blue curves show contributions at NLL' accuracy from one of the three ingredients with its associated scale variation. Obviously, the scale dependence is strongly reduced from NLL to NLL' for jet and hard corrections. The soft scale dependence, on the other hand, is only modestly reduced after including one-loop soft function corrections. The scale bands mostly overlap with each other, which indicates that perturbative convergence is reasonably good in all the three cases.

In the last plot of Figure 4.8 we show the effect of adding the  $\mathcal{O}(\alpha_s)$  power corrections to the NLL' results. The LO power corrections for the heavy-jet mass are known analytically

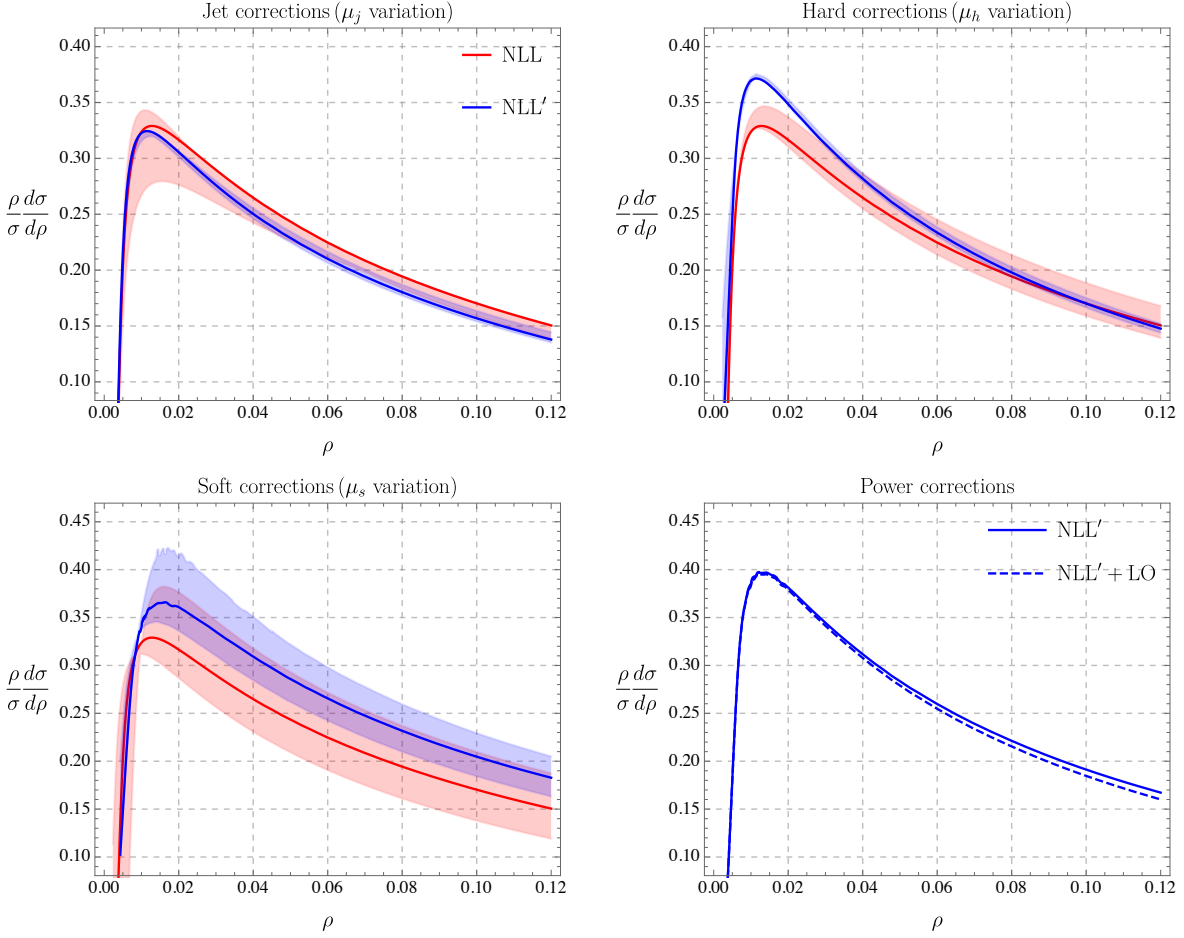


FIGURE 4.8: NLL' corrections from the jet, hard and soft functions and their scale uncertainties. Each band comes from varying the scale associated with the correction by a factor of two around the default value. In the last plot we show LO power corrections from the fixed-order computation. We have multiplied the distributions by  $\rho$  in order to make the results at larger  $\rho$  visible.

and given in Appendix 4.E. They are the same as for thrust, because the three-parton results for jet mass and thrust agree. Since the light-jet mass vanishes at  $\mathcal{O}(\alpha_s)$ , we can immediately also obtain the LO power corrections for the jet mass distribution. From the plot, we observe that the difference between NLL' and NLL' + LO is very small, and that the contributions from power corrections will reduce the resummed result in the large jet mass region. In order to reproduce the full fixed order result, we use  $C_F = 4/3$  instead of the strict large- $N_c$  value  $C_F = 3/2$  for the hard, jet and soft one-loop corrections in the resummed results. We also use the exact color factors in the evolution factors of the global part (4.45).

The end-point of the jet mass distribution is at  $\rho_{\max} = 1/3$  at  $\mathcal{O}(\alpha_s)$ , corresponding to a symmetrical configuration of the three partons. We will work with the same profile function (4.49) to switch off the higher-order terms at the end point. To adapt it to the present case, we set  $Q_0 = \rho Q$  and  $Q_{\max} = Q/3$ . For simplicity, we will adopt the canonical value  $\mu_j = \sqrt{\mu_s \mu_h}$  in the following and only indirectly vary the jet scale through the variations of  $\mu_s$  and  $\mu_h$ , which we vary independently by a factor of two around their default values.



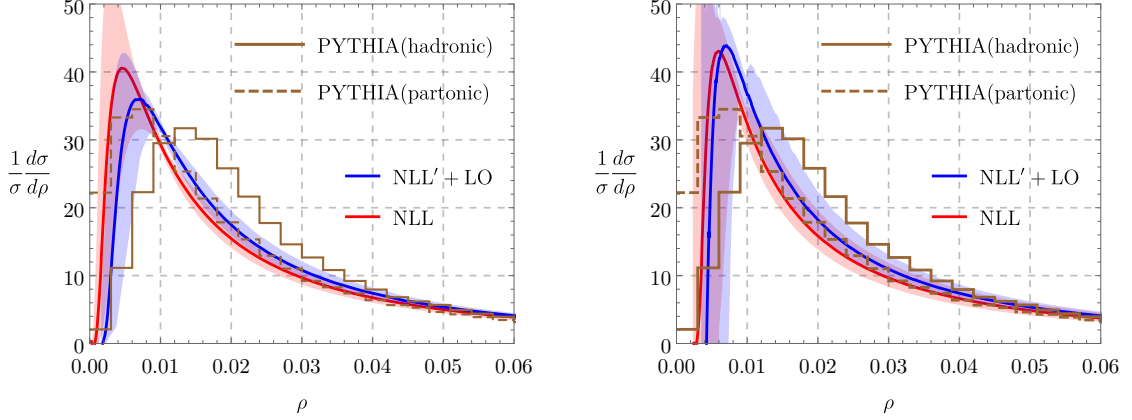


FIGURE 4.9: Jet-mass distribution compared to PYTHIA results. On the left side we plot our default result, based on using the profile scale (4.49) and exponentiating the matching corrections. On the right-hand side, we do not perform these modifications such that we get a negative cross section at low  $\rho$  and hit the Landau pole at a nonzero  $\rho$ .

At very low values of  $\rho$ , the scale  $\mu_s(Q_0)$  hits the Landau pole at  $\Lambda = 0.23 \text{ GeV}$ . Near the pole the soft corrections become large and negative, resulting in a negative cross section. To avoid this unphysical behaviour, we replace  $\mu_s(Q_0) \rightarrow \mu_s(Q_0) + \Lambda$  so that the pole occurs at  $\rho = 0$ . We also exponentiate the hard, jet and soft corrections to avoid the negative cross section. In the left plot of Figure 4.9 we show our result for the jet mass distribution after these modifications. In the right plot, we show the result with  $\mu_s(Q_0) = \rho Q$  and without exponentiation. We observe that the soft scale dependence changes sign at a point to the right of the peak. In this region the soft scale dependence becomes very small. With the modifications in  $\mu_s$ , we end up with quite small scale bands to the right of the peak, which are likely not an accurate characterization of the true uncertainties. The NLL' peak in the right-hand plot is quite a bit higher because the cross section becomes negative below  $\rho = 0.004$  and our distributions are by construction normalized. An important feature of our result is that peak occurs at a very low value  $\rho \approx 0.006$ , which corresponds to  $\mu_s \approx 0.5 \text{ GeV}$  so that the peak region is strongly affected by nonperturbative effects. In Figure 4.9 we also show the PYTHIA [123] results, both on the parton level (dashed lines) and including hadronisation. The hadronisation effects shift the peak to the right by about  $\Delta\rho \approx 0.006$ , in accordance to what one expects from non-perturbative effects in the soft functions [124, 125]. The parton-level PYTHIA result is quite close to the NLL' result.

In Figure 4.10 we compare the NLL' + LO jet mass distribution with ALEPH results [118], obtained by combining their measurements for the light-jet and the heavy-jet mass using (4.2) and adding the uncertainties on the individual measurements in quadrature. One immediately sees that the experimental peak shifted to the right from non-perturbative effects and the shift is compatible with the PYTHIA hadronization result. We also observe that the jet mass distribution falls off quite rapidly and to make the region of larger  $\rho$  visible, we include also a logarithmic plot in Figure 4.10. The plot also illustrates what motivated the profile function (4.49) with  $n = 4$ . The choices ensures that we start switching off the resummation fairly quickly about half-way to the endpoint and go over to the fixed-order result. The plots show that, compared the LO fixed-order result, resummation greatly improved the description of the experimental data. On the other hand there is — if

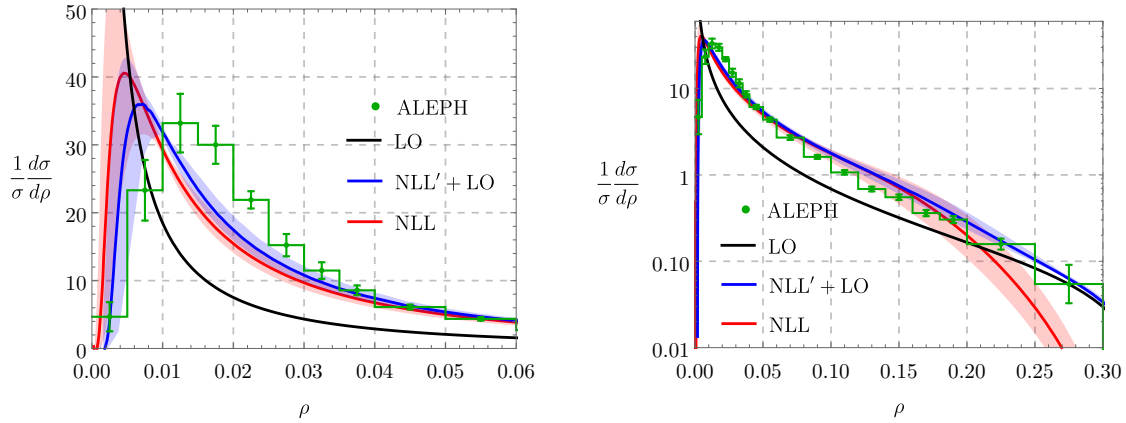


FIGURE 4.10: Jet-mass distribution and comparison to ALEPH data [118] (green dots with error bars). The black curve represents the LO prediction for jet mass, where its analytical expression is given in (4.72). The red curve is the NLL resummation result and the band is from scale variation. The blue curve corresponds to NLL' + LO results, in which we switched off resummation effects at large  $\rho$  using (4.49).

at all — only a relatively narrow region in  $\rho$  in which both higher-order power corrections and non-perturbative corrections are small.

For completeness, we show in Figure 4.11 numerical results for the heavy-jet mass  $\rho_h$  and the light-jet mass  $\rho_\ell$ . The heavy-jet mass is global and provides a reference variable at the same accuracy, but free from all the complications which arise for the jet mass. From the difference of the heavy-jet mass and the jet mass we obtain the light-jet mass. This is more sensitive to the non-global structure and also only has a nontrivial distribution at  $\mathcal{O}(\alpha_s^2)$  so that there is no matching at the accuracy we work. The end-point for the NLO light-jet mass is at  $\rho_{\max} = 1/6$ , which is achieved when the four parton momenta form a tetrahedron, and we use this as the endpoint in our profile function (4.49). From the plot, one observes that also the heavy-jet distribution is affected by nonperturbative effects in the peak region, however, the peak is at a larger  $\rho$  value than for the jet mass itself. Not surprisingly, the worst description of the data arises for the light-jet mass distribution. At larger  $\rho$  values the description is worse because the fixed-order result starts at  $\mathcal{O}(\alpha_s^2)$  so that the matching corrections are beyond the accuracy of our computation. The peak region is not well described because it is in the nonperturbative regime and very narrow.

#### 4.5 CONCLUSION AND OUTLOOK

In this paper we analyzed non-global observables and, for the first time, went beyond a resummation of only the leading non-global logarithms. Specifically, we analyzed the single-logarithmic interjet energy flow at LL' and the double-logarithmic jet mass at NLL'. The prime indicates that we included the full next-to-leading-order corrections to the hard and soft functions, as well as the jet function in the case of jet mass. The practical implementation of these corrections is the main result of the present paper. To achieve full NLL resummation for the interjet energy flow, and NNLL accuracy for the jet mass, we will need to also include the two-loop corrections the RG running, but we observe that the inclusion of the one-loop matching corrections already leads to an improved description of these observables. Since the jet mass peaks at a low value corresponding to a soft scale of  $M_J^2/Q \approx 0.5 \text{ GeV}$  for LEP

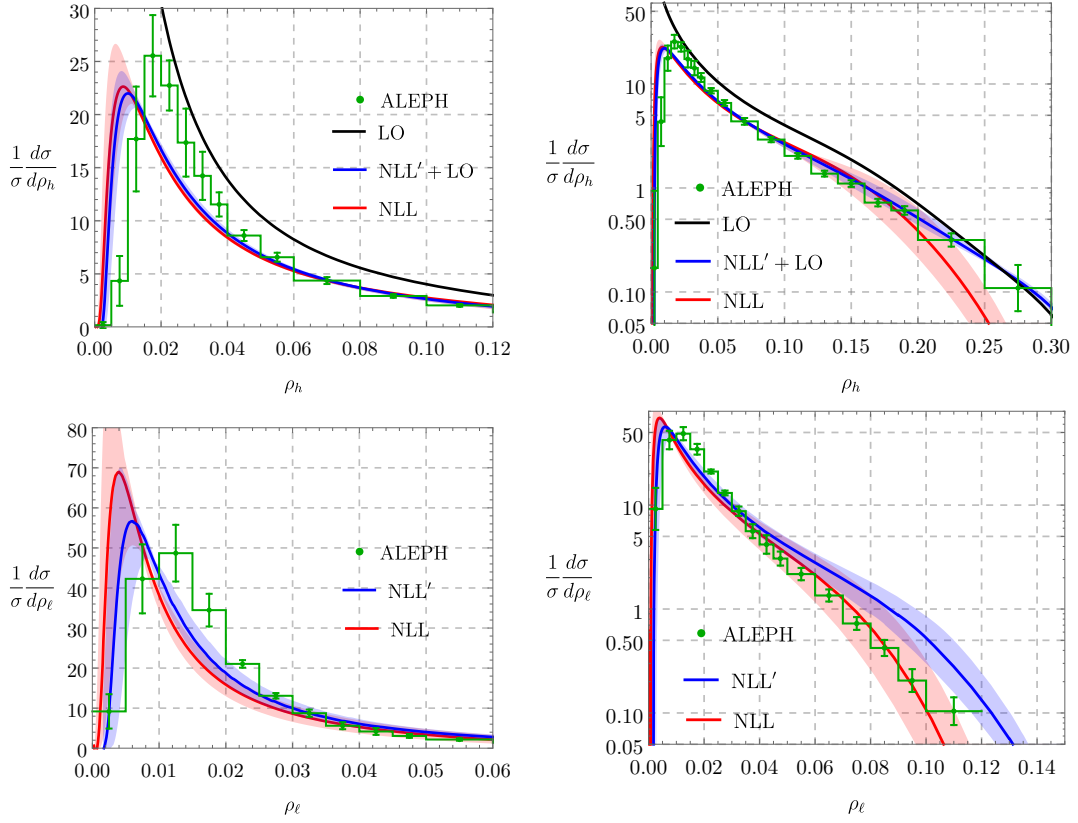


FIGURE 4.11: Light-jet and heavy-jet mass distribution in comparison to ALEPH data [118].

energies, the peak region is strongly affected by non-perturbative effects, similar to what is observed for other event shapes.

Due to the intricate structure of the soft emissions, factorization theorems for non-global observables and the associated RG evolution are much more complicated than in the global case. Instead of analytical computations, one needs to resort to a numerical Monte Carlo framework to perform the resummation. While the global heavy-jet mass only involves a soft function with two Wilson lines, the shower evolution for jet mass produces additional legs, and for low jet masses we can end up with soft emissions from hundreds of hard partons. However, concerning the NLO soft function, this is a minor complication, since we only connect pairs of legs at this accuracy. Indeed, the inclusion of the NLO corrections to the soft function is a minor modification of the leading-logarithmic shower framework. Using the shower emissions which end up in the veto region, we are able to compute the next-to-leading-order correction to the soft function in a general way, with almost no additional computer time.

The more involved part is the implementation of the NLO hard functions. These are in essence the usual real and virtual fixed-order corrections to the Born-level process, but individually suffer from collinear divergences. Computing them in dimensional regularization and renormalizing, one ends up with distributions in the angles of the hard partons which must be implemented into the Monte Carlo framework. We do this with a simple slicing scheme, which works well for two-jet production in  $e^+e^-$  but is certainly not the most efficient method. The problem of combining a parton shower with fixed-order results arises of course also for general purpose showers and elegant solutions such as MC@NLO [126]

and POHWEG [127] are available and have by now been fully automated. A complication in our case is that our shower systematically neglects small soft momenta and therefore does not conserve momentum. As a result, its kinematics is different from the one in the hard functions. While more work is needed on the NLO hard functions, let us note that we have achieved full automation for the leading-order hard functions in our previous paper [18] by working with Les Houches event files generated by the tree-level generator in MADGRAPH5\_AMC@NLO. The same code also provides NLO shower matching and it would be very interesting to adapt it to our shower.

An important next step is of course the inclusion of second-order corrections into the RG-running to achieve the full resummation of subleading non-global logarithms. The corresponding anomalous dimension matrix involves three types of corrections: Double real emissions, real-virtual terms and fully virtual two-loop corrections. The relevant anomalous dimension matrix has been presented in a related framework by Caron-Huot [96]. We are working on determining the anomalous dimension also in our formalism. The implementation into a Monte Carlo framework will be nontrivial, because one needs to numerically handle the collinear singularities of the individual entries. There are a number of recent papers addressing the issue of double emissions in general parton showers [30, 32, 33, 128].

A second interesting challenge is the inclusion of finite- $N_c$  effects, especially for non-global observables at hadron colliders. Our RG-evolution framework is in the general class of showers characterized in [129] and valid at finite  $N_c$ , but implementing the interference effects and complex phases which arise beyond  $N_c \rightarrow \infty$  is challenging. Interesting progress towards the computation of such corrections has been made in [56, 58].

We have analyzed two simple non-global observables in the present paper. This is a first step, but our ultimate goal is of course to use the same methods to understand jet structure at the LHC. For narrow jets, the non-global structure actually factorizes into a structure for each separate jet [24, 25, 107]. Boosting our hemisphere jet mass result such that the left hemisphere transforms into a cone of radius  $R$ , one immediately obtains the non-global structure of the jet mass for an LHC jet of this radius. It will be interesting to analyze such observables in the future.

## ACKNOWLEDGMENTS

The research of T.B. is supported by the Swiss National Science Foundation (SNF) under grant 200020\_182038. T.B. and D.Y.S. would like to express a special thanks to the Mainz Institute for Theoretical Physics (MITP) for its hospitality and support. D.Y.S. acknowledges helpful discussions with Pier Monni on numerical Monte Carlo resummation methods. The authors thank Rudi Rahn and Thomas Rauh for comments on the manuscript.

## 4.A HARD AND SOFT FUNCTIONS FOR INTERJET ENERGY FLOW

### 4.A.1 *Hard functions in the slicing scheme*

We discussed in Section 4.2 that one can use a simple slicing method to implement the plus distribution terms inside hard function  $\mathcal{H}_3^{(1)}(u, v)$  into the shower. In the main text, we have explained the procedure using the toy example (4.25) in which we disregarded the  $u$  dependence. In this appendix we now provide the full expression for the hard function. As explained in Section 4.2, we can directly integrate over  $u$  for the  $\delta(v)$  terms and combine

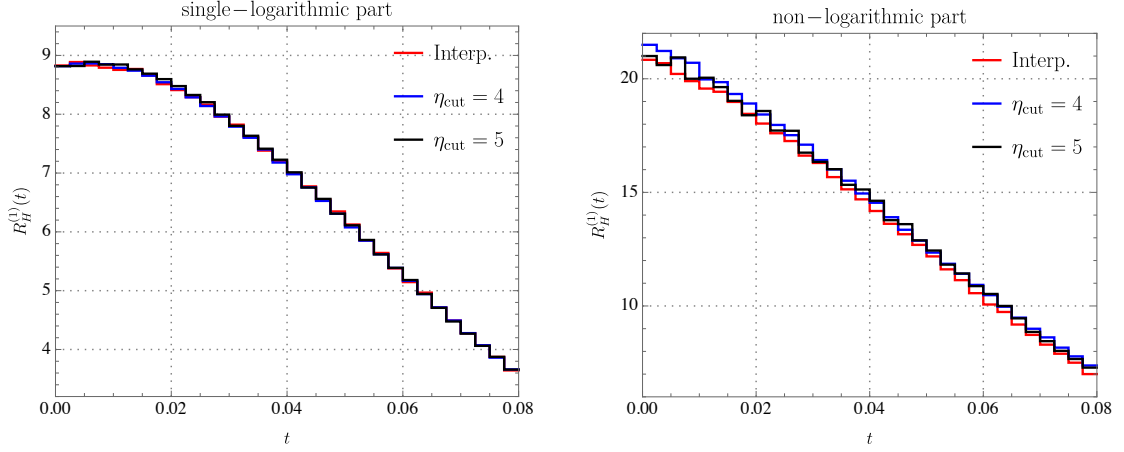


FIGURE 4.12: Numerical comparison among different Monte Carlo implementations of the one-loop hard corrections  $R_H^{(1)}$  to the gap fraction. The red line corresponds to the interpolation method, the other two are obtained using the slicing method with different values of the cutoff  $\eta_{\text{cut}}$ . Left: Coefficient of the single logarithmic part. Right: Non-logarithmic terms.

them with  $\hat{S}_2$ . Since there are no singularities inside Region III, we only give expressions for Regions I and II,

$$\begin{aligned} \mathcal{H}_{3,\text{I}}^{(1)}(u, v, Q, \mu) = C_F \bigg\{ & \left[ 4 \ln^2 \frac{\mu}{Q} + \ln \frac{\mu}{Q} \left( \frac{7}{2} + 8 \ln 2 - 8 \ln v_0 \right) + 4 - \frac{\pi^2}{6} + \frac{7}{2} \ln 2 + 4 \ln^2 2 \right. \\ & + \ln v_0 \left[ \frac{-7 + 2u_0 + 5u_0^2}{2(1+u_0)^2} - 8 \ln 2 + 8 \ln(1+u_0) \right] + 4 \ln^2 v_0 \bigg] \delta(u) \delta(v) \\ & + F(0, v) \delta(u) \frac{\theta(v-v_0)}{v} \left[ \ln u_0 - \ln \frac{\mu}{Q} + \ln v \right] + F(u, v) \frac{\theta(u-u_0) \theta(v-v_0)}{uv} \bigg\} \Theta_{\text{in}}(v), \end{aligned} \quad (4.50)$$

$$\begin{aligned} \mathcal{H}_{3,\text{II}}^{(1)}(u, v, Q, \mu) = C_F \bigg\{ & \left[ \left( \ln \frac{\mu}{Q} - \ln v_0 \right) \left( \frac{5}{2} - 8 \ln 2 \right) + 3 - \frac{2\pi^2}{3} + \frac{5}{2} \ln 2 - 4 \ln^2 2 \right] \delta(u) \delta(v) \\ & + G(u, v) \frac{\theta(v-v_0)}{v} \bigg\} \Theta_{\text{in}}(v), \end{aligned} \quad (4.51)$$

where the cutoffs on  $u$  and  $v$  are chosen as  $u_0 = v_0 = e^{-\eta_{\text{cut}}-1}$  in the parton shower code. The cutoff  $\eta_{\text{cut}}$  is imposed in the parton shower on the rapidity of the emitted hard partons. It can be imposed in the lab frame or in the COM frame of the emitting dipole, see [18] for more discussions. We have checked that the cutoff dependence can be neglected, as can be observed in Figure 4.12 in which we show a numerical comparison between the results based on interpolating the soft function and the slicing method for different cutoffs.

#### 4.A.2 One-loop soft functions

At the one-loop level, virtual corrections from soft gluons are scaleless (and therefore vanish in dimensional regularization), and we only need to include real-emission contributions.

The soft function consists of a  $d$ -dimensional integral with phase-space cuts which ensure that the real emission is outside the jets (the inside part is again scaleless). The relevant soft integral is given by

$$\frac{\alpha_s}{4\pi} S_m^{(1)}(\{\underline{n}\}, Q_0, \epsilon) = -g_s^2 \sum_{(ij)} \mathbf{T}_{i,L} \cdot \mathbf{T}_{j,R} \tilde{\mu}^{4-d} \int \frac{d^d k}{(2\pi)^{d-1}} \frac{n_i \cdot n_j}{n_i \cdot k n_j \cdot k} \delta(k^2) \theta(k^0) \theta(Q_0 - v \cdot k) \Theta_{\text{out}}(n_k), \quad (4.52)$$

with  $\tilde{\mu} = e^{\gamma_E} \mu^2 / (4\pi)$  with  $v^\mu = (1, 0, 0, 0)$  and  $v \cdot k = k^0$ . To evaluate the contribution of the  $(n_i, n_j)$  dipole, we Lorentz transform into a frame where the vectors  $n_i$  and  $n_j$  are back-to-back and the reference vectors take the form

$$\hat{n}_i^\mu = \frac{M}{2}(1, 0, 0, 1), \quad \hat{n}_j^\mu = \frac{M}{2}(1, 0, 0, -1), \quad \hat{v}^\mu = \frac{2}{M}(1, 0, \beta, 0), \quad (4.53)$$

where  $M^2 = 2 n_i \cdot n_j$  is the invariant mass of the dipole pair, and  $\beta = \sqrt{1 - M^2/4}$ . In this frame, we parameterize the integration momentum as

$$k = \hat{k}_T (\cosh \hat{y}, \sin \hat{\phi}, \cos \hat{\phi}, \sinh \hat{y}). \quad (4.54)$$

With  $d = 4 - 2\epsilon$ , the integral then reads

$$\begin{aligned} \int d^d k \frac{\hat{n}_i \cdot \hat{n}_j}{\hat{n}_i \cdot k \hat{n}_j \cdot k} \delta(k^2) \theta(k^0) \theta(Q_0 - k \cdot \hat{v}) \Theta_{\text{out}}(\hat{n}_k) = \\ \frac{\Omega_{d-3}}{2} \int_0^\infty \frac{d\hat{k}_T}{\hat{k}_T^{1+2\epsilon}} \int_{-\infty}^\infty d\hat{y} \int_0^\pi d\hat{\phi} |\sin \hat{\phi}|^{-2\epsilon} \theta(Q_0 - k \cdot \hat{v}) \Theta_{\text{out}}(\hat{n}_k), \end{aligned} \quad (4.55)$$

where  $\Omega_d$  is the surface of the  $d$ -dimensional unit sphere and  $\Omega_1 = 2$ . Introducing the auxiliary function  $f_{ij}$  via

$$k \cdot \hat{v} = f_{ij}(\hat{y}, \hat{\phi}) \hat{k}_T = \frac{2}{M} (\cosh \hat{y} - \beta \cos \hat{\phi}) \hat{k}_T, \quad (4.56)$$

we can perform the integral over  $\hat{k}_T$ . This integration yields a soft divergence, which is renormalized away in the  $\overline{\text{MS}}$  scheme. After expanding in  $\epsilon$  we then immediately arrive at expression (4.29) which only involves a finite angular integration which we perform with the parton shower, which generates its emissions using the variables  $\hat{y}$  and  $\hat{\phi}$ .

#### 4.B MONTE CARLO ALGORITHM FOR THE INTERJET ENERGY FLOW

The inclusion of the NLO soft function is only a minor modification of the algorithm for LL resummation. In fact, the first three steps are identical to what was shown in Appendix B of [18]. The only difference arises in the last step, where we also compute the soft function. To record the results of the shower, we fill three histograms:  $h_U$  contains the LL evolution,  $h_L$  the coefficient of the logarithm of the soft function (4.29) and  $h_c$  its non-logarithmic part.

The shower algorithm for the evolution of the function  $\mathcal{H}_2^{(0)}(\{n_1, n_2\}, Q, \mu_h)$  to lower scales involves the following steps:

1. Start at evolution time  $t = 0$  from an initial event  $E$  with vectors  $\{n_1, n_2\}$  and weight  $w = 1$ .

2. Generate a random time step  $\Delta t$  according to the probability distribution  $\mathcal{P}_E(t) = V_E \exp(-V_E \Delta t)$ , and insert the event weight  $w$  into the histogram  $h_U$  at time  $t + \Delta t$ .
3. Choose a dipole associated with a pair of neighbouring vectors  $n_i$  and  $n_j$  in  $E$  with probability  $V_{ij}/V_E$ . Generate a new random vector  $n_k$  and multiply the weight by the factor  $R_{ij}^k/V_{ij}$ , expressed in the random variables chosen to generate the direction of the new vector  $n_k$ .
4. If  $n_k$  is outside the veto region, add this new vector to the event which then becomes  $E' = \{n_1, \dots, n_i, n_k, n_j, \dots, n_2\}$ , multiply the weight by a factor  $V_E/V_{E'}$  and return to Step 2. Otherwise, add the weight factors

$$w \quad \text{and} \quad \ln \frac{2 |\sin \hat{\phi}|}{f_{ij}(\hat{\phi}, \hat{y})} w \quad (4.57)$$

to  $h_L$  and  $h_c$  at time  $t$ , go to Step 1 and start a new event.

In terms of these histograms, the soft function correction reads

$$\frac{\alpha_s(\mu_s)}{4\pi} \sum_{m=2}^{\infty} \langle \mathcal{H}_2^{(0)} \otimes U_{2m} \hat{\otimes} \mathcal{S}_m^{(1)} \rangle = \frac{N_c}{2} \frac{\alpha_s(\mu_s)}{4\pi} \left[ -4 \ln \frac{\mu}{Q_0} h_L(t) + 4 h_c(t) \right], \quad (4.58)$$

while the LL evolution factor is

$$\sum_{m=2}^{\infty} \langle \mathcal{H}_2^{(0)} \otimes U_{2m} \hat{\otimes} \mathbf{1} \rangle = h_U(t). \quad (4.59)$$

We discussed the implementation of  $\mathcal{H}_3^{(1)}$  in the main text. The shower algorithm is the same as the one described above, up to the fact that one starts the shower with a three parton configuration and does not need to compute the one-loop soft function.

#### 4.C HARD AND SOFT FUNCTIONS FOR THE JET MASS

In this appendix we list one-loop ingredients for the jet mass. The ingredients are closely related to the ones relevant for the interjet energy flow, but the notation is somewhat different. For the jet mass, the hard function  $\mathcal{H}_m^{q(1)}$  denotes the configuration with a quark on the left and  $m$  partons in the right hemisphere, while  $m$  simply counts the total number of hard partons for the interjet energy flow. In the large  $N_c$  limit the renormalized one-loop hard function  $\mathcal{H}_1^i$  are thus given by

$$\mathcal{H}_1^{q(1)}(\hat{\theta}_1, Q, \mu) = \mathcal{H}_1^{\bar{q}(1)}(\hat{\theta}_1, Q, \mu) = \frac{1}{2} \delta(\hat{\theta}_1) H_2(Q^2, \mu). \quad (4.60)$$

The factor of one half is present because the LO total cross section is a sum of two identical contributions with the quark and anti-quark in the left hemisphere, respectively. The  $\delta$ -function of  $\hat{\theta}_1 = \tan(\theta_1/2)$  with  $\theta_i$  ensures that the right parton flies along  $n$ -direction, opposite to the left parton along  $\bar{n}$ .

Since the thrust axis points along the opposite direction of the most energetic parton for a three-jet configuration, also the hard functions  $\mathcal{H}_1^{i(1)}(\hat{\theta}_1, Q, \mu)$  are the same as for the interjet energy flow. We use the same variables  $u$  and  $v$  introduced for the interjet energy flow to



parameterize the angular variables in order to resolve the overlapping divergences inside the angular integration:

$$\begin{aligned} \text{Region I } (\theta_g > \theta_{\bar{q}}) : v &= \tan \frac{\theta_g}{2}, \quad u v = \tan \frac{\theta_{\bar{q}}}{2}, \\ \text{Region II } (\theta_g < \theta_{\bar{q}}) : v &= \tan \frac{\theta_{\bar{q}}}{2}, \quad u v = \tan \frac{\theta_g}{2}, \\ \text{Region III } (\theta_q > \theta_{\bar{q}}) : v &= \tan \frac{\theta_q}{2}, \quad u v = \tan \frac{\theta_{\bar{q}}}{2}, \end{aligned}$$

where the regions are depicted in Figure 4.3. For the jet mass case, we no longer impose a cone constraint (i.e. we can set  $\delta = 1$ ), but we need to add the constraint

$$\Theta_T(u, v) = \theta \left[ \sqrt{1 + u^2 v^2} - (1 + u) v \right] \quad (4.61)$$

to ensure that the thrust axis does not flip. On the level of the bare function, this constraint was given in (4.4) of [104], but was trivially fulfilled for our choice of the cone angle. Due to this constraint, the angle of any parton to the thrust axis cannot be larger than  $\frac{\pi}{3}$ .

Performing the variable transformation and writing the angular convolution as integrals over  $u$  and  $v$  as in (4.23) we have

$$\mathcal{H}_{2,I}^{q(1)}(u, v, Q, \mu) = \frac{1}{2} \mathcal{H}_{3,I}^{(1)}(u, v, Q, \mu) \Theta_T(u, v), \quad (4.62)$$

$$\mathcal{H}_{2,II}^{q(1)}(u, v, Q, \mu) = \frac{1}{2} \mathcal{H}_{3,II}^{(1)}(u, v, Q, \mu) \Theta_T(u, v), \quad (4.63)$$

$$\mathcal{H}_{2,III}^{g(1)}(u, v, Q, \mu) = \frac{1}{2} \mathcal{H}_{3,III}^{(1)}(u, v, Q, \mu) \Theta_T(u, v), \quad (4.64)$$

where the factor  $\frac{1}{2}$  has the same source as in (4.60) and the interjet functions were given in (4.17), (4.19) and (4.21). The anti-quark hard function  $\mathcal{H}_2^{\bar{q}(1)}$  is equal to the quark function. For the gluon function, there is also a region  $\theta_{\bar{q}} > \theta_q$  which is parameterized analogously and gives an identical contribution.

As explained in [104], the soft function for the light-jet mass is directly related to the coft function in Stermann-Weinberg dijet cross section defined in [24]. In Laplace space, we have

$$\begin{aligned} \frac{\alpha_s}{4\pi} \tilde{\mathcal{S}}_m^{(1)}(\{\underline{n}\}, \tau, \epsilon) = \\ - g_s^2 \tilde{\mu}^{2\epsilon} \sum_{(ij)} \mathbf{T}_{i,L} \cdot \mathbf{T}_{j,R} \int \frac{d^d k}{(2\pi)^{d-1}} \delta(k^2) \theta(k^0) e^{-\bar{n} \cdot k / (\tau e^{\gamma_E})} \frac{n_i \cdot n_j}{n_i \cdot k n_j \cdot k} \theta(n \cdot k - \bar{n} \cdot k). \end{aligned} \quad (4.65)$$

The evaluation of this expression proceeds along the same lines as for the interjet energy flow case derived in detail in Appendix 4.A. If both emitting partons are in the right hemisphere, the renormalized one-loop result is given by

$$\tilde{\mathcal{S}}_m^{(1)}(\{\underline{n}\}, \tau, \mu) = \frac{N_c}{2} \sum_{i,j=1}^m \delta_{i,j \pm 1} \int d\hat{y} \frac{d\hat{\phi}}{2\pi} \left[ -4 \ln \frac{\mu}{\tau} + 4 \ln \frac{2 |\sin \hat{\phi}|}{g_{ij}(\hat{\phi}, \hat{y})} \right] \Theta_L^{\text{lab}}(\hat{y}, \hat{\phi}), \quad (4.66)$$

with the measurement function  $\Theta_L^{\text{lab}}(\hat{y}, \hat{\phi})$  constraining the soft radiation to the left hemisphere, and a function

$$\begin{aligned} g_{ij}(\hat{\phi}, \hat{y}) = \frac{1}{\beta M} \left[ 2\beta \cosh \hat{y} + \beta e^{\hat{y}} \tanh y_i + \beta e^{-\hat{y}} \tanh y_j - \cos \hat{\phi} [2\beta^2 + \tanh y_i + \tanh y_j] \right. \\ \left. + \text{sech } y_i \text{sech } y_j \sin \hat{\phi} \sin(\phi_i - \phi_j) \right]. \end{aligned} \quad (4.67)$$

If one of the two partons is on the left, the function has a collinear divergence, which can be subtracted, as detailed in Section 4.3. The subtraction was given in (4.41).

#### 4.D MONTE CARLO ALGORITHM FOR THE JET MASS DISTRIBUTION

In this appendix we provide the Monte Carlo algorithm used for jet mass resummation, which is also applicable for other non-global observables with soft-collinear double logarithms. Compared to interjet energy flow, we need to subtract the global anomalous dimension and the one-loop global soft function. As for the interjet energy case, we fill three histograms:  $h_U$  contains the LL evolution,  $h_L$  the coefficient of the logarithm of the soft function (4.66) and  $h_c$  its non-logarithmic part.

The algorithm for evolving  $\mathcal{H}_1^q$  to lower scales involves the following steps:

1. Start at evolution time  $t = 0$  from an initial event  $E$  with vectors  $\{\bar{n}, n_1\}$  and weight  $w = 1$ .
2. Generate a random time step  $\Delta t$  according to the probability distribution  $\mathcal{P}_E(t) = \bar{V}_E \exp(-\bar{V}_E \Delta t)$ , and insert the event weight  $w$  into the histogram  $h_U$  at time  $t + \Delta t$ .
3. Choose a dipole associated with a pair of neighbouring vectors  $n_i$  and  $n_j$  in  $E$  with probability  $V_{ij}/V_E$ . Generate a new random vector  $n_k$  and multiply the weight by the factor  $R_{ij}^k/V_{ij}$ , expressed in the random variables chosen to generate the direction of the new vector  $n_k$ .
4. If  $n_k$  is in the right hemisphere, add this new vector to the event so that  $E' = \{\bar{n}, \dots, n_i, n_k, n_j, \dots, n_1\}$ , multiply the weight by a factor  $V_E/\bar{V}_{E'}$  and return to Step 2. If  $n_k$  is in the left hemisphere and was emitted from dipole  $(\bar{n}, n_j)$ , we need to subtract the global one-loop soft function  $\tilde{S}_G^{q(1)}$  in equation (4.41). This is achieved with the weight factors

$$[1 - X(\hat{\phi}, \hat{y})] w \quad \text{and} \quad \ln \frac{2 |\sin \hat{\phi}|}{g_{0j}(\hat{\phi}, \hat{y})} [1 - X(\hat{\phi}, \hat{y})] w, \quad (4.68)$$

which are added to the histograms  $h_L$  and  $h_c$  at time  $t$ . After filling the histograms go to Step 1 and start a new event. Otherwise, add the unsubtracted weight factor

$$w \quad \text{and} \quad \ln \frac{2 |\sin \hat{\phi}|}{g_{ij}(\hat{\phi}, \hat{y})} w \quad (4.69)$$

to the respective histograms, go to Step 1 and start a new event.

The quantity  $\bar{V}_E$  denotes the subtracted global anomalous dimension  $\bar{V}_E = V_E - V_0$ , where  $V_0$  is the large- $N_c$  result for the subtraction (4.35) obtained by replacing the Casimir operator  $C_i$  in this equation by  $N_c/2$  for a quark jet, or  $N_c$  for a gluon jet, respectively.

## 4.E INGREDIENTS FOR JET MASS RESUMMATION

For convenience, we collect here the perturbative results for ingredients used in the resummation formula for jet mass distribution. The evolution factors at NLL accuracy are given by

$$S(\nu, \mu) = \frac{\gamma_0^{\text{cusp}}}{4\beta_0^2} \left\{ \frac{4\pi}{\alpha_s(\nu)} \left( 1 - \frac{1}{r} - \ln r \right) + \left( \frac{\gamma_1^{\text{cusp}}}{\gamma_0^{\text{cusp}}} - \frac{\beta_1}{\beta_0} \right) (1 - r + \ln r) + \frac{\beta_1}{2\beta_0} \ln^2 r \right\},$$

$$A_\gamma(\nu, \mu) = \frac{\gamma_0}{2\beta_0} \ln r, \quad (4.70)$$

with  $r = \alpha_s(\mu)/\alpha_s(\nu)$ . The expressions of the anomalous dimensions used in our paper are

$$\begin{aligned} \gamma_0^{\text{cusp}} &= 4, \quad \gamma_1^{\text{cusp}} = \left( \frac{268}{9} - \frac{4\pi^2}{3} \right) C_A - \frac{80}{9} T_F n_f, \\ \gamma_0^{J_q} &= -3C_F, \quad c_1^{J_q} = C_F \left( 7 - \frac{2\pi^2}{3} \right), \quad \gamma_0^{J_s} = -\beta_0, \\ \beta_0 &= \frac{11}{3} C_A - \frac{4}{3} T_F n_f, \quad \beta_1 = \frac{34}{3} C_A^2 - \frac{20}{3} C_A T_F n_f - 4C_F T_F n_f. \end{aligned} \quad (4.71)$$

The LO integrated jet mass distribution is written as

$$\begin{aligned} \frac{1}{\sigma_0} \int_0^\rho d\bar{\rho} \frac{d\sigma^{\text{LO}}}{d\bar{\rho}} &= 1 + C_F \frac{\alpha_s}{2\pi} \left[ -\ln^2 \rho - \frac{3}{2} \ln \rho + \frac{1}{4} + \frac{\pi^2}{6} - 2 \text{Li}_2 \left( \frac{\rho}{1-\rho} \right) + \frac{9\rho^2}{4} + 3\rho \right. \\ &\quad \left. - \ln^2(1-\rho) + \frac{3}{2}(1-2\rho) \ln(1-2\rho) + [3\rho + 2\ln(1-\rho)] \ln \rho \right]. \end{aligned} \quad (4.72)$$

The integrated light-jet mass distribution is trivial at this order

$$\int_0^\rho d\bar{\rho} \frac{d\sigma^{\text{LO}}}{d\bar{\rho}} = \sigma_0 \left( 1 + C_F \frac{3\alpha_s}{4\pi} \right) = \sigma, \quad (4.73)$$

because the light jet has zero mass for three partons.

## RESUMMATION OF NON-GLOBAL LOGARITHMS IN CROSS SECTIONS WITH MASSIVE PARTICLES

---

*Quarantine, quarantine, drinkin' whiskey like vaccine;  
Wavin' at the neighbors, social distancing;  
Quarantine, quarantine, wearing Lysol like sunscreen;  
Quarantine, quarantine, oh, lonesome quarantine...*

— Mat Best & Tim Montana

This chapter is a copy of [20], accepted for publication in the Journal of High-Energy Physics (JHEP).

### ABSTRACT

A factorization formalism for jet processes involving massive colored particles such as the top quark is developed, extending earlier results for the massless case. The factorization of soft emissions from the underlying hard process is implemented in an effective field theory framework, which forms the basis for the resummation of large logarithms. The renormalization group evolution giving rise to non-global logarithms is implemented into a parton shower code in the large- $N_c$  limit. After a comparison of the massive and massless radiations patterns, the cross section for  $t\bar{t}$  production with a veto on additional central jet activity is computed, taking into account radiation both from the production and the decay of the top quarks. The resummation of the leading logarithms leads to an improved description of ATLAS measurements at  $\sqrt{s} = 7$  TeV.

### 5.1 INTRODUCTION

The study of jet cross sections plays a crucial role in high-energy physics. While theoretical calculations are carried out in terms of interactions at the field level, detectors are only able to measure properties of outgoing particles after they have fully hadronized, i.e. transformed from colored quarks and gluons to color-neutral final states such as mesons. Consequently, it is impossible to measure the underlying hard scattering process directly, but one needs to reconstruct it by measuring jets and analyzing their properties.

While the total energy of the particles inside the jets is typically of the same order as the partonic center-of-mass energy of the collision, the total energy of the particles not ending up in a jet is considerably lower. Due to this scale separation effective field theory methods, in particular Soft-Collinear Effective Theory (SCET) [23, 27, 28] (see [7, 29, 130] for reviews), are useful in the study of jet cross sections. In the effective theory the cross sections factor into hard, collinear and soft functions, each of which can be safely evaluated in fixed-order perturbation theory at their characteristic energy scale. To connect these factors, it is then necessary to evolve one of the factors from its characteristic scale to the scale of the other factor by using the Renormalization Group (RG) equation. This procedure was first applied to jet cross sections in [24, 25].

Because of their multi-scale nature, jet cross sections are sensitive to potentially large logarithmic corrections. When evaluating the phase-space integrals of matrix elements and applying cuts to the allowed energies, logarithms of the ratios of the energy scales involved in the process appear in the calculations. For example, when the energy of particles inside the jets (denoted by  $Q$ ) is unconstrained and of the same order as the partonic center-of-mass energy, i.e.  $Q^2 \sim \hat{s}$ , but the energy outside the jets (denoted by  $Q_0$ ) is required to be small, the phase-space integrals produce terms proportional to  $\ln(Q/Q_0)$ . These logarithms become large if  $Q_0 \ll Q$ . The pattern of logarithms encountered in jet cross sections is particularly complicated since they are examples of non-global observables, as was first observed in [26]. Due to the complexity of these observables analytic resummation is not possible and the paper [26] introduced a parton-shower approach to capture the enhanced higher-order terms.

The factorization formula studied in [24, 25], and in a closely related form in [96], are derived within the effective field theory approach and can be used to resum these corrections, in principle to all logarithmic orders, extending the earlier approaches [26, 38] which were restricted to leading logarithmic (LL) accuracy. Based on this theoretical framework, a dedicated parton shower code was developed and applied to resum the large logarithms appearing in jet processes and isolation-cone cross sections up to LL order in [18]. Subsequently, higher-order matching corrections in both the hard and the soft function were added. This led to the resummation of the interjet energy flow up to LL' accuracy and to the resummation of the jet mass up to next-to-leading-logarithmic (NLL') accuracy in [19]. As usual, the prime in LL' and NLL' indicates that the matching corrections are included one order higher than what it would be required in RG improved perturbation theory. In the present case, this means that NLO hard and soft functions were used. By supplementing these calculations with the two-loop corrections to the anomalous dimension matrix one would achieve full NLL and next-to-next-to-leading logarithmic (NNLL) accuracy, respectively.

The work done so far was carried out in the high-energy limit where all partons can be considered massless. The purpose of this paper is to extend the approach of [18, 19, 24, 25] to processes involving heavy colored particles and to develop and validate a parton shower code for the resummation of jet cross sections in top-quark production processes. Soft radiation is obtained from matrix elements of Wilson line operators along the directions of the emitting particles, independently of the mass of the emitting parton. Because of this fact, the factorization theorem has the same general form as in the purely massless case. However, the soft radiation pattern and its generation by the parton shower code differ significantly in the two cases. At one-loop order, the angular dependence of the radiation of a soft parton with momentum  $k^\mu = E n_k^\mu$  between legs carrying momenta  $p_i$  and  $p_j$  is given by the usual product of eikonal factors

$$W_{ij}^k = \frac{p_i \cdot p_j}{p_i \cdot n_k \, n_k \cdot p_j}. \quad (5.1)$$

This factor is the same in both cases, but massless particles are traveling along light-like directions, while massive particles travel along time-like directions. This difference in kinematics must be accounted for in the shower code. Furthermore, in contrast to what happens in the high-energy limit, the radiation factor in (5.1) does not vanish when  $i = j$ , if  $p_i$  is a time-like momentum. Therefore, in addition to the usual dipole emission pattern, it is necessary to include monopole contributions in the massive case. The latter describes radiation that is emitted and absorbed by the same Wilson line rather than exchanged

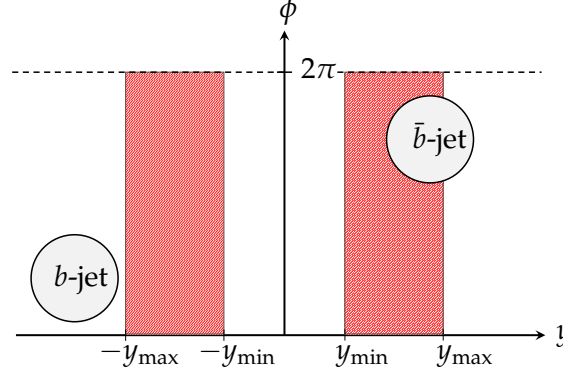


FIGURE 5.1: Sketch of the veto region as defined by ATLAS in [134]. The gap, in which additional radiation is vetoed, is represented by the shaded red area with rapidity  $y_{\min} < |y| < y_{\max}$ . Radiation inside the  $b$ -tagged jets is not vetoed. For  $y_{\min} = 0$ , this setup reduces to the usual central jet veto.

between two color-connected Wilson lines. This difference in the massive and massless radiation pattern is of course well known, in particular the different collinear behavior, which is often referred to as the *dead cone effect* [2, 131–133].

As an application of the new parton shower code described in this work, we consider  $t\bar{t}$  production with a veto on additional central jet energy. This process was measured by ATLAS at the Large Hadron Collider (LHC) with the goal of testing the description of soft radiation in parton showers [134]. The top pair production process involves two initial-state partons producing a  $t\bar{t}$ -pair in the final state. The top quarks then decay into bottom quarks and  $W$  bosons. The measurement is performed using events in which the  $W$ 's decay leptonically and in which two  $b$ -jets are detected. The veto on central jets is imposed by requiring that, with the exception of the two bottom-tagged jets, no additional jets above a given transverse momentum  $Q_0$  are allowed to be present in the rapidity range  $y_{\min} < |y| < y_{\max}$  (see Figure 5.1). With the veto, only particles of low energy are allowed inside this rapidity range, while the energy is unconstrained anywhere else. This is a typical situation in which large non-global logarithms appear. In this work these logarithms are resummed at LL accuracy and the results of the resummation are matched to NLO predictions in fixed-order perturbation theory.

In addition to radiation effects associated with the production process, one should also include radiation emerging from the decay products of the top quarks. We work in the narrow-width approximation for the top quarks, in which they are treated as stable particles and the process factorizes into a production cross section multiplied by the decay of the top quarks. It is well known that radiation from the  $b$ -quarks that would contribute to non-factorizable corrections in fixed-order perturbation theory is suppressed by factors of  $\mathcal{O}(\Gamma_t/m_t)$  [135–140]. To account for the factorizable contributions, we run a separate shower for the top decay to also account for the  $b$ -quark radiation. Numerically, the effect of this radiation is smaller than the one from the production of the top pair since the radiation inside the  $b$ -jet is not constrained. However, the radiation from the decay is large enough that it must be taken into account. Figure 5.2 shows one of the several tree-level diagrams contributing to the  $t\bar{t}$ -pair production process measured by ATLAS in [134]. We also depict the color dipoles, which are the source of the emissions in the large- $N_c$  limit.

The remainder of this paper is organized as follows. In Section 5.2 the factorization theorem [24, 25] is reviewed and the changes needed in presence of massive partons are

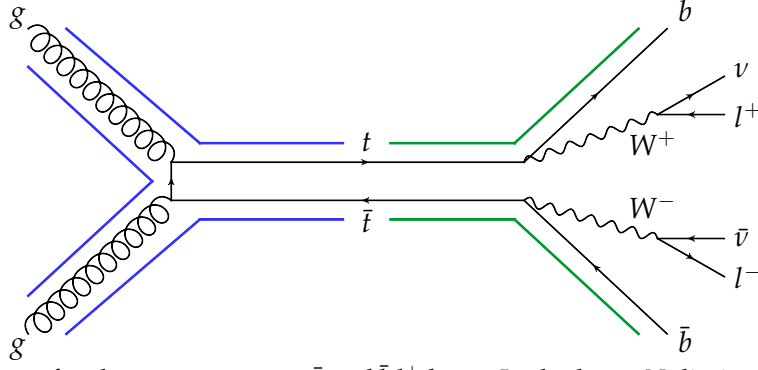


FIGURE 5.2: Diagram for the process  $gg \rightarrow t\bar{t} \rightarrow b\bar{b} l^+ l^- \nu \bar{\nu}$ . In the large- $N_c$  limit, the radiation can be split into a set of color dipoles. The color dipoles associated to the production of the  $t\bar{t}$  pair are shown in blue, the ones associated to the decay in green. The full LL cross section will include the emissions from all five dipoles.

discussed. Section 5.3 describes in detail how the relevant phase-space integrals can be evaluated in the parton shower code. In Section 5.4 we assess the impact of massive partons in the resummation of non-global logarithms. An explicit example of the resummation of non-global logarithms for a cross section involving top quarks at LL accuracy is presented in Section 5.5. As indicated above, the observable we consider is top-pair production with a veto on central jet energy. The predictions for this observable are then matched to the NLO result and compared to experimental measurements carried out by ATLAS. Section 5.6 contains our conclusions and an outlook. In Appendix 5.A, we use a sample event to illustrate our parton shower code step by step. In Appendix 5.B we explain how to use the shower to also compute the first two orders of the fixed-order expansion of the resummed result.

## 5.2 FACTORIZATION FOR CROSS SECTIONS INVOLVING MASSIVE QUARKS

Before discussing the factorization of the cross section, we should determine which scales are present and which scale hierarchies can arise in the observable under study. Throughout this paper, we consider scattering processes at a large center-of-mass energy  $Q$  and impose a veto on radiation in a certain phase-space region. We are interested in a regime where the energy scale  $Q_0$  of the soft radiation in the veto region is much smaller than  $Q$ . The presence of the massive particles introduces additional scales in the process. On top of the masses themselves, which we denote generically with  $M$ , the most important new scale is the production threshold: when massive particles are produced, only part of the energy  $Q$  is available for additional radiation. We denote by  $Q_1$  the energy above threshold that can be radiated. For  $t\bar{t}$  production, the threshold is at  $Q_T = 2m_t$  and the maximal energy available to radiation is

$$Q_1 = \frac{Q^2 - 4m_t^2}{2Q}. \quad (5.2)$$

Kinematically, this value corresponds to a configuration where a collinear  $t\bar{t}$  pair recoils against a gluon. This is a corner of phase space and the typical gluon energy will be much lower. However, the scale of the hardest possible emission plays an important role since it corresponds to the large scale in the emission process which should be compared to the veto scale  $Q_0$ . Since we are interested in non-global logarithms associated with soft radiation, we



only consider  $Q_1 \gg Q_0$ , but even under this assumption, one should consider two different hierarchies, namely a)  $Q \sim Q_1$  and b)  $Q \gg Q_1$ .

The simpler of the two cases is  $Q \sim Q_1$ , which implies that the process energy is far larger than the threshold energy, and that the masses are smaller than the maximum emission energy,  $Q_1 \gg M$ . It is then interesting to ask what role the masses themselves play and whether we encounter logarithms of the masses. If the heavy partons are not in the veto region, the vetoed cross section is collinear safe and mass effects are power suppressed in the limit  $M \rightarrow 0$ ; the massless limit is smooth. On the other hand, if the massive partons are inside the veto region, the limit  $M \rightarrow 0$  becomes complicated. Of course, in top-pair production, several additional complications arise when considering the limit  $m_t \rightarrow 0$ . In this paper, we only consider the case where  $M$  is larger or of the same order as  $Q_0$ .

In the case in which  $Q \gg Q_1$  instead, the process occurs near threshold and the emissions are always soft compared to the particle masses. At the same time, we want to have  $Q_1 \gg Q_0$ , therefore the distance of  $Q$  from the threshold must still be large compared to the scale of soft radiation. Phenomenologically, this situation can only be relevant for top quarks and quite stringent vetoes. Since the radiation is always soft compared to the heavy particles, we should describe the entire process in Heavy Quark Effective Theory (HQET) (for reviews see [141, 142]). One would first match QCD onto HQET at the scale  $Q$  and evolve to  $Q_1$  before computing the soft emissions. It should be noted that this first matching will also have to be performed for the total cross section in the same kinematic regime. The effect will therefore largely cancel in ratios of cross sections such as the gap fraction. Furthermore, if one gets very close to the threshold  $Q_1 \sim M\alpha_s$ , the heavy quarks become non-relativistic, but in view of  $Q_1 \gg Q_0$  this regime is not important phenomenologically. When we apply our formalism to top-pair production at the LHC at  $\sqrt{s} = 7$  TeV, we find that the average  $Q$  of the partonic collisions is  $Q \approx 520 \text{ GeV} \sim 3m_t$  and  $Q_1 \approx 150 \text{ GeV}$ . Therefore, in the phenomenological application considered in this work the scale hierarchy lies in between cases a) and b). In our application, we also include the decay of the tops. The large scale for the emissions associated with the decay is  $\sqrt{m_t^2 + p_T^2}$ , where  $p_T$  is the average transverse momentum of the produced top quarks. For simplicity and since they are numerically similar, we will evaluate this contribution with the same hard scale that is relevant for the production.

We discussed the two scenarios a) and b), but together with the scale  $M$ , also combinations of scenarios can arise. For example, for  $Q_1 \gg M$ , it is possible to emit additional massive partons (at leading logarithmic accuracy only gluons are emitted). Then, for  $Q_1 \gg M \gg Q_0$ , one could imagine a two step procedure, where one would start in scenario a), but after a number of emissions, only a small energy is left and one would switch over to scenario b). Massive theories have a much richer set of kinematic configurations than massless ones and can involve complicated interplays of different scales.

Here we first describe factorization for the simple case a), restricting ourselves to  $e^+e^-$  cross sections for the moment. After presenting the result, we discuss how it should be modified to account for the case b). The factorization formula for a jet production with a veto on radiation in part of the phase space takes the form

$$\sigma(Q, Q_0) = \sum_{m=m_0}^{\infty} \langle \mathcal{H}_m(\{\underline{v}\}, \{\underline{n}\}, Q, \mu) \otimes \mathcal{S}_m(\{\underline{v}\}, \{\underline{n}\}, Q_0, \mu) \rangle, \quad (5.3)$$

where  $m_0$  is the number of final-state jets. The hard function  $\mathcal{H}_m$  describes the production of  $m$  partons in the unconstrained region and the soft function  $\mathcal{S}_m$  is the matrix element

squared of the emission from Wilson lines along the  $m$  partons of the hard function. Both of these functions depend on the directions of the  $k$  massive partons  $\{\underline{v}\} = \{v_1, \dots, v_k\}$  and  $m - k$  massless partons  $\{\underline{n}\} = \{n_{k+1}, \dots, n_m\}$ . As discussed above, the hard functions  $\mathcal{H}_m$  also depend on the particle masses and derived quantities such as  $Q_1$ . In order not to overburden the notation, we suppress this dependence. The symbol  $\otimes$  indicates an integral over the directions of the  $m$  particles and  $\langle \dots \rangle$  denotes the color trace which is taken after combining the functions. Up to the fact that some reference vectors are time-like, this formula is identical to the one studied in [18, 19, 24].

The hard functions  $\mathcal{H}_m$  are free of large logarithms if one chooses a value  $\mu \sim Q$  for the renormalization scale. The same is achieved for the soft functions  $\mathcal{S}_m$  for  $\mu \sim Q_0$ . For  $Q \gg Q_0$ , at least one of these two functions will involve large logarithms, irrespective of the scale choice. These large logarithms can be resummed by solving the RG equation of the hard function and evolving it from its characteristic scale  $\mu_h \sim Q$  down to a soft scale  $\mu_s \sim Q_0$ , leading to

$$\sigma(Q, Q_0) = \sum_{l=m_0}^{\infty} \langle \mathcal{H}_l(\{\underline{v}\}, \{\underline{n}'\}, Q, \mu_h) \otimes \sum_{m \geq l}^{\infty} U_{lm}(\{\underline{v}\}, \{\underline{n}\}, \mu_s, \mu_h) \hat{\otimes} \mathcal{S}_m(\{\underline{v}\}, \{\underline{n}\}, Q_0, \mu_s) \rangle, \quad (5.4)$$

where the evolution factor is just the path-ordered exponential of the anomalous dimension

$$U(\{\underline{n}\}, \mu_s, \mu_h) = \mathbf{P} \exp \left[ \int_{\mu_s}^{\mu_h} \frac{d\mu}{\mu} \mathbf{\Gamma}^H(\{\underline{v}\}, \{\underline{n}\}, \mu) \right], \quad (5.5)$$

which evolves the  $l$ -parton configuration along the time-like directions  $\{\underline{v}\} = \{v_1, \dots, v_k\}$  and the light-like directions  $\{\underline{n}'\} = \{n_{k+1}, \dots, n_l\}$  into an  $m$ -parton final state including the time-like directions  $\{\underline{v}\}$  and the light-like directions  $\{\underline{n}\} = \{n_{k+1}, \dots, n_l, n_{l+1}, \dots, n_m\}$ . RG evolution generates additional massless particles and  $\hat{\otimes}$  denotes the integration over their directions before integrating over the hard directions.

Up to now we worked under the assumptions that  $Q_1 \sim Q$ . Alternatively, if  $Q \gg Q_1$ , the hard functions involve large logarithms of the ratio  $Q_1/Q$  which are not resummed by the above treatment. In order to factorize the two scales, one must first match onto HQET. For  $e^+e^- \rightarrow \gamma^* \rightarrow t\bar{t}$ , it is necessary to match the electromagnetic current operator which induces the process onto the corresponding HQET operator

$$J_{\text{e.m.}}^\mu = \bar{t} \gamma^\mu t \rightarrow C_V(v \cdot v', Q, \mu) \bar{h}_{v'} \gamma^\mu h_v, \quad (5.6)$$

where  $h_v$  and  $h_{v'}$  are the two HQET fields describing the top and the anti-top quarks. One would then derive an expression analogous to (5.4) in HQET. The hard functions arising would be related to the ones in (5.4) by

$$\mathcal{H}_l(\{\underline{v}\}, \{\underline{n}'\}, Q, \mu) = |C_V(v \cdot v', Q, \mu)|^2 \mathcal{H}_l^{\text{HQET}}(\{\underline{v}\}, \{\underline{n}'\}, Q_1, \mu) + \mathcal{O}(Q_1/Q). \quad (5.7)$$

To resum the logarithms of  $Q_1/Q$ , one will first solve the RG of  $C_V$  to run from the scale  $\mu \approx Q$  down to  $\mu \approx Q_1$ . When computing the gap fraction, one will also compute the total cross section in HQET using (5.6). The anomalous dimension driving the running of  $C_V$  is the massive cusp anomalous dimension with the cusp angle defined by the two vectors  $v$  and  $v'$ . In the ratio defining the gap fraction, the Wilson coefficient  $C_V$  and its running will drop out. The situation is more complicated for hadron colliders, which involve sums of different partonic channels with different running so that the cancellation between numerator and

denominator will not be complete. The general form of the anomalous dimension for a process with massive partons was given in [143] and the explicit forms relevant for top production can be found in [144], but we will not study the small effect of this running in this work. However, an important lesson from the above discussion is that one should set the scale  $\mu_h \sim Q_1$  in observables such as the gap fraction, since most of the running above this scale will drop out in the ratio of cross sections.

In (5.5) we have presented the formal solution to the evolution equation. We will now discuss how the general solution simplifies at LL accuracy and how it can be implemented as a parton shower. In dijet processes at lepton colliders, one only needs to consider the case  $l = m_0 = 2$  at LL, as the contribution of additional partons to the hard function would be suppressed by additional powers of  $\alpha_s$  for  $\mu_h \sim Q$ . On the other side of the energy spectrum, the LL soft function is simply the unit matrix in the color space of the  $m$  final-state partons, since any soft correction would again be suppressed by a factor  $\alpha_s$  at the low scale  $\mu_s \sim Q_0$ . When computing  $t\bar{t}$  production at a future electron-positron collider with a sufficiently high center-of-mass energy at LL accuracy, the general result (5.4) therefore simplifies to

$$\sigma_{\text{LL}}(Q, Q_0) = \sum_{m=2}^{\infty} \langle \mathcal{H}_2(\{v_1, v_2\}, \{\}, Q, \mu_h) \otimes U_{2m}(\{v_1, v_2\}, \{\underline{n}\}, \mu_s, \mu_h) \hat{\otimes} \mathbf{1} \rangle. \quad (5.8)$$

The situation is more complicated at hadron colliders such as the LHC, where the initial state contains two additional colored hard partons, which give rise to non-perturbative Parton-Distribution Functions (PDFs). In addition, Glauber gluons can induce interactions between soft and collinear partons. This complication is absent in the large- $N_c$  limit in which we perform our computations. In this limit, the only difference to the  $e^+e^-$  case is that there are two additional Wilson lines which describe the soft initial-state radiation.

For LL resummation one needs the anomalous dimension only at one-loop accuracy. Consequently, the exponent of the evolution matrix in (5.5) reduces to

$$\int_{\mu_s}^{\mu_h} \frac{d\mu}{\mu} \mathbf{\Gamma}^H = \int_{\alpha_s(\mu_s)}^{\alpha_s(\mu_h)} \frac{d\alpha}{\beta(\alpha)} \frac{\alpha}{4\pi} \mathbf{\Gamma}^{(1)} = \frac{1}{2\beta_0} \ln \frac{\alpha_s(\mu_s)}{\alpha_s(\mu_h)} \mathbf{\Gamma}^{(1)} \equiv t \mathbf{\Gamma}^{(1)}. \quad (5.9)$$

The “evolution time”  $t$  measures the separation of the scales  $\mu_s$  and  $\mu_h$ : one finds  $t = 0$  for  $\mu_s = \mu_h$  and a growing  $t$  for increasing separation  $\mu_s < \mu_h$ . As the soft scale approaches the Landau pole, one finds  $t \rightarrow \infty$ . If the scale  $\mu_h$  is kept fixed the function  $t \equiv t(\mu_s)$  is bijective.

The discussion so far applies both to massive and to massless partons. The difference between the two cases becomes evident when one considers the one-loop anomalous dimension matrix

$$\mathbf{\Gamma}^{(1)} = \begin{pmatrix} \mathbf{V}_2 & \mathbf{R}_2 & 0 & 0 & \dots \\ 0 & \mathbf{V}_3 & \mathbf{R}_3 & 0 & \dots \\ 0 & 0 & \mathbf{V}_4 & \mathbf{R}_4 & \dots \\ 0 & 0 & 0 & \mathbf{V}_5 & \dots \\ \vdots & \vdots & \vdots & \vdots & \ddots \end{pmatrix}, \quad (5.10)$$

where the matrix elements  $\mathbf{R}_m$  and  $\mathbf{V}_m$  (which are themselves matrices in color space) are associated with the emission of a real or virtual soft gluon

$$\begin{aligned} \mathbf{V}_m = 2 \sum_{i,j=1}^m (\mathbf{T}_{i,L} \cdot \mathbf{T}_{j,L} + \mathbf{T}_{i,R} \cdot \mathbf{T}_{j,R}) \int \frac{d\Omega(n_k)}{4\pi} W_{ij}^k \\ - 2i\pi \sum_{i,j=1}^m (\mathbf{T}_{i,L} \cdot \mathbf{T}_{j,L} - \mathbf{T}_{i,R} \cdot \mathbf{T}_{j,R}) \Pi_{ij}, \end{aligned} \quad (5.11)$$

$$\mathbf{R}_m = -4 \sum_{i,j=1}^m \mathbf{T}_{i,L} \cdot \mathbf{T}_{j,R} W_{ij}^{m+1} \Theta_{\text{in}}(n_{m+1}). \quad (5.12)$$

The color matrices  $\mathbf{T}_{i,L}$  act on the hard function from the left, i.e. on the amplitude, while  $\mathbf{T}_{i,R}$  act on the conjugate amplitude. The function  $\Theta_{\text{in}}$  enforces that the hard emission is inside the allowed region. The factor  $\Pi_{ij}$  is equal to +1 if  $i$  and  $j$  are both incoming or outgoing legs, and equal to 0 otherwise. When considering both massless and massive partons, the dipole radiator takes one of the following forms:

$$\text{massless:} \quad W_{ij}^k = \frac{n_i \cdot n_j}{(n_i \cdot n_k)(n_k \cdot n_j)}, \quad (5.13)$$

$$\text{mixed:} \quad W_{ij}^k = \frac{v_i \cdot n_j}{(v_i \cdot n_k)(n_k \cdot n_j)}, \quad (5.14)$$

$$\text{massive:} \quad W_{ij}^k = \frac{v_i \cdot v_j}{(v_i \cdot n_k)(n_k \cdot v_j)}. \quad (5.15)$$

In the special case of  $i = j$  (which can not occur in the mixed case (5.14), as it implies that the two legs are the same), the radiator (5.13) vanishes for massless legs, as  $n_i \cdot n_i = 0$ , but is non-zero for massive quarks (5.15). The different kinematics and the presence of the monopoles distinguish the massive from the massless case.

As mentioned above, we work in the large- $N_c$  limit in which the color structure becomes trivial and reduces to factors of  $N_c$ . This is a huge simplification over the general case in which the  $m$ -parton terms act in the color-space of the  $m$ -partons. There is currently a large effort by several groups aiming to extend parton showers beyond the large- $N_c$  case, but we restrict ourselves to this limit. The fact that the color structure becomes trivial implies that the Glauber phases in  $\mathbf{V}_m$  in (5.11) vanish. Furthermore, all interference effects are suppressed and exchanges are only possible between neighbouring legs. However, the monopole contributions are present and need to be included, as is obvious from the diagrams shown in Figure 5.3.

The full corrections in the large- $N_c$  limit read

$$\mathbf{V}_m = -4N_c \mathbf{1} \sum_{i=1}^{m-1} \int \frac{d\Omega(n_k)}{4\pi} \tilde{W}_{ii+1}^k, \quad (5.16)$$

$$\mathbf{R}_m = 4N_c \mathbf{1} \sum_{i=1}^{m-1} \tilde{W}_{ii+1}^k \Theta_{\text{in}}(n_k). \quad (5.17)$$

The sum includes all dipoles  $i$  consisting of the legs  $i$  and  $i + 1$  and we have absorbed the monopole contributions into the dipoles by defining

$$\tilde{W}_{ij}^k \equiv W_{ij}^k - \frac{1}{2} (W_{ii}^k + W_{jj}^k). \quad (5.18)$$

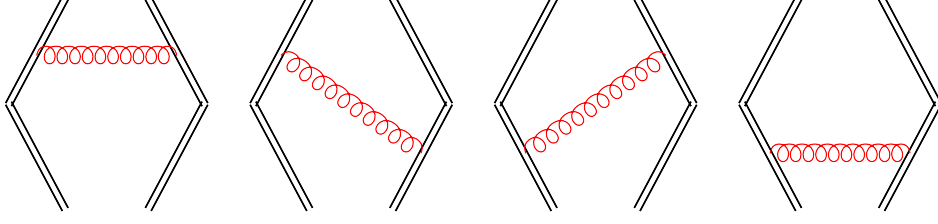


FIGURE 5.3: The four possible radiation patterns for a dipole of two massive legs. From left to right: monopole correction to leg 1 corresponding to the term  $(i, j) = (1, 1)$  in (5.12), dipole correction  $(1, 2)$ , dipole correction  $(2, 1)$ , and monopole correction  $(2, 2)$ .

In the rest of this work, the framework discussed here is applied to top-pair production. In this case the massive legs are always chosen to be the first and the last in the list of Wilson-line directions, so that monopole radiation can only occur at  $i = 1$  and  $i = m - 1$ , as the monopole radiator  $W_{ii}^k$  is manifestly zero for the massless gluonic legs in between.

In Figure 5.3, we have depicted all possible real emissions for one dipole of two massive Wilson lines. The relative sign of the dipole and monopole contributions in (5.18) can be understood intuitively by looking at the figure: the partons in the dipole have opposite charge, in contrast the monopole. The factor of two of the dipole term compared to the monopole ones arises because one has to add the identical contribution of the two dipoles  $(ij)$  and  $(ji)$ .

The details on how one gets from the RG equation to a parton shower are thoroughly explained in [18], but for completeness we briefly review the derivation here. The parton shower is based on the RG equation of the hard function which reads

$$\frac{d}{d \ln \mu} \mathcal{H}_m(\{\underline{n}\}, Q, \mu) = - \sum_{l=2}^m \mathcal{H}_l(\{\underline{n}\}, Q, \mu) \Gamma_{lm}^H(\{\underline{n}\}, Q, \mu). \quad (5.19)$$

By changing variable from the scale  $\mu$  to the evolution time  $t$  and by making use of the fact that the one-loop anomalous dimension matrix has the simple form (5.10), the evolution equation at LL accuracy takes the form

$$\frac{d}{dt} \mathcal{H}_m(t) = \mathcal{H}_m(t) V_m + \mathcal{H}_{m-1}(t) R_{m-1}. \quad (5.20)$$

This differential equation (5.20) can also be rewritten as an integral equation:

$$\mathcal{H}_m(t) = \mathcal{H}_m(t_0) e^{(t-t_0)V_m} + \int_{t_0}^t dt' \mathcal{H}_{m-1}(t') R_{m-1} e^{(t-t')V_m}. \quad (5.21)$$

Starting from (5.21), one can generate the hard functions in an iterative way as

$$\begin{aligned} \mathcal{H}_2(t) &= \mathcal{H}_2(0) e^{tV_2}, \\ \mathcal{H}_3(t) &= \int_0^t dt' \mathcal{H}_2(t') R_2 e^{(t-t')V_3}, \\ \mathcal{H}_4(t) &= \int_0^t dt' \mathcal{H}_3(t') R_3 e^{(t-t')V_4}, \\ \mathcal{H}_5(t) &= \dots, \end{aligned} \quad (5.22)$$

since  $\mathcal{H}_k(0) = 0$  for  $k > 2$ . The cross-section at LL finally reads

$$\begin{aligned}\sigma_{\text{LL}}(Q, Q_0) &\equiv \sigma_{\text{tot}} R(t) \\ &= \sum_{m=2}^{\infty} \langle \mathcal{H}_m(t) \hat{\otimes} \mathbf{1} \rangle = \langle \mathcal{H}_2(t) + \int \frac{d\Omega_3}{4\pi} \mathcal{H}_3(t) + \int \frac{d\Omega_3}{4\pi} \int \frac{d\Omega_4}{4\pi} \mathcal{H}_4(t) + \dots \rangle.\end{aligned}\quad (5.23)$$

The iterative structure of (5.22) is well suited for implementation into a Monte Carlo code which generates successive emissions and thereby also performs the angular phase-space integrals of (5.23). For later convenience, we introduced the quantity  $R(t)$  given by the ratio of the resummed cross section with a veto to the inclusive cross section  $\sigma_{\text{tot}}$ . At LL accuracy, one can replace  $\sigma_{\text{tot}}$  by the Born-level result  $\sigma_0$ .

The inclusion of the massive Wilson lines into the Monte Carlo code is achieved in a straightforward way. The change compared to the massless case boils down to implementing the angular integrations in (5.16), where the modified dipole emitter  $\tilde{W}_{ij}^k$  replaces the massless one. A general algorithm for the evaluation of the angular integrals is discussed in the next section. The details of the Monte Carlo algorithm, which showers tree-level event files obtained by means of MADGRAPH5\_AMC@NLO [34], are presented in Appendix 5.A.

### 5.3 EVALUATION OF THE MASSIVE ANGULAR PHASE SPACE INTEGRALS

The goal of this section is to evaluate the integral

$$\int \frac{d\Omega(n_k)}{4\pi} \tilde{W}_{ij}^k = \int \frac{d\Omega(n_k)}{4\pi} \left( W_{ij}^k - \frac{1}{2} (W_{ii}^k + W_{jj}^k) \right) \quad (5.24)$$

for arbitrary Wilson lines  $u_i$  and  $u_j$ , which are either both massless ( $u_i = n_i$  and  $u_j = n_j$ ), both massive ( $u_i = v_i$  and  $u_j = v_j$ ) or one massive and one massless ( $u_i = v_i$  and  $u_j = n_j$  or vice versa).

For the discussion below, it is convenient to normalize all reference vectors in such a way that the zero component of the four-vector is equal to one, i.e.

$$u_i^\mu \equiv \frac{p_i^\mu}{E_i}, \quad (5.25)$$

where  $E_i$  is the energy component of the vector  $p_i^\mu$ . With this convention, one finds that  $u_i^0 = u_j^0 = n_k^0 = 1$  and  $u_i \cdot u_i = 1 - \beta_i^2$  with  $\beta_i = |\vec{p}_i|/E_i = |\vec{p}_i|/\sqrt{\vec{p}_i^2 + m_i^2}$ . This differs from the definition adopted in heavy-quark effective theory, where one usually normalizes to the mass, i.e. with our convention (5.25)  $v^2 \neq 1$ .

The integral in (5.24) is evaluated by first boosting the vectors into the center-of-mass frame of the dipole and by subsequently changing the angular integration variables to (an appropriate generalization of) rapidity. The reader who is not interested in the technical details of the calculation of (5.24) can skip the following discussion and move directly to Section 5.4.

### 5.3.1 Boost to the center-of-mass frame

In order to calculate the integral in (5.24), it is convenient to first boost the dipole momenta from the laboratory frame into the center-of-mass frame of the dipole. To construct the relevant boost we use a form of the Lorentz transformation introduced by Householder [145]

$$\Lambda_\nu^\mu(\Delta) = \delta_\nu^\mu - \frac{2}{\Delta^2} \Delta^\mu \Delta_\nu, \quad (5.26)$$

where  $\Delta_\mu = n_\mu - \tilde{n}_\mu$  is the difference of two light-like vectors  $n_\mu$  and  $\tilde{n}_\mu$ . One immediately verifies that  $\Lambda_\nu^\mu(\Delta)n^\nu = \tilde{n}^\mu$ , so the transformation maps  $n_\mu \rightarrow \tilde{n}_\mu$ . In addition, it is straightforward to check that  $\Lambda_\rho^\mu \Lambda_\nu^\rho = \delta_\nu^\mu$  and  $\det(\Lambda) = -1$ .

The transformation (5.26) is easily implemented into a computer code and here we use it to construct a boost of two arbitrary time-like or light-like directions  $u_i$  and  $u_j$  into a frame where these momenta are back-to-back alongside the  $z$ -axis. The transformation is carried out in three steps, denoted by  $X_\nu^\mu$ ,  $B_\nu^\mu$  and  $Z_\nu^\mu$ . We denote lab frame vectors  $p_i^\mu$  in the three frames reached by each of the transformations as

$$p^\nu \xrightarrow{X_\nu^\mu} \check{p}^\mu \xrightarrow{B_\nu^\mu} \tilde{p}^\rho \xrightarrow{Z_\nu^\sigma} p'^\sigma. \quad (5.27)$$

The transformation  $X$  rotates the total dipole three momentum such that it points along the  $x$ -axis. Then  $B$  boosts into the center-of-mass frame and the last step  $Z$  rotates the system so that the back-to-back vectors lie along the  $z$ -axis.

Let us now discuss the three transformations in turn. The sum of the momenta associated to the two vectors  $p_i = E_i u_i$  and  $p_j = E_j u_j$  is

$$P \equiv p_i + p_j = E(1, \beta \vec{n}_P). \quad (5.28)$$

By using the transformation (5.26) one can find the rotation to a frame where the spatial component of the light-like vector  $n_P \equiv (1, \vec{n}_P)$  points along the  $x$ -axis. This rotation (more precisely a rotation with parity inversion since  $\det(\Lambda) = -1$ ) is defined as

$$X_\nu^\mu \equiv \Lambda_\nu^\mu(\Delta_P), \quad (5.29)$$

where

$$\Delta_P \equiv n_P - n_X, \quad \text{and} \quad n_X \equiv (1, 1, 0, 0). \quad (5.30)$$

Consequently, by applying the rotation  $X_\nu^\mu$  to the total momentum one finds

$$\check{P}^\mu = X_\nu^\mu P^\nu, \quad \text{with} \quad \check{P} = E(1, \beta, 0, 0). \quad (5.31)$$

The Lorentz transformation needed to obtain two back-to-back vectors  $\tilde{u}_i$  and  $\tilde{u}_j$  from the original vectors  $u_i$  and  $u_j$  is now a boost along the  $x$ -axis. The corresponding transformation in matrix form is

$$B \equiv \begin{pmatrix} \gamma & -\beta\gamma & 0 & 0 \\ -\beta\gamma & \gamma & 0 & 0 \\ 0 & 0 & 1 & 0 \\ 0 & 0 & 0 & 1 \end{pmatrix}, \quad (5.32)$$



where  $\beta$  was introduced in (5.28) and  $\gamma = 1/\sqrt{1-\beta^2}$ . Consequently, the two vectors

$$\begin{aligned}\tilde{p}_i^\mu &= B_\rho^\mu X_\nu^\rho p_i^\nu, & \tilde{p}_i &= \tilde{E}_i(1, \tilde{\beta}_i \vec{n}_i), \\ \tilde{p}_j^\mu &= B_\rho^\mu X_\nu^\rho p_j^\nu, & \tilde{p}_j &= \tilde{E}_j(1, \tilde{\beta}_j \vec{n}_j),\end{aligned}\quad (5.33)$$

are in a back-to-back configuration, i.e.

$$\tilde{E}_i \tilde{\beta}_i \vec{n}_i = -\tilde{E}_j \tilde{\beta}_j \vec{n}_j. \quad (5.34)$$

Finally, it is convenient to apply a last rotation in order to align the vectors along the z-axis. This can be achieved by employing again a Lorentz transformation of the form described in (5.26). In particular one can define

$$Z_\nu^\mu \equiv \Lambda_\nu^\mu(\Delta_Z), \quad (5.35)$$

with

$$\Delta_Z \equiv \tilde{n}_i - \tilde{n}_Z, \quad \text{and} \quad \tilde{n}_i \equiv (1, \vec{n}_i), \quad \tilde{n}_Z \equiv (1, 0, 0, 1). \quad (5.36)$$

In conclusion, the complete Lorentz transformation of any vector from the lab frame into a frame where the vectors  $u'_i = p'_i/E'_i$  and  $u'_j = p'_j/E'_j$  are back to back and aligned along the z-axis is

$$L_\nu^\mu \equiv Z_\rho^\mu B_\sigma^\rho X_\nu^\sigma. \quad (5.37)$$

One finds that  $\det(L) = 1$ , since  $L$  is the product of one proper and two improper transformations.

### 5.3.2 Evaluation of the angular integral

After applying the Lorentz transformation  $L$  and normalizing the vectors according to (5.25), one finds

$$u'_i = (1, 0, 0, \beta'_i), \quad u'_j = (1, 0, 0, -\beta'_j). \quad (5.38)$$

In this frame, one can write the integral over the dipole as

$$\begin{aligned}\int \frac{d\Omega(n_k)}{4\pi} W_{ij}^k &= \int \frac{d\Omega(n_k)}{4\pi} \frac{u_i \cdot u_j}{u_i \cdot n_k n_k \cdot u_j} \\ &= \frac{1 + \beta'_i \beta'_j}{\beta'_i + \beta'_j} \int_0^{2\pi} \frac{d\phi'}{2\pi} \int_{y_{\min}}^{y_{\max}} dy' \\ &= \frac{1 + \beta'_i \beta'_j}{\beta'_i + \beta'_j} (y_{\max} - y_{\min}),\end{aligned}\quad (5.39)$$

where the light-like momentum  $n_k$  in the center-of-mass system is parameterized as

$$n'_k = (1, \sin \theta \cos \phi, \sin \theta \sin \phi, \cos \theta), \quad (5.40)$$

and  $y$  indicates the rapidity-like quantity

$$y = \frac{1}{2} \ln \frac{n_k'^0 + \beta'_j n_k'^3}{n_k'^0 - \beta'_j n_k'^3} = \frac{1}{2} \ln \frac{1 + \beta'_j \cos \theta}{1 - \beta'_j \cos \theta}. \quad (5.41)$$

The boundaries of the rapidity integration are

$$y_{\max} = \frac{1}{2} \ln \left( \frac{1 + \beta'_j}{1 - \beta'_i} \right) > 0, \quad y_{\min} = \frac{1}{2} \ln \left( \frac{1 - \beta'_j}{1 + \beta'_i} \right) < 0. \quad (5.42)$$

In the massless limits,  $\beta'_i$  and/or  $\beta'_j$  become equal to 1 and  $y_{\max}$  and/or  $y_{\min}$  go to infinity. In that case, the collinear divergence in the integral (5.39) needs to be regularized. To this end, we apply a hard cutoff  $|y| < y_{\text{cut}}$  in numerical computations, in addition to the constraints (5.42). We then verify that the physical cross sections are cutoff independent. The specific form of the collinear cutoff we use in our code is given in Appendix 5.A, see (5.77). A discussion of different cutoffs can be found in Appendix A of [18].

The integral over the monopoles gives

$$\int \frac{d\Omega(n_k)}{4\pi} W_{ii}^k = \int \frac{d\Omega(n_k)}{4\pi} \frac{v_i \cdot v_i}{(v_i \cdot n_k)^2} = \int \frac{d\Omega(n_k)}{4\pi} \frac{1 - \beta_i^2}{(1 - \cos \theta \beta_i)^2} = 1. \quad (5.43)$$

Combining the monopole and dipole contributions, the final result for the virtual correction reads

$$\mathbf{V}_m = -4N_c \mathbf{1} \sum_{i=1}^m \left[ \frac{1 + \beta'_i \beta'_{i+1}}{\beta'_i + \beta'_{i+1}} (y_{\max} - y_{\min}) - \frac{1}{2} (\delta_{v_i} + \delta_{v_{i+1}}) \right], \quad (5.44)$$

with  $\delta_{v_i} = 1$  if  $v_i$  is a time-like direction and zero otherwise. Note that the integration boundaries  $y_{\max}$  and  $y_{\min}$  depend on  $\beta'_i$  and  $\beta'_j$ , see (5.42).

The real emission corrections

$$\mathbf{R}_m = 4N_c \mathbf{1} \sum_{i=1}^m W_{ii+1}^k \left( 1 - \frac{1}{2} \frac{W_{ii}^k + W_{i+1i+1}^k}{W_{ii+1}^k} \right) \Theta_{\text{in}}(n_k) \quad (5.45)$$

are evaluated using Monte Carlo methods by randomly choosing a value of  $y'$  and  $\phi'$  in the integrand of (5.39). The factor inside the bracket in (5.45) is a positive weight factor, as shown below. To see whether a given real-emission vector is inside the jet region, one transforms the vector  $n'_k$  back to the laboratory frame by using the inverse transformation to  $L$  given in (5.37).

### 5.3.3 Positive definiteness of $\tilde{W}_{ij}^k$

We now show that the weight factor in (5.45) is positive. This is done most conveniently in the center-of-mass frame. When written in terms of scalar products, the factor  $\tilde{W}_{ij}^k$  reads

$$\tilde{W}_{ij}^k = \frac{u'_i \cdot u'_j}{(u'_i \cdot n'_k)(n'_k \cdot u'_j)} - \frac{1}{2} \left( \frac{u'_i \cdot u'_i}{(u'_i \cdot n'_k)^2} + \frac{u'_j \cdot u'_j}{(u'_j \cdot n'_k)^2} \right). \quad (5.46)$$

To see that this expression is indeed non-negative, one replaces the scalar products by

$$\begin{aligned} u'_i \cdot u'_j &= 1 + \beta'_i \beta'_j, \\ u'_i \cdot n'_k &= 1 - \beta'_i \cos \theta, \\ u'_j \cdot n'_k &= 1 + \beta'_j \cos \theta. \end{aligned} \quad (5.47)$$

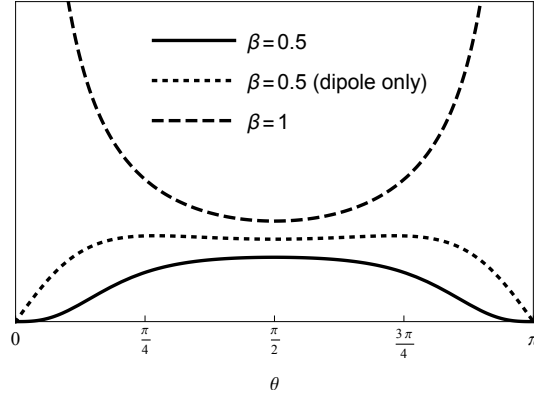


FIGURE 5.4: Angular dependence of the radiation (5.48) in the massive case for  $\beta_i = \beta_j = 0.5$  (solid line) and the massless case  $\beta_i = \beta_j = 1$  (dashed line). In the massive case, we show the dipole contribution separately (dotted line).

By inserting the relations in (5.47) in (5.46) one finds

$$\tilde{W}_{ij}^k = \frac{(\beta'_i + \beta'_j)^2 \sin^2 \theta}{2(1 - \beta'_i \cos \theta)^2 (1 + \beta'_j \cos \theta)^2}. \quad (5.48)$$

Consequently, the factor  $\tilde{W}_{ij}^k$  in (5.46) is always larger than or equal to zero.

#### 5.4 EMISSIONS FROM MASSIVE PARTONS AND NON-GLOBAL LOGARITHMS

In Section 5.2 we have shown that in the large- $N_c$  limit the monopole contributions can be absorbed into the dipole terms by replacing the usual dipole emitter  $W_{ij}^k$  given in (5.1) by the modified emitter  $\tilde{W}_{ij}^k$  introduced in (5.18). It is interesting to compare the massless and massive cases to illustrate the dead cone effect [2, 131–133] mentioned in the introduction. In Figure 5.4 we plot the real-emission integrand (5.48) multiplied by the measure  $\sin \theta$  as a function of  $\theta$ . The plot shows the collinear divergences at  $\theta = 0$  and  $\theta = \pi$ , which are present in the massless case  $\beta_i = \beta_j = 1$ , while the massive integrand vanishes at the end points. One also observes that the monopole contribution significantly reduces the radiation, compared to the pure dipole contribution shown by the dotted line in the plot.

To see what effect the mass has on the size of non-global corrections, we consider the gap fraction in  $e^+e^-$  collisions. To define a gap region, we fix a direction  $\vec{n}$  for each event and impose a veto  $E_{\text{tot}} < Q_0$  on radiation outside a cone around this direction. We then define the rapidity of an emission with momentum  $k$  as

$$y = \frac{1}{2} \ln \frac{k^0 + \vec{n} \cdot \vec{k}}{k^0 - \vec{n} \cdot \vec{k}}. \quad (5.49)$$

An emission is outside the cone, i.e. inside the gap region, if  $|y| < y_{\text{max}}$  and we define the gap fraction as

$$R(Q_0) = \frac{\sigma_{\text{veto}}(Q_0)}{\sigma_{\text{tot}}}. \quad (5.50)$$

For massless final-state quarks  $e^+e^- \rightarrow q\bar{q}$ , one has to ensure that the reference vector  $\vec{n}$  is chosen such that radiation collinear to the original partons is included to obtain a collinear

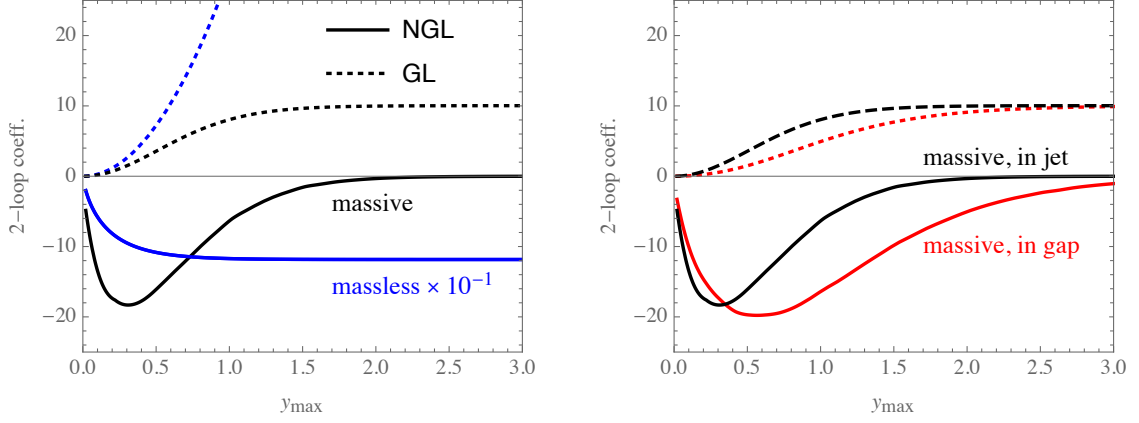


FIGURE 5.5: Size of the two-loop terms in (5.57) as a function of the rapidity  $y_{\max}$  of the gap region. The global contributions  $\mathcal{S}_{\text{GL}}^{(2)}$  are shown with dashed lines, the non-global parts  $\mathcal{S}_{\text{NGL}}^{(2)}$  using solid lines. The black lines in both panels are identical and correspond to radiation from a massive dipole with  $\beta_i = \beta_j = 0.5$  and a reference vector  $\vec{n}$  along the direction of the massive quarks. Left panel: Comparison to the massless case. Note that the massless coefficients (blue lines) have been divided by 10 to make their size similar to the massive ones. Right panel: Comparison to the same  $\beta_i = \beta_j = 0.5$  dipole with  $\vec{n}$  perpendicular to the quarks, corresponding to emissions from a massive quark inside the gap region (red lines).

safe cross section. To do so, one uses for  $\vec{n}$  the thrust axis or the direction obtained from running a jet algorithm on the events. In the massive case  $e^+e^- \rightarrow t\bar{t}$ , on the other hand, we are completely free to choose the reference vector and we compare results obtained when choosing  $\vec{n}$  collinear or perpendicular to the top-quark direction.

To study the contribution from the first two emissions, we expand

$$R(Q_0) = R(t) = 1 + \mathcal{S}^{(1)}t + \mathcal{S}^{(2)}t^2 + \dots \quad (5.51)$$

in the evolution time  $t$ , which is directly related to  $Q_0$ , see (5.9). The coefficients of the expansion can be obtained by iterating the one-loop anomalous dimension which determines the evolution factor (5.5) at LL. Following the steps outlined in Section 5.2 of [24] for the massless case, one finds

$$\begin{aligned} \mathcal{S}^{(1)} &= \langle \mathbf{R}_2 \hat{\otimes} \mathbf{1} + \mathbf{V}_2 \rangle, \\ \mathcal{S}^{(2)} &= \frac{1}{2} \langle \mathbf{R}_2 \hat{\otimes} (\mathbf{R}_3 \hat{\otimes} \mathbf{1} + \mathbf{V}_3) + \mathbf{V}_2 (\mathbf{R}_2 \hat{\otimes} \mathbf{1} + \mathbf{V}_2) \rangle. \end{aligned} \quad (5.52)$$

The real-emission parts  $\mathbf{R}_m$  of the anomalous dimension in (5.17) generate an additional parton and the symbol  $\hat{\otimes}$  indicates the integral over its direction. The angular brackets denote the normalized color trace, which in the large- $N_c$  limit reduces to the trivial trace  $\langle \mathbf{1} \rangle = 1$ . Let us first discuss  $\mathcal{S}^{(1)}$ . We label the initial hard partons as 1 and 2 and the newly emitted gluon as 3. Then

$$\langle \mathbf{R}_2 \hat{\otimes} \mathbf{1} \rangle = 4N_c \int_{\Omega} \mathbf{3}_{\text{in}} \tilde{W}_{12}^3, \quad (5.53)$$

where we introduced the short-hand notation

$$\int_{\Omega} \mathbf{3}_{\text{in}} = \int \frac{d\Omega(n_3)}{4\pi} \Theta_{\text{in}}(n_3). \quad (5.54)$$

The virtual correction  $V_m$  given in (5.16) has opposite sign and includes an integral over the entire solid angle. Combining it with the real-emission part, one finds that

$$\mathcal{S}^{(1)} = \langle \mathbf{R}_2 \hat{\otimes} \mathbf{1} + \mathbf{V}_2 \rangle = -4N_c \int_{\Omega} \mathbf{3}_{\text{out}} \tilde{W}_{12}^3, \quad (5.55)$$

where  $\mathbf{3}_{\text{out}} = 1 - \mathbf{3}_{\text{in}}$ . The dipole structure after the first emission is  $(\bar{q}, g, q) = (1, 3, 2)$ . To be consistent with the notation in the anomalous dimensions (5.16) and (5.17) one should relabel the particles after the emission as  $(1, 2, 3)$ , but we prefer to keep the original labels so that the neighboring dipoles in the second step are  $(1, 3)$  and  $(3, 2)$ , and

$$\langle \mathbf{R}_2 \hat{\otimes} \mathbf{R}_3 \hat{\otimes} \mathbf{1} \rangle = (4N_c)^2 \int_{\Omega} \mathbf{3}_{\text{in}} \mathbf{4}_{\text{in}} \tilde{W}_{12}^3 \left( \tilde{W}_{13}^4 + \tilde{W}_{32}^4 \right). \quad (5.56)$$

We can rewrite all terms appearing in (5.52) in terms of angular integrals and combine real and virtual parts as we did in (5.55). This leads to the two-loop result

$$\begin{aligned} \mathcal{S}^{(2)} &= \mathcal{S}_{\text{NGL}}^{(2)} + \mathcal{S}_{\text{GL}}^{(2)} \\ &= \frac{(4N_c)^2}{2!} \int_{\Omega} \left[ -\mathbf{3}_{\text{in}} \mathbf{4}_{\text{out}} \tilde{W}_{12}^3 \left( \tilde{W}_{13}^4 + \tilde{W}_{23}^4 - \tilde{W}_{12}^4 \right) + \mathbf{3}_{\text{out}} \mathbf{4}_{\text{out}} \tilde{W}_{12}^3 \tilde{W}_{12}^4 \right], \end{aligned} \quad (5.57)$$

in agreement with the results given in [24] for the massless case. The global part of  $\mathcal{S}^{(2)}$  is just one half of the squared one-loop contribution, while the non-global piece has a more complicated structure that arises from the emission of a second gluon from the one produced in the first emission.

Figure 5.5 shows the two-loop coefficients in different situations. In the left plot, where the cone is chosen along the direction of the original dipole, we compare the massive case with  $\beta = 1/2$  to the massless one. In the massless case (shown in blue)  $\mathcal{S}^{(1)} \propto y_{\text{max}}$  so that the global part increases quadratically as  $y_{\text{max}}$  is increased. In the massive case (shown in black), on the other hand, the radiation stops as the gluon becomes collinear to the quark so that the global part of the gap fraction goes to a constant as  $y_{\text{max}}$  becomes large. Interestingly, the non-global part becomes constant as  $y_{\text{max}} \rightarrow \infty$  in the massless case, while it vanishes for a non-zero mass. The radiation from a massless dipole is much larger than the one in the massive case; indeed it was necessary to divide the massless two-loop coefficients by a factor of ten to make them similar in size to the massive ones in the figure. In the right panel of Figure 5.5 we check how much of a difference the choice of the cone vector  $\vec{n}$  makes. The red curves show the result when  $\vec{n}$  is chosen perpendicular to the direction of the massive quarks instead of collinear to them. In this case, the massive quarks lie in the middle of the gap region. We observe that the size of the two-loop coefficients for the two choices of  $\vec{n}$  is quite similar.

Having discussed the two-loop corrections, it is interesting to see how the fixed-order expansions compare to the full resummed result. In Figure 5.6 we show the result of the LL resummation of the gap fraction starting with a single dipole in the center of mass along the cone axis  $\vec{n}$  for a gap with maximal rapidity  $y_{\text{max}} = 0.8$ . The left plot shows the result for a massive dipole ( $\beta = 1/2$ ) while the one on the right starts with a massless one ( $\beta = 1$ ). Along with the full LL result, we also plot its NLO and NNLO expansion. The point made above is fully confirmed; the radiation from a massless dipole is much stronger than from a massive dipole. In fact, both the one-loop and two-loop coefficients are an order of magnitude larger for the massless case than for the massive one. On the other hand, the large-order behavior will be identical to the massless case studied in [103], since the

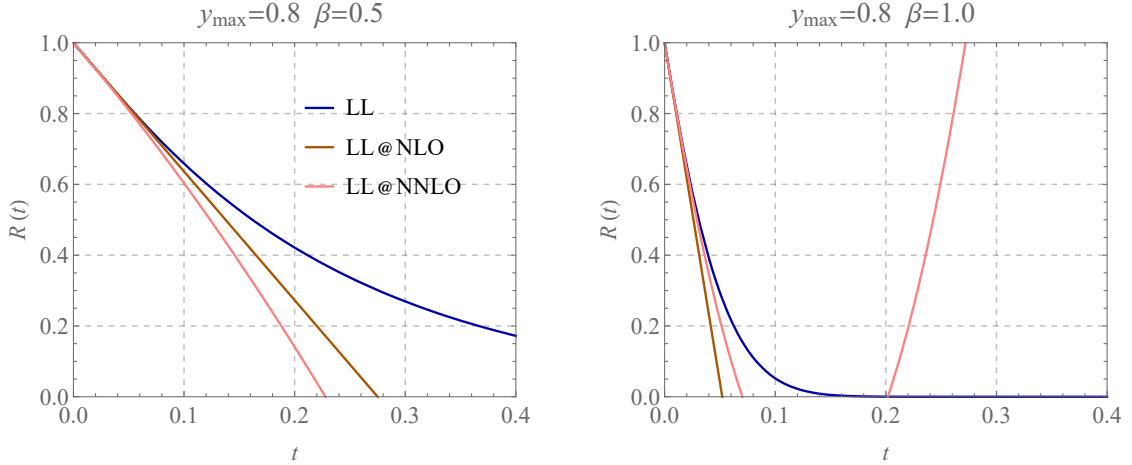


FIGURE 5.6: Results of the LL resummation of the gap fraction from a dipole along the cone direction  $\vec{n}$ . The left plot shows a massive dipole with  $\beta = 0.5$ , the right one a massless one. The LL resummed result is shown in blue, fixed-order expansions at NLO in brown and at NNLO in pink.

contributions arise from emissions off two massive quarks with a large number of gluons. The figure shows the gap fraction as a function of  $t$ . The relation among  $t$  and  $Q_0$  depends on the value of  $Q$ . We stress that the larger values of  $t$  in the figure correspond to very small values of  $Q_0$ . Indeed, for  $Q_1 = 1$  TeV,  $t \geq 0.1$  corresponds to  $Q_0 \lesssim 1$  GeV.

## 5.5 RESUMMATION OF $t\bar{t}$ PRODUCTION WITH VETO ON CENTRAL JETS

In this section, the formalism is applied to the resummation of non-global logarithms in a cross section involving soft radiation from top quarks. We consider  $t\bar{t}$  production at the LHC with a veto on additional central jet activity as measured by ATLAS [134]. This measurement was performed to test the modeling of soft radiation from top quarks in parton shower Monte Carlo codes and is therefore well suited to study resummation effects.

In the measurement ATLAS considers events with at least two energetic  $b$ -jets, opposite-sign leptons and missing energy, subject to a set of selection requirements designed to enhance the  $t\bar{t}$  signal and reject background. In detail, the imposed cuts are as follows: Two of the  $b$ -jets must have  $p_T > 25$  GeV,  $|y| < 2.4$  and  $\Delta R(j, l) > 0.4$ , where  $\Delta R(x, y) = \sqrt{(\Delta\phi(x, y))^2 + (\Delta\eta(x, y))^2}$  with  $\Delta\phi(x, y)$  and  $\Delta\eta(x, y)$  being the difference of the azimuthal angle and the rapidity of particles  $x$  and  $y$ . The opposite charged leptons must fulfill the usual ATLAS cuts: for muons  $p_T > 20$  GeV,  $|\eta| < 2.5$  and for electrons  $p_T > 25$  GeV,  $|\eta| < 2.47$ . If the two leptons are of the same flavor, one imposes that their invariant mass is not too small,  $m_{\ell\ell} > 15$  GeV, and not near the  $Z$ -resonance,  $|m_{\ell\ell} - m_Z| > 10$  GeV. In addition one requires missing  $E_T^{\text{miss}} > 40$  GeV. In the mixed-flavor  $\mu e$ -channel, one instead imposes that  $H_T > 130$  GeV, where  $H_T$  is the scalar sum of the visible transverse momenta.

Starting with this event sample, ATLAS then defines a gap region as depicted in Figure 5.1. The gap consists of rapidity intervals  $y_{\min} < |y| < y_{\max}$ , but the bottom-tagged jets are removed from the gap region. In [134], four rapidity regions with various  $y_{\min}$  and  $y_{\max}$  are measured. We will focus on the two regions with gap regions  $|y| < 0.8$  and  $|y| < 2.1$ .

For a given region, the gap fraction is defined as the fraction of events which do *not* involve a jet with transverse momentum above  $Q_0$  in the gap. The luminosity drops out in

the ratio so that the gap fraction is the ratio of the corresponding cross sections, which are both computed in the presence of the selection cuts discussed above, as defined in (5.50).

For our fixed-order predictions we use MADGRAPH5\_AMC@NLO [34] and the Les-Houches Event (LHE) files produced by this code are taken as an input for our resummation code. We use NNPDF2.3 leading-order PDF sets, with  $\alpha_s(M_Z) = 0.130$  [68]. For the fixed-order prediction of the gap fraction, we use the relation

$$R(Q_0) = 1 - \frac{1}{\sigma_{\text{tot}}} \int_{Q_0}^{\infty} dQ'_0 \frac{d\sigma}{dQ'_0}. \quad (5.58)$$

Up to corrections of  $\mathcal{O}(\alpha_s^2)$ , we can use lowest-order cross sections in this formula. We obtain these by generating tree-level events for  $t\bar{t}$  and  $t\bar{t}g$  with MADGRAPH5\_AMC@NLO. To be able to impose the selection cuts, specifically the exclusion of the bottom-tagged jets, we let the  $t\bar{t}$  pair decay into leptons and a  $b\bar{b}$  pair. The  $b$  and  $\bar{b}$  are then acting as centers of a jet with size  $R = 0.4$  in the plane of azimuthal angle and rapidity. Therefore, a particle  $q$  belongs to the gap region, if

$$\Delta R(b, q) > 0.4, \quad \Delta R(\bar{b}, q) > 0.4, \quad y_{\min} < |y(q)| < y_{\max}. \quad (5.59)$$

In the plots of this section the fixed-order predictions for the cross section are shown in green. As in any multi-scale problem, it is not clear what default value one should use for the renormalization and factorization scales. The average partonic center-of-mass energy  $\sqrt{s}$  for tree-level  $t\bar{t}$  events at the LHC with  $\sqrt{s} = 7$  TeV in the presence of the ATLAS selection cuts is about 520 GeV, which is about three times bigger than the top-quark mass and significantly larger than  $Q_0$ , the lowest scale in the problem. We use an intermediate value  $\mu_r = \mu_f = 2m_t$  as the default choice for the renormalization and factorization scales, but one could argue that the relevant scale for  $\alpha_s$  in the ratio in (5.58) is a lower value  $\mu_r \sim \mu_s \sim Q_0$  since the factors of  $\alpha_s$  associated with the production cross section drop out in the ratio and only the coupling constant associated with the soft gluon emission remains. Indeed, choosing a lower scale would somewhat improve the agreement of the fixed-order prediction with data. The fixed-order uncertainty bands in the plots come from varying the scales  $\mu_r$  and  $\mu_f$  by factors of two around their default values while imposing  $1/2 \leq \mu_r/\mu_f \leq 2$ , i.e. we are using the 7-point method to get the scale bands. Looking at the predictions for different scale values, we observe that the largest variations arise when both scales are simultaneously varied up or down. The fixed-order scale bands are fairly narrow. While the cross sections themselves have a relatively large scale uncertainty, most of it drops out in the ratio in (5.58).

Let us now turn to the resummation, which is performed on the basis of the LHE files for  $t\bar{t}$  production. The shower code reads out the momenta of the top quarks and the initial-state particles in order to obtain the directions of the initial Wilson lines. These, together with the large- $N_c$  color dipole structure provided in the event file are the starting point for the shower, which then emits gluons until an emission goes into the gap. The value of the evolution time  $t \equiv t(\mu_h, \mu_s)$  in (5.9) is later translated into a value of  $Q_0$ , the scale associated with the emission. The shower also calculates the angular integrals in (5.23) as it evolves from the hard to the soft scale.

As the default hard scale we use  $\mu_h = Q_1 = 150$  GeV which was calculated using (5.2) with an average  $Q = \sqrt{s} \approx 520$  GeV. The soft scale  $\mu_s$  should be chosen to be of the order of  $Q_0$ . However, we want to switch off the resummation at larger  $Q_0$  values where we enter the fixed-order regime. To this end, we use a profile function which switches off the



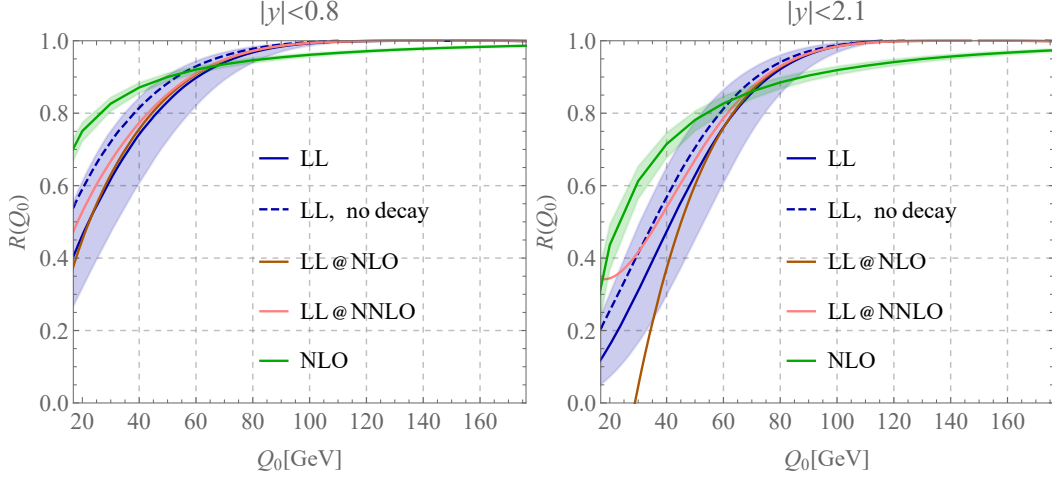


FIGURE 5.7: Results of the resummation of the non-global logarithms in  $t\bar{t}$  production at  $\sqrt{s} = 7$  TeV with a veto on additional jets in the two regions with  $|y| < 0.8$  (left) and  $|y| < 2.1$  (right). The full leading logarithmic resummed result is shown in blue, its expansions to NLO in brown and to NNLO in pink. The blue dashed line is the resummed result when the radiation from the decay is omitted. The fixed-order calculation to NLO is shown in green. The uncertainty bands are from scale variation, see text.

resummation for  $Q_0 \rightarrow Q_{\max}$ . We choose  $Q_{\max} = \mu_h = 150$  GeV and use the same functional form as in [19], namely

$$\mu_s = \frac{x_s Q_0}{1 + \frac{x_s Q_0}{\mu_h} - 4\hat{Q}_0 + 6\hat{Q}_0^2 - 4\hat{Q}_0^3 + \hat{Q}_0^4}, \quad (5.60)$$

where  $\hat{Q}_0 = Q_0 / Q_{\max}$ . The profile function is constructed such that  $\mu_s \rightarrow x_s Q_0$  for  $Q_0 \rightarrow 0$  and that  $\mu_s \rightarrow \mu_h$  for  $\hat{Q}_0 \rightarrow 1$ . The higher-power terms in the denominator are chosen such that the first few derivatives at  $\hat{Q}_0 = 1$  vanish and the parameter  $x_s = \{\frac{1}{2}, 1, 2\}$  is used for scale variation. Beyond  $Q_0 = Q_{\max}$  all resummation effects are switched off and only the fixed-order prediction remains.

The results of the resummation (blue) along with its fixed-order expansion to the second order (brown and pink) as well as the fixed-order calculation results (green) are given in Figure 5.7. From this plot, one can clearly see that the difference between the LL result (blue) and its first-order expansion (brown) is moderate for the gap region with  $|y| < 0.8$ , while this difference is very large when the gap covers the interval  $|y| < 2.1$ . The effect of the radiation from the top decays is not negligible and reduces the gap fraction. By leaving it out (dashed blue line) one obtains a gap fraction that is sizeably larger especially at low  $Q_0$ .

The ultimate goal of this section is to match the NLO calculation to the LL resummation in order to obtain LL+NLO predictions. The size of the difference between the LL result and its first order expansion, which we denote by LL@NLO, is relevant for the matching procedure, as discussed below.

When expanding the LL resummed result, we also expand the evolution time

$$t = \frac{\alpha_s(\mu_r)}{4\pi} \ln \frac{\mu_h}{\mu_s} - \left( \frac{\alpha_s(\mu_r)}{4\pi} \right)^2 \beta_0 \ln^2 \frac{\mu_h}{\mu_s} + \mathcal{O}(\alpha_s^3) \quad (5.61)$$

so that the expanded LL result depends on  $\mu_r$ ,  $\mu_h$ ,  $\mu_s$  as well as the factorization scale  $\mu_f$  at which the PDFs are evaluated. To estimate the scale uncertainties of the matched result, we

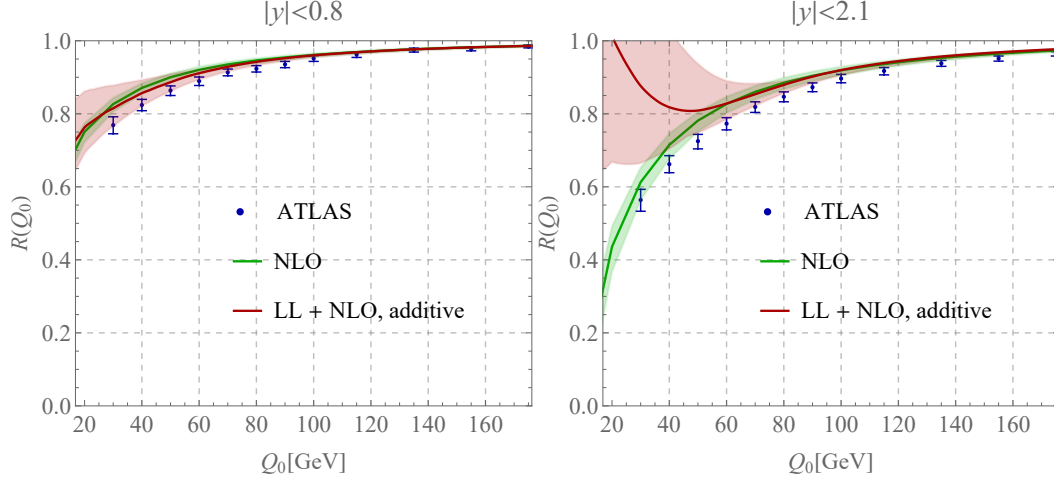


FIGURE 5.8: Results of the resummation of the non-global logarithms in  $t\bar{t}$  production at  $\sqrt{s} = 7\text{TeV}$  with a veto on additional jets in the two regions with  $|y| < 0.8$  (left) and  $|y| < 2.1$  (right). Shown are the ATLAS measurements (blue points with error bars), the fixed order result (green bands) and the resummed and matched cross section (red bands). The uncertainty bands are from scale variation, see text.

vary the scales  $\mu_r$ ,  $\mu_h$ ,  $\mu_s$  and  $\mu_f$  individually by a factor of two and then take the envelope. It turns out that the variation of the soft scale is dominant throughout the plot.

There are two classes of schemes to combine resummed results and fixed-order predictions: additive and multiplicative matching. In the additive matching scheme, one simply adds the LL gap fraction to the NLO prediction and subtracts the one-loop expansion of the LL gap fraction to avoid double counting

$$R_{\text{additive}} = R_{\text{LL}}(\mu_f, \mu_h, \mu_s) + R_{\text{NLO}}(\mu_f, \mu_r) - R_{\text{LL@NLO}}(\mu_f, \mu_r, \mu_h, \mu_s). \quad (5.62)$$

Predictions obtained with the additive matching scheme (red) are shown in Figure 5.8 together with the NLO fixed-order results and data from the ATLAS measurement.

In multiplicative matching, one factors out the resummed prediction before matching to fixed order. One way to achieve this is to perform the matching for the logarithm of the distribution, a scheme called log- $R$  matching [146]. This amounts to exponentiating the matching corrections in the form

$$R_{\text{log-}R} = R_{\text{LL}}(\mu_f, \mu_h, \mu_s) \exp(R_{\text{NLO}}(\mu_f, \mu_r) - R_{\text{LL@NLO}}(\mu_f, \mu_r, \mu_h, \mu_s)). \quad (5.63)$$

The results obtained by means of log- $R$  matching are shown in red in Figure 5.9. This prescription exponentiates the entire first emission, which is similar in spirit to what is done in the POWHEG method [65, 147]. A simpler form of multiplicative matching factors out the resummation but keeps the matching corrections only to NLO. This was called the  $M$  scheme in [148] and leads to results which are numerically similar to the ones in the log- $R$  scheme.

The ATLAS paper compared their measurements to NLO results matched to parton showers using POWHEG and also MC@NLO [126, 149]. Both schemes reproduce the data to better than 5%, POWHEG is typically even within 1%-2% of the measurement. The ATLAS paper does not provide the uncertainties of the theory prediction to which they compare, but we would expect them to be similar in size to the NLO uncertainty bands in our plots. In Section 5.4 it was shown that the radiation from massless legs is numerically much larger

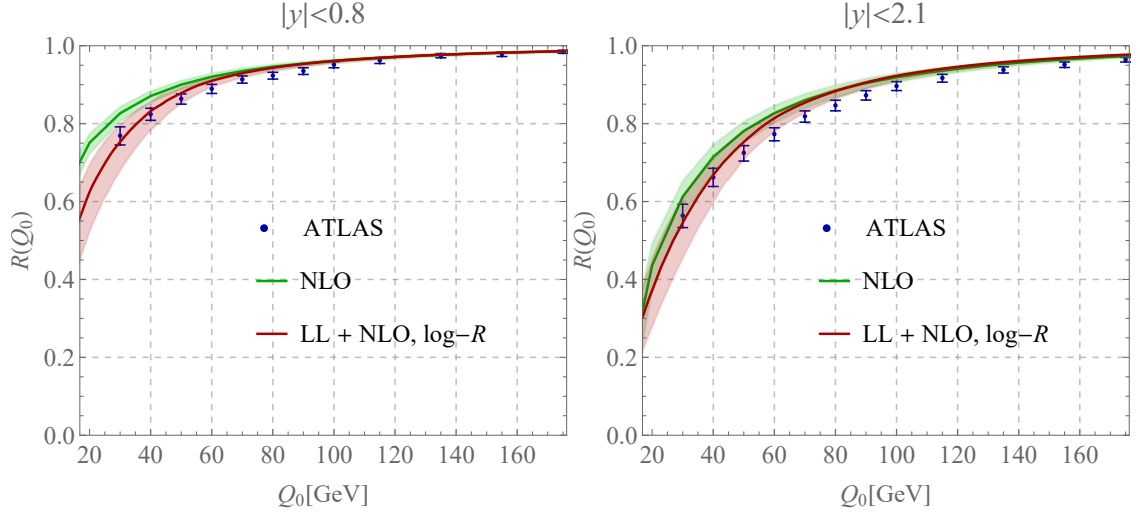


FIGURE 5.9: Same as Figure 5.8, except that the log- $R$  matching scheme was adopted.

than from massive ones. Consequently, we expect that, in order to get a good description of the gap fraction, the modeling of the initial-state radiation is the most important effect. For this reason, it is not clear to us if a comparison to the ATLAS data provides a sufficiently stringent test of the description of soft radiation from massive quarks in a parton shower.

One observes that the additive matching scheme works well for the gap region  $|y| < 0.8$  and actually mildly improves the agreement of central value with the data. However, for the case in which the gap region is  $|y| < 2.1$ , the predictions obtained with additive matching become unphysical for small values of  $Q_0$ . This is not surprising, since the higher-order emissions are enhanced by factors of the gap size  $\Delta y$ . If these rapidity logarithms become larger, they must be resummed. The formalism to carry out this resummation exists [24, 25] but we do not implement it in the present work.

Multiplicative matching leads to better results since the matched gap fraction correctly vanishes for  $Q_0 \rightarrow 0$ , as the resummed result does. Predictions obtained by means of log- $R$  matching are shown in Figure 5.9, which shows that they are in good agreement with the experimental data, within the large scale uncertainty bands. To reduce these, it would be important to go to higher logarithmic accuracy, or to at least include higher-order corrections to the hard and soft functions, as it was done in the massless case [19].

In order to compare predictions to the Run I ATLAS measurement [134], all calculations were carried out at  $\sqrt{s} = 7$  TeV. For the tree-level top production process at  $\sqrt{s} = 13$  TeV, one finds that the average partonic center-of-mass energy is  $Q \approx 550$  GeV, which translates into  $Q_1 \approx 170$  GeV, only 20 GeV higher than at 7 TeV. Consequently, we conclude that the result for the gap fraction at  $\sqrt{s} = 13$  TeV would be quite similar to the ones at Run I.

## 5.6 CONCLUSION

In this paper, we have developed the necessary formalism to carry out the resummation of non-global logarithms for processes involving massive quarks. More specifically, we discussed how the parton shower approach needs to be modified to go beyond the high-energy limit, implemented those changes and then compared the radiation patterns of massive and massless partons. As an application, we have performed the leading logarithmic

resummation of the cross section for  $t\bar{t}$  production with a veto on central jet activity, an observable measured at Run I of the LHC.

Soft radiation has a well-known eikonal form, independent of the mass of the emitting parton. However, in the massive case, the velocity vector of the emitting parton is time-like rather than light-like. This fact makes the kinematics of the process more complicated. A second important difference to the massless case is that for massive emitters one needs to account for monopole radiation. The radiator  $W_{ij}^k$  describing an emission between legs  $i$  and  $j$  is nonzero for  $i = j$  for massive legs; therefore the parton shower must also include radiation from a single leg, despite the fact that it is a purely soft shower. We have shown that in the large- $N_c$  limit this radiation can be absorbed into the dipoles by replacing the usual radiator with a modified one, indicated with  $\tilde{W}_{ij}^k$ . The monopole radiation has a negative relative sign with respect to the dipole contribution, but the total contribution  $\tilde{W}_{ij}^k$  remains positive. These properties make it straightforward to implement massive partons in the shower code that was previously developed for the emission from massless quarks [18, 19].

Comparing the two cases, we observe that the massive dipole radiator is numerically significantly smaller than the massless one and that the radiation is further reduced by the monopole terms. For example, when analyzing the fixed-order expansion of the leading logarithmic resummation for a gap in the central rapidity region of size  $\Delta y = 1.6$ , both the one-loop and the two-loop coefficients are an order of magnitude larger for a massless dipole compared to one with two massive legs with  $\beta = 0.5$  each.

ATLAS measured the gap fraction in  $t\bar{t}$  production with a veto on central jet activity [134]. This provides an interesting test case for the computational framework developed here. However, to compare to experiment we also need to account for radiation from the top-quark decay. To do so, we work in the narrow-width approximation in which the process factors into production and decay and then apply the parton shower to all color dipoles associated to the  $t\bar{t}$  production as well as to the dipoles associated with the decay of the  $t\bar{t}$  pair. The predictions that we compare to the ATLAS measurements are obtained by matching the LL resummed result to the NLO fixed-order computation of the gap fraction. There are two schemes commonly used to combine resummed and fixed order results: additive and multiplicative matching. For small gap sizes  $\Delta y$  both schemes give similar results while for larger gaps the additive matching yields unphysical gap fractions. The problems for large gap sizes are not unexpected since the higher order corrections (and also the power-suppressed terms added in the matching) are enhanced by  $\Delta y$ , i.e. by collinear logarithms. If these logarithms become large they must be resummed as well. The formalism necessary to implement this resummation exists [24, 25], but the corresponding calculation is beyond the scope of the present paper.

In the present work, we resummed the leading non-global logarithms. In order to go to higher logarithmic accuracy, one needs to include the one-loop corrections to both the hard and the soft function, the tree-level result of the hard function with one additional emission, and to evolve with the two-loop anomalous dimension matrix. In the massless case, calculations including the first three ingredients listed above were recently presented [19]. Work on the final ingredient, the two-loop anomalous dimension matrix, is ongoing.

In this paper, we have extended the resummation of non-global observables to processes involving massive partons in the large- $N_c$  limit. Obviously, it would be desirable to extend the formalism to include logarithmic corrections beyond the large- $N_c$  limit. This would be especially interesting since Glauber phase effects then start to play a role in hadronic

collisions. There are a few first finite- $N_c$  results in [100, 150] based on a different formalism [151] and there is a considerable amount of ongoing work focused on the inclusion of subleading color effects into parton showers [56–58, 152–157], but a full implementation of all subleading-color effects, in particular Glauber phases, is not yet available.

An understanding of non-global logarithms could prove useful in the context of the top-quark mass determination. Given the complicated structure of these types of logarithms and our limited ability to perform all-order resummations, it is of course desirable to avoid them in the context of precision physics. On the other hand, to maximize sensitivity to the top-quark mass, jet observables are preferable to inclusive cross sections. It has been proposed to use jet substructure techniques such as grooming to reduce the sensitivity to soft radiation [158] and a factorization theorem implementing grooming has been put forward [159]. These techniques can reduce the size of non-global logarithms, and our approach could be used to get a better understanding of the remaining effects and their uncertainty.

#### ACKNOWLEDGMENTS

The authors thank Paolo Nason and Thomas Rauh for useful comments and discussions. The research of T.B. is supported by the Swiss National Science Foundation (SNF) under grant 200020\_182038. The work of A.F. is supported in part by the PSC-CUNY Award 62243-00 50. M.B. thanks the New York City College of Technology of CUNY for hospitality during a visit July 2019. A.F. would like to thank the Albert Einstein Center for Fundamental Physics at Bern University for hospitality in September and October 2017, during the early stages of this project.

#### 5.A DETAILS OF THE MONTE CARLO ALGORITHM

This appendix describes in detail the algorithm used to obtain the results presented in Section 5.5. We will start with a sample tree-level file and will then show how it is processed step by step by our code. This level of detail is not necessary for most readers, but should be useful for someone implementing a similar shower. It can also serve as a documentation of our code (written in PYTHON), which we plan to make public in the future.

The starting point for the LL resummation algorithm is a Les Houches Event File (LHEF) [59] for the hard process produced using MADGRAPH5\_AMC@NLO [34]. The generated process is the collision of two protons with center-of-mass energy  $\sqrt{s} = 7$  TeV producing a  $t\bar{t}$  pair. Each top quark in the pair decays in a bottom quark and a  $W$ -boson. The latter is required to decay leptonically. In this way, the final state includes a  $b\bar{b}$  pair, two leptons and two neutrinos. In MADGRAPH5\_AMC@NLO syntax, the process is generated by the following command:

```
generate p p > t t~ > vl l+ vl~ l- b b~
```

In  $t\bar{t}$  production at leading order, the partonic initial state includes either two incoming gluons (gluon fusion channel) or two incoming quarks (quark annihilation channel). MADGRAPH5\_AMC@NLO computes the cross section for  $N_c = 3$  and then randomly assigns one of the possible large- $N_c$  color structures to each tree-level event so that it can be analyzed by a parton shower. The large- $N_c$  color structure is given by a set of dipoles, as illustrated in Figure 5.2. An event consists of four or five dipoles in total, namely two (quark annihilation)

or three (gluon fusion) dipoles associated to the production of the top pair and two dipoles from the radiation in the decay to bottom quarks.

In narrow-width approximation, the amplitudes squared factorize into production and decay. We will separately compute the emissions from production and decay and obtain the cross section as a product

$$\sigma_{\text{LL}}^{\text{Event}}(t) = \sigma_0^{\text{Event}} R_{t\bar{t}}(t) R_{t \rightarrow b}(t) R_{\bar{t} \rightarrow \bar{b}}(t), \quad (5.64)$$

where  $\sigma_0^{\text{Event}}$  is the Born-level event weight supplied by MADGRAPH5\_AMC@NLO. The factors  $R_{t\bar{t}}(t)$ ,  $R_{t \rightarrow b}(t)$  and  $R_{\bar{t} \rightarrow \bar{b}}(t)$  are computed by showering the color dipoles arising in the production and decay process. The product form (5.64) holds on the level of the squared amplitudes in the large- $N_c$  limit, but the observable  $Q_0$ , the energy inside the veto region, is additive and the cross section will therefore be a convolution of the different pieces, not simply a product. However, at LL accuracy, the cross section is  $Q_0$ -independent as it only depends on  $t \equiv t(\mu_h, \mu_s)$  and the convolution then reduces to the product in (5.64).

Below, we illustrate the parton shower using the production process  $R_{t\bar{t}}(t)$ , but we run exactly the same shower for the dipoles in the decay. We consider an event in the gluon fusion channel to discuss the showering process in detail in the following, since this is the most involved case. The dipole structure of this event is shown in Figure 5.10. We could separately shower each of the three dipoles, but it is more efficient to treat the event as one dipole with two intermediate gluons, see below. The form of the shower for  $R_{t\bar{t}}(t)$  is then similar to (5.23) except that the process starts with four partons

$$\sigma_0^{t\bar{t}} R_{t\bar{t}}(t) = \mathcal{H}_4(t) + \int \frac{d\Omega_5}{4\pi} \mathcal{H}_5(t) + \int \frac{d\Omega_5}{4\pi} \int \frac{d\Omega_6}{4\pi} \mathcal{H}_6(t) + \dots, \quad (5.65)$$

where  $\sigma_0^{t\bar{t}}$  is the Born-level production cross section, and  $\mathcal{H}_i \equiv \langle \mathcal{H}_i \rangle$ . In the quark annihilation channel, the two dipoles need to be showered separately.

The remainder of this appendix is organized as follows. The set up of the shower is discussed in Section 5.A.1 by looking at an explicit example. The shower procedure is discussed in 5.A.2, also in this case an explicit event is considered as an example. Finally, a brief outline of the algorithm is provided in Section 5.A.3.

### 5.A.1 Interface to LHE files

The LHEF produced by MADGRAPH5\_AMC@NLO contains, for each event, a list of particles with their momenta and information about the nature of the particles. One of these events is listed below. For simplicity, only the particle id, status, colors and four-momenta are provided here.

This particular event consists of two incoming (status: -1) gluons (id: 21), four intermediate particles (status: 2), namely a top quark (id: 6), a  $W^+$ -boson (id: 24) and their antiparticles (denoted with a negative id), and the six final-state particles (status: 1)  $\nu_\mu$  (id: 14),  $\mu^+$  (id: -13),  $\bar{\nu}_e$  (id: -12),  $e^-$  (id: 11) and the  $b\bar{b}$ -pair (id: (-)5). The color-connection indices  $c_1$  and  $c_2$  will be explained below. For illustrative purposes in the rest of this appendix, calculations are carried out by rounding to three digits after the decimal point.



id	s	c1	c2	x mom	y mom	z mom	energy
21	-1	503	502	+0.000e+00	+0.000e+00	+9.106e+01	9.106e+01
21	-1	501	503	-0.000e+00	-0.000e+00	-6.834e+02	6.834e+02
6	2	501	0	+1.256e+02	+8.244e+01	-4.504e+02	5.047e+02
24	2	0	0	+1.165e+02	-4.050e+00	-2.698e+02	3.042e+02
-6	2	0	502	-1.256e+02	-8.244e+01	-1.419e+02	2.697e+02
-24	2	0	0	-2.846e+01	-6.129e+00	-5.262e+00	8.540e+01
14	1	0	0	+4.077e+01	+2.321e+01	-4.318e+01	6.377e+01
-13	1	0	0	+7.575e+01	-2.726e+01	-2.266e+02	2.404e+02
-12	1	0	0	+2.455e+01	-1.372e+01	+9.769e+00	2.978e+01
11	1	0	0	-5.301e+01	+7.597e+00	-1.503e+01	5.562e+01
5	1	501	0	+9.077e+00	+8.649e+01	-1.806e+02	2.005e+02
-5	1	0	502	-9.715e+01	-7.631e+01	-1.366e+02	1.842e+02

The final state leptons in the event must satisfy the cuts listed in Table 1 of [134]. The momenta of the  $b\bar{b}$  pair are needed, because they define the direction of the  $b$ -jets, which are cut out of the gap region (or veto region), see (5.59) and Figure 5.1.

In the following we illustrate the shower algorithm with the  $t\bar{t}$  production process. The additional dipoles arising from the top-quark decay can be showered exactly in the same way. In the end, it is necessary to multiply the results of each shower to get the complete result of each event, see (5.64). The showering process of the dipoles associated to the top-pair production starts by selecting the momenta of the initial-state partons and the momenta of the  $t\bar{t}$  pair. These momenta are stored in dipoles according to the large- $N_c$  color information assigned by MADGRAPH5\_AMC@NLO. In the sample event depicted in Figure 5.10, the color index associated to the top quark is c1: 501, while the color indices associated to the gluon in the second line of the list above ( $g_2$ ) are c1: 501, c2: 503. The color indices of the gluon in the first line of the list ( $g_1$ ) are c1: 503, c2: 502 and the color index of the anti-quark is c2: 502. The color indices indicate which lines are color connected and the shower algorithm orders the particles in such a way that equal color indices are adjacent to each other; so that the list of the color indices is 501, 501, 503, 503, 502, 502. Therefore the ordering of the particles is  $(t, g_2, g_1, \bar{t})$  which represents a dipole with two intermediate gluons.

Since the algorithm only requires information about the direction of the particles, we normalize the components of the momenta to their energy. These normalized momenta are stored in an array

$$\{\underline{u}\} = \left\{ \frac{p_t}{E_t}, \frac{p_{g_2}}{E_{g_2}}, \frac{p_{g_1}}{E_{g_1}}, \frac{p_{\bar{t}}}{E_{\bar{t}}} \right\} = \left\{ \begin{pmatrix} 1 \\ 0.249 \\ 0.163 \\ -0.892 \end{pmatrix}, \begin{pmatrix} 1 \\ 0 \\ 0 \\ -1 \end{pmatrix}, \begin{pmatrix} 1 \\ 0 \\ 0 \\ 1 \end{pmatrix}, \begin{pmatrix} 1 \\ -0.466 \\ -0.306 \\ -0.526 \end{pmatrix} \right\} \quad (5.66)$$

such that each adjacent pair of vectors represents a color dipole.

We then calculate the virtual correction of each dipole using (5.44) by boosting the two vectors in each dipole into a frame where they are back-to-back, as explained in Section 5.3,



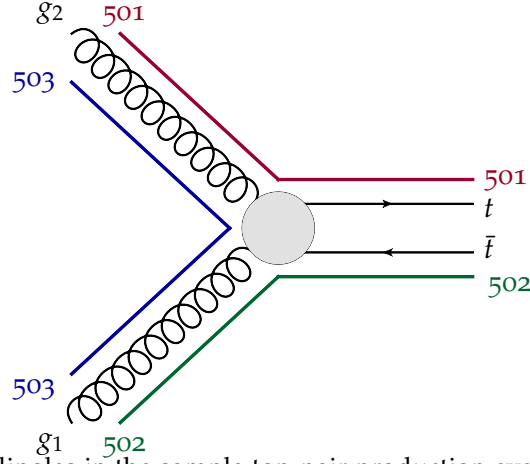


FIGURE 5.10: Color dipoles in the sample top-pair production event discussed in text.

and by subsequently evaluating the velocities  $\beta'_i, \beta'_j$ . Each dipole contributes to the virtual corrections a factor

$$V_{ij} = 4N_c \left( \frac{1 + \beta'_i \beta'_j}{\beta'_i + \beta'_j} (y_{\max} - y_{\min}) - \frac{1}{2} (\delta_{v_i} + \delta_{v_j}) \right), \quad (5.67)$$

where  $N_c = 3$ .

Let us illustrate the process by explicitly calculating the virtual corrections for the first dipole in the list,  $V_{12}$ , according to the method put forward in Section 5.3. The first step consists in boosting the two normalized momenta in the rest frame. The sum of the two normalized momenta is

$$U = u_1 + u_2 = \begin{pmatrix} 2 \\ 0.249 \\ 0.163 \\ -1.892 \end{pmatrix}. \quad (5.68)$$

This vector is then aligned to the  $x$ -axis by means of the matrix

$$X = \begin{pmatrix} 1 & 0 & 0 & 0 \\ 0 & 0.130 & 0.085 & -0.988 \\ 0 & 0.085 & 0.992 & 0.097 \\ 0 & -0.988 & 0.097 & -0.122 \end{pmatrix}, \quad (5.69)$$

which leads to the vectors

$$\check{U} \equiv \begin{pmatrix} 2 \\ 1.916 \\ 0 \\ 0 \end{pmatrix}, \quad \check{u}_1 = \begin{pmatrix} 1 \\ 0.928 \\ 0.097 \\ -0.122 \end{pmatrix}, \quad \check{u}_2 = \begin{pmatrix} 1 \\ 0.987 \\ -0.097 \\ 0.122 \end{pmatrix}, \quad (5.70)$$

with  $\check{U}$  having vanishing  $y$  and  $z$  components by construction.

For the dipole under consideration the factor  $\beta$  introduced in (5.28) is  $\beta = 0.958$ , which leads to boost matrix  $B$  in (5.32) with the following entries

$$B = \begin{pmatrix} 3.481 & -3.334 & 0 & 0 \\ -3.334 & 3.481 & 0 & 0 \\ 0 & 0 & 1 & 0 \\ 0 & 0 & 0 & 1 \end{pmatrix}. \quad (5.71)$$

By applying the matrix  $B$  to the vectors in (5.70) one finds

$$\tilde{U} = \begin{pmatrix} 0.575 \\ 0 \\ 0 \\ 0 \end{pmatrix}, \quad \tilde{u}_1 = \begin{pmatrix} 0.387 \\ -0.104 \\ 0.097 \\ -0.122 \end{pmatrix}, \quad \tilde{u}_2 = \begin{pmatrix} 0.187 \\ 0.104 \\ -0.097 \\ 0.122 \end{pmatrix}, \quad (5.72)$$

with  $\vec{\tilde{u}}_1 = -\vec{\tilde{u}}_2$  and  $\vec{\tilde{U}} = 0$  by construction.

Finally one needs to apply the rotation matrix that aligns the two vectors along the  $z$  axis (5.35)

$$Z = \begin{pmatrix} 1 & 0 & 0 & 0 \\ 0 & 0.811 & 0.175 & -0.558 \\ 0 & 0.175 & 0.838 & 0.517 \\ 0 & -0.558 & 0.517 & -0.649 \end{pmatrix}. \quad (5.73)$$

By applying the matrix  $Z$  to the vectors in (5.72) one finds

$$U' = \tilde{U}, \quad u'_1 = \begin{pmatrix} 0.387 \\ 0 \\ 0 \\ 0.187 \end{pmatrix}, \quad u'_2 = \begin{pmatrix} 0.187 \\ 0 \\ 0 \\ -0.187 \end{pmatrix}. \quad (5.74)$$

In this frame we obtain the factors  $\beta'_1, \beta'_2, y_{\min}, y_{\max}$  that are needed in the calculation of the virtual corrections

$$\begin{aligned} \beta'_1 &= 0.483, & \beta'_2 &= 1, \\ y_{\min} &= -y_{\text{cut}} = -4.184, & y_{\max} &= \frac{1}{2} \ln \left( \frac{1 + \beta'_2}{1 - \beta'_1} \right) = 0.677, \end{aligned} \quad (5.75)$$

and the full boost and inverse boost

$$L = \begin{pmatrix} 3.481 & -0.433 & -0.284 & 3.293 \\ -2.705 & 0.933 & 0.360 & -2.704 \\ -0.583 & -0.360 & 0.933 & -0.583 \\ 1.860 & 0.433 & 0.284 & 2.047 \end{pmatrix}, \quad L^{-1} = g L^T g, \quad (5.76)$$

with  $g = \text{diag}(1, -1, -1, -1)$ . Let us briefly explain the value of  $y_{\text{cut}}$  which cuts off the collinear divergence arising for massless partons. Following (A.1) of [18], we obtain the value of the cut-off by imposing a rapidity cut  $\eta_{\text{cut}}$  in the lab frame and then computing the

value of  $y_{\text{cut}}$  that this corresponds to in the center-of-mass frame. This leads to the somewhat complicated expression

$$y_{\text{cut}} = \ln \left( \cos \left( \frac{\theta}{2} \right) + \sqrt{\cos^2 \left( \frac{\theta}{2} \right) + \sin^2 \left( \frac{\theta}{2} \right) e^{2\eta_{\text{cut}}}} \right), \quad (5.77)$$

where  $\theta$  is the angle between the two vectors forming the dipole in the lab frame. One immediately sees that  $y_{\text{cut}} = \eta_{\text{cut}}$  for back-to-back vectors  $\theta = \pi$ . The value  $y_{\text{cut}}$  for the dipole under consideration is obtained after setting  $\eta_{\text{cut}} = 6$ .

Since the top quark is massive and the gluon is massless, one has  $\delta_{v_1} = 1$  and  $\delta_{v_2} = 0$  in calculating the contribution of this dipole to the virtual corrections (5.67). The virtual correction associated to the first dipole in the event is given by  $V_{12} = 52.332$ . The value of the virtual corrections in (5.67) for each of the three dipoles in the event is stored in another array

$$\{\underline{V}\} = (52.332, 144.000, 78.443). \quad (5.78)$$

#### 5.A.2 Monte Carlo implementation of $\mathcal{H}_i(t)$

As outlined in the introduction of this appendix, we could also have set up the showering of each of these three dipoles individually and then multiplied the results. To reduce computation time, we treat color-connected dipole structures such as (5.66) as a single dipole which has already emitted two gluons at  $t = 0$ . It is convenient to multiply (5.65) by the virtual correction and to define

$$\hat{R}_{i\bar{i}}(t) = V_4 R_{i\bar{i}}(t) = \hat{\mathcal{H}}_4(t) + \int \frac{d\Omega_5}{4\pi} \hat{\mathcal{H}}_5(t) + \int \frac{d\Omega_5}{4\pi} \int \frac{d\Omega_6}{4\pi} \hat{\mathcal{H}}_6(t) + \dots, \quad (5.79)$$

where the hat indicates a multiplication of the hard functions by the total virtual correction of the four legs

$$V_4 \equiv V_{\text{tot}} = V_{12} + V_{23} + V_{34}, \quad (5.80)$$

and division by the LO cross section, see (5.65). The term  $\mathcal{H}_4(t)$  corresponds to the initial tree-level configuration with associated dipole-structure (5.66), while  $\mathcal{H}_5(t)$  contains an additional gluon emitted from one of the dipoles in (5.66).

Let us now analyze the individual terms in (5.79). The first term  $\hat{\mathcal{H}}_4(t)$  denotes the evolution from the hard scale to the low scale without any radiation from any of the dipoles (compare to the first line of (5.22)) and is given by

$$\hat{\mathcal{H}}_4(t) = V_4 \frac{\mathcal{H}_4(0)}{\sigma_0^{t\bar{t}}} e^{-tV_4} = V_4 e^{-tV_4}, \quad (5.81)$$

since by definition  $\hat{\mathcal{H}}_4(0) = R_{i\bar{i}}(0) = 1$ . At this stage it is convenient to define the probability distribution

$$\mathcal{P}(V, t) = V e^{-Vt} \quad (5.82)$$

such that  $\hat{\mathcal{H}}_4(t) = \mathcal{P}(V_4, t)$ .

The function  $\hat{\mathcal{H}}_5(t)$  consists of the initial four hard partons plus one additional parton emitted by any of the dipoles at an evolution time earlier than  $t$ . In the large- $N_c$  limit, the new emission occurs from any one of the three dipoles in the list so that we get three terms

$$\begin{aligned}\hat{\mathcal{H}}_5(t) &= \hat{\mathcal{H}}_5^{(1)}(t) + \hat{\mathcal{H}}_5^{(2)}(t) + \hat{\mathcal{H}}_5^{(3)}(t) \\ &= \int_0^t dt' \hat{\mathcal{H}}_4(t') \left( R_{12}^5 e^{-(t-t')V_5^{(1)}} + R_{23}^5 e^{-(t-t')V_5^{(2)}} + R_{34}^5 e^{-(t-t')V_5^{(3)}} \right),\end{aligned}\quad (5.83)$$

each evolving with its specific virtual correction

$$\begin{aligned}V_5^{(1)} &= V_{15} + V_{52} + V_{23} + V_{34}, \\ V_5^{(2)} &= V_{12} + V_{25} + V_{53} + V_{34}, \\ V_5^{(3)} &= V_{12} + V_{23} + V_{35} + V_{54}.\end{aligned}\quad (5.84)$$

The quantity  $R_{ij}^5$  corresponds to the real correction factor as given in (5.45) when the fifth parton is emitted in the direction  $n_5$  from the dipole of legs  $i$  and  $j$

$$R_{ij}^5 = 4N_c \tilde{W}_{ij}^5 \Theta_{\text{in}}(n_5). \quad (5.85)$$

To bring (5.83) into a form suitable for Monte Carlo implementation, we now strategically insert factors of one. We rewrite the first term on the right-hand side of the first line in the form

$$\begin{aligned}\hat{\mathcal{H}}_5^{(1)}(t) &= \int_0^t dt' \hat{\mathcal{H}}_4(t') \frac{R_{12}^5}{V_{12}} \frac{V_{12}}{V_4} \frac{V_4}{V_5^{(1)}} V_5^{(1)} e^{-(t-t')V_5^{(1)}} \\ &= \int_0^t dt' \mathcal{P}(V_4, t') \frac{R_{12}^5}{V_{12}} \frac{V_{12}}{V_4} \frac{V_4}{V_5^{(1)}} \mathcal{P}(V_5^{(1)}, t-t').\end{aligned}\quad (5.86)$$

The integral  $\int d\Omega_5/4\pi$ , over the direction of the emission in (5.79), is evaluated by Monte Carlo methods. The factor  $V_{12}/V_4$  is the weight of the dipole (12) in the total virtual correction  $V_4$  and is interpreted as the probability of having an emission from the dipole (12).

For the case of  $\hat{\mathcal{H}}_5^{(1)}(t)$  the sets of direction vectors and of associated virtual corrections are

$$\{\underline{u}\} = (u_t, n_5, u_{g_2}, u_{g_1}, u_{\bar{t}}), \quad \{\underline{V}\} = (V_{15}, V_{52}, V_{23}, V_{34}). \quad (5.87)$$

The contribution of terms arising from  $\hat{\mathcal{H}}_5^{(1)}(t)$  to  $\hat{\mathcal{H}}_6(t)$  in (5.79) is denoted by

$$\hat{\mathcal{H}}_6^{(1)}(t) = \hat{\mathcal{H}}_6^{(11)}(t) + \hat{\mathcal{H}}_6^{(12)}(t) + \hat{\mathcal{H}}_6^{(13)}(t) + \hat{\mathcal{H}}_6^{(14)}(t). \quad (5.88)$$

It involves four terms  $\hat{\mathcal{H}}_6^{(1i)}(t)$ , where  $i$  denotes the position of the dipole which makes the next emission. These terms have the same structure as the ones in the first emission. For example

$$\hat{\mathcal{H}}_6^{(12)}(t) = \int_0^t dt'' \hat{\mathcal{H}}_5^{(1)}(t'') R_{52}^6 e^{-(t-t'')V_6^{(12)}}, \quad (5.89)$$

where the relevant virtual contribution is given by

$$V_6^{(12)} = V_{15} + V_{56} + V_{62} + V_{23} + V_{34}. \quad (5.90)$$

One can rewrite the quantity in (5.89) by strategically inserting factors of one, as it was done in (5.86), to find

$$\hat{\mathcal{H}}_6^{(12)}(t) = \int_0^t dt'' \hat{\mathcal{H}}_5^{(1)}(t'') \frac{R_{52}^6}{V_{52}} \frac{V_{52}}{V_5^{(1)}} \frac{V_5^{(1)}}{V_6^{(12)}} \mathcal{P}(V_6^{(12)}, t - t''). \quad (5.91)$$

This iterative procedure can be repeated to calculate all of the terms  $\hat{\mathcal{H}}_i(t)$ .

In the parton shower algorithm, this procedure is implemented as follows. For the numerical example, we again consider the event already set up for the showering in Appendix 5.A.1. At first, the shower is initialized as follows:

$$t = 0, \quad V_{\text{tot}} = V_4 = V_{12} + V_{23} + V_{34} = 274.765, \quad w = \frac{1}{n_{sh}}. \quad (5.92)$$

The initial weight  $w$  of an individual event is the inverse of the number of showerings of a tree-level event in the LHE file,  $n_{sh}$ ; additional weight factors arising from integrands such as the one in (5.86) are discussed below.

At first it is necessary to randomly generate a time step  $\Delta t$  according to the probability density  $\mathcal{P}(V_{\text{tot}}, \Delta t)$ . We generate random time steps  $\Delta t$  according to this distribution by taking the cumulant  $u \equiv \mathcal{P}/V_{\text{tot}} \in [0, 1]$ , inverting it

$$\Delta t = -\frac{\ln u}{V_{\text{tot}}}, \quad (5.93)$$

and using an equally distributed random variable  $u \in [0, 1]$ . For our sample event, we choose  $u = 0.5$  for illustration, which yields  $\Delta t = 0.00252$ . To account for  $\hat{\mathcal{H}}_4(\Delta t) = \mathcal{P}(V_4, \Delta t)$ , we add a weight  $w$  into a histogram in a bin corresponding to the time  $t^{\text{new}} = \Delta t = 0.00252$ . Once the shower will be finished, this histogram will provide the gap fraction  $\hat{R}_{if}(t)$ .

Next, we use (5.83) to iteratively compute  $\hat{\mathcal{H}}_5(t)$  at a time  $t > t^{\text{new}}$ . To do so, we interpret  $t^{\text{new}}$  as the time at which one of the three original dipoles emits a parton. Looking at (5.83), one sees that  $\hat{\mathcal{H}}_5(t)$  has three terms. The first of these terms is given in (5.86); it involves a product of several factors. The first factor is the probability density  $\mathcal{P}(V_4, t')$  which was taken into account when generating the time step  $\Delta t$ . Showering multiple times, one gets a Monte Carlo approximation of the integral over  $dt'$ . We then have the three factors  $R_{12}^5/V_{12}$ ,  $V_{12}/V_4$  and  $V_4/V_5^{(1)}$ . The last two of these factors can be treated as probabilities since the value of these ratios is always in the interval  $[0, 1]$ . The factor  $R_{12}^5/V_{12}$  corresponds to the phase-space integral and will be treated as a weight. The very last factor  $\mathcal{P}(V_5^{(1)}, t - t')$  in (5.86) represents the emission probability in the time interval  $t - t'$ .

The factor  $V_{12}/V_4$  in (5.86) is the weight of the dipole (12) in the total virtual correction  $V_4$  and is interpreted as a probability of selecting the dipole (12) for the emission. The shower algorithm selects one of the terms  $\hat{\mathcal{H}}_5^{(i)}(t)$  according to the probabilities  $\{\underline{V}\}/V_{\text{tot}} = \{V_{12}, V_{23}, V_{34}\}/V_4$ . To implement this, one can draw a random value  $u \in [0, 1]$ . Then, the  $i$ -th dipole is assumed to emit, if the cumulative sum of the virtual corrections of all the dipoles from 1 through  $i$  divided by the total virtual corrections is smaller than  $u$ . In the example under consideration, this means that if  $u < 0.190 = V_{12}/V_{\text{tot}}$  it is the first dipole that emits, if  $0.190 < u < 0.715 = (V_{12} + V_{23})/V_{\text{tot}}$  the emission arises from the second dipole, and if  $0.715 < u$  the third dipole emits. For the purposes of this discussion, let us assume that  $u = 0.1$ , such that first dipole emits.

Now that the algorithm has determined which dipole does radiate, one can boost into the back-to-back frame of the selected dipole. The procedure to do this for the first dipole was

already illustrated in Appendix 5.A.1. In this frame, the algorithm draws two more random numbers, namely

$$\begin{aligned}\phi' &= 2\pi u_\phi, \\ y' &= y_{\min} + u_y (y_{\max} - y_{\min}),\end{aligned}\tag{5.94}$$

with  $u_i \in [0, 1]$  and the integration boundaries  $y_{\min}$  and  $y_{\max}$  as given previously in (5.75). For illustration, assume that  $u_\phi = u_y = 0.5$ , which yields  $\phi' = \pi$  and  $y' = -1.754$ . With this input one then obtains the four-vector of the newly emitted parton as

$$n'_5 = \begin{pmatrix} 1 \\ n_T \cos \phi' \\ n_T \sin \phi' \\ n_z \end{pmatrix} = \begin{pmatrix} 1 \\ -0.293 \\ 0 \\ -0.956 \end{pmatrix},\tag{5.95}$$

with  $n_z = (e^{2y'} - 1) / (\beta'_1 e^{2y'} + \beta'_2)$  and  $n_T = \sqrt{1 - n_z^2}$ .

The new vector is then boosted back to the lab frame by using the inverse boost matrix  $L^{-1}$  given in (5.76). Subsequently, the vector is normalized in such a way that the energy component is 1:

$$p_5 = L^{-1} n'_5 = \begin{pmatrix} 4.466 \\ -0.254 \\ -0.093 \\ -4.458 \end{pmatrix} \Rightarrow n_5 = \begin{pmatrix} 1 \\ -0.057 \\ -0.021 \\ -0.998 \end{pmatrix}.\tag{5.96}$$

With the new vector  $n_5$ , the algorithm evaluates the factor

$$\frac{R_{12}^5}{V_{12}} = \frac{4N_c \frac{1+\beta'_1\beta'_2}{\beta'_1+\beta'_2} (y_{\max} - y_{\min}) \left(1 - \frac{1}{2} \frac{W_{11}^5}{W_{12}^5}\right)}{V_{12}} = 1.106.\tag{5.97}$$

The quantity in (5.97) is strictly positive (as shown in Section 5.3.3), but it can not be treated as a probability, since it can exceed unity.<sup>1</sup> Therefore the algorithm accounts for it by modifying the weight factor

$$w^{\text{new}} = w \frac{R_{12}^5}{V_{12}}.\tag{5.98}$$

We have to ensure that the real emission is not in the veto region, as imposed by the  $\Theta_{\text{in}}(n_5)$ -function in (5.85). This is done by checking the conditions (5.59) with  $q = n_5$ . We obtain

$$\Delta R(b, n_5) = 2.860, \quad \Delta R(\bar{b}, n_5) = 2.561, \quad y(n_5) = -3.496,\tag{5.99}$$

implying that the new emission fulfills all the conditions  $\Theta_{\text{in}}(n_5)$  and one can proceed to the next step of the algorithm. If the condition would have not been fulfilled, the shower would

<sup>1</sup> This arises because we include the monopoles as a weight factor into the dipole integral. Alternatively, one could integrate the full, modified dipole  $\tilde{W}_{ij}^k$  given in (5.48). The integral can be done and leads to a more complicated version of the rapidity variable (5.41). However, the inversion to the angle  $\theta$  can then not be done analytically, in contrast to (5.41).

have been stopped at this point and the algorithm would have restarted at the beginning, after erasing all information on this showering other than the histogram entry for  $\hat{\mathcal{H}}_4(t)$  at  $t = \Delta t$ .

Since the generated vector  $n_5$  was not in the gap region, the algorithm continues by adding the new vector to the list of vectors in between the first and second vector of the list in (5.66). In addition, the algorithm updates the virtual correction list by replacing the virtual correction  $V_{12}$  by  $V_{15}$  and  $V_{52}$ :

$$\{\underline{u}\} = \left\{ \begin{pmatrix} 1 \\ 0.248 \\ 0.163 \\ -0.892 \end{pmatrix}, \begin{pmatrix} 1 \\ -0.057 \\ -0.021 \\ -0.998 \end{pmatrix}, \begin{pmatrix} 1 \\ 0 \\ 0 \\ -1 \end{pmatrix}, \begin{pmatrix} 1 \\ 0 \\ 0 \\ 1 \end{pmatrix}, \begin{pmatrix} 1 \\ -0.466 \\ -0.306 \\ -0.526 \end{pmatrix} \right\}, \quad (5.100)$$

$$\{\underline{V}\} = \{54.806, 61.974, 144.000, 78.433\} \Rightarrow V_{\text{tot}}^{\text{new}} = V_5^{(1)} = 339.212. \quad (5.101)$$

There is one last factor in  $\hat{\mathcal{H}}_5^{(1)}(t)$  that was not accounted for so far, namely the factor  $V_4/V_5^{(1)}$ . This last factor can again be treated as a probability, as the new virtual corrections are always larger than the old ones.<sup>2</sup> This means that instead of multiplying the weight by this factor, one can again draw a random variable  $u \in (0, 1)$  and if  $u < 0.810 = V_4/V_5^{(1)} = V_{\text{tot}}^{\text{old}}/V_{\text{tot}}^{\text{new}}$ , the algorithm continues with the generation of a time step starting at  $t = t^{\text{new}}$  with weight  $w = w^{\text{new}}$ . In the opposite case, the shower is stopped. One could also treat  $V_4/V_5^{(1)}$  as a weight factor, but, due to the iterative nature of the shower, the weights of the individual steps multiply each other, leading to events with small weight which would render the shower inefficient.

The new time step is generated in exactly in the same way as before according to the new probability density  $\mathcal{P}(V_{\text{tot}}^{\text{new}}, \Delta t')$  and completes the calculation of  $\hat{\mathcal{H}}_5(t)$  by writing the weight into the histogram at  $t = \Delta t + \Delta t'$ . After this is done, the algorithm proceeds to calculate  $\hat{\mathcal{H}}_6(t)$ . Looking at (5.89), one sees that the same procedure described for the calculation of  $\hat{\mathcal{H}}_5(t)$  can be used, since it involves the same type of ingredients:

- a) An emitting dipole is chosen, each with probability of  $V_{ij}/V_{\text{tot}}$ .
- b) The emission is generated and the factor  $R_{ij}^6/V_{ij}$  is calculated and multiplied to the weight.
- c) If the emission is not in the veto region, the algorithm proceeds with probability  $V_{\text{tot}}/V_{\text{tot}}^{\text{new}}$  and generates a new time step using  $\mathcal{P}(V_{\text{tot}}^{\text{new}}, \Delta t'')$ , which gives  $\hat{\mathcal{H}}_6(t)$  with  $t = \Delta t + \Delta t' + \Delta t''$ .

The iterative calculation of all the  $\hat{\mathcal{H}}_i(t)$  with  $i > 6$  can be carried out in the same way until one reaches the necessary maximal value for  $t$  determined by the lowest value of  $\mu_s \sim Q_0$  in the problem under consideration. Each showering generates several hard functions at successively larger times until it terminates. In the calculations presented in this work, we used an upper limit of  $t_{\text{max}} = 0.1$ , which corresponds to  $\mu_s \approx 0.75 \text{ GeV}$  after applying the profile (5.60) and  $\mu_h = 150 \text{ GeV}$ .

<sup>2</sup> Whether this is true depends on the form of the angular cutoff used in the shower, see [18].



### 5.A.3 Parton shower algorithm

This section summarizes the different steps in the shower algorithm, which were discussed in detail in Appendix 5.A.2 in the context of the showering of a particular event. The shower algorithm described below is applied  $n_{sh}$  times to each tree-level event. In the following, we describe one such shower event. For the results presented in our paper, we used about  $10^5$  tree-level events and worked with  $n_{sh} = 10^4$ .

#### Step 0. Set up the shower

Store all Wilson-line directions according to their color information into an array, and calculate the virtual corrections of each dipole

$$\begin{aligned}\{\underline{u}\} &= \{u_1, u_2, \dots, u_m\}, \\ \{\underline{V}\} &= \{V_{12}, V_{23}, \dots, V_{(m-1)m}\},\end{aligned}\tag{5.102}$$

where

$$V_{ij} = 4N_c \left( \frac{1 + \beta'_i \beta'_j}{\beta'_i + \beta'_j} (y_{\max} - y_{\min}) - \frac{1}{2} (\delta_{v_i} + \delta_{v_j}) \right).\tag{5.103}$$

An expression for the rapidity values can be found in (5.42). Initiate the shower algorithm with the initial settings

$$t = 0, \quad V_{\text{tot}} = \sum_i V_i, \quad w = \frac{1}{n_{sh}}.\tag{5.104}$$

#### Step 1. Generate time step

Generate a random number  $u \in [0, 1]$  and calculate

$$\Delta t = -\frac{\ln(u)}{V_{\text{tot}}},\tag{5.105}$$

which is added to the variable of the evolution time

$$t \rightarrow t = t + \Delta t.\tag{5.106}$$

#### Step 2. Insert weight into histogram

At this new time  $t$ , insert  $w$  into the histogram.

#### Step 3. Choose emitting dipole

Randomly choose a dipole which emits the next emission, where each dipole with legs  $i$  and  $j$  emits with probability

$$p_{ij} = \frac{V_{ij}}{V_{\text{tot}}}.\tag{5.107}$$

*Step 4. Create emission*

Boost to the frame where the emitting legs are back-to-back along the  $z$ -axis and in that frame choose an emission direction  $n'_k$  by generating a random angle  $\phi' \in [0, 2\pi]$  and rapidity  $y' \in [y_{\min}, y_{\max}]$ . Boost  $n'_k$  back into the lab frame and normalize it as  $n_k = (1, \vec{n}_k)$ . Update the event weight according to

$$w \rightarrow w = w \frac{R_{ij}^k}{V_{ij}} = w \frac{4N_c \frac{1+\beta'_i\beta'_j}{\beta'_i+\beta'_j} (y_{\max} - y_{\min}) \left(1 - \frac{1}{2} \frac{W_{ii}^k + W_{jj}^k}{W_{ij}^k}\right)}{V_{ij}}. \quad (5.108)$$

*Step 5a. Emission not in veto region*

If the emission  $n_k$  is in the allowed region, add the new direction to the list  $\{\underline{u}\}$  of particles in the event and replace the virtual corrections between legs  $i$  and  $j$  by the two virtual corrections between the legs  $i, k$  and  $k, j$ :

$$\begin{aligned} \{\underline{u}\} &= \{u_1, \dots, u_i, u_j, \dots, u_m\} \Rightarrow \{\underline{u}\} = \{u_1, \dots, u_i, n_k, u_j, \dots, u_m\}, \\ \{\underline{V}\} &= \{V_{12}, \dots, V_{ij}, \dots, V_{(m-1)m}\} \Rightarrow \{\underline{V}\} = \{V_{12}, \dots, V_{ik}, V_{kj}, \dots, V_{(m-1)m}\}. \end{aligned} \quad (5.109)$$

Go back to step 1 with a probability

$$\frac{V_{\text{tot}}}{V_{\text{tot}}^{\text{new}}} := \frac{V_{12} + \dots + V_{ij} + \dots + V_{(m-1)m}}{V_{12} + \dots + V_{ik} + V_{kj} + \dots + V_{(m-1)m}}. \quad (5.110)$$

The algorithm restarts from step 1 with the new arrays  $\{\underline{u}\}$ ,  $\{\underline{V}\}$  and  $V_{\text{tot}} = V_{\text{tot}}^{\text{new}}$ .

With the probability of  $1 - (V_{\text{tot}}/V_{\text{tot}}^{\text{new}})$  the shower is stopped. Of course one can also set an upper limit  $t_{\max}$  on  $t$  after which the shower stops.

*Step 5b. Emission into veto region*

If the emission  $n_k$  lands in the gap region, the shower stops.

## 5.B FIXED-ORDER EXPANSION OF THE LL RESULT

In this appendix, we detail how one can obtain the coefficients  $\mathcal{S}^{(1)}$  and  $\mathcal{S}^{(2)}$  in the fixed-order expansion of the leading logarithmic resummation (5.51) from the parton shower. When extracting the fixed-order coefficients for a given tree-level event, we look at each dipole at  $t = 0$  individually, calculate its expansion coefficients and then combine the results. Averaging the expansion coefficients of the individual events then gives the final result for the two-loop expansion of the resummed cross section. In the following we describe the computation for a single dipole.

### 5.B.1 One-loop coefficient

The one-loop coefficient of the fixed-order expansion may be extracted easily from the shower. To do so we write (5.55) as

$$\mathcal{S}^{(1)} = -V_{12} \int \frac{d\Omega(n_3)}{4\pi} \frac{R_{12}^3}{V_{12}} \Theta_{\text{out}}(n_3), \quad (5.111)$$

where 1 and 2 are the legs of the dipole and  $R_{12}^3 = 4N_c \tilde{W}_{12}^3$ . Please note that throughout this appendix we write out the appropriate  $\Theta_{\text{in}}(n_k)$  and  $\Theta_{\text{out}}(n_k)$  angular constraints and we do not include the factors  $\Theta_{\text{in}}(n_k)$  into the definition of  $R_{ij}^k$  as we did in (5.85).

The factor  $R_{12}^3/V_{12}$  is produced by the shower, see Appendix 5.A, and gives  $\mathcal{S}^{(1)}$  after multiplication by  $-V_{12}$ . All that needs to be done is to account for the constraint  $\Theta_{\text{out}}(n_3)$  which ensures that the emission is in the veto region. From the first step of the parton shower one obtains

$$\mathcal{S}^{(1)} = - \sum_{i=1}^{n_{\text{sh}}} s_1, \quad \text{with} \quad s_1 \equiv \begin{cases} \frac{R_{12}^3 V_{12}}{V_{12} n_{\text{sh}}}, & \text{if } \Theta_{\text{out}}(n_3) = 1, \\ 0, & \text{otherwise.} \end{cases} \quad (5.112)$$

### 5.B.2 Two-loop coefficient

While the global part of the two-loop coefficient is just one half of the one-loop coefficient squared, the non-global part is much more involved mainly due to collinear divergences in individual terms in the integrand in (5.57). Rewriting the non-global part as

$$\mathcal{S}_{\text{NGL}}^{(2)} = -\frac{1}{2} \int \frac{d\Omega(n_3)}{4\pi} \int \frac{d\Omega(n_4)}{4\pi} R_{12}^3 \left( R_{13}^4 + R_{23}^4 - R_{12}^4 \right) \Theta_{\text{in}}(n_3) \Theta_{\text{out}}(n_4), \quad (5.113)$$

one notices that collinear singularities arise in  $R_{12}^3$  since the light-like direction  $n_3$  is in the jet region (not in the veto region) and can become collinear to  $n_1$  or  $n_2$ . However, the full expression  $\mathcal{S}_{\text{NGL}}^{(2)}$  is collinear finite since the terms multiplying  $R_{12}^3$  vanish in both collinear limits:

$$R_{13}^4 + R_{23}^4 - R_{12}^4 \rightarrow 0 \quad \text{for} \quad n_3 \rightarrow n_1 \quad \text{or} \quad n_3 \rightarrow n_2. \quad (5.114)$$

The two terms  $R_{12}^3 R_{13}^4$  and  $R_{12}^3 R_{23}^4$  have a simple interpretation in the parton shower. The first emission of the shower produces  $R_{12}^3$  and results in the dipole configuration (1, 3, 2). The term  $R_{13}^4$  arises when the second emission occurs in the dipole (1, 3), while  $R_{23}^4$  corresponds to the emission from (3, 2). However, the subtraction term  $R_{12}^4$  does not arise in the parton shower. To include it, the factor  $R_{12}^4$  can be split in two parts according to

$$R_{12}^4 = R_{12}^4 \theta(n_2 \cdot n_3 - n_1 \cdot n_3) + R_{12}^4 \theta(n_1 \cdot n_3 - n_2 \cdot n_3). \quad (5.115)$$

In this way, the first term is evaluated if the spatial angle between  $n_3$  and direction  $n_1$  is smaller than the one between  $n_3$  and direction  $n_2$  and is therefore used to cure the collinear singularity when  $n_3 \rightarrow n_1$ . The same argument holds for  $1 \leftrightarrow 2$  and removes the other divergence. One can thus write

$$\begin{aligned} \mathcal{S}_{\text{NGL}}^{(2)} = & -\frac{1}{2} \int \frac{d\Omega(n_3)}{4\pi} \int \frac{d\Omega(n_4)}{4\pi} \Theta_{\text{in}}(n_3) \Theta_{\text{out}}(n_4) \\ & \times \left[ R_{12}^3 R_{13}^4 \left( 1 - \frac{R_{12}^4}{R_{13}^4} \theta(n_1 \cdot n_3 - n_2 \cdot n_3) \right) \right. \\ & \left. + R_{12}^3 R_{23}^4 \left( 1 - \frac{R_{12}^4}{R_{23}^4} \theta(n_2 \cdot n_3 - n_1 \cdot n_3) \right) \right]. \end{aligned} \quad (5.116)$$

The terms in the second and third line of this expression are separately collinear finite and the factors multiplying the dipoles  $R_{12}^3 R_{13}^4$  and  $R_{12}^3 R_{23}^4$  in the two lines can be implemented as weight factors in the shower.

To implement (5.116) in the shower, we store the weight  $R_{12}^3/V_{12}$  of the first emission. We then go on to the second emission and check whether it is emitted by the dipole  $(n_1, n_3)$  or  $(n_3, n_2)$ . We also check if  $n_3$ , the direction of the first emission, is closer to  $n_1$  or  $n_2$ . With this information, one can then calculate the two-loop coefficient as a sum of weights

$$\mathcal{S}_{\text{NGL}}^{(2)} = -\frac{1}{2} \sum_{i=1}^{n_{\text{sh}}} s_2. \quad (5.117)$$

The weights for the two cases  $(i, j) = (1, 2)$  and  $(i, j) = (2, 1)$ , corresponding to the second emission  $R_{i3}^4$ , are obtained as follows

$$s_2 \equiv \begin{cases} \frac{R_{12}^3}{V_{12}} \frac{V_{12}}{V_3} \frac{V_{i3}}{V_3} \frac{R_{i3}^4}{V_{i3}} \frac{(V_3)^2}{n_{\text{sh}}} \left(1 - \frac{R_{12}^4}{R_{i3}^4}\right), & \text{if } \Theta_{\text{out}}(n_4) = 1 \text{ and } n_i \cdot n_3 > n_j \cdot n_3, \\ \frac{R_{12}^3}{V_{12}} \frac{V_{12}}{V_3} \frac{V_{i3}}{V_3} \frac{R_{i3}^4}{V_{i3}} \frac{(V_3)^2}{n_{\text{sh}}}, & \text{if } \Theta_{\text{out}}(n_4) = 1 \text{ and } n_i \cdot n_3 < n_j \cdot n_3, \\ 0, & \text{otherwise.} \end{cases} \quad (5.118)$$

We have written  $s_2$  in terms of factors  $V_{12}/V_3$  and  $V_{i3}/V_3$ , with  $V_3 = V_{13} + V_{32}$ , which arise in the shower algorithm, analogous to (5.86). They represent the probability to continue the shower after the first emission and the probability to choose the dipole  $(n_i, n_3)$  rather than  $(n_j, n_3)$  for the second emission.

## CONCLUSION AND OUTLOOK

---

*Anyone who stops learning is old, whether at twenty or eighty.  
Anyone who keeps learning stays young. The greatest thing in life  
is to keep your mind young.*

— Henry Ford

We made good progress in improving the understanding of non-global observables during the course of my PhD studies over the last four years, but a lot more remains to be done. Thankfully, the field of Soft-Collinear Effective Theory is still relatively young and with the number of scientists working collinear to its direction growing steadily, we are confident that more will be learned so that the field will not grow old too fast.

Using a factorization theorem for wide-angle jets in Soft-Collinear Effective Theory and the renormalization group evolution belonging to it, we were able to resum non-global logarithms in various observables in collider physics. To achieve this goal we wrote a dedicated computer code `NGL_RESUM`, implementing a parton-shower equation derived from first principles to resum non-global logarithms at LL in the large- $N_c$  limit.

An early version of `NGL_RESUM` was applied to resum non-global logarithms at LL for the interjet energy flow and cross sections involving isolation cones. To realize this resummation, we interfaced our code with the tree-level event generator of `MADGRAPH5_AMC@NLO`, which provided the kinematic configuration and color structure of the hard partons. This early proof-of-concept of our parton-shower approach reproduces results obtained by the dipole shower of the original paper on non-global logarithms by Dasgupta and Salam and successfully applied SCET to new observables, for example cross sections with photon isolation cones.

Due to the fact that our parton-shower framework is derived from first principles, the ingredients needed to resum non-global logarithms at subleading logarithmic accuracy are clear. At NLL we need a) the NLO corrections to the hard functions, b) the NLO corrections to the soft functions, and c) the two-loop anomalous dimension. In a first improvement of `NGL_RESUM`, we achieved for the first time a resummation of non-global logarithms beyond LL. We included both a) and b) from above, but did not yet include the two-loop anomalous dimension into the renormalization group evolution (see below). Even though it is not yet full NLL, this so-called LL' resummation is an important first step towards higher-logarithmic calculations. As an application, we were able to calculate the interjet energy flow at LL' accuracy and the jet mass even at NLL', as this is a double-logarithmic observable, improving both predictions compared to crude LL and NLL resummation, respectively. While the NLO corrections of the soft function were uncomplicated to implement in a general way, the ones of the hard functions are highly non-trivial due to the loop-corrections and real emissions suffering individually from collinear divergences. Of course, this problem also occurs in general-purpose parton showers, which by now have achieved a fully automated implementation. Our parton shower comes with the additional complication that it does not conserve momentum, rendering it impossible to use its first emission as the collinear subtraction term for the hard function with one additional real emission.

Let us note that these first two applications of the formalism were done in the high-energy limit, where all partons are treated as massless. We were able to adapt the theoretical framework to also allow the resummation of non-global logarithms in cross sections with massive quarks. After developing the necessary formalism, we extended the first version of `NGL_RESUM` such that it also works for massive quarks. We investigated the different behavior of time-like and light-like Wilson lines and observed that massive dipoles emit significantly less soft radiation compared to massless ones. We also did a phenomenological study and compared the LL resummation of the interjet energy flow in  $t\bar{t}$  production to ATLAS measurements. In doing that, were able to slightly improve the predictions of the NLO fixed-order calculations.

By this point, `NGL_RESUM` is a general-purpose computer code to resum the non-global logarithms at LL for a multitude of observables, involving both massive and massless particles. However, it certainly is far from perfect and there is room for improvement.

The most obvious one would be to allow for subleading logarithmic accuracy, in a first step to NLL. As discussed above, we achieved the inclusion of NLO corrections to both the hard and soft functions for certain di-jet observables, but we did not yet include the two-loop anomalous dimension. This matrix looks similar to the one-loop anomalous dimension, but in addition to the entries in the diagonal and off-diagonal, it comes with a third entry per line. The entries on the diagonal are now accounting for double-virtual corrections, the off-diagonal ones for the emission of an additional leg with a one-loop correction, and the second-off-diagonal entries account for the double-real correction, which is the emission of two additional legs. Even though this general form is known, the explicit result is still missing. The challenge is to find a formulation of the three entries in such a way that all intermediate collinear divergences cancel in a consistent way.

Even if the anomalous dimension matrix is complicated, one should at least resum the logarithms at  $LL'$  and implement this part in our code `NGL_RESUM`. While we managed to do this for certain di-jet observables as discussed above, our solution is at the moment still process-specific and we restrained from including it into the general tool `NGL_RESUM`. An automation of the hard corrections would be an important next step.

In addition, let us also not forget that our framework is fundamentally based on the large- $N_c$  limit. If we would include non-planar diagrams, the two entries in each line of the one-loop anomalous dimension would become much more involved. However, it would be very interesting to get away from this specific limit, especially for non-global observables at hadron colliders. At finite  $N_c$ , such calculations would then include Glauber phase effects. While some general-purpose parton showers start to include such finite- $N_c$  results, a full implementation of subleading-color effects has not yet been realized.

One additional limitation of the current version of `NGL_RESUM` is that it does not return reliable results for narrow-angle cones. In any jet observable, we also have terms enhanced by the logarithms of the cone size. If the cone size becomes small, these logarithmically enhanced terms should also be accounted for and get resummed. The intrinsic structure of narrow-jet physics is however more involved than its wide-angle counterpart. Factorization theorems for such processes exist and we look forward to the resummation of non-global logarithms also in this case!

## BIBLIOGRAPHY

---

1. Campbell, J., Huston, J. & Krauss, F. *The Black Book of Quantum Chromodynamics: A Primer for the LHC Era* (Oxford University Press, 2017).
2. Ellis, R., Stirling, W. & Webber, B. *QCD and collider physics* (Cambridge University Press, 2011).
3. Perelstein, M. *Introduction to Collider Physics in Theoretical Advanced Study Institute in Elementary Particle Physics: Physics of the Large and the Small* (2011), 421.
4. Peskin, M. E. & Schroeder, D. V. *An Introduction to quantum field theory* (Addison-Wesley, Reading, USA, 1995).
5. Schwartz, M. D. *Quantum Field Theory and the Standard Model* (Cambridge University Press, 2014).
6. Davidson, S., Gambino, P., Laine, M. & Neubert, M. *Effective Field Theories in Particle Physics and Cosmology. Lecture Notes of the Les Houches Summer School: Volume 108, July 2017* (Oxford University Press, 2020).
7. Becher, T., Broggio, A. & Ferroglia, A. *Introduction to Soft-Collinear Effective Theory* pp.1 (2015).
8. Aad, G. *et al.* Expected Performance of the ATLAS Experiment - Detector, Trigger and Physics (2009).
9. Simonyi, K. *Cultural History of Physics* (CRC Press).
10. <http://en.wikipedia.org/wiki/CERN>. Accessed July 28, 2020.
11. <http://home.cern/resources/image/accelerators/lhc-images-gallery>. Accessed July 28, 2020.
12. <http://home.cern/resources/image/experiments/atlas-images-gallery>. Accessed July 28, 2020.
13. [http://en.wikipedia.org/wiki/ATLAS\\_experiment](http://en.wikipedia.org/wiki/ATLAS_experiment). Accessed July 28, 2020.
14. <http://twiki.cern.ch/twiki/bin/view/AtlasPublic/EventDisplayRun2Physics>. Accessed July 28, 2020.
15. <https://visit.cern/cern-shop>. Accessed July 28, 2020.
16. Tanabashi, M. *et al.* Review of Particle Physics. *Phys. Rev. D* **98**, 030001 (3 2018).
17. Sudakov, V. Vertex parts at very high-energies in quantum electrodynamics. *Sov. Phys. JETP* **3**, 65 (1956).
18. Balsiger, M., Becher, T. & Shao, D. Y. Non-global logarithms in jet and isolation cone cross sections. *JHEP* **08**, 104 (2018).
19. Balsiger, M., Becher, T. & Shao, D. Y. NLL' resummation of jet mass. *JHEP* **04**, 020 (2019).
20. Balsiger, M., Becher, T. & Ferroglia, A. Resummation of non-global logarithms in cross sections with massive particles (2020).



21. Beneke, M. & Smirnov, V. A. Asymptotic expansion of Feynman integrals near threshold. *Nucl. Phys. B* **522**, 321 (1998).
22. Smirnov, V. A. Applied asymptotic expansions in momenta and masses. *Springer Tracts Mod. Phys.* **177**, 1 (2002).
23. Beneke, M., Chapovsky, A. P., Diehl, M. & Feldmann, T. Soft collinear effective theory and heavy to light currents beyond leading power. *Nucl. Phys.* **B643**, 431 (2002).
24. Becher, T., Neubert, M., Rothen, L. & Shao, D. Y. Factorization and Resummation for Jet Processes. *JHEP* **11**. [Erratum: JHEP05,154(2017)], 019 (2016).
25. Becher, T., Neubert, M., Rothen, L. & Shao, D. Y. Effective Field Theory for Jet Processes. *Phys. Rev. Lett.* **116**, 192001 (2016).
26. Dasgupta, M. & Salam, G. P. Resummation of nonglobal QCD observables. *Phys. Lett.* **B512**, 323 (2001).
27. Bauer, C. W., Fleming, S., Pirjol, D. & Stewart, I. W. An Effective field theory for collinear and soft gluons: Heavy to light decays. *Phys. Rev.* **D63**, 114020 (2001).
28. Bauer, C. W., Pirjol, D. & Stewart, I. W. Soft collinear factorization in effective field theory. *Phys. Rev.* **D65**, 054022 (2002).
29. Becher, T. *Les Houches Lectures on Soft-Collinear Effective Theory in Les Houches summer school: EFT in Particle Physics and Cosmology Les Houches, Chamonix Valley, France, July 3-28, 2017* (2018).
30. Li, H. T. & Skands, P. A framework for second-order parton showers. *Phys. Lett.* **B771**, 59 (2017).
31. Nagy, Z. & Soper, D. E. What is a parton shower? *Phys. Rev.* **D98**, 014034 (2018).
32. Höche, S. & Prestel, S. Triple collinear emissions in parton showers. *Phys. Rev.* **D96**, 074017 (2017).
33. Höche, S., Krauss, F. & Prestel, S. Implementing NLO DGLAP evolution in Parton Showers. *JHEP* **10**, 093 (2017).
34. Alwall, J., Frederix, R., Frixione, S., Hirschi, V., Maltoni, F., Mattelaer, O., Shao, H. S., Stelzer, T., Torrielli, P. & Zaro, M. The automated computation of tree-level and next-to-leading order differential cross sections, and their matching to parton shower simulations. *JHEP* **07**, 079 (2014).
35. Aad, G. *et al.* Measurement of dijet production with a veto on additional central jet activity in  $pp$  collisions at  $\sqrt{s} = 7$  TeV using the ATLAS detector. *JHEP* **09**, 053 (2011).
36. Aad, G. *et al.* Measurements of jet vetoes and azimuthal decorrelations in dijet events produced in  $pp$  collisions at  $\sqrt{s} = 7$  TeV using the ATLAS detector. *Eur. Phys. J.* **C74**, 3117 (2014).
37. Hatta, Y., Marquet, C., Royon, C., Soyez, G., Ueda, T. & Werder, D. A QCD description of the ATLAS jet veto measurement. *Phys. Rev.* **D87**, 054016 (2013).
38. Banfi, A., Marchesini, G. & Smye, G. Away from jet energy flow. *JHEP* **08**, 006 (2002).
39. Abe, F. *et al.* Observation of rapidity gaps in  $\bar{p}p$  collisions at 1.8 TeV. *Phys. Rev. Lett.* **74**, 855 (1995).
40. Abachi, S. *et al.* Jet Production via Strongly-Interacting Color-Singlet Exchange in  $p\bar{p}$  Collisions. *Phys. Rev. Lett.* **76**, 734 (1996).

41. Abe, F. *et al.* Dijet production by color - singlet exchange at the Fermilab Tevatron. *Phys. Rev. Lett.* **80**, 1156 (1998).
42. Oderda, G. & Sterman, G. F. Energy and color flow in dijet rapidity gaps. *Phys. Rev. Lett.* **81**, 3591 (1998).
43. Dasgupta, M., Dreyer, F., Salam, G. P. & Soyez, G. Small-radius jets to all orders in QCD. *JHEP* **04**, 039 (2015).
44. Dasgupta, M., Dreyer, F. A., Salam, G. P. & Soyez, G. Inclusive jet spectrum for small-radius jets. *JHEP* **06**, 057 (2016).
45. Kolodrubetz, D. W., Pietrulewicz, P., Stewart, I. W., Tackmann, F. J. & Waalewijn, W. J. Factorization for Jet Radius Logarithms in Jet Mass Spectra at the LHC. *JHEP* **12**, 054 (2016).
46. Dai, L., Kim, C. & Leibovich, A. K. Fragmentation of a Jet with Small Radius. *Phys. Rev.* **D94**, 114023 (2016).
47. Kang, Z.-B., Ringer, F. & Vitev, I. The semi-inclusive jet function in SCET and small radius resummation for inclusive jet production. *JHEP* **10**, 125 (2016).
48. Kang, Z.-B., Ringer, F. & Vitev, I. Semi-inclusive jet cross sections within SCET. *PoS QCDEV2016*, 022 (2017).
49. Kang, Z.-B., Ringer, F. & Waalewijn, W. J. The Energy Distribution of Subjets and the Jet Shape. *JHEP* **07**, 064 (2017).
50. Forshaw, J. R., Kyrieleis, A. & Seymour, M. H. Super-leading logarithms in non-global observables in QCD. *JHEP* **08**, 059 (2006).
51. Forshaw, J. R., Kyrieleis, A. & Seymour, M. H. Super-leading logarithms in non-global observables in QCD: Colour basis independent calculation. *JHEP* **09**, 128 (2008).
52. Cacciari, M., Salam, G. P. & Soyez, G. The anti- $k_t$  jet clustering algorithm. *JHEP* **04**, 063 (2008).
53. Farhi, D., Feige, I., Freytsis, M. & Schwartz, M. D. Streamlining resummed QCD calculations using Monte Carlo integration. *JHEP* **08**, 112 (2016).
54. Catani, S. & Seymour, M. H. The Dipole formalism for the calculation of QCD jet cross-sections at next-to-leading order. *Phys. Lett.* **B378**, 287 (1996).
55. Catani, S. & Seymour, M. H. A General algorithm for calculating jet cross-sections in NLO QCD. *Nucl. Phys.* **B485**. [Erratum: *Nucl. Phys.*B510,503(1998)], 291 (1997).
56. Platzer, S. & Sjodahl, M. Subleading  $N_c$  improved Parton Showers. *JHEP* **07**, 042 (2012).
57. Plätzer, S. Summing Large- $N$  Towers in Colour Flow Evolution. *Eur. Phys. J.* **C74**, 2907 (2014).
58. Ángeles Martínez, R., De Angelis, M., Forshaw, J. R., Plätzer, S. & Seymour, M. H. Soft gluon evolution and non-global logarithms. *JHEP* **05**, 044 (2018).
59. Alwall, J. *et al.* A Standard format for Les Houches event files. *Comput. Phys. Commun.* **176**, 300 (2007).
60. Berger, C. F., Kucs, T. & Sterman, G. F. Energy flow in interjet radiation. *Phys. Rev.* **D65**, 094031 (2002).
61. Dasgupta, M. & Salam, G. P. Accounting for coherence in interjet  $E(t)$  flow: A Case study. *JHEP* **03**, 017 (2002).

62. Hatta, Y., Iancu, E., Mueller, A. H. & Triantafyllopoulos, D. N. Resumming double non-global logarithms in the evolution of a jet. *JHEP* **02**, 075 (2018).
63. Sjostrand, T., Mrenna, S. & Skands, P. Z. PYTHIA 6.4 Physics and Manual. *JHEP* **05**, 026 (2006).
64. Bahr, M. *et al.* Herwig++ Physics and Manual. *Eur. Phys. J.* **C58**, 639 (2008).
65. Alioli, S., Nason, P., Oleari, C. & Re, E. A general framework for implementing NLO calculations in shower Monte Carlo programs: the POWHEG BOX. *JHEP* **06**, 043 (2010).
66. Banfi, A., Dasgupta, M., Khelifa-Kerfa, K. & Marzani, S. Non-global logarithms and jet algorithms in high-pT jet shapes. *JHEP* **08**, 064 (2010).
67. Duran Delgado, R. M., Forshaw, J. R., Marzani, S. & Seymour, M. H. The dijet cross section with a jet veto. *JHEP* **08**, 157 (2011).
68. Ball, R. D. *et al.* Parton distributions with LHC data. *Nucl. Phys.* **B867**, 244 (2013).
69. Sjöstrand, T., Ask, S., Christiansen, J. R., Corke, R., Desai, N., Ilten, P., Mrenna, S., Prestel, S., Rasmussen, C. O. & Skands, P. Z. An Introduction to PYTHIA 8.2. *Comput. Phys. Commun.* **191**, 159 (2015).
70. Forshaw, J., Keates, J. & Marzani, S. Jet vetoing at the LHC. *JHEP* **07**, 023 (2009).
71. Höche, S., Reichelt, D. & Siegert, F. Momentum conservation and unitarity in parton showers and NLL resummation. *JHEP* **01**, 118 (2018).
72. Andersen, J. R. & Smillie, J. M. Multiple Jets at the LHC with High Energy Jets. *JHEP* **06**, 010 (2011).
73. Andersen, J. R., Brooks, H. M. & Lönnblad, L. Merging High Energy with Soft and Collinear Logarithms using HEJ and PYTHIA. *JHEP* **09**, 074 (2018).
74. Frixione, S. Isolated photons in perturbative QCD. *Phys. Lett.* **B429**, 369 (1998).
75. Catani, S., Cieri, L., de Florian, D., Ferrera, G. & Grazzini, M. Diphoton production at hadron colliders: a fully-differential QCD calculation at NNLO. *Phys. Rev. Lett.* **108**. [Erratum: *Phys. Rev. Lett.* **117**, no.8, 089901 (2016)], 072001 (2012).
76. Campbell, J. M., Ellis, R. K., Li, Y. & Williams, C. Predictions for diphoton production at the LHC through NNLO in QCD. *JHEP* **07**, 148 (2016).
77. Campbell, J. M., Ellis, R. K. & Williams, C. Direct Photon Production at Next-to-Next-to-Leading Order. *Phys. Rev. Lett.* **118**, 222001 (2017).
78. Catani, S., Fontannaz, M., Guillet, J. P. & Pilon, E. Cross-section of isolated prompt photons in hadron hadron collisions. *JHEP* **05**, 028 (2002).
79. Becher, T. & Schwartz, M. D. Direct photon production with effective field theory. *JHEP* **02**, 040 (2010).
80. Becher, T., Bell, G., Lorentzen, C. & Marti, S. Transverse-momentum spectra of electroweak bosons near threshold at NNLO. *JHEP* **02**, 004 (2014).
81. Aad, G. *et al.* Measurement of the inclusive isolated prompt photon cross section in pp collisions at  $\sqrt{s} = 8$  TeV with the ATLAS detector. *JHEP* **08**, 005 (2016).
82. Catani, S., Fontannaz, M., Guillet, J. P. & Pilon, E. Isolating Prompt Photons with Narrow Cones. *JHEP* **09**, 007 (2013).

83. Gordon, L. E. & Vogelsang, W. Polarized and unpolarized prompt photon production beyond the leading order. *Phys. Rev.* **D48**, 3136 (1993).
84. Gluck, M., Reya, E. & Vogt, A. Parton fragmentation into photons beyond the leading order. *Phys. Rev.* **D48**. [Erratum: *Phys. Rev.* **D51**, 1427(1995)], 116 (1993).
85. Bourhis, L., Fontannaz, M. & Guillet, J. P. Quarks and gluon fragmentation functions into photons. *Eur. Phys. J.* **C2**, 529 (1998).
86. Aad, G. *et al.* Measurement of  $W^+W^-$  production in pp collisions at  $\sqrt{s}=7$  TeV with the ATLAS detector and limits on anomalous WWZ and  $WW\gamma$  couplings. *Phys. Rev.* **D87**. [Erratum: *Phys. Rev.* **D88**, no.7, 079906(2013)], 112001 (2013).
87. Chatrchyan, S. *et al.* Measurement of the  $W^+W^-$  Cross Section in  $pp$  Collisions at  $\sqrt{s} = 7$  TeV and Limits on Anomalous  $WW\gamma$  and WWZ Couplings. *Eur. Phys. J.* **C73**, 2610 (2013).
88. Banfi, A., Salam, G. P. & Zanderighi, G. NLL+NNLO predictions for jet-veto efficiencies in Higgs-boson and Drell-Yan production. *JHEP* **06**, 159 (2012).
89. Becher, T. & Neubert, M. Factorization and NNLL Resummation for Higgs Production with a Jet Veto. *JHEP* **07**, 108 (2012).
90. Banfi, A., Monni, P. F., Salam, G. P. & Zanderighi, G. Higgs and Z-boson production with a jet veto. *Phys. Rev. Lett.* **109**, 202001 (2012).
91. Becher, T., Neubert, M. & Rothen, L. Factorization and  $N^3LL_p$ +NNLO predictions for the Higgs cross section with a jet veto. *JHEP* **10**, 125 (2013).
92. Stewart, I. W., Tackmann, F. J., Walsh, J. R. & Zuberi, S. Jet  $p_T$  resummation in Higgs production at  $NNLL' + NNLO$ . *Phys. Rev.* **D89**, 054001 (2014).
93. Becher, T., Frederix, R., Neubert, M. & Rothen, L. Automated NNLL + NLO resummation for jet-veto cross sections. *Eur. Phys. J.* **C75**, 154 (2015).
94. Hornig, A., Kang, D., Makris, Y. & Mehen, T. Transverse Vetoes with Rapidity Cutoff in SCET. *JHEP* **12**, 043 (2017).
95. Becher, T., Rahn, R. & Shao, D. Y. Non-global and rapidity logarithms in narrow jet broadening. *JHEP* **10**, 030 (2017).
96. Caron-Huot, S. Resummation of non-global logarithms and the BFKL equation. *JHEP* **03**, 036 (2018).
97. Kunszt, Z. & Trocsanyi, Z. QCD corrections to photon production in association with hadrons in  $e^+e^-$  annihilation. *Nucl. Phys.* **B394**, 139 (1993).
98. Hatta, Y. Relating  $e^+e^-$  annihilation to high energy scattering at weak and strong coupling. *JHEP* **11**, 057 (2008).
99. Avsar, E., Hatta, Y. & Matsuo, T. Soft gluons away from jets: Distribution and correlation. *JHEP* **06**, 011 (2009).
100. Hatta, Y. & Ueda, T. Resummation of non-global logarithms at finite  $N_c$ . *Nucl. Phys.* **B874**, 808 (2013).
101. Larkoski, A. J., Moult, I. & Neill, D. Non-Global Logarithms, Factorization, and the Soft Substructure of Jets. *JHEP* **09**, 143 (2015).
102. Neill, D. The Edge of Jets and Subleading Non-Global Logs (2015).

103. Larkoski, A. J., Moulst, I. & Neill, D. The Analytic Structure of Non-Global Logarithms: Convergence of the Dressed Gluon Expansion. *JHEP* **11**, 089 (2016).
104. Becher, T., Pecjak, B. D. & Shao, D. Y. Factorization for the light-jet mass and hemisphere soft function. *JHEP* **12**, 018 (2016).
105. Neill, D. The Asymptotic Form of Non-Global Logarithms, Black Disc Saturation, and Gluonic Deserts. *JHEP* **01**, 109 (2017).
106. Neill, D. Non-Global and Clustering Effects for Groomed Multi-Prong Jet Shapes. *JHEP* **02**, 114 (2019).
107. Dasgupta, M., Khelifa-Kerfa, K., Marzani, S. & Spannowsky, M. On jet mass distributions in Z+jet and dijet processes at the LHC. *JHEP* **10**, 126 (2012).
108. Chien, Y.-T., Kelley, R., Schwartz, M. D. & Zhu, H. X. Resummation of Jet Mass at Hadron Colliders. *Phys. Rev.* **D87**, 014010 (2013).
109. Liu, Z. L., Li, C. S., Wang, J. & Wang, Y. Resummation prediction on the jet mass spectrum in one-jet inclusive production at the LHC. *JHEP* **04**, 005 (2015).
110. Idilbi, A. & Kim, C. Factorization of the Jet Mass Distribution in the Small  $R$  Limit. *J. Korean Phys. Soc.* **73**, 1230 (2018).
111. Kang, Z.-B., Lee, K., Liu, X. & Ringer, F. The groomed and ungroomed jet mass distribution for inclusive jet production at the LHC. *JHEP* **10**, 137 (2018).
112. Becher, T. & Neubert, M. Toward a NNLO calculation of the anti-B  $\rightarrow$  X(s) gamma decay rate with a cut on photon energy. II. Two-loop result for the jet function. *Phys. Lett.* **B637**, 251 (2006).
113. Becher, T. & Bell, G. The gluon jet function at two-loop order. *Phys. Lett.* **B695**, 252 (2011).
114. Brüser, R., Liu, Z. L. & Stahlhofen, M. Three-Loop Quark Jet Function. *Phys. Rev. Lett.* **121**, 072003 (2018).
115. Banerjee, P., Dhani, P. K. & Ravindran, V. Gluon jet function at three loops in QCD. *Phys. Rev.* **D98**, 094016 (2018).
116. Cal, P., Ringer, F. & Waalewijn, W. J. The jet shape at NLL'. *JHEP* **05**, 143 (2019).
117. Becher, T. & Neubert, M. Threshold resummation in momentum space from effective field theory. *Phys. Rev. Lett.* **97**, 082001 (2006).
118. Buskulic, D. *et al.* Properties of hadronic Z decays and test of QCD generators. *Z. Phys.* **C55**, 209 (1992).
119. Abbate, R., Fickinger, M., Hoang, A. H., Mateu, V. & Stewart, I. W. Thrust at N<sup>3</sup>LL with Power Corrections and a Precision Global Fit for  $\alpha_s(m_Z)$ . *Phys. Rev.* **D83**, 074021 (2011).
120. Gehrmann-De Ridder, A., Gehrmann, T., Glover, E. W. N. & Heinrich, G. NNLO corrections to event shapes in  $e^+ e^-$  annihilation. *JHEP* **12**, 094 (2007).
121. Weinzierl, S. Event shapes and jet rates in electron-positron annihilation at NNLO. *JHEP* **06**, 041 (2009).
122. Del Duca, V., Duhr, C., Kardos, A., Somogyi, G. & Trócsányi, Z. Three-Jet Production in Electron-Positron Collisions at Next-to-Next-to-Leading Order Accuracy. *Phys. Rev. Lett.* **117**, 152004 (2016).

123. Sjostrand, T., Mrenna, S. & Skands, P. Z. A Brief Introduction to PYTHIA 8.1. *Comput. Phys. Commun.* **178**, 852 (2008).
124. Korchemsky, G. P. *Shape functions and power corrections to the event shapes in QCD and high energy hadronic interactions. Proceedings, 33rd Rencontres de Moriond, Les Arcs, France, March 21-28, 1998* [,179(1998)] (1998), 489.
125. Korchemsky, G. P. & Sterman, G. F. Power corrections to event shapes and factorization. *Nucl. Phys.* **B555**, 335 (1999).
126. Frixione, S. & Webber, B. R. Matching NLO QCD computations and parton shower simulations. *JHEP* **06**, 029 (2002).
127. Nason, P. A New method for combining NLO QCD with shower Monte Carlo algorithms. *JHEP* **11**, 040 (2004).
128. Dulat, F., Höche, S. & Prestel, S. Leading-Color Fully Differential Two-Loop Soft Corrections to QCD Dipole Showers. *Phys. Rev.* **D98**, 074013 (2018).
129. Nagy, Z. & Soper, D. E. Parton showers with quantum interference. *JHEP* **09**, 114 (2007).
130. Cohen, T. As Scales Become Separated: Lectures on Effective Field Theory. *PoS TASI2018*, 011 (2019).
131. Dokshitzer, Y. L., Khoze, V. A. & Troian, S. Particle spectra in light and heavy quark jets (1991).
132. Dokshitzer, Y. L., Khoze, V. A. & Troian, S. On specific QCD properties of heavy quark fragmentation ('dead cone') (1991).
133. Maltoni, F., Selvaggi, M. & Thaler, J. Exposing the dead cone effect with jet substructure techniques. *Phys. Rev. D* **94**, 054015 (2016).
134. Aad, G. *et al.* Measurement of  $t\bar{t}$  production with a veto on additional central jet activity in pp collisions at  $\sqrt{s} = 7$  TeV using the ATLAS detector. *Eur. Phys. J. C* **72**, 2043 (2012).
135. Fadin, V. S., Khoze, V. A. & Martin, A. D. Interference radiative phenomena in the production of heavy unstable particles. *Phys. Rev. D* **49**, 2247 (1994).
136. Fadin, V. S., Khoze, V. A. & Martin, A. D. How suppressed are the radiative interference effects in heavy instable particle production? *Phys. Lett. B* **320**, 141 (1994).
137. Melnikov, K. & Yakovlev, O. I. Top near threshold: All  $\alpha$ -S corrections are trivial. *Phys. Lett. B* **324**, 217 (1994).
138. Melnikov, K. & Yakovlev, O. I. Final state interaction in the production of heavy unstable particles. *Nucl. Phys. B* **471**, 90 (1996).
139. Beenakker, W., Berends, F. A. & Chapovsky, A. One loop QCD interconnection effects in pair production of top quarks. *Phys. Lett. B* **454**, 129 (1999).
140. Denner, A., Dittmaier, S. & Roth, M. Nonfactorizable photonic corrections to  $e^+ e^- \rightarrow W W \rightarrow$  four fermions. *Nucl. Phys. B* **519**, 39 (1998).
141. Neubert, M. Heavy quark symmetry. *Phys. Rept.* **245**, 259 (1994).
142. Manohar, A. V. & Wise, M. B. *Heavy quark physics* (2000).
143. Becher, T. & Neubert, M. Infrared singularities of QCD amplitudes with massive partons. *Phys. Rev. D* **79**. [Erratum: *Phys.Rev.D* 80, 109901 (2009)], 125004 (2009).

144. Ahrens, V., Ferroglia, A., Neubert, M., Pecjak, B. D. & Yang, L. L. Renormalization-Group Improved Predictions for Top-Quark Pair Production at Hadron Colliders. *JHEP* **09**, 097 (2010).
145. Householder, A. S. Unitary Triangularization of a Nonsymmetric Matrix. *J. ACM* **5**, 339–342 (1958).
146. Catani, S., Trentadue, L., Turnock, G. & Webber, B. Resummation of large logarithms in  $e^+ e^-$  event shape distributions. *Nucl. Phys. B* **407**, 3 (1993).
147. Frixione, S., Nason, P. & Oleari, C. Matching NLO QCD computations with Parton Shower simulations: the POWHEG method. *JHEP* **11**, 070 (2007).
148. Dasgupta, M. & Salam, G. P. Event shapes in  $e^+ e^-$  annihilation and deep inelastic scattering. *J. Phys. G* **30**, R143 (2004).
149. Frixione, S., Nason, P. & Webber, B. R. Matching NLO QCD and parton showers in heavy flavor production. *JHEP* **08**, 007 (2003).
150. Hagiwara, Y., Hatta, Y. & Ueda, T. Hemisphere jet mass distribution at finite  $N_c$ . *Phys. Lett. B* **756**, 254 (2016).
151. Weigert, H. Nonglobal jet evolution at finite  $N(c)$ . *Nucl. Phys. B* **685**, 321 (2004).
152. Nagy, Z. & Soper, D. E. Effects of subleading color in a parton shower. *JHEP* **07**, 119 (2015).
153. Isaacson, J. & Prestel, S. Stochastically sampling color configurations. *Phys. Rev. D* **99**, 014021 (2019).
154. Nagy, Z. & Soper, D. E. Parton showers with more exact color evolution. *Phys. Rev. D* **99**, 054009 (2019).
155. Forshaw, J. R., Holguin, J. & Plätzer, S. Parton branching at amplitude level. *JHEP* **08**, 145 (2019).
156. Höche, S. & Reichelt, D. Numerical resummation at sub-leading color in the strongly ordered soft gluon limit (2020).
157. Forshaw, J. R., Holguin, J. & Plätzer, S. Building a consistent parton shower (2020).
158. Andreassen, A. & Schwartz, M. D. Reducing the Top Quark Mass Uncertainty with Jet Grooming. *JHEP* **10**, 151 (2017).
159. Hoang, A. H., Mantry, S., Pathak, A. & Stewart, I. W. Extracting a Short Distance Top Mass with Light Grooming. *Phys. Rev. D* **100**, 074021 (2019).



## **Declaration of consent**

on the basis of Article 18 of the PromR Phil.-nat. 19

Name/First Name: Balsiger Marcel

Registration Number: 10-102-705

Study program: PhD Physics

Bachelor ☐

Master ☐

Dissertation ☒

Title of the thesis: Resummation of Non-Global Logarithms

Supervisor: Prof. Dr. Thomas Becher

I declare herewith that this thesis is my own work and that I have not used any sources other than those stated. I have indicated the adoption of quotations as well as thoughts taken from other authors as such in the thesis. I am aware that the Senate pursuant to Article 36 paragraph 1 litera r of the University Act of September 5th, 1996 and Article 69 of the University Statute of June 7th, 2011 is authorized to revoke the doctoral degree awarded on the basis of this thesis.

For the purposes of evaluation and verification of compliance with the declaration of originality and the regulations governing plagiarism, I hereby grant the University of Bern the right to process my personal data and to perform the acts of use this requires, in particular, to reproduce the written thesis and to store it permanently in a database, and to use said database, or to make said database available, to enable comparison with theses submitted by others.

Bern, 24.09.2020

Place/Date

Signature



